The Mass Transfer and Hydrodynamics of a Gas - Liquid Centrifugal De-oxygenator

by

James R.A.Peel, MEng.

Thesis submitted for the Degree of Doctor of Philosophy
Faculty of Engineering, University of Newcastle-upon-Tyne

October 1995

Dept. of Chemical and Process Engineering
University of Newcastle-upon-Tyne

To God be the Glory :

" Where is the wise man ? Where is the scholar ? Where is the philosopher of this age ? Has not God made foolish the wisdom of the world ? .....For the foolishness of God is wiser than man's wisdom, and the weakness of God is stronger than man's strength.

.....God chose the foolish things of the world to shame the wise; God chose the weak things of the world to shame the strong. "

1 Corinthians ch.1 vs.20 - 27
(New Testament (N.I.V.))

" Of making many books there is no end, and much study wearies the body. Now all has been heard; here is the conclusion of the matter :

Fear God and keep his commandments, for this is the whole duty of man. "

Ecclesiastes ch.12 vs.12 - 13
(Old Testament (N.I.V.))

Acknowledgements

I would like to express my sincere thanks and appreciation for the many people who have helped me during my three years of research and made this thesis a reality. In particular my thanks goes to Dr. Colin Howarth whose supervision and help throughout the last three years has been invaluable to me, and made my thesis an enjoyable experience. Special thanks also go to Professor Colin Ramshaw and Dr. Craig Branch whose expert contributions to this thesis far outweigh my own.

Many thanks go to Mr. Eric Horsley who spent many hours not only taking the photographic work for this thesis but also developing the films, and making much of the experimental work very interesting and great fun. Special mention and thanks must also go to Mr. Brian Grover who's expertise and help in the design and manufacture of the rotor used made all this work possible, and for all his suggestions regarding any modifications that needed to be made during the three years. I would also like to mention and thank Mr. Vince Scott who spent a long time making circuit boards for the optical diodes used in the tracer experimental work.

Many other people associated both with and outside the Department of Chemical and Process Engineering at the University of Newcastle-upon-Tyne have made my time here a very memorable and enjoyable one, and although I can not mention everyone by name I would like to say a big THANK YOU to you all.

Finally special recognition goes to my father, the Department of Chemical Engineering at Newcastle University, Vortoil, and Proctor and Gamble who have all contributed financially to this programme of research and made it all possible.

Abstract

The mass transfer and hydrodynamic characteristics of a packed rotary contactor with a continuous liquid phase for the de-oxygenation of water using a stripping gas has been investigated. The primary purpose of this research was to gain a clearer understanding of the physical processes that occur within packings between the gas and liquid phases in an increased gravitational environment. The eventual aim is to design and develop a more efficient and cost effective industrial piece of equipment for the removal of dissolved oxygen from river or sea water.

The mass transfer between two phases is directly related to the interfacial area which, in turn, is dependant on the gas bubble size. The use of centrifugal acceleration to generate increased gravitational environments leads to smaller bubbles being produced, with subsequent improvements in the mass transfer. In order to produce this increased gravitational environment, a one metre diameter rotor filled with a torus shaped packing was rotated between 200 and 400 rpm, with the gas phase dispersed in the liquid phase and passing through counter-currently.

An examination of the overall gas and liquid flow through the packing in the rotor using visual and tracer techniques has been made which shows that the gas nozzle design and liquid flowrate are the two dominant parameters in achieving an effective and uniform distribution throughout. The gas bubble sizes produced have been visually analysed throughout the packing, and found to range from between 0.4 - 1.0 mm in diameter. The mass transfer achieved in the rotor showed general trends of increasing with the gas flowrate and rotational speed, whilst falling as the liquid flowrate increased. For the entire range of rotor operating conditions, the number of mass transfer units achieved was found to lie in the range 1.5 - 4.5, and the corresponding height of a transfer unit between 4.5 - 12 cm.

Key Words : Mass Transfer, Hydrodynamics, Packed Rotary Contactor, Continuous Liquid Phase, Increased Gravitational Environment, De-Oxygenation of Water, Centrifugal Acceleration

TABLE OF CONTENTS

Headings		Page No.
Acknowledgements		
Abstract		
Chapter 1	**Introduction**	1
	1.1 Background	1
	1.2 Scope of Investigation	3
Chapter 2	**Gas - Liquid Separation**	4
	2.1 General Separation Processes	4
	2.2 Current Industrial Operations for Oxygen Stripping	6
	2.3 Theory of Gas Stripping	7
	2.4 Design of Stripping Columns	10
	2.4.1 Mass Transfer Design	11
	2.4.2 Column Design	13
	2.5 Mass Transfer Coefficients	14
	2.5.1 Theoretical Analysis	15
	2.5.2 Experimental Analysis	17
	2.6 Hydrodynamic Studies	20
	2.6.1 Flow Regimes	20
	2.6.1.1. Ideal Flow	20
	2.6.1.2. Non-Ideal Flow	21
	2.6.1.2.1. Axial Dispersion Model	21
	2.6.1.2.2. Tanks in Series Model	24
	2.6.1.2.3. Multi-Parameter Models	24
	2.6.2 Bubble Size	26
	2.6.2.1. Bubble Formation	26
	2.6.2.2. Effect of Splitting	29
	2.6.2.3. Effect of Coalescence	30
	2.6.2.4. Effect of Superficial Gas Velocity	32
	2.6.3. Bubble Velocity	33
	2.6.4. Hold-Up	35
	2.7 Effect of High Gravitational Fields	38
	2.7.1. Current Commercial Applications	39
	2.7.2. Advantages of Increasing the Gravitational Acceleration	39

	Headings	Page No.
Chapter 3	**Design of a Continuous Liquid Phase Rotor**	41
	3.1 History and Development	41
	3.2 Mark I Rotor	42
	3.2.1. Results	43
	3.3 Mark II Rotor	44
	3.3.1 Mechanical Design	44
	3.3.2 Experimental Set-Up	48
	3.3.3 Oxygen Concentration Analysis	49
	3.3.3.1 Oxygen Probe	50
	3.3.3.2 Sampling Technique	51
	3.3.4 Photographic Equipment	51
	3.3.5 Rotor Design Modifications	52
	3.3.5.1 Nitrogen Blanket System	52
	3.3.5.2 Gas Injector Nozzles	53
	3.3.5.3 Liquid Sampling System	56
	3.3.5.4 Tracer Sensors \ Equipment	58
Chapter 4	**Modelling of a Packed Gas-Liquid Rotor**	60
	4.1 Rotor Hydrodynamics	60
	4.1.1 Gas Hold-up	60
	4.1.2 Gas Bubble Formation	62
	4.1.3 Gas Bubble Size	63
	4.1.4 Gas Bubble Velocity	65
	4.2 Liquid Mass Transfer Coefficient	66
	4.3 Computer Model of Rotor	67
	4.4 Model Results	71
	4.4.1 Gas Hold-up	71
	4.4.2 Gas Bubble Size	72
	4.4.3 Gas Bubble Velocity	73
	4.4.4 Mass Transfer Performance	74
	4.5 Discussion	77

	Headings	Page No.
Chapter 5	**Hydrodynamic Characteristics of the 1m diameter Rotor**	79
	5.1 Introduction	79
	5.2 Overall Rotor Hydrodynamics	79
	5.2.1 Original Gas Injector Nozzles	80
	5.2.2 Modified Gas Nozzles (Increased Gas Velocity)	83
	5.2.3 Modified Gas Nozzles (Reduced Orifice Diameter)	83
	5.3 Liquid Phase Hydrodynamics	86
	5.3.1 Calibration of Optical Diode	87
	5.3.2 Data Processing and Analysis	87
	5.3.3 Experimental Results	88
	5.3.3.1 End Effects	88
	5.3.3.2 Tracer Input Signal	90
	5.3.3.3 Initial Tracer Output Response	91
	5.3.3.4 Tracer Output at Full Packed Length	92
	5.3.3.5 Tracer Output at 1/2 Packed Length	95
	5.3.4 Mathematical Modelling	96
	5.4 Gas Phase Hydrodynamics	98
	5.5 Salt Water	107
	5.6 Discussion	110
Chapter 6	**Mass Transfer Performance of the 1m diameter Rotor**	112
	6.1 Introduction	112
	6.2 Initial Mass Transfer Findings	112
	6.3 Mass Transfer Analysis using Modified Sampling System	114
	6.4 Mass Transfer Analysis using Radial Vanes	116
	6.5 Overall Rotor Mass Transfer Performance	118
	6.5.1 Declon HC20 Packing	119
	6.5.2 Declon HC30 Packing	120
	6.5.3 Conclusions	121
	6.6 Salt Water	122
	6.7 Discussion	123

Headings **Page No.**

Chapter 7 Conclusions 126

7.1 Rotor Model 126
7.2 Rotor Hydrodynamics 126
7.3 Rotor Mass Transfer 128

Chapter 8 Recommendations for Future Work 130

Nomenclature 132

Bibliography 135

Appendices

Appendix I : Fortran Computer Model Listing
Appendix II : MathCad Model for Tracer Response
Appendix III : Gas and Liquid Flowrate Correction Methods
Appendix IV : Inferred Method of Calculation of Mass Transfer and Initial Results
Appendix V : Initial Mass Transfer Results at Different Radial Positions in Rotor
Appendix VI : Mass Transfer Results using Radial Vanes
Appendix VII : Overall Mass Rotor Mass Transfer Results
Appendix VIII : Repeated Results
Appendix IX : Miscellaneous Rotor Photographic Work

Publications

CHAPTER 1 : INTRODUCTION

1.1 Background

This thesis is concerned with a relatively new and exciting concept in the field of Chemical Engineering known as *Process Intensification*. Process Intensification is the science of intensifying transport processes, such as heat and mass transfer, with the aim of reducing the size of main plant items, and ultimately the total size of a chemical plant required to achieve a given production objective. The primary incentive for doing this is to reduce the overall cost of a production system but further benefits may include improved safety standards, shorter response times, or higher achievable throughputs. Table 1.1 shows a cost analysis of a plant, and as can be seen, a surprisingly large proportion of the total cost is taken up with piping, support structures and other civil engineering items. If the size of the equipment could be reduced by a factor of 100 - 1000, then major opportunities for capital savings on a plant system could be made.

Table 1.1 : Capital Cost Breakdown of a 90,000 TPA Ammonium Sulphate Plant[1]

	Unit	Spares	Installation	Insulation/ Painting	Design	Extras	Total
Mechanical	26.1	1.2	8.1	2.5	1.3	2.6	42.0
Civil	7.4			0.9	1.3	1.3	10.9
Structure	8.3			1.0	1.3	1.3	12.9
Pipework	13.8		4.3	1.5	0.2	2.0	21.8
Instruments	4.5	0.1	0.8		1.0	0.9	7.4
Electrical	1.6		0.1		0.3	0.2	2.3
Control room	2.4				0.4	0.4	3.1
Total	64.1	1.3	13.3	6.8	5.8	8.6	100.0

(Figures in Table represent the % of the total plant cost)

A prime target for Process Intensification must be the offshore oil industry where space and weight are of crucial importance, and the need for light and compact equipment is very great. One such process used in the offshore industry is water de-oxygenation, where currently the dissolved oxygen concentration levels in the water are reduced from 9 parts per million (ppm) to 20 parts per billion (ppb) using a traditional counter current stripping column with a stripping gas, typically methane. The purpose in stripping dissolved oxygen from water is so that water can be used in the **secondary recovery** of the oil from the well, without microbiological growth, which leads to contamination of the oil and fouling of the drilling

apparatus and pipelines, occurring. The production life of an oil well can be clearly defined in three stages :

Primary Recovery : The recovery of oil by natural drive mechanisms - those being gas cap drive, solution gas, water influx, or gravity drainage.

Secondary Recovery : The recovery of oil using techniques such as gas or water injection in order to maintain the pressure in the well.

Tertiary Recovery : This refers to any technique applied after the secondary stage and these are usually Enhanced Oil Recovery (E.O.R.) techniques.

(E.O.R. is oil recovery by the injection of materials not normally present in the well, and all E.O.R. uses either thermal, chemical, or solvent methods.[2])

A time will come in the life of an oil field when the natural pressure of the reservoir has declined to such an extent where it is no longer sufficiently large enough to force the oil out of the pores in the rock into the bottom of the well. The simplest method of then forcing the oil out of the reservoir rock is by direct displacement with another fluid. When water is used the secondary recovery process is called 'water flooding', and whereas about 20% of the oil is typically recovered during the primary stage process, it is not uncommon for the secondary stage to recover a further 20% or more of the oil[3]. It can therefore be seen that the secondary recovery process plays a significant part in the total quantity of oil extracted from the well, and hence the overall profitability. At present water de-oxygenation is achieved using a conventional packed or plate column which, in terms of manufacturing costs, is very costly due to the column size and the extra platform support needed. It must therefore be very apparent that if significant size reduction could be found in the process of removing oxygen from sea water, then this would greatly impact the overall profitability of the well.

One such possibility is the use of Higee[4,5] techniques which utilise centrifugal force to intensify mass and heat transfer between phases. Higee may be applicable to a number of different fields of chemical engineering, such as gas scrubbing and fermentation, but the focus of this research examines the application of Higee to the process of removing oxygen from water, and assesses the future potential development of this process for the oil industry. The traditional stripping column operates under a '1-g' environment with the liquid and gas throughputs limited by the relative forces experienced by each phase under the same environment. If this limit is exceeded then the phenomenon known as flooding will occur in the column with a resulting loss in performance. If a packing is used in the column to improve the contact time and surface area between the gas and liquid, and therefore the amount of mass transfer, the problem of flooding is accentuated. However the imposition of much higher gravitational accelerations, typically 100 g, should permit either the gas flow or packing surface area, a_t, to be increased, and therefore profoundly impact the mass transfer performance and the hydraulic capacity of the system[6]. In addition previous research and mathematical theories[7,8] have shown that the average bubble size decreases as the centrifugal

field increases, and this decrease in bubble size logically suggests that there is an increase in the interfacial area between the gas and liquid, and hence an improved mass transfer performance. Sherwood[9] showed that flooding in a column was linked to the group, $u_g^2 a_t/g\varepsilon^3$, and so an increase in g allows an increase in the gas velocity, u_g, and therefore the hydraulic capacity before the onset of flooding occurs (see Fig. 2.8).

1.2 Scope of Investigation

To achieve an environment of high gravitational acceleration a variety of rotary machines have been designed and built to generate large centrifugal accelerations. A few small diameter prototype packed machines have been built and tested but these were essentially 'black box' units with only input and output measurements. If these machines are to be scaled it will be necessary to design and manufacture a 1 m diameter rotary machine, the performance and operation of one segment of such a machine being the focus of this research, but with the important facility of observing the hydrodynamics and mass transfer *within* the machine being incorporated into the research. The full design details and specifications of the 1 m diameter rotor are given in Chapter 3 of this thesis. As the field of Process Intensification is a relatively new concept there is presently limited knowledge and understanding of the hydrodynamic characteristics of the gas and liquid phases as they pass through centrifugally created high gravitational environments. The aim of this thesis is therefore to further investigate the flow characteristics and the resulting mass transfer achieved between the gas and liquid, which for this research is nitrogen and water, to examine the effect of the gas flowrate, liquid flowrate, speed of rotation, and packing pore size on the mass transfer performance of the rotor, and to see how the experimental findings correspond with theoretically predicted results. It is hoped that with the findings of this research a greater understanding of Higee phenomena may lead to a more efficient and cost effective design of current industrial processes, in particular that of the removal of oxygen from water.

CHAPTER 2. GAS - LIQUID SEPARATION

The objective of the following chapter is to place the subject of this research into its relevant context. The chapter begins by looking at some general separation techniques currently used in the chemical industry, and then more specifically examines the removal of a dissolved gas from a liquid, a process commonly known as **Stripping**. Following this the general design approach and operation of stripping columns is detailed leading to equations for predicting the height and width of a column for the required mass transfer duty, and liquid and gas throughputs. The mass transfer coefficient is a key parameter in predicting the transfer that occurs between the two phases, and both experimental correlations and theoretical equations for estimating the mass transfer coefficient for the stripping of oxygen from water are investigated. The hydrodynamics that occur inside the column are also of fundamental importance in the overall performance of the unit. These include the flow patterns of the two phases through the column, the bubble formation, the bubble velocity, and the bubble splitting and coalescence inside the packing. All these parameters will effect the contact time and area between the gas and liquid and therefore the mass transfer that occurs.

Finally turning from the current industrial methods and operating environment, the concept of Higee is introduced, and the potential benefits in performance cost and efficiency that this may make for the stripping of dissolved oxygen from water are assessed.

2.1 General Separation Processes

There are a wide range of separation techniques used in the chemical industry today and these separation processes significantly impact the total industrial energy consumption, manufacturing profits, and product costs for the consumer. It is estimated that these processes make up 40%-70% of both capital and operating costs for many industries, and in the chemical and petroleum industries approximately 43% of the total energy consumed is by separation processes.[10] Table 2.1 summarises the various commercial separation techniques used in the chemical industry :

Table 2.1 Commercial Separation Processes[10]

Process	Separation Property	Separating Agent	Major Area of Use
Absorption	Solubility	Liquid	Separating gas mixtures Acid gas removal
Adsorption & Ion Exchange	Affinity	Adsorbent	Xylene Separations Solvent Recovery
Chromatography	Affinity	Adsorbent	Separation of sugars
Crystallization	Freezing point	Heat Transfer	Xylenes
Dialysis	Molecular size / polarity	Membrane material	Spent acid recovery
Distillation	Boiling point	Heat	Chemical / Petroleum mixtures
Drying	Boiling point	Heat	Ceramics/plastics/food
Electrodialysis	Charge/size	Membrane material	Water desalination
Electrolytic Processes	Charge	Electric energy	Metal winning
Evaporation	Boiling point	Heat	Desalination
Extraction	Solubility	Solvent	Caffeine from coffee
Filtration	Size	Filter material	Suspended solids in fluid
Flotation	Molecular attraction	Gas	Removal of oil/solids from water
Membranes	Size/solubility	Membrane material / Pressure	Water purification
Stripping	Volatility	Gas	Contaminants from wastewater
Thermal Diffusion	Molecular size / polarity	Membrane material / Pressure	Isotopes

The main technique used for separations in the chemical and petroleum industries is Distillation, which accounts for about 95% of all separation processes. However the separation method used as the subject matter of this thesis is Stripping, and more specifically, the removal of dissolved oxygen from water using an inert gas, typically nitrogen.

2.2 Current Industrial Stripping Methods for the Removal of Oxygen from Water

Water treatment in the oil or water industries is for one of two purposes :

(a) To remove undesirable gases from water

(b) To introduce a gas into water for the purpose of causing chemical or biochemical reactions.

This project is concerned only with (a). The traditional method of stripping oxygen or dissolved gases from water is to use either a Plate or Packed Column, and this section examines the current industrial performance and operation of these stripping columns for the removal of oxygen from water in the oil industry. Vacuum de-aeration is commonly used in industry but for this process it has several disadvantages. The main disadvantages are that other dissolved gases, such as carbon dioxide, would be removed leading to an increase in the pH of the water, and hence possible carbonate scale formation. Also because the column would be operating under vacuum conditions, it would be more expensive to manufacture and would weigh significantly more due to the increase in the required wall thickness of the vessel. As weight and cost is of primary importance for the offshore oil industry this technique is unlikely to be the most cost effective. Another important consideration however is the type of water used in the process. If the oil field is offshore then sea water, which contains a salt concentration of 3 - 3.5 % by weight, will be used, whereas if the oil well is located in-land then river water is most likely to be readily available. As will be seen the salt water behaviour differs significantly from that of ordinary river water, especially in the coalescence characteristics, and this needs to be accounted for in the design of the column.

(i) Off-Shore

The North Sea provides a ready source of gas and oil for which sea water would be used during the secondary recovery stage. During the late 70's, B.P. planned to reach a peak water injection rate of 450,00 b/d for its North Sea oil fields[11]. Figure 2.1 shows the design of the water injection system to be used on the off-shore platforms. Sea water is pumped aboard the platform by 4 submersible pumps each capable of generating 75,000 b/d. After the initial filtration, the sea water flows into two deoxygenation towers, part of the stream passing directly into the towers and the remainder via the platform utilities and gas coolers where the water temperature is raised from 8 °C - 12 °C. The deoxygenation towers are typically 4m in diameter and 10m high, and each have a capacity of 75,000 b/d. The oxygen level in the water is reduced from 8 ppm to less than 0.5 ppm by counterflow using the produced associated gas from the well. The remaining oxygen is removed using an oxygen scavenger typically ammonium bisulfite.

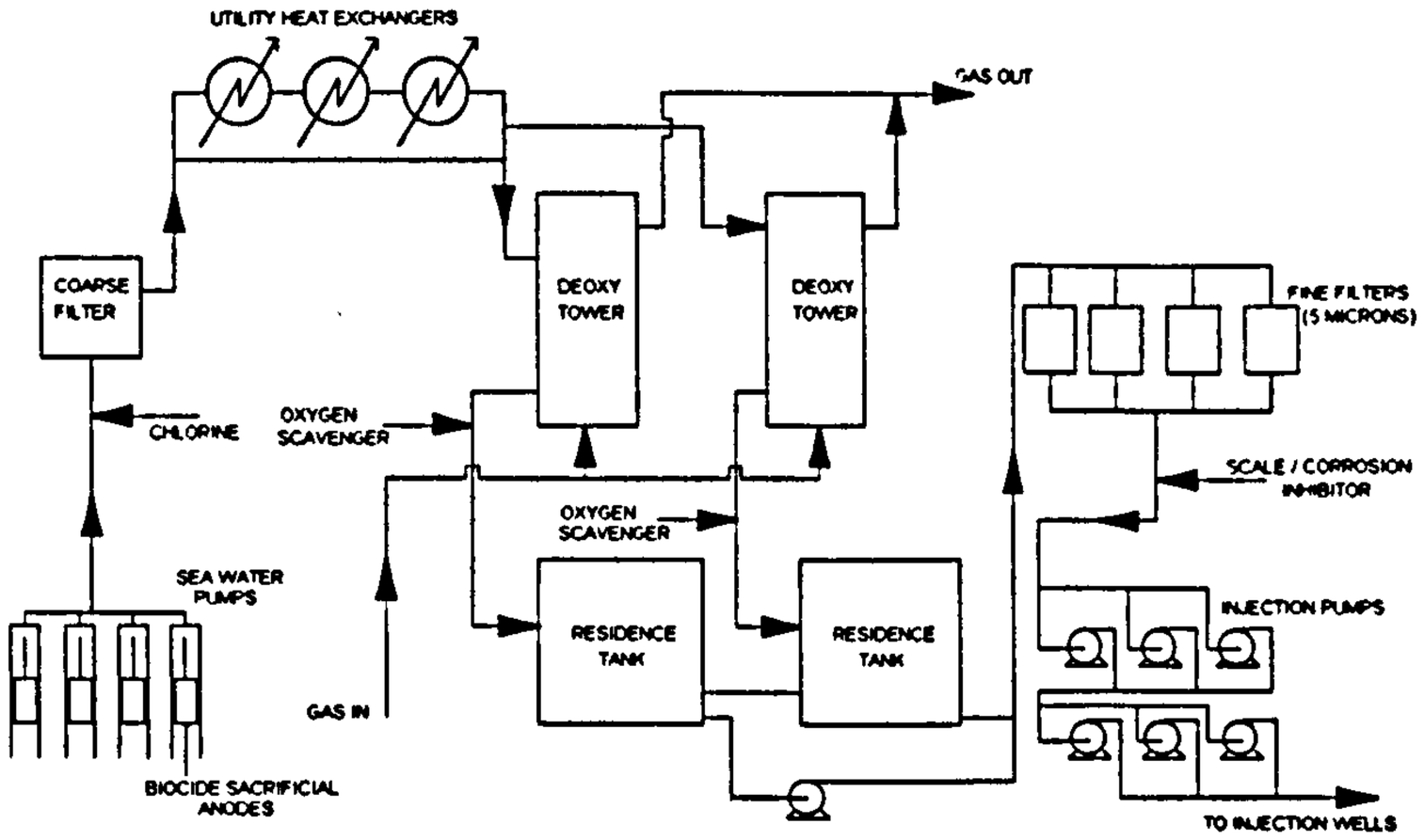

Figure 2.1 : Diagramatic Layout of a Field Water Injection System

(ii) In-Land

The design and operation of water de-aeration columns will vary slightly from off-shore to on-shore due to the type of water readily available. In Ohio 1130 b/d of ordinary river water was treated with 56 m^3/d of natural gas[12]. The column used was 0.5m in diameter and packed to a depth of 4 m. The dissolved oxygen concentration in the water fell from 11.7 ppm to 0.43 ppm. The Victory oil fields, Shandong in China use 4 de-oxygenation waters each 10m tall for treating 5000 tonnes/day of water and reducing the dissolved oxygen concentration from 10 ppm to less than 50 ppb.[13] In all oil recovery processes it is likely that natural gas will be used to strip the oxygen from the water as this will be the most readily available gas.

2.3 Theory of Gas Stripping

The relative success of gas stripping is dependant upon the equilibrium between the gas and water, and the greater the solubility of the gas in water, the easier the transfer. Henry's law states that the amount of any specific gas dissolved by a given volume of water, at constant temperature, is proportional to the partial pressure of the gas in equilibrium with the solution. In gas liquid processes true equilibrium is seldom achieved, but the equilibrium or saturation concentration of a gas in water at a given temperature and partial pressure is important as the difference between this concentration and the actual concentration represents the driving force for mass transfer between the two phases. The greater the difference the greater the driving force. (See Fig.2.2)

The transfer between the gas and water occurs at the gas-water interface. In the stripping of oxygen from water the transfer is occurring from the liquid phase into the gas

phase. The oxygen dissolved in the water reaches the interface through a diffusive mechanism, and the rate of diffusion depends upon the concentration gradient. Surface properties of the water influence the interchange between the water and the gas. A water surface film of orientated molecules acts as a barrier to the transfer of oxygen from the water into the gas bubbles, and oils, soaps, detergents and organic acids increase the barrier effect of this film whereas increased temperature and turbulence reduce the film resistance. The type of water used is therefore an important consideration when designing a stripping column as sea water properties for mass transfer will be more inhibitive than those of ordinary water. There is also a gas film resistance but this film resistance is small compared with the diffusion resistance.

Gases can be classified as very soluble, slightly soluble, or of intermediate solubility. With a very soluble gas, the moment the gas contacts the water it is absorbed into solution, and the liquid film does not significantly affect the absorption process, but is dependent on the diffusion of the gas through the gas film. Gases of low solubility, such as oxygen, have a low rate of absorption and the gas film is negligible compared with the diffusive process across the liquid film. Under these conditions in which the liquid film offers the principle resistance, the liquid at the interface may be assumed to be in equilibrium with the main body of the gas (i.e. $C_i \approx C_e$). With gases of intermediate solubility, both the liquid film and gas film are significant in the mass transfer process.

The rate of mass transfer is proportional to the difference between the actual and the equilibrium concentration of oxygen in water, C_e, the interfacial area between gas and liquid, a, and the overall mass tansfer coefficient, K_l, and can be expressed as follows:

$$\frac{dC}{dt} = K_l a\left(C - C_e\right) \qquad 2.0$$

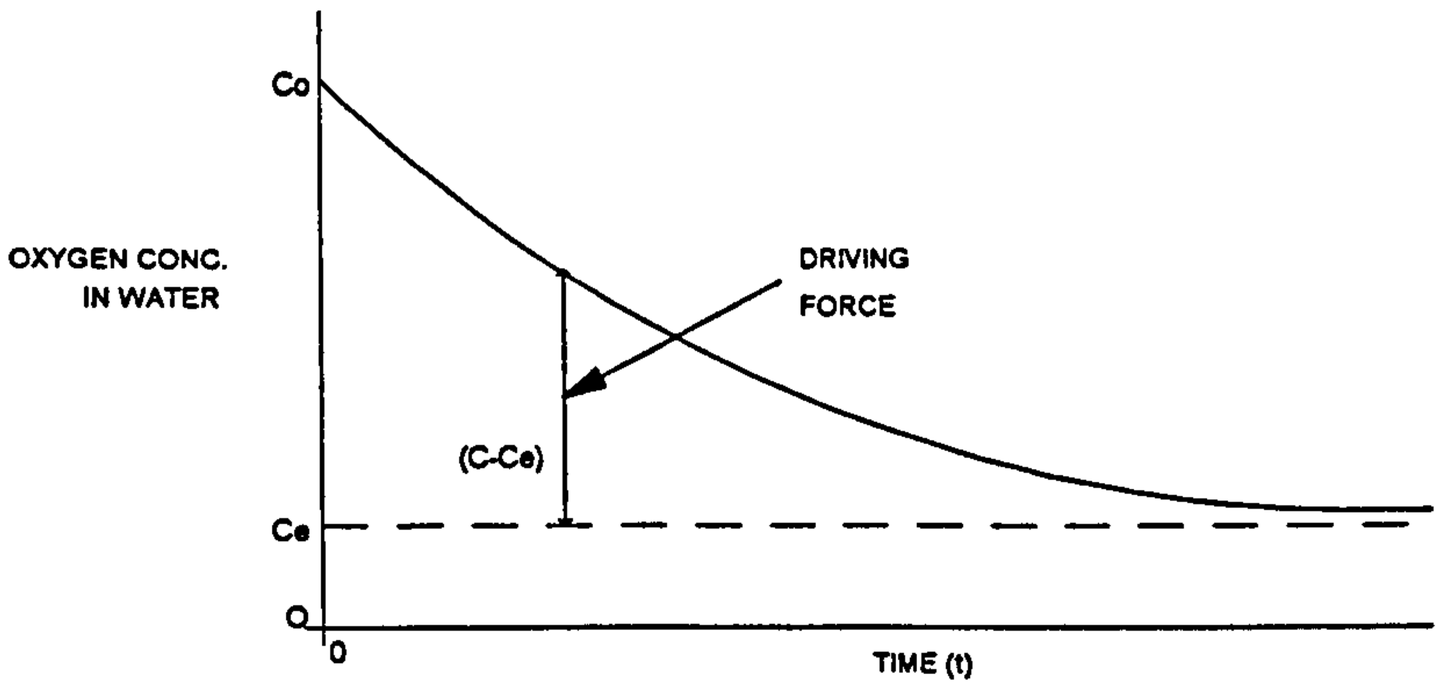

Figure 2.2 : Graphical Representation of the Driving Force for Gas Stripping

Temperature and pressure influence C_e and so effect the mass transfer rate. The gas and liquid flowrates through the column are also crucial to it's performance, as the greater the residence time in the column, the greater the amount of mass transfer achieved.

(i) Temperature

The solubility of gases in water increases as the water temperature decreases and the following graph (Fig.2.3) shows how the solubility of oxygen in water varies with temperature at atmospheric pressure.

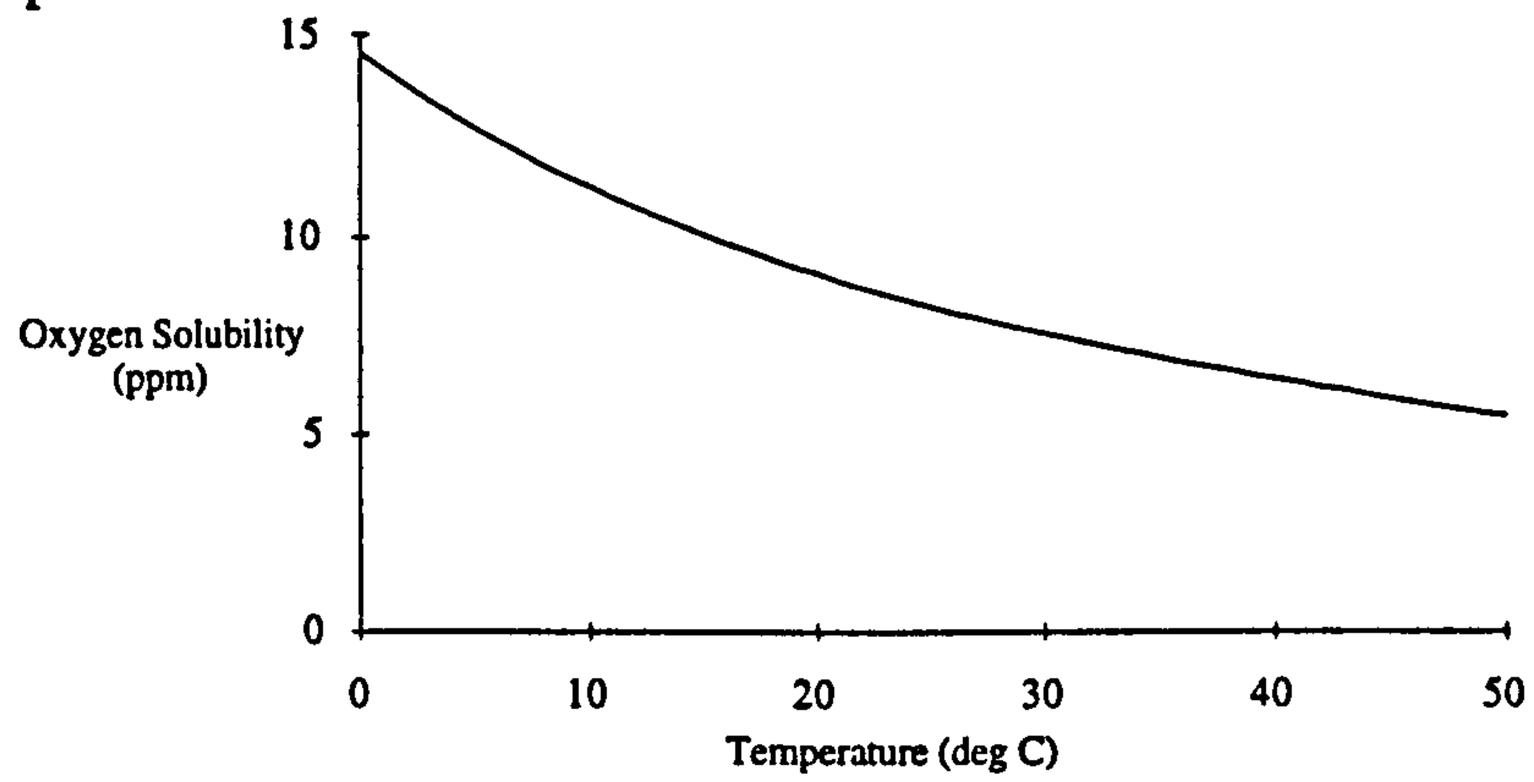

Figure 2.3 : Oxygen Solubility in Water [14]

As well as the increase in solubility at lower temperatures, the rate of diffusion of oxygen through water decreases as the water temperature decreases which means a greater resistance to mass transfer and an increase in the liquid film coefficient. Hence for the stripping of oxygen from water, a tower should be designed for the coldest operating conditions.

(ii) Pressure

Figure 2.4 shows how the equilibrium solubility of oxygen in water varies with pressure.

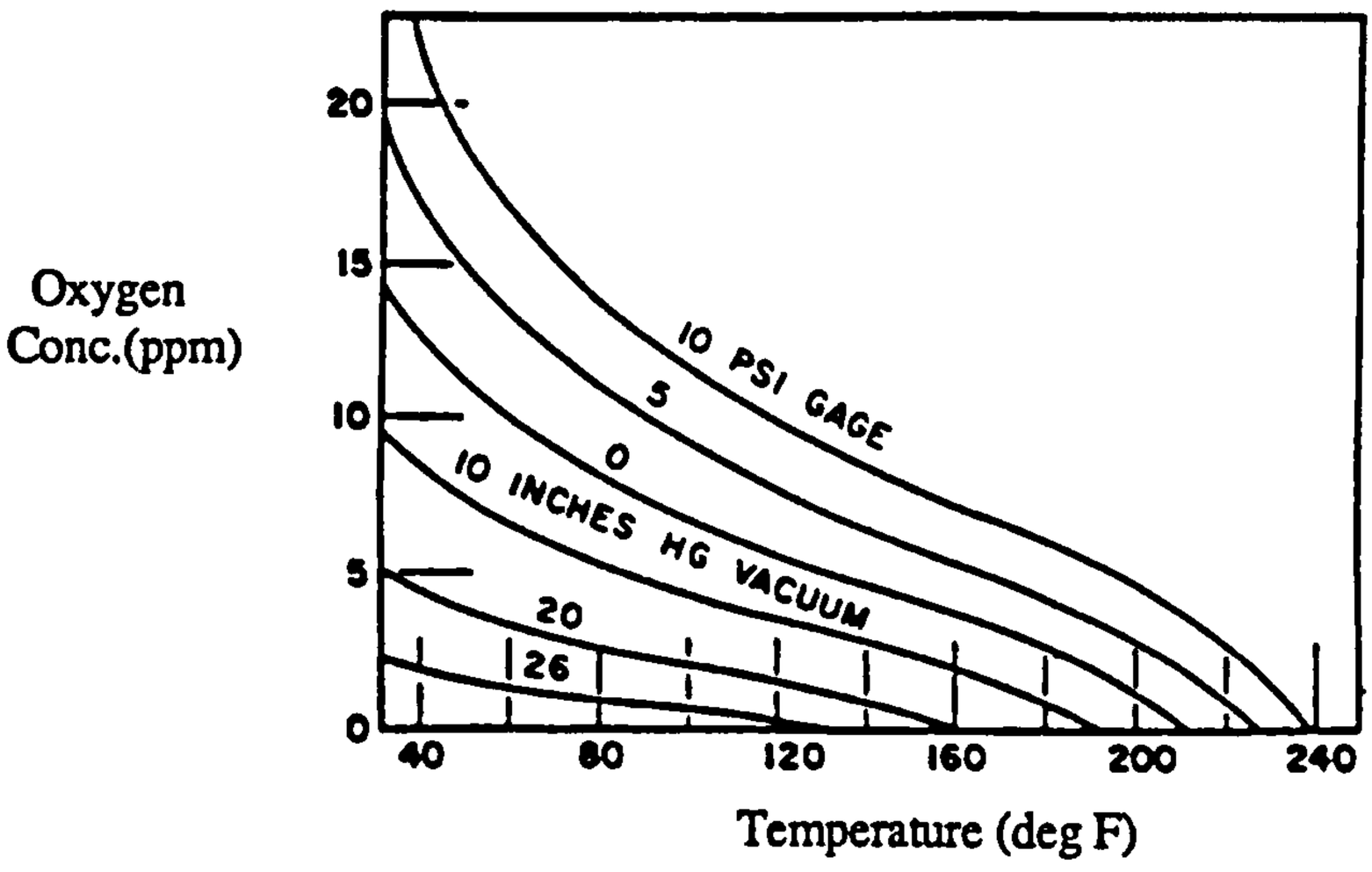

Figure 2.4 : Effect of Temperature and Pressure on Oxygen Solubility in Water[12]

The above graph shows that operating under vacuum conditions will increase stripping of oxygen from water. As mentioned earlier, vacuum de-aeration is often used in industry but

for this process has several disadvantages, these being the removal of dissolved carbon dioxide leading to an increase in the pH of the water and hence possible scale formation, and also operating under vacuum conditions leads to greater weight and expense in vessel manufacture due to the increase in the wall thickness. As weight and cost is of primary importance for the offshore oil industry this technique is unlikely to be the most cost effective.

(iii) Gas and Liquid Flowrates

The gas and liquid flowrates are also of crucial importance for the mass transfer performance and design of the column. If the gas flowrate is increased then the amount of oxygen removed will also increase, but higher operating costs will be incurred due to a higher pressure drop. The gas flow is also limited before entrainment of the liquid by the gas occurs in the column.

Increasing the water flowrate for a given gas flow however leads to a decrease in the amount of oxygen removed due to a shorter residence time inside the column. Again the water flowrate is controlled by the characteristics of the column which will determine the point at which the onset of flooding occurs.

(iv) Packing / Number of Plates

Finally the packing or number of plates used inside the column is very important as the rate of oxygen removal is proportional to the interfacial area, and the greater the interfacial area the greater the amount of mass transfer between the two phases. However the smaller the packing porosity or larger numbers of plates in the column, the larger the pressure drop of the gas and liquid through the column which in turn will lead to higher overall operating costs.

2.4 Design of Gas Stripping Columns

The previous section gave a qualitative analysis of how the solubility of the gas in water, the temperature and pressure, the gas and liquid flowrates, and the packing all influence the mass transfer performance of a stripping column. A detailed quantitative analysis for an industrial continuous counter-current packed stripping column is now considered. The approach for a plate column is identical except that a plate column is stage wise continuous, and the resulting equations vary slightly. The analysis is centred on a packed column as the Higee rotor used for the research uses packing to contact the gas and liquid.

2.4.1 Mass Transfer Design

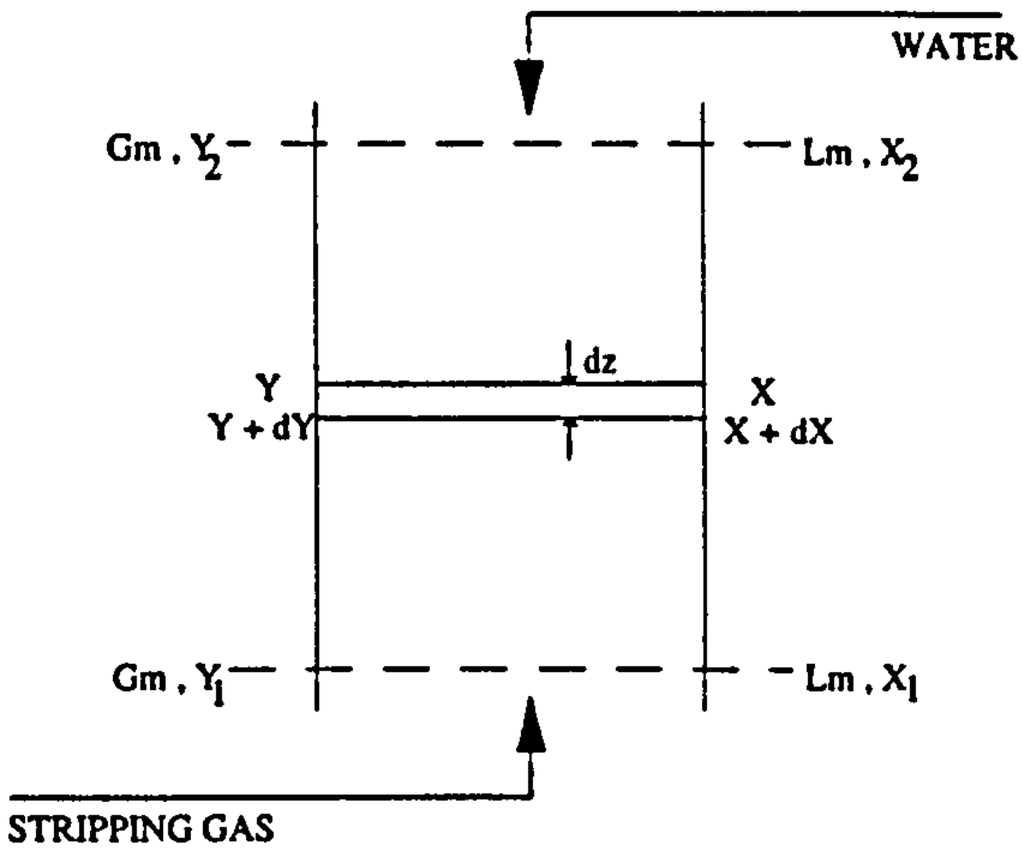

Figure 2.5 : Countercurrent Stripping Column

Figure 2.5 shows a sketch through a packed column. By carrying out a mass balance across the whole column at steady state then :

Number of moles of solute from the liquid = Number of moles of solute taken by gas

$$L_m(X_2 - X_1) = G_m(Y_2 - Y_1)$$

or in general for any point (X,Y) in the column :

$$G_m(Y - Y_1) = L_m(X - X_1) \qquad 2.1$$

Equation 2.1 is a straight line with slope L_m/G_m, passing through the point (X_1,Y_1), and known as the *operating line*. The line also passes through the point (Y_2,X_2). Figure 2.6 shows graphically the operating line and gas liquid equilibrium line for the stripping of oxygen from water.

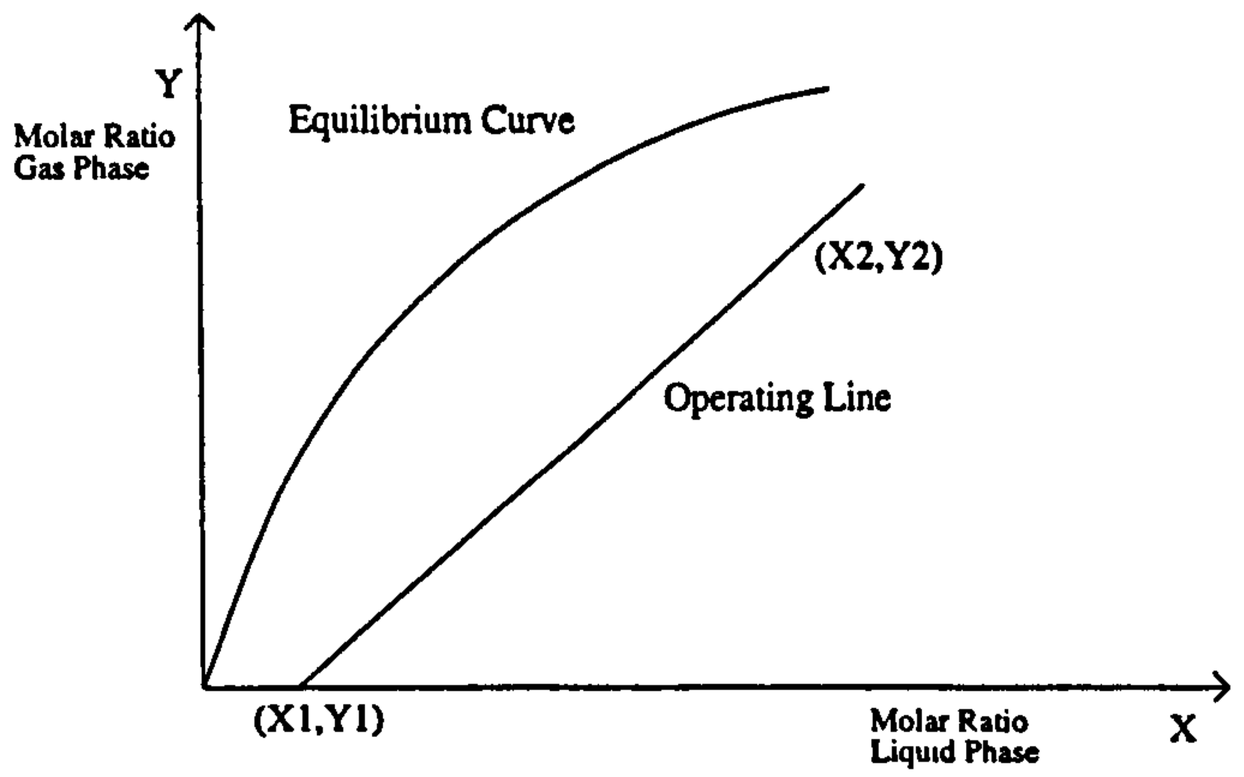

Figure 2.6 : Operating Line and Equilibrium Curve for Oxygen Stripping

Consider a cross section of the column of height dz :

Number of moles of O_2 from water = Number of moles of O_2 transferred into the gas

The rate of Molar Transfer in volume dV is therefore :

$$N_{O_2} aAdz = k_l(C - C_i)aAdz \qquad 2.2$$

where No_2 is the number of kmols of oxygen absorbed into the gas phase per unit time and interfacial area. If dX is the change in molar concentration of solute over height dz then the rate of transfer from water into the gas is given by L_mAdX, and therefore :

$$L_m dX = k_l(C - C_i)adz \qquad 2.3$$

Expressing the concentrations C, Ci in terms of X and substituting into equation 2.3 leads to:

$$\int_0^z dz = z = \frac{L_m}{k_l a C_T}\int_{X_1}^{X_2}\frac{(1+X)(1+X_i)}{X - X_i}dX$$

where C_T is the mean molar density of the liquid, and the values of C_T, k_l are assumed to be constant over the column. As the oxygen concentration in the water is *dilute*, (1+X)(1+Xi) ≈ 1 and the above reduces to:

$$z = \frac{L_m}{k_l a C_T}\int_{X_1}^{X_2}\frac{dX}{X - X_i} \qquad 2.4$$

Equation 2.4 represents the height of the column based on the liquid film mass transfer coefficient. However the difficulty in using this equation is that the interfacial molar ratio is not known. Under these conditions in which the liquid film is controlling, the interfacial concentration is assumed to be in equilibrium with the bulk gas concentration (i.e. Xi ≈ Xe). Instead if the driving force based on the liquid concentration is written as (X - Xe) and the overall liquid mass transfer coefficient as K_l ($k_l \approx K_l$), then these can be substituted into equation 2.4 and a value for z found. Also for *dilute* concentrations the mole ratio is approximately equal to the mole fraction (i.e. X ≈ x) and so equation 2.4 becomes :

$$z = \frac{L_m}{K_l a C_T}\int_{x_1}^{x_2}\frac{dx}{x - x_e}$$

The group $\int_{x_1}^{x_2}\frac{dx}{x - x_e}$ has been defined by Chilton and Colburn[15] to be the number of overall liquid mass transfer units N_{TU}, and is an integrated value of the change in composition per unit driving force (i.e. it represents the difficulty of separation). The number of mass transfer units attained is the overall height divided by the height of one transfer unit (i.e. $N_{TU} = z / H_{TU}$). This gives the following equation for the height of one mass transfer unit :

$$H_{TU} = \frac{L_m}{K_l a C_T} \qquad 2.5$$

For *dilute* concentrations the molar ratio is approximately equal to the mole fraction and the operating line (equation 2.1) can be written in terms of mole fractions :

$$G_m(y_1 - y) = L_m(x_1 - x)$$

But the gas entering the column is solute free (i.e. there is no oxygen) and therefore y_1=0

$$y = \frac{L_m}{G_m}(x - x_1) \qquad 2.6$$

For *dilute* concentrations of gases in liquids Henry's Law, which states that the partial pressure of a solute in the gas phase is proportional to the mol fraction in the liquid phase, holds :

$$p.p._{solute} = H \times x_{solute}$$

Therefore as : $p.p._{solute} = y_{solute} \times P_T$, the equilibrium constant m, linking x and y by $y=mx_e$ is given by : $$m = \frac{H}{P_T}$$

Substituting $y=mx_e$ into equation 2.6 we have the expression :

$$x_e = \frac{L_m}{mG_m}(x - x_1)$$

and putting the above expression for x_e into the equation $N_{TU} = \int_{x_1}^{x_2} \frac{dx}{x - x_e}$ gives an integral in terms of the mol fraction in the water, that can be evaluated to give :

$$N_{TU} = \frac{1}{1 - \frac{L_m}{mG_m}} Ln\left[\left(1 - \frac{L_m}{mG_m}\right)\left(\frac{x_2}{x_1}\right) + \frac{L_m}{mG_m}\right] \qquad 2.7$$

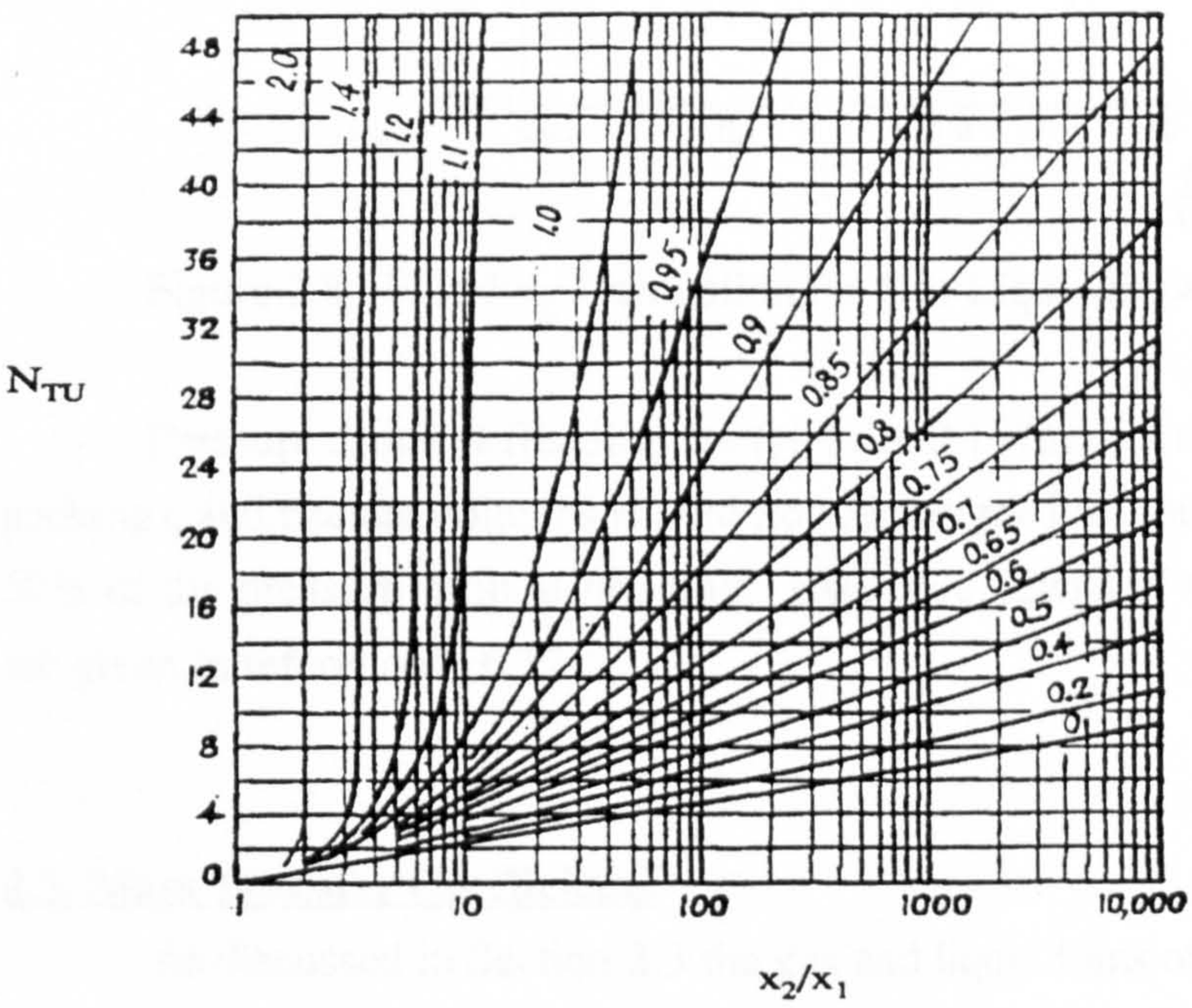

Parameter $\frac{L_m}{mG_m}$ is the ratio of the gradient of operating line to the equilibrium constant

Figure 2.7 : Number of Transfer Units as a function of x_2/x_1 with Parameter L_m/mG_m

(Adapted from Reference 9 - P.134,135)

2.4.2 Column Design

Section 2.4.1 detailed the mass transfer design of a continuous counter current column and from the resulting equations the number of transfer units needed for the required stripping duty can be found, and hence the total height of the column. However the column still has to be sized to handle the required gas and liquid throughputs. Section 2.3. briefly described how the column performance characteristics are affected by the liquid and gas flowrates, and by the type of packing used.

For Packed Towers flooding determines the minimum possible diameter, and the usual design criteria is to operate at 50 - 70% of the flooding velocity[16,17]. Flooding in packed beds has been correlated by the Sherwood Plot as shown in Figure 2.8.

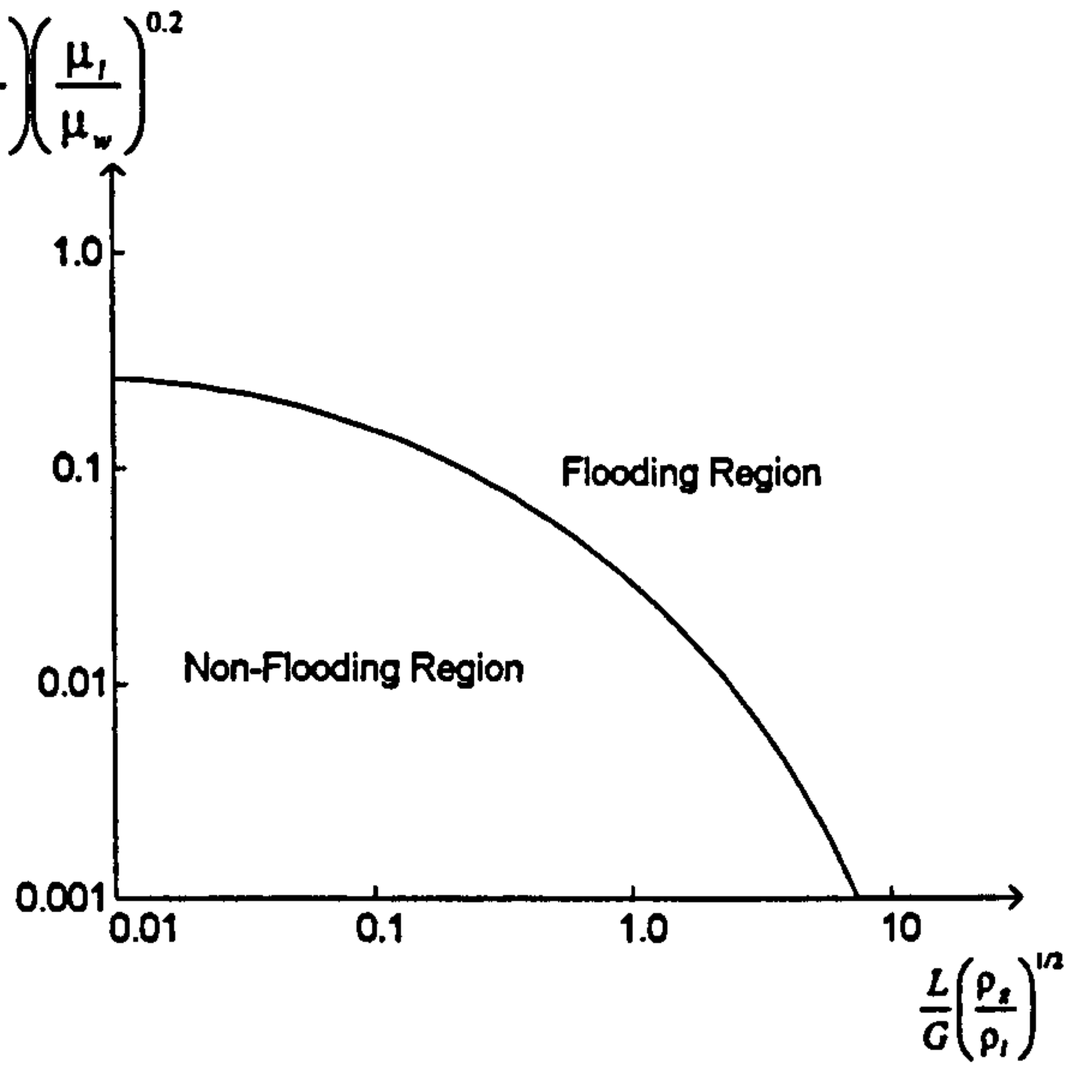

Figure 2.8 : Flooding Correlation for Gas-Liquid Flow in Packed Beds[9]

Pressure drops at flooding are typically 0.167m of water / m of packing (1.64 kN/m²/m packing), and packed columns should not be designed to operate at pressure drops larger than 50% of the pressure drop at flooding. Extensive details of the design procedure for columns are given in references 16,17.

2.5. Mass Transfer Coefficients

As discussed in Section 2.3 the gas and liquid films offer the resistance of mass transfer between the gas and liquid phase. The amount of resistance offered by each film is dependant upon the equilibrium solubility between the gas and liquid. A measure of the resistance is given by the mass transfer coefficients of the liquid film (k_l), and gas film (k_g). For systems in which the gas is sparingly soluble in the liquid, such as oxygen in water, the liquid film resistance is much greater than the gas film resistance, (i.e. $1/k_l >> 1/k_g$) and is therefore strongly controlling.

For the effective design of stripping columns an accurate prediction of the interfacial mass transfer coefficient needs to be known. This will depend on whether the gas is dispersed in the liquid phase or the liquid dispersed in the gas phase. If the gas is the dispersed phase then the interfacial area will be governed by the bubble size, whereas in liquid dispersed systems the interfacial area is dependant on the thin liquid films flowing across the packing surface area. Extensive research, both theoretical and experimental, has been carried out into the mass transfer coefficients between gases and liquids.

2.5.1 Theoretical Analysis

The modelling of gases and liquids as they pass through a column is a very complex and difficult task. Therefore calculating the mass transfer coefficients between gases and liquids in columns is also extremely complicated, and many assumptions and approximations have to be made. The following theories all look at the mass transfer from a single bubble into a bulk phase.

One of the earliest models was the *Film Model* first put forward in 1923 by Lewis and Whitman[18]. This model assumes that there is a film region in which steady state molecular diffusion acts as the transfer mechanism. According to the model steady state mass transfer occurs by molecular diffusion across a stagnant (laminar flow) film at the interface between the phases in which the fluid is turbulent. All the resistance is considered to be due to the film, and the concentrations in the phases are constant at some average value. The mass flux can be written as :

$$m' = \frac{-D}{\delta}(c_0 - c_{in}) = -k(c_0 - c_{in})$$

where c_o, c_{in} are the average concentrations in the bulk fluid and at the interface respectively. The main flaw of the Film theory is that the velocity of the fluid surface is not zero and the exposure time of the fluid to mass transfer is so short that the steady state characteristics of the Film theory would not have time to develop, and therefore linearity between the mass flux and the molecular diffusion coefficient would not occur. In reality turbulence in the bulk diminishes only gradually as the film surface is approached, and so the transfer from eddy diffusion ($m' \sim D^0$) to molecular diffusion ($m' \sim D$) is gradual and not instantaneous. The exponent for D should therefore lie between 0 and 1. The reason for this flaw is the introduction of a definite film thickness (δ). The *Modified Film Theory* takes into consideration the effect of liquid motion on the mass transfer and the absence of a clearly defined layer thickness, and it has shown that for gas-liquid systems $k \sim D^{1/2}$.

The *Penetration* (or *Surface Renewal*) *Model* assumes that the interface is continuously being impacted upon by eddies, and that in these eddies mass transfer is controlled by unsteady molecular diffusion. Higbie[19] assumed that the mass transfer would take place during brief, repeated contacts with the interface the motion for which being produced by the turbulence in the bulk, with fresh liquid elements continually replacing those interacting with the interface. The contact time of these elements with the interface is assumed to be identical, equal to the time taken for the gas bubble to pass by, and so short that steady state characteristics do not have time to develop, and any transfer is due to unsteady molecular diffusion. Starting from the Fick's second law Higbie showed that :

$$k = \left(\frac{4D}{\pi\tau}\right)^{1/2} \qquad 2.8$$

where τ is the surface contact time. The surface contact time is impossible to measure, but Higbie arbitrarily assigned τ to be the ratio between the gas bubble diameter and the bubble rise velocity. Substituting this ratio into eqn. 2.8 leads to the following dimensionless correlation :

$$\frac{k}{u_r} = 1.13 Sc^{-1/2}\,\mathrm{Re}^{-1/2} \qquad 2.9$$

Further developments of the penetration theory have been tried to improve the model. Dankwerts[20] suggested that the exposure time at the interface for each element was not constant but ranged from zero to infinity and could be better described by the probability density function : $\phi = se^{-st}$, where s = fractional rate of renewal. Again using this idea the mass transfer coefficient was found to be :

$$k = (Ds)^{1/2}$$

Toor and Marchello[21] tried to combine the film and penetration models into one theory by allowing either for a finite fluid element depth, of for eddies of a limited time duration at the surface, and found the exponent of D to lie somewhere in the range of between 1/2 and 1.

Onda et al.[22], in their investigation of gas absorption by water in a packed tower and with the liquid as the dispersed phase, separated out the individual liquid mass transfer coefficient (k_l) by dividing the volumetric coefficient ($k_l a$) by the wetted surface area (a_w), and discussed k_l using both the film and penetration models. In order to do this they assumed that $a \propto a_w$. Using both models they deduced the following equation for the liquid film coefficient :

$$k_l\left(\frac{\rho_l}{\mu_l g}\right)^{1/3} = c\left(\frac{L}{a_t \mu_l}\right)^{1/2}\left(\frac{\mu_l}{\rho_l D_l}\right)^{-1/2} = c\,\mathrm{Re}^{1/2}\,Sc^{-1/2}$$

where c = 0.021 using the film model, and c = 0.013 using the penetration model.

Langmuir[23] showed that pure radial diffusion from a sphere to an infinite stagnant medium was described by :

$$Sh = \frac{k_l d}{D} = 2$$

where d was the sphere diameter. This idea was later further developed to account for inertial effects which are significant in most practical cases, and Frossling proposed an equation, which was later developed by Rowe, Claxton and Lewis[23], for 'rigid sphere' bubble behaviour (i.e. no internal circulation and the mass transfer determined by diffusion and boundary layer flow):

$$Sh_l = 2 + 0.79 Sc^{1/3}\,\mathrm{Re}^{1/2} \qquad 2.10$$

Equation 2.10 holds for $30 < \mathrm{Re} < 2000$. If the bubbles are considered to be completely 'mobile' (i.e. internal circulation with mass transfer occurring under potential flow conditions), the following equation first put forward by Stefan[23] can be applied :

$$Sh_l = 1.13\,\mathrm{Re}^{1/2}\,Sc^{1/2} \qquad 2.11$$

which is the same as equation 2.9. In practice bubble behaviour ranges all the way from completely rigid to completely mobile and the following graph (Fig. 2.9) shows some results obtained for air and water by Siddique[23] :

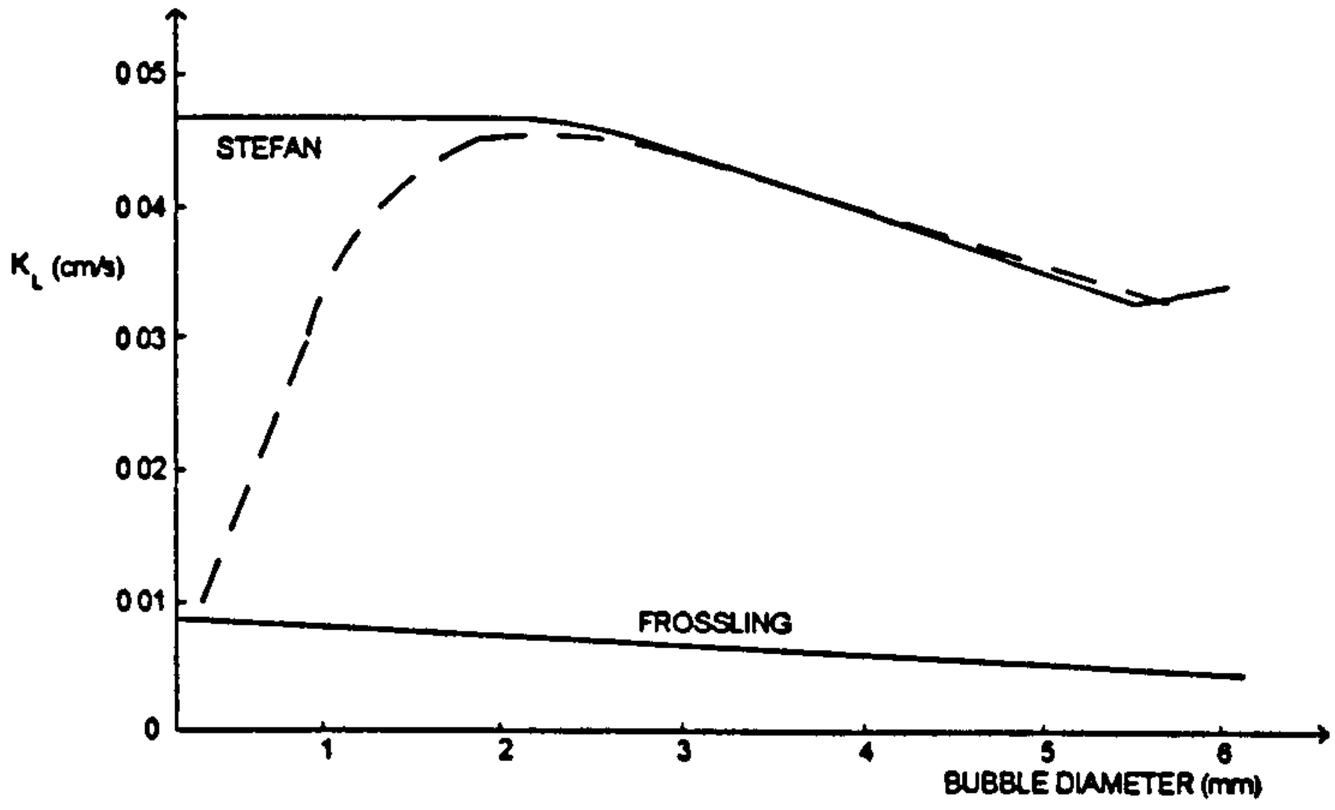

Figure 2.9 : Variation of Liquid Phase Mass Transfer Coefficient with Bubble Diameter

As can be seen from the above, bubble mobility begins around 0.2 mm bubble size and reaching full mobility at about 2 mm, but it should be noted that the mobility is strongly affected by surface-active impurities in the water.

All the above theories have made no attempt to account for the non-sphericity of the larger bubbles, and any interference and coalescence of the bubbles with each other. Although the sizes and rise velocity of single bubbles (and therefore the mass transfer coefficients) are only slightly affected by the presence of other bubbles[23], Calderbank and Moo-Young[23] produced a general correlation for the liquid phase mass transfer coefficient in bubble swarms :

$$Sh = 0.31\,\mathrm{Re}^{2/3}\,Sc^{1/3}\,Fr^{-1/3}\left(\Delta\rho/\rho\right)^{1/2} \qquad 2.12$$

Finally, Cockx, Roustan, Line and Hebrard[24] looked at modelling the mass transfer coefficient in a bubble column, and for the transfer of oxygen from the gas phase into a liquid phase they found : $\frac{K_l}{u_l^*}Sc^{0.5} = 0.13 \pm 0.02$ 2.13

u^*_I is defined as the interfacial momentum transfer velocity which can be calculated from the hydrodynamic modelling of bubbly flow :

$$u_l^* = \sqrt{\frac{c_d}{2}}\left(u_l - u_g\right)^2$$

(where u_l and u_g are liquid and gas velocities respectively, and c_d the drag coefficient which the authors found to be 0.16)

2.5.2. Experimental Analysis

A number of empirical equations based on experimental data have been developed by various authors to describe the liquid phase mass transfer coefficient for gas-liquid systems in which the liquid film resistance is controlling for both gas and liquid as the dispersed phases. For prediction of the overall mass transfer rate the product of the liquid phase mass transfer coefficient and the effective interfacial area per unit volume ($k_l a$) is needed. Two approaches are used, those being to either, (1) obtain separate correlations for k_l and for a, or (2) find a correlation for the overall volumetric coefficient ($k_l a$).

(i) Liquid Dispersed

Sherwood and Holloway[9,25] studied the desorption of oxygen, hydrogen and carbon dioxide from water and found that the liquid film coefficient was a function of the liquid flowrate but independent of the gas flowrate The experimental findings using various packings, such as Raschig rings, Berl saddles and tiles, could be correlated by the following equation :

$$\frac{k_l a_e}{D_l} = \alpha\left(305\frac{L}{\mu_l}\right)^{1-n}\left(\frac{\mu_l}{\rho_l D_l}\right)^{0.5} \qquad 2.13$$

where α varies from 260 - 920, and n varies from 0.22 - 0.35 depending on the size and type of packing used. The results shown by the above equation were generally confirmed by a number of other authors[17], and gives typical values for 1-inch Raschig rings packing for the volumetric mass transfer coefficient $k_l a$ of 10 - 200 hr^{-1} with the corresponding height of a transfer unit H_L ranging 0.18 - 1 m as the liquid mass flux varies from 1 - 40 kg/m^2sec.

Shulman[26] developed an equation for the individual liquid film coefficient (k_l) for Raschig rings and Berl saddles :

$$\frac{k_l d_s}{D_l} = 25.1\left(\frac{d_s L}{\mu_l}\right)^{0.45} Sc_l^{0.5} \qquad 2.14$$

with the effective interfacial area found from available data. The effective area is the area which participates in the gas-liquid mass transfer and maybe less than the total interfacial area due to stagnant pools which have reached saturation within the system. It should also not be confused with the wetted area while although the liquid film across the packing surface is a contributor, the effective area will also include contributions from rivulets and gas bubbles.

Onda et al.[27] produced the following equation replacing the Reynold's number based on a_t (sect.2.5.1) with a Reynold's number based on a_w, and found that, assuming the wetted surface area is identical to the interfacial area, the liquid side coefficient in gas absorption and desorption for a number of packings could be predicted within $\pm 20\%$.

$$k_l\left(\frac{\rho_l}{\mu_l g}\right)^{1/3} = 0.0051\left(\frac{L}{a_w\mu_l}\right)^{2/3}\left(\frac{\mu_l}{\rho_l D_l}\right)^{-1/2}\left(a_t d_p\right)^{0.4} \qquad 2.15$$

where d_p is the nominal size of the packing.

(ii) Gas Dispersed

The above empirical correlations are dependant on the packing characteristics used in the column, but a number of correlations have been proposed for the mass transfer coefficient in which the gas is dispersed in the liquid phase. For systems in which the gas phase is dispersed, the packing will control the bubble size but the interfacial area will depend only on the gas bubble size and not on the packing pore size and characteristics. Calderbank[28] proposed the following dimensionless correlation for the liquid film coefficient for small bubbles ($d_b < 0.5$ mm) :

$$\frac{k_l d_b}{D_l} = 2 + 0.31\left(\frac{d_b^3 g \Delta\rho}{D_l \mu_l}\right)^{1/3} \qquad 2.16$$

Although many semi-theoretical equations of the form : $Sh_l = 2 + a(Sc)^{1/3}(\mathrm{Re})^{1/2}$ (see equation 2.9) have been used to correlate experimental data for mass transfer from single spherical surfaces to flowing liquid streams, Hughmark[29] proposed that these correlations were not applicable to experimental data for mass transfer from single bubbles in liquids., and modified the form to correlate the data for mass transfer for single bubbles in liquids :

$$Sh_l = 2 + b' \mathrm{Re}_b^{0.779}\, Sc_l^{0.546}\left(\frac{d_b g^{1/3}}{D_l^{2/3}}\right)^{0.116} \qquad 2.17$$

where Re_b is the bubble Reynold's number based on the bubble slip velocity, and b' = 0.061 for single bubble, 0.0187 for swarm of bubbles. The above equation calculates the liquid phase coefficient to within 15% for systems in which the liquid mass transfer coefficient is strongly controlling.

Finally, Hikita et al.[30] modified previous empirical equations and found that only the liquid diffusivity, surface tension, gas superficial velocity, gas and liquid densities and viscosities, and the gravitational acceleration has any significant effect on the volumetric mass transfer coefficient. Applying dimensional analysis and the least squares method to experimental results for pure liquids, they presented a dimensionless correlation to calculate the volumetric mass transfer coefficient :

$$\frac{k_l a u_g}{g} = 14.9\left(\frac{u_g \mu_l}{\sigma}\right)^{1.76}\left(\frac{\mu_l^4 g}{\rho_l \sigma^3}\right)^{-0.248}\left(\frac{\mu_g}{\mu_l}\right)^{0.243}\left(\frac{\mu_l}{\rho_l D_l}\right)^{-0.604} \qquad 2.18$$

where σ is the interfacial surface tension which for air-water has a value of 0.0723 kg/s^2.[30] The experimental values of the volumetric coefficient were correlated by the above equation with an average deviation of 2.5%, although the desorption of oxygen from water using carbon dioxide resulted in values consistently lower than those predicted by equation 2.18. The reason for this was attributed to the gas shrinkage taking place due to the carbon dioxide being dissolved into the water. As nitrogen gas is sparingly soluble in water gas shrinkage will be minimal, and therefore equation 2.18 should be applicable to the studied gas liquid system. Hikita et al. also investigated the effect of electrolytes on $k_l a$ and found that salt concentrations of less than 1% led to increases in $k_l a$ of up to 50%.

2.6. Hydrodynamic Studies

As has already been mentioned, the modelling of the gas and liquid flows through a packed column is extremely complicated, but also essential for an accurate design of a column. For any process the physical properties of the gas and liquid will effect the bubble size in the column, but in addition to this, the packing pore size, the gas superficial velocity, bubble coalescence and splitting due to collisions with other bubbles or packing elements, all play an important role in determining the hydrodynamic flow patterns and bubble size at any point in time inside the column.

2.6.1 Flow Regimes

The type of flow of gas and liquid through a column will to a large extent depend on the flowrates of the phases and column diameter, and will determine the mass transfer performance of the column. The introduction of packing to the internals of the column helps to disperse both gas and liquid throughout the entire cross section, thereby improving the contact time and area between the gas and liquid. Columns can be operated within a broad range of flow regimes depending on the ratio of the gas to liquid flowrate. Bubble columns with no internals produce an *homogeneous* flow regime at low gas flows, the bubbles being uniformly distributed in the liquid and having a narrow range of bubble size distributions. At higher gas flows the flow becomes *heterogeneous* leading to large bubble aggregates forming and rising more rapidly than the smaller bubbles. For packed columns low gas to liquid ratios produce the bubble flow regime in which the gas phase is dispersed into a continuous liquid phase the packing helping to distribute and break up the bubbles, whereas at high gas to liquid ratios the film flow regime occurs in which liquid drops are dispersed in the gas stream and flow as films and rivulets across the packing surface.

2.6.1.1 Ideal Flow

The flow or mixing of a phase can be characterised in terms of two ideal flow patterns, that being plug flow or complete mixing.

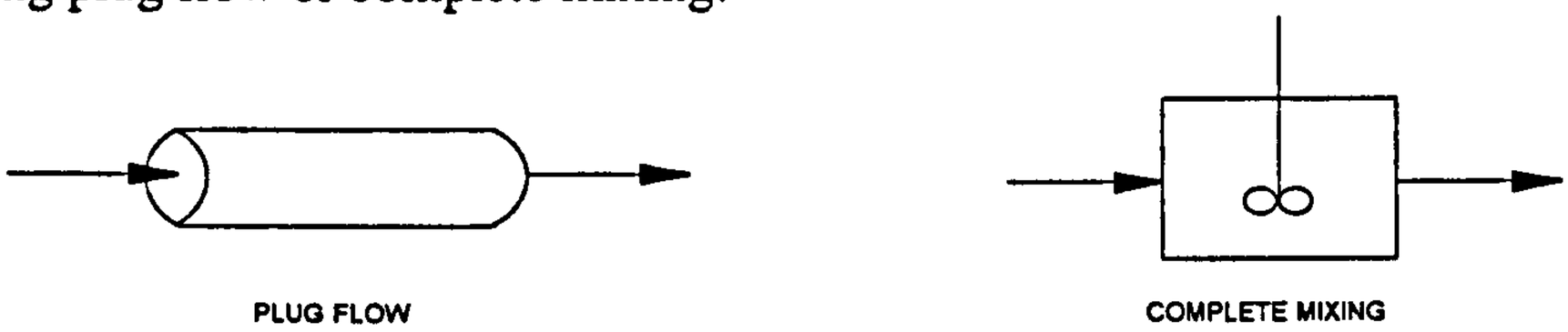

Figure 2.10 : Two Ideal Flow Systems

In plug flow axial mixing of fluid particles is non-existent but complete radial mixing takes place. Consequently, all fluid particles within the system have the same velocity, and therefore identical residence times. In contrast, with completely mixed systems the output stream

composition leaving is identical to that of the fluid within the system, and the residence time distribution of fluid particles in a completely mixed system follows an exponential curve.

2.6.1.2 Non-Ideal Flow

In reality the flow and mixing of the two phases deviates considerably from the two ideal limits and an appropriate representation of non-ideal flow has to be developed to accurately model the system. Deviations in the liquid flow can be the result of non uniformity of the packing and maldistribution of liquid leading to channelling or regions where the liquid flow is abnormally great. For the gas flow, the resistance at the column walls and in relatively dry regions of the packing is different from that elsewhere, and in counter-current systems the downward movement of liquid may induce downward movement of the gas. As a result true plug flow does not occur within each phase as there is relative movement parallel to the axis of the column described as axial mixing, axial dispersion, and back mixing. *Axial dispersion* is the spreading of the residence time in unidirectional flow owing to the departure from plug flow, i.e. the fluid particles move forward but at different speeds. *Back mixing* is the backward flow in a direction opposite to that of the net flow caused by the frictional drag between one phase and the other.

As exact mathematical models of non-ideal flow based on the knowledge of complete velocity field distribution of phases is not feasible, the character of flow has been described by various approximate models, which can be classified as either differential (continuous) models or combined (discrete) models. Such differential models include the axial dispersion model where the model is represented by a set of differential equations, whereas for discrete models such as the series of perfect mixers model, cross-flow model, and time delay model, the models are represented by a set of algebraic equations. The differential models are more applicable when modelling deviations from true plug flow, whereas the discrete models are better at describing deviations from perfectly mixed systems. In packed bed columns the liquid phase flow has been shown to be most suitably modelled by the axial dispersion model[31].

2.6.1.2.1 Axial Dispersion Model

The axial dispersion model[32,33] is the fundamental differential mixing model developed for the description of axial (longitudinal) mixing. Due to the simplicity and compatibility, the axial dispersion model is the most popularly used model of non-ideal flow. The model describes plug flow of fluid with some degree of axial mixing superimposed, the magnitude of which is not dependant on the position in the column (see Fig. 2.11). This condition is called dispersed plug flow and assumes that no stagnant pockets exist, and that no gross bypassing of liquid in the vessel occurs.

Figure 2.11 : Representation of the Axial Dispersion Model

The axial mixing is described as being analogous to molecular diffusion and therefore using Fick's second law :

$$\frac{\partial C}{\partial t} = D_{ax}\frac{\partial^2 C}{\partial x^2}$$

where D_{ax} is the axial dispersion coefficient which characterises the degree of axial mixing during flow, and includes contributions of molecular and turbulent (convective) diffusion. Putting the diffusion equation in dimensionless form where $z = x/L$, $\theta = t/\tau = tu/L$:

$$\frac{\partial C}{\partial \theta} = \left(\frac{D_{ax}}{uL}\right)\frac{\partial^2 C}{\partial z^2} - \frac{\partial C}{\partial z} \qquad 2.19$$

where the dimensionless group (D_{ax} / uL) called the dispersion number which is the inverse of the Peclet number measures the extent of axial dispersion. As the dispersion number $\rightarrow 0$ there is negligible dispersion and hence plug flow exists. If the dispersion number $\rightarrow \infty$ the flow is completely mixed.

Figure 2.12 shows graphically the varying responses, and therefore flow characteristics, of a system to a pulse tracer.

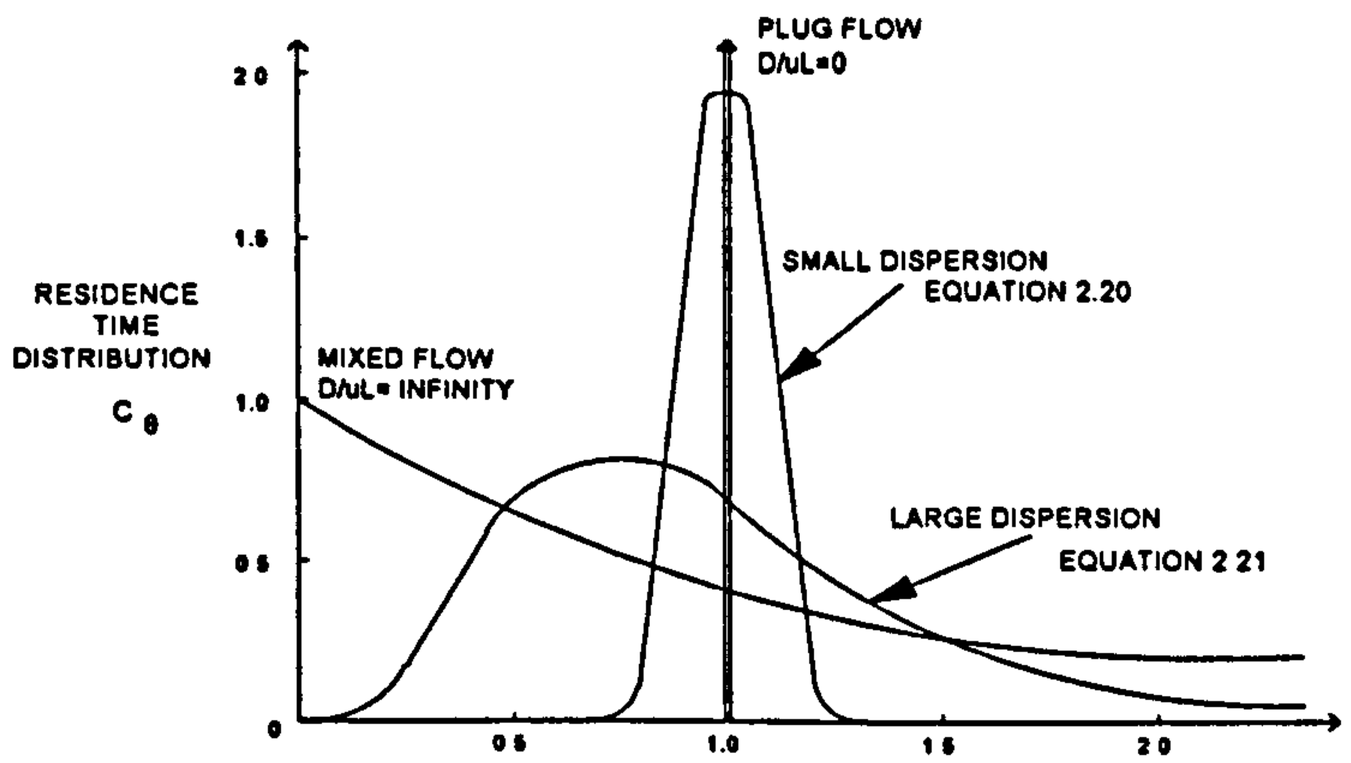

Figure 2.12 : ResidenceTime Distribution Curves from the Axial Dispersion Model

For systems where there is little dispersion ($D_{ax}/uL < 10^{-3}$) the resulting response is a normal distribution and the solution to equation 2.19 is given by :

$$C_\theta = \frac{1}{2\sqrt{\pi(D_{ax}/uL)}}\exp\left[-\frac{(1-\theta)^2}{4(D_{ax}/uL)}\right]. \qquad 2.20$$

where C_θ is the C-curve which represents the response to a pulse tracer input, and is the residence time distribution of the tracer in the system. The normal distribution (eqn. 2.20) has mean $\overline{\theta} = 1$ and variance $\sigma_\theta^2 = 2\left(\frac{D_{ax}}{uL}\right)$.

For systems that contain significant mixing ($D_{ax}/uL > 0.01$), the C-curve becomes increasingly skewed as the dispersion number increases (see Fig. 2.12), and it is in these cases that the boundary conditions will be significant and influence the shape. Considering two common boundary cases - an *open* system and a *closed* system.

(i) Closed System

A closed system is a system where there is no axial mixing beyond the boundary conditions (the injection and measurement point). It is not possible to obtain an analytical expression for the C-curve for a closed system, but the mean and variance can be solved using numerical methods, and are found to be :

Mean: $\overline{\theta} = 1$

Variance: $\sigma_\theta^2 = 2\frac{D_{ax}}{uL} - 2\left(\frac{D_{ax}}{uL}\right)^2\left(1 - e^{-uL/D_{ax}}\right)$

(ii) Open System

If the system is open, that is axial mixing does take place at the boundary conditions, then it is possible to derive an analytical expression for the C-curve. The resulting expression of the distribution is given by :

$$C_\theta = \frac{1}{2\sqrt{\pi\theta(D_{ax}/uL)}}\exp\left[-\frac{(1-\theta)^2}{4\theta(D_{ax}/uL)}\right] \qquad 2.21$$

which has a mean and variance as follows :

Mean: $\overline{\theta} = 1 + 2\left(\frac{D_{ax}}{uL}\right)$

Variance: $\sigma_\theta^2 = 2\left(\frac{D_{ax}}{uL}\right) + 8\left(\frac{D_{ax}}{uL}\right)^2$

For systems that contain significant amounts of mixing, the assumptions of the axial dispersion model become increasingly unlikely to be satisfied by the real system, and the model therefore should be used with caution.

2.6.1.2.2 Tanks in Series Model

Besides the axial dispersion model, the other most widely used model to represent non-ideal flow is the tanks in series model[32]. The tanks in series model is a model in which the fluid flow is viewed through a series of equal sized stirred tanks, and like the dispersion model it is a one parameter model, the one parameter being the number of tanks in series.

Since the problems of boundary conditions are not a factor, the residence time distribution (R.T.D.) curve is easily obtained. Performing a mass balance on one tank the R.T.D. is found to be :

$$E(t) = \frac{1}{\bar{t}} e^{-\frac{t}{\bar{t}}}$$

and for n tanks in series :

$$E(t) = \frac{1}{\bar{t}} \left(\frac{t}{\bar{t}}\right)^{N-1} \frac{1}{(N-1)!} e^{-\left(\frac{t}{\bar{t}}\right)} \qquad 2.22$$

Figure 2.13 shows graphically equation 2.22 as N increases from 1 to infinity using a dimensionless time scale, $\frac{t}{\bar{t}}$. As N becomes increasingly large it can be seen that the R.T.D. curve approaches the normal curve given by the axial dispersion model (see Eqn. 2.20)

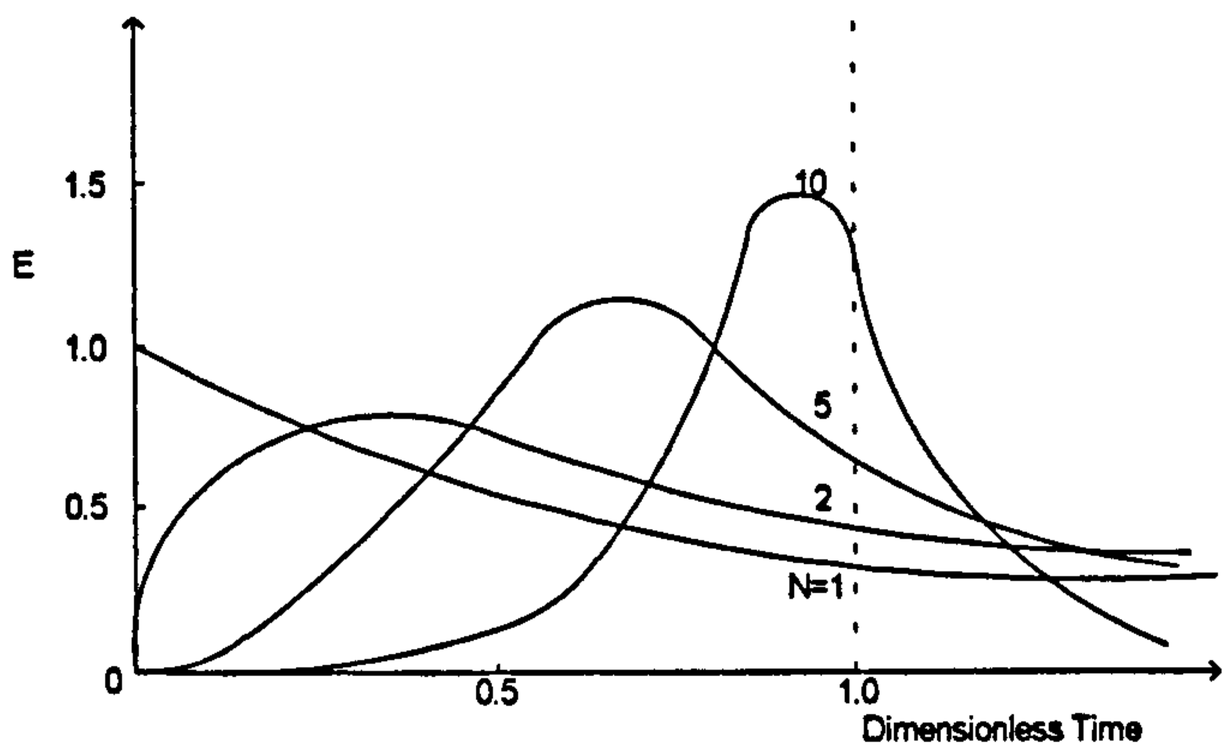

Figure 2.13 : Tanks in Series Model

2.6.1.2.3. Multi-Parameter Models

When one parameter models are unable to satisfactorily account for the real system behaviour more complicated models must be attempted. These models usually consider the system to consist of different flow regions such as plug, dispersed plug, mixed, deadwater interconnected in various ways. The term deadwater accounts for the portion of fluid which is relatively slow moving, and sometimes taken to be stagnant.

A common R.T.D. curve encountered in real systems is the Gaussian distribution with extended tail[32]. This curve deviates slightly from plug flow and is explained by the fact that some of the liquid is held up by being trapped within packing pores or in stagnant regions. A number of models have been used to describe this behaviour, one of which is shown below in Fig. 2.14.

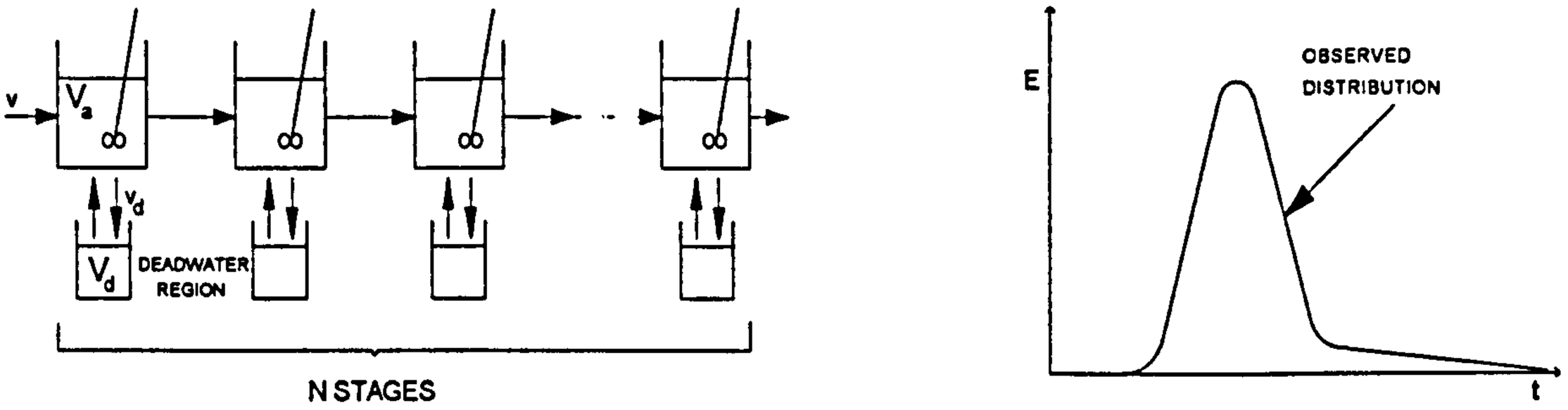

Figure 2.14 : Multi-Parameter Model and Resulting Distribution

The above model is a three parameter model :

N - The number of stages consisting of active and deadwater regions in series

X - The crossflow ratio per tank = v_d / v

The fraction volume that is not active = $V_d / (V_a+V_d)$

The model shows that in passing through the vessel some fluid is delayed once, some twice, some more etc., by fluid flow into the deadwater regions. If f_i is the fraction of fluid delayed *i* times and E_i the R.T.D. for that fluid then :

$$E = f_0 E_0 + f_1 E_1 + \cdots + f_i E_i + \cdots \qquad 2.23$$

As the fluid must flow through N active regions regardless of the number of delays, E_i is the convolution of the N active and *i* deadwater regions.

$$E_i = E_{N(active)} * E_{i(delays)}$$

where both $E_{N(active)}$ and $E_{i(delays)}$ are found from equation 2.22. For relatively small crossflow ($Nv_d < v$)most of the fluid passes through with no delay, a small fraction is delayed once, and the fraction delayed more than once even smaller. Therefore based on this assumption, equation 2.23 can be simplified to :

$$E = f_0 E_{N(active)} + f_1 \left(E_{N(active)} * E_{1(delay)} \right) \qquad 2.24$$

Figure 2.14 shows the output graph of equation 2.24, which represents the superposition of a large N tanks in series curve and a smaller curve with long tail which Levich first showed can be approximated by a Gaussian curve and an exponential decay curve. This model provides a way of estimating the parameters to fit the physical system. The location of the Gaussian portion estimates the fraction of vessel volume which is active, its width and peak height gives a value for N, while the exponential tail estimates the crossflow (see Fig. 5.11). The above multi-parameter model is further detailed in section 5.3.4, and is used in the modelling of the liquid flow through the rotor packing.

2.6.2 Bubble Sizes in Columns

2.6.2.1 Bubble Formation at a Single Orifice

The formation of bubbles at a single orifice is dependant upon many factors, the principal ones being the orifice diameter, gas flowrate, the gas and liquid density and viscosity, the submergence, the surface tension and the pressure drop. Much work has been carried out in this area to determine the effect of these different parameters, and a review of this work[34] showed little agreement in the findings, especially at high gas flows. However it is generally agreed upon that 3 regimes of bubble production exist as the gas flowrate is varied, and that the theory of bubble formation at very low gas flowrates accurately fits experimental findings.

(i) Single Bubble Regime

In this regime bubbles are produced one at a time. The forces commonly acting on a bubble as it forms at an orifice are the bouyancy, convection currents in the fluid, and the surface tension between the bubble and the orifice (see Fig. 2.15), but in this regime where the gas flowrate is very low, and when the viscosity of the liquid is small and therefore convection forces negligible, the bubble size on detachment from the orifice is determined by a balance of the bouyancy and surface tension forces giving:

$$d_b = \left(\frac{6\sigma D_{or}}{(\rho_l - \rho_g) g} \right)^{1/3} \qquad 2.25$$

where D_{or} is the orifice diameter, and σ is the surface tension. Equation 2.25 has been found to be valid for $Re_{or} < 200$, where $Re_{or} = \frac{\rho_l u_{or} D_{or}}{\mu_l}$.

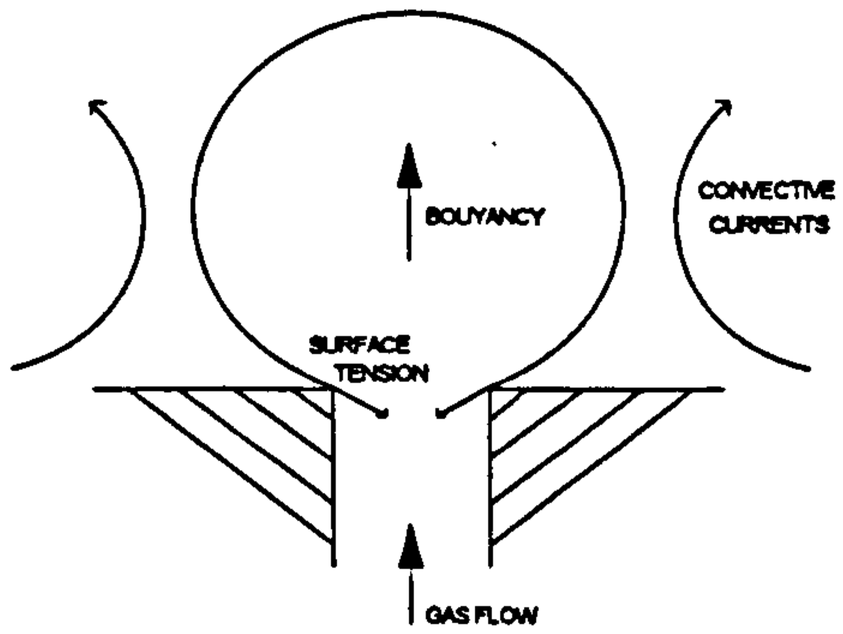

Figure 2.15 : Forces acting on a Bubble forming at an Orifice

(ii) Intermediate Regime

It has been found that this regime extends from a Reynolds number of 200 - 2100. The qualitative form of the relation between the bubble diameter and the gas flow in this region has also been generally agreed upon. As the gas flow is increased the bubble diameter at first remains reasonably constant while the frequency of formation increases. At higher flows the

frequency of formation becomes approximately constant while the bubble diameter increases with the gas flowrate. The bubble size is still affected by the orifice diameter, but becomes increasingly dependant upon liquid inertia effects, liquid density and viscosity, and the relationship between the constancy of gas flow and gas pressure at the orifice. For conditions approaching constant gas flow through the orifice, Davidson[35] showed the following equation to reasonably fit experimental data

$$d_b^3 = 1.378\left(\frac{6V_g^{1.2}}{\pi g^{0.6}}\right) \qquad 2.26$$

where V_g is the gas volumetric flowrate.

Ramakrishman, Kumar and Kuloor[36] proposed a model in this range for Reynolds number $200 < Re_{or} < 1000$. The model proposes that the bubble formation goes through an *expansion* and *detachment* phase. During the first stage the bubble is attached to the orifice, and during the second stage the bubble moves away but keeping in contact with the orifice through a 'neck'. The final volume of the bubble V_b is then :

$$V_b = V_E + Q\tau_f$$

where V_E is the volume of the bubble generated during the expansion phase, Q the gas volumetric flowrate, and τ_f the detachment time. A force balance, considering the bouyancy, viscous drag, surface tension, and inertia, leads to an expression for determining V_E using an iterative procedure:

$$V_E^{5/3} = \frac{11Q^2}{192\pi\left(3/4\pi\right)^{2/3} g} + \frac{3\mu_f Q V_E^{1/3}}{2\left(3/4\pi\right)^{1/3} g\rho_l} + \frac{\pi D_{or}\sigma V_E^{2/3}}{g\rho_l} \qquad 2.27$$

The first term accounts for the inertial effects, the second term the viscous drag, and the third term the effect of surface tension. At low gas flowrates the third term in equation 2.27 dominates and as $Q \rightarrow 0$, the above tends to equation 2.25. When the bubble formation enters the detachment phase, the volume of the 'neck' has to be found to give the final bubble volume. The length of the neck is taken to be equal to r_E, the bubble radius at detachment, as this assumption avoids the possibility of the next bubble coalescing with the first. For the second stage (detachment) the final bubble volume V_b is obtained using the second law of motion taking into account viscosity, buoyancy, added mass, and surface tension. The resulting equation is shown below with parameters A,B,C,E, and G all functions of the liquid density, viscosity, orifice diameter and gas flow.

$$r_E = \frac{B}{2Q(A+1)}\left(V_b^2 - V_E^2\right) - \frac{C}{AQ}(V_b - V_E) - \frac{3G}{2Q(A-1/3)}(V_b^{2/3} - V_E^{2/3})$$

(iii) Jet Regime

It is this regime for which $Re_{or} > 2100$ that produces many contradictory reports and theories. Bubbles of a single size are not produced but rather a continuous jet with a spread of bubble sizes which breaks up a certain distance above the orifice. Calderbank[34] concluded that most industrial applications operated in this region and found that regular 'chain bubbling' occurred, i.e. bubbles being formed in rapid succession at the orifice and moving away in contact with each other. He found the frequency of formation to be relatively constant at around 20 / sec, and this being independent of the gas flow, orifice dimensions, physical properties of the gas and liquid, and the submergence. It therefore follows that the volume of each bubble is proportional to the gas flow, and increases steadily in this region. Leibson et al.[34] also investigated in this region and found that constant frequency bubbling giving bubbles of uniform size occurred up to $Re_{or} = 2100$. Above this, coalescence took place near the orifice and the resulting large irregular bubbles were broken into small fragments an inch or two above the orifice. Above $Re_{or} = 10{,}000$ the gas left the orifice in the form of a swirling jet which subsequently disintegrated into numerous small bubbles. The findings of Calderbank and Leibson agree when $Re_{or} < 2100$, i.e. constant bubbling occurs, but above this their findings differ considerably. Subsequent investigations by Rennie and Smith revealed that bubbles produced in rapid succession at the orifice soon deform and shatter into a number of much smaller bubbles. By looking at the experimental methods of Calderbank and Leibson it was concluded that the findings of Calderbank were for those bubbles formed at the orifice, whereas the findings of Leibson referred to the small bubbles produced after the break up of the primary bubbles. As the principal reason for determining the bubble size is to provide estimates of the interfacial area for mass transfer calculations, the system in question would need to be examined to see which prediction is most appropriate when applied.

So far the bubble formation has been limited to the case of a single orifice. In practice the gas is distributed in columns through a sintered or perforated plate which contains multiple orifices. At low gas flowrates, multiple orifices have shown to operate independently and produce the same size bubble as a corresponding single orifice. When the flow is increased either a froth or cellular foam is formed, and correlations for predicting the bubble size have been proposed although with some criticism.

After formation, a gas bubble will enter the packed area of a column where it will experience many collisions with the packing and other bubbles. These collisions may result in the bubble splitting or coalescing either of which will result in a change in the bubble size and shape.

2.6.2.2 Effect of Splitting

Ramshaw[8] proposed that when a droplet, travelling at its terminal velocity, collides normally with a thin lamina baffle it will either on impact split into two daughter bubbles, or else be deformed as shown in Fig. 2.16

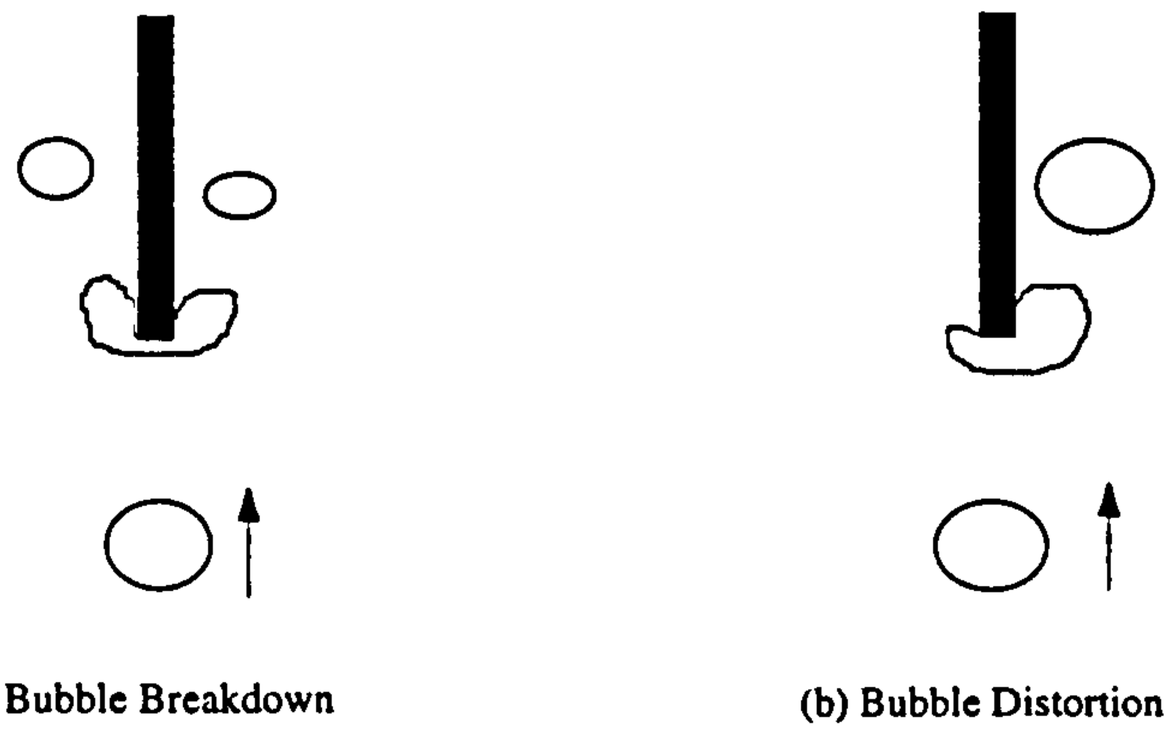

(a) Bubble Breakdown (b) Bubble Distortion

Figure 2.16 : Bubble Collision Behaviour

The total energy of a bubble is considered to be made up of the kinetic, potential and surface energy, and by carrying out an energy balance on the bubble before and after the collision, it is possible to determine whether the bubble will break down or merely deform on impact. Splitting of the bubble will occur if the total energy of the initial bubble is sufficient to provide the excess surface energy associated with the production of two daughter bubbles. However certain simplifying assumptions need to be made. The bubbles are assumed to be spherical before impact, all the kinetic and potential energy lost on impact is converted into surface energy, the breakdown process is not complete until the base of the daughter bubbles are level with the lower edge of the baffle, and the baffle has no finite thickness.

Carrying out an energy balance shows that at the limit of breakdown the critical bubble diameter is given by :

$$d_c u_t^2 \rho_g + 1.8 d_c^2 \Delta\rho g - 3.12\sigma = 0 \qquad 2.28$$

However, the initial studies were carried out on droplets in liquid-liquid systems where typical values of $\Delta\rho \approx 0.2$ kg/m^3, and not bubbles in gas-liquid systems for which $\Delta\rho \approx 10^3$ kg/m^3. When applying the above model to gas bubbles the 'virtual mass' of the bubble has to be taken into account. Darwin[37] was the first to show that when a body is moving in a liquid medium, the liquid motion is not fixed relative to the body. By looking at the transverse and radial velocity components and integrating, the drift function, a function defining the position of a liquid particle at time t relative to the initial undisturbed position, can be found. The mass of liquid affected by the body motion is called the *drift mass*, and is equal to the product of the density and the integral of the drift function. By considering the kinetic energy of a body in a liquid it can be shown that the presence of the liquid effectively increases the mass of the body, this additional mass being known as the *hydrodynamic mass*. Darwin proved that for bodies

moving in a straight line in unbounded liquid, the hydrodynamic mass was equal to the drift mass. The hydrodynamic mass for a sphere has been shown to be half the mass of the displaced liquid, and therefore as the gas bubbles in the system are assumed to be spherical :

Virtual Mass of Bubble = Mass of Gas Bubble + 1/2 Mass of the Displaced Liquid

The virtual mass of a bubble can be thought of as the liquid associated with the wake of that bubble. Therefore equation 2.28 becomes :

$$d_c u_t^2 (\rho_g + \rho_l/2) + 1.8 d_c^2 \Delta\rho g - 3.12\sigma = 0 \qquad 2.29$$

The significance of the critical bubble size is that it represents the minimum bubble size that can be achieved by collision with a packing element, if the bubble breaks down as a result. If the bubble is involved in an offset collision with an element of packing, one of the daughter bubbles may be smaller, but the total energy of the bubble before collision is not dissipated in creating new surface area.

2.6.2.3 Effect of Coalescence

The process of coalescence is considered to take place in two stages :

(a) Drainage of the liquid from the region separating the elements which are to coalesce until the liquid is reduced to a critical film thickness

(b) Rupture of the film and the resulting coalescence

The speed of coalescence is determined by a number of factors forcing the elements towards each other, the resistance of the separating film to drainage, and the critical thickness and ultimate strength of the final film.

Coalescence can take place either between two bubbles or between a bubble and a plane interface. In order that drainage can take place, the elements must be held together somehow for a sufficient length of time. In the case of coalescence at an interface, gravitational forces hold the elements of the bubbles against the interface and provide the force necessary for drainage. In a swarm of bubbles coalescence occurs principally due to the relative motion of the elements of the bubbles of different sizes. Large bubbles rise faster and grow in size by collecting small bubbles as they pass through the swarm, and coalescence of bubbles of comparable sizes seems to be a rare occurrence.

It is well known that surface active contaminants effects bubble coalescence but it has also been found that mass transfer has a significant effect on the ease of coalescence. Considerable turbulent motion of the interface can occur during mass transfer which is attributed to local surface tension variations associated with concentration gradients. This is known as the Marangoni effect[34].

Calderbank, Moo-Young, and Bibby[38] investigated coalescence in bubble columns, examining the rate of bubble coalescence in bubble clouds rising through a pool of liquid with and without mass transfer taking place. They found that in air-water systems, where water was

the continuous phase, there was an absence of large spherical cap bubbles produced under their experimental conditions, and therefore by assuming that all the bubbles rose with the same velocity they derived the following expression for the coalescence frequency, f :

$$f = u_t\left[2\frac{d\ln\phi}{dh} - 3\frac{d\ln a}{dh}\right]$$

where u_t is the average terminal bubble velocity, ϕ the gas hold-up, a the interfacial area, h the column height. They also investigated the effect of mass transfer on coalescence, and found that in absorption systems, (CO_2 absorption into water), the number of bubbles per unit volume of dispersion decreased while the mean bubble size remained fairly constant ($d_b \approx 3.5$mm). The coalescence frequency was shown to be proportional to the concentration gradient, and therefore a dynamic equilibrium is set up while simultaneous dissolution and coalescence takes place. It is clear therefore that the mass transfer promotes bubble coalescence in absorption systems. For desorption systems (stripping of CO_2 from water) they found that the number of bubbles decreased, but in contrast to the absorption case the mean bubble diameter increased. Although some coalescence does occur they found the rate to be well below that found in gas absorption.

De Nevers and Wu[39] looked at bubbles rising in a chain through a stagnant liquid, and from their observations deduced that when the bubbles are spaced closely enough one bubble will suddenly accelerate and overtake the preceding one. This is explained by saying that the lower bubble moves into the wake of the upper bubble, resulting in the lower bubble moving more rapidly relative to a fixed point than before. This happens as a result of encountering the upward moving wake of the bubble rather that the fluid at rest. Based on these observations they proposed a model which assumed that the only forces acting on the lower bubble were it's bouyancy force and inertia drag force which decreases as the bubble enters the wake. The experimental results agreed closely with the model predictions when using a viscous fluid such as glycerine, but for water a great deal more scatter of experimental data from the model was seen. The model assumed the coalescing bubbles to be hemispherical and of equal size, which as mentioned earlier is rare in most practical cases, and the authors observations when using water revealed shape oscillations of the bubbles. The model also solely concentrates on the profile of the lower bubble in the wake of the upper bubble, and takes no account of the rupturing of the film between elements of the two bubbles, which is generally regarded as part of the coalescence process. It is therefore likely that the application of this model in most practical systems is very limited.

When considering oxygen stripping from water, as the oxygen is a sparingly soluble gas, the concentration of oxygen in the water is unlikely to have any significant effect on the surface tension of the water film, and therefore the Marangoni effect will be negligable. *Therefore the mass transfer taking place will have minimal effect on the coalescence properties of the system, and any coalescence that occurs will be mainly due to the hydrodynamics of the system.*

2.6.2.4 Effect of Gas Velocity

As mentioned in section 2.6.1, the gas flowrate / velocity will also play a significant part in determining the hydrodynamic characteristics of the column. The following theory was put forward to describe the behaviour of a bubble column as the superficial gas velocity is varied[40]. Although this theory specifically looks at the hydrodynamics of a bubble column and not a packed column, it is detailed as it may be applicable in estimating the gas bubble size.

(i) Uniform Bubbling Regime (Homogeneous Regime)

The uniform bubbling regime occurs at low gas superficial velocities ($0.6 < d_b < 8$ mm, $0.001 < Re_b < 300$). This theory describes the hydrodynamic behaviour of the column by assuming plug flow of the liquid through the column, with small spherical bubbles ascending which are homogeneously distributed over the cross section of the column, and a uniform void fraction (ε) of the bubbles throughout the entire column. As a result the theory provides a relation between the bubble void fraction, the superficial gas and liquid velocities (u_g, u_l), and the mean bubble size (d_b).

The origins of this theory come from consideration of particle fluidization behaviour. By assuming steady state throughput of the continuous phase with the dispersed phase at rest on average, the following equation can be used to find the bubble size :

$$\beta^3 = 18\left\{1+0.341\left[\frac{r_0}{d_p}+\frac{1}{2}\left(\frac{r_0}{d_p}\right)^2\right]\right\}\mathrm{Re}+3\left[1+0.07\left(\frac{r_0}{d_p}\right)^{3/2}\right]\mathrm{Re}^{3/2}+\left[0.3+\frac{0.68}{\mathrm{Re}^{0.1}}\left(\frac{r_0}{d_p}\right)\right]\mathrm{Re}^2 \qquad 2.30$$

where β is a dimensionless bubble diameter, r_0 is the bubble size($d_b/2$), and d_p is the pore size. The above dimensionless quantities are defined as :

$$\beta^3 = \left(\frac{\rho_l-\rho_g}{\rho_l}\right)\frac{d_b^3 g}{\upsilon^2}, \qquad \mathrm{Re} = \frac{u_r d_b}{\upsilon} \equiv \left[\left(\frac{u_g}{\varepsilon}-\frac{u_l}{1-\varepsilon}\right)d_b\right]\upsilon^{-1}, \qquad \frac{r_0}{d_p} \equiv \frac{1}{\left(\zeta/\sqrt[3]{\varepsilon}\right)-1} \quad (\zeta=0.9)$$

As the Reynolds number contains the bubble size, equation 2.30 has to be solved implicitly. Comparison of the bubble sizes found by equation 2.30 and those found experimentally show the degree of accuracy to be $\pm 20\%$.[40]

(ii) Liquid Circulation Regime (Heterogeneous Regime)

As the gas superficial velocity is increased the hydrodynamics of the bubble column change, and liquid circulation results. The liquid circulation regime[40] model assumes the column to have a core in which large bubbles/slugs of gas ascend, with monosized spherical small bubbles ascending homogeneously distributed throughout the column relative to the circulating liquid. The liquid ascends in the core region, and flows down in the remaining annular region of the column and no net throughput of liquid is assumed in the model. The

model has been proved successful when looking at the residence time distributions of the gas bubbles in the bubble column.

When considering this model for a packed column, none of the assumptions made in the homogeneous region are unreasonable, and it is felt that *this theory could be applied to the hydrodynamic behaviour of a packed column at low superficial gas velocities.* However the model is unlikely to accurately predict packed column behaviour in the heterogeneous regime as the large bubbles / slugs formed in the core region would be broken up on impact with the packing, and the assumption of no net liquid throughput would not be valid.

2.6.3 Bubble Velocity

As seen in section 2.6.2.2. the gas velocity is essential for being able to predict the critical gas bubble size. After formation at the orifice a bubble will accelerate from rest through the liquid until the terminal velocity of the bubble is reached, this being the point at which the frictional drag force on the bubble is equal to the bouyancy force. However the analysis of bubble dynamics in a liquid is further complicated by the bubble shape and internal circulation, both of which affect the drag coefficient and terminal velocity. The simplest case to analyse is that for *spherical, rigid particles*. Carrying out a force balance leads to :

$$\frac{d(mu)}{dt} = V_b(\rho_l - \rho_g)g - \frac{1}{2}\rho_g A_p C_d u_r^2 \qquad 2.31$$

where C_d is the drag coefficient, and A_p the projected area of the spherical particle. When the particle has reached its terminal velocity, d(mu)/dt = 0 and equation 2.31 can be reduced to :

$$u_r = u_t = \sqrt{\frac{4d_b g(\rho_l - \rho_g)}{3C_d\rho_l}} \qquad 2.32$$

C_d is a function of the particle Reynold's number and is found to vary as follows[17]:

$$C_d = 24/\mathrm{Re} \qquad 10^{-4} < \mathrm{Re} < 0.1$$

$$C_d = (24/\mathrm{Re})(1 + 0.14\,\mathrm{Re}^{0.7}) \qquad 0.1 < \mathrm{Re} < 1000$$

$$C_d = 0.445 \qquad \mathrm{Re} < 350{,}000$$

Substituting the drag coefficient at low Reynold's numbers (< 0.1) into equation 2.32 leads to :

$$u_t = \frac{g d_b^2(\rho_l - \rho_g)}{18\mu_l} \qquad 2.33$$

which is the equation Stokes (1880) first discovered through his work on the motion of rigid spherical bodies in creeping flow through fluids.

However, gas bubbles are fluid, that is, they do not have a fixed shape and have internal circulation, which in turn will effect the drag force. Hadamard and Rybczynski[23] investigated the motion for a fluid sphere at Re < 1, the motion being only restricted by viscous forces, and modified the drag coefficient : $C_d = (24/\mathrm{Re})(2\mu_l + 3\mu_g)/(3\mu_l + 3\mu_g)$, which when $\mu_g \ll \mu_l$ reduces to $C_d = 16/\mathrm{Re}$. They used purified water and air in their investigations, but for most practical situations, trace impurities in the water will exist and hinder the motion on the surface of the bubbles, the effect of which is to make the bubbles behave more rigidly. Therefore equation 2.33 to has been found to accurately predict the free rise of single gas bubbles for Re<1. Lochiel and Moore[23] derived an expression for the drag coefficient on spherical mobile bubbles for larger Reynolds numbers :

$$C_d = \frac{48}{\mathrm{Re}}\left[1 + \frac{\mu_g}{\mu_l} - \left(\frac{0.314}{\mathrm{Re}^{0.5}}\right)\left(\frac{4}{3} + \frac{2\mu_g}{\mu_l}\right)\right]$$

which has been verified by other authors. Simpler correlations[36] show the drag coefficient on bubbles to vary at the higher Reynolds number as :

$$C_d = \frac{18.5}{\mathrm{Re}^{0.6}} \qquad 2 < \mathrm{Re} < 500$$

$$C_d = 0.445 \qquad 500 < \mathrm{Re} < 200{,}000$$

Work looking at the shapes of gas bubbles has also been extensively investigated. Although there is generally agreement on the nature and shape of the bubbles as the diameter increases, there is some disagreement as to the actual size of the bubbles at which their shape and nature changes. For gas bubbles in low viscosity liquids, it is generally agreed that bubbles with $d_b < 1$ mm are approximately spherical in shape and rise in straight lines. Intermediate sized bubbles, $1 < d_b < 6$ mm, are generally ellipsoidal becoming increasingly irregular at larger diameters the degree of which is given by the eccentricity, E (the ratio of the major to minor axis), and large bubbles, $d_b > 6$ mm, assume a spherical cap shape. Tadaki and Maeda[23] determined correlations linking the eccentricity of the bubbles with Reynolds number, and found that for spherical cap bubbles E = 3.5.

Experimental data for the 'free' rise bubble velocity has been found by a number of authors, Haberman & Morton, and Motarjemi & Jameson[41] looking at oxygen bubbles in water. Their experimental findings showed the gas bubble terminal velocity to vary from 3 - 15 cm/sec for bubble diameters ranging from 0.2 - 1.5 mm. These results correspond well with earlier work carried out by Allen[42]. In his experimental investigations of air bubbles in water, he showed that for small diameter bubbles, $d_b < 0.15$ cm, the bubble terminal velocity was proportional to the bubble diameter, and found that :

$$u_t = k\left(\frac{(\rho_l - \rho_g)g}{\rho_l}\right)^{2/3} \frac{r_b - k'r_c}{\upsilon^{1/3}} \qquad 2.34$$

where the constants k and k' were found to be 1/2 and 2/5 respectively, and r_c, the critical bubble radius which occurs when $u_t r_b = \upsilon$, i.e. $r_c = \upsilon / u_t$. Motarjemi & Jameson[41] also showed that in general, the smaller the bubble the more sensitive its motion and drag is to trace impurities in the water, i.e. the closer it becomes to rigid behaviour. As the bubbles become larger, the terminal 'free' rise velocity of bubbles of size $0.2 < d_b < 8$ cm in water and other low viscosity liquids has been described by Mendelson[43,26]. The bubbles are no longer spherical and rise in a zigzag or helical path with a terminal velocity given by :

$$u_t = \sqrt{\left(\frac{2\sigma}{d_b \rho_l} + \frac{d_b g}{2}\right)} \qquad 2.35$$

As a result of this literature review it is possible to collate all the bubble velocity regimes as seen graphically in Figure 2.17, which plots the gas bubble terminal velocity against the gas bubble diameter for air in water.

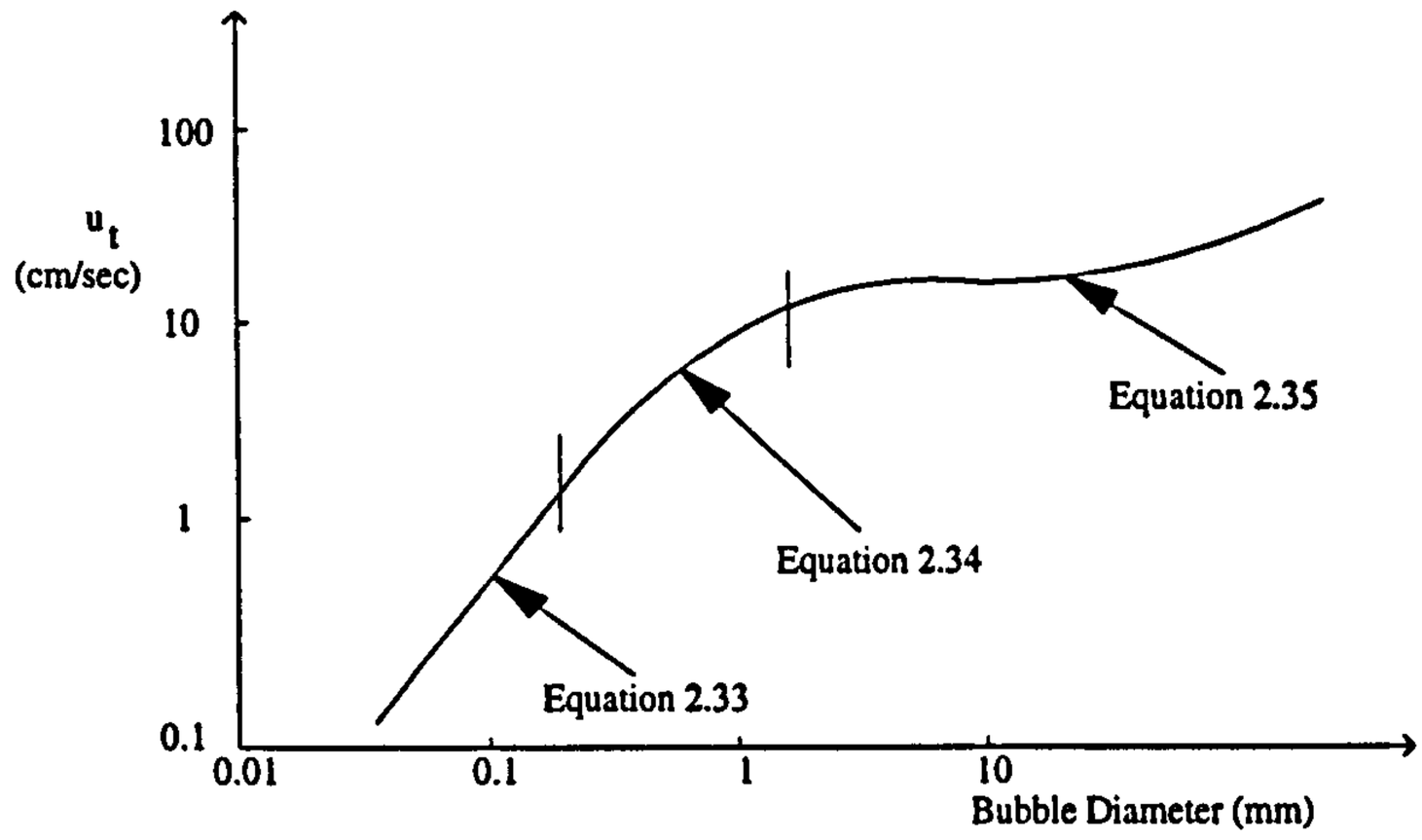

Figure 2.17 : Rising Terminal Velocity of Single Gas Bubbles

The correlations covered in this section will be used for predicting the gas bubble velocity through the packed rotary contactor.

2.6.4 Gas Hold-up

The Gas Hold-up, ϕ_g, is defined as the volume fraction occupied by the gas in a gas-liquid system, and by comparing the liquid heights in the column during operation, L, and without any gas flow, L', the holdup is given by :

$$\phi_g = \frac{L - L'}{L}$$

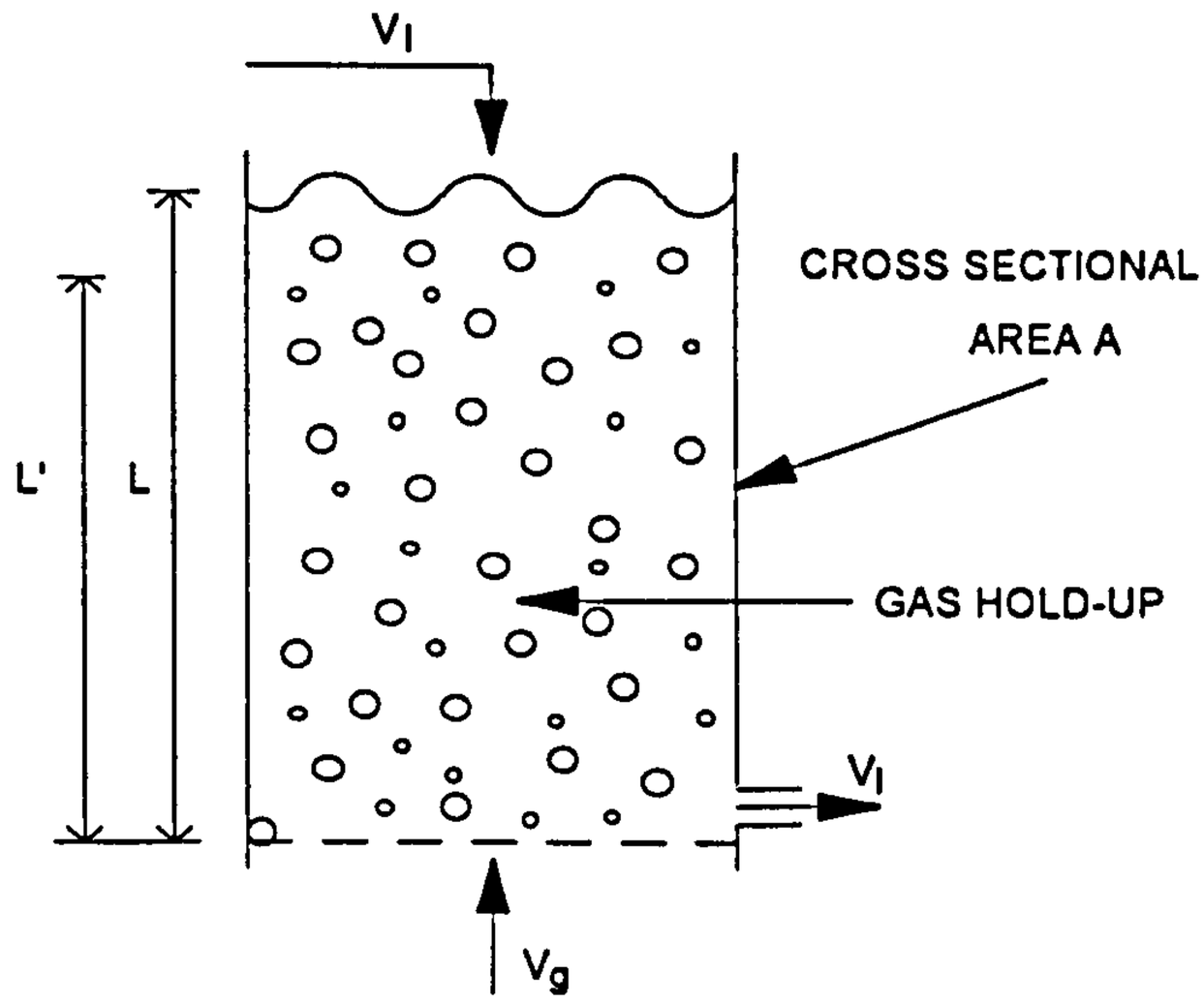

Figure 2.18 : Hold-up in Gas Bubble Column

In practice probably the easiest method of measuring the gas hold-up is to measure the operating level and the 'gas free' liquid level, which will give the average column gas hold-up. However, the gas hold-up will vary throughout the column both radially and axially, and will be a function of many parameters such as the column size, gas and liquid flowrates, gas distributor, and physical properties of the gas and liquid. By assuming ideal bubble flow ($\phi_g <$ 20%), i.e. bubbles of uniform size, terminal rise velocity, and even distribution throughout the column cross section, the gas and liquid superficial velocities relative to the vessel walls are given by u_g/ϕ_g, and $u_l/(1-\phi_g)$ respectively. For *counter-current* flow of liquid and gas, equation 2.36, which shows the relative (or slip) bubble rise velocity, u_r, can be used as a good basis to find the hold-up.

$$u_r = \frac{u_g}{\phi_g} + \left(\frac{u_l}{1-\phi_g}\right) \qquad 2.36$$

As the liquid phase generally has a greater material capacity than the gas phase, and with the liquid velocity normally low thus having minimal influence on the hold-up, the hold-up is best described by :

$$\phi_g = u_g^n$$

where n is dependant on the flow regime, gas distributor and material properties, and ranges from 0.7-1.0 in the *homogeneous* region and 0.4-0.7 in the *heterogeneous* region. In many bubble columns the liquid superficial velocity is low (u_l < 1 cm/sec), and Hughmark[29] correlated the hold-up in sparged columns of different diameters (see Fig. 2.19) with the superficial gas velocity at zero liquid flow, or for cocurrent liquid systems if the hold-up is defined by :

$$\phi_g = \frac{u_g}{u_r} = \frac{u_g}{u_t + u_l}$$

The effect of the gas distributor type and gas and liquid physical properties on the hold-up is complex, but work by Schugerl, Lucke, and Oels[44] show that the hold-up increases as a function of the gas distributor in the following way : perforated plate < sintered plate < injector nozzle < ejector nozzle. Their findings also reveal that the hold-up increases with different substrates / salt solutions such that : demineralized water < 1% salt solution < 1% alcohol solution, and these findings are explained by considering the coalescence properties of the liquid. In attempting to predict the gas hold-up they derived the following relation which agreed, for all gas distributor types, with the experimental data to within a mean relative error of 14.5%.[44]

$$\phi_g = 0.91 Fr^{1.19} \qquad 2.37$$

where the Froude Number, $Fr = \frac{u_g}{\sqrt{g d_s}}$, and d_s the Sauter mean bubble diameter (eqn. 2.39).

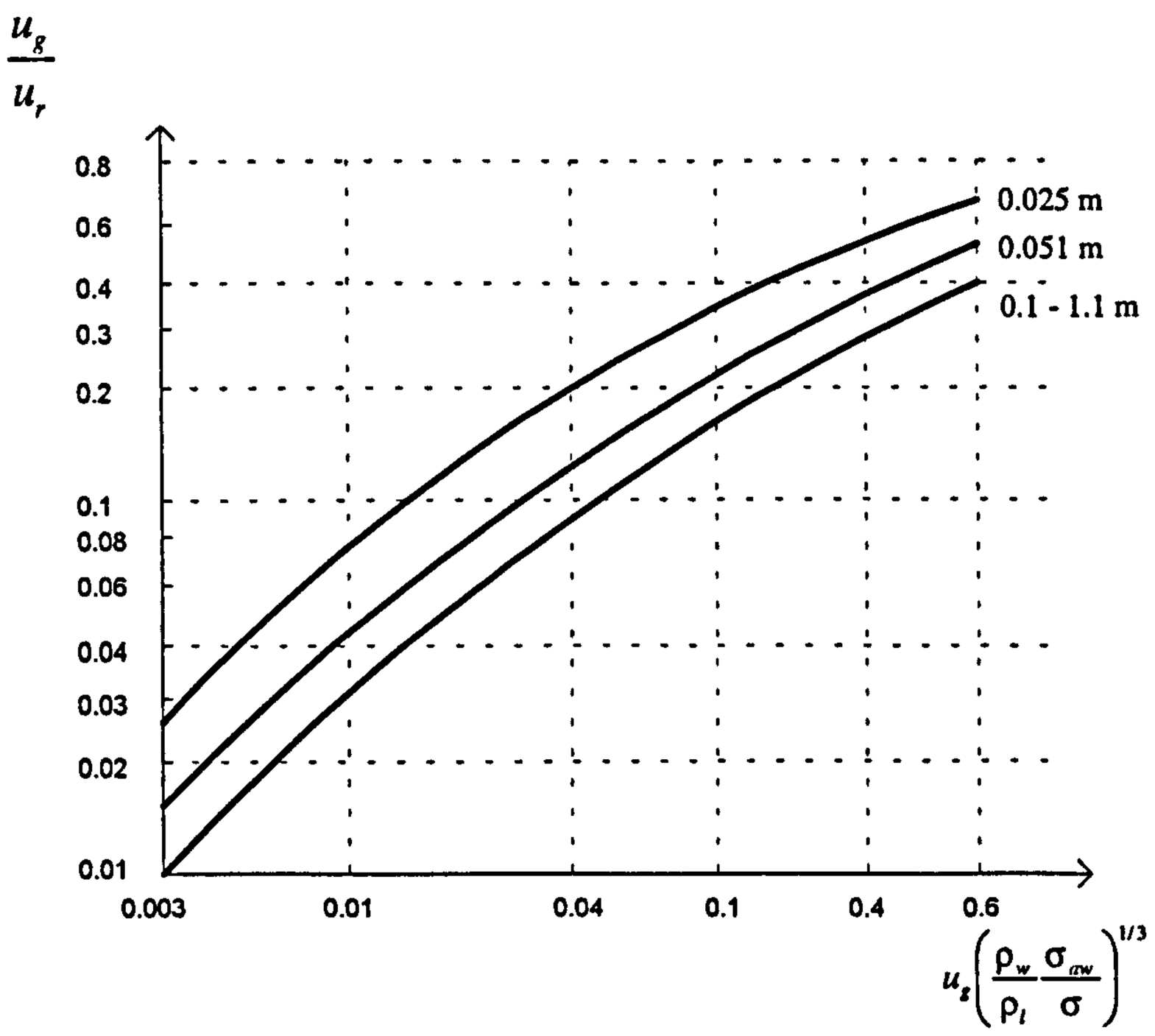

Figure 2.19 : Hughmark Correlation for Slip Velocity in Bubble Columns of varying Diameters[34]

In cases where the liquid superficial velocity is high (u_l > 5 cm/sec), the gas hold-up is significantly effected. For cocurrent gas-liquid systems the hold-up falls as the liquid superficial velocity rises, and for counter-current systems the hold-up rises as the liquid superficial velocity rises. Bridge, Lapidus, and Elgin[45] in investigating the similarities between counter-current gas-liquid and fluidized bed systems, studied an air and water system, and found that the gas hold-up increased as the liquid superficial velocity increased and this increase became more pronounced at higher gas superficial velocities. However below

superficial gas velocities of 1-2 cm/sec they found that the air and water system could be described well using Zenz's correlation for fluidized beds. Using an air-water system also, Hills[43] found that for $u_l > 30$ cm/sec the hold-up could be described by :

$$\frac{u_g}{\phi_g} = 0.24 + 1.35(u_g + u_l)^{0.93}$$

The hold-up is a very important parameter in characterising the packed column hydrodynamics, as it determines the fraction of gas in the column which leads to the phase residence time, and in combination with the bubble size distribution the hold-up gives the interfacial area between the two phases and therefore the interfacial mass transfer rate. The gas hold-up and interfacial mass transfer area, a, are related by the following expression :

$$a = \frac{6\phi_g}{d_b} \qquad 2.38$$

where d_b is the bubble diameter. In gas-liquid systems the bubble diameter will vary over a range of values, but the Sauter mean bubble diameter[31], defined by equation 2.39, is most widely accepted as the best measure of the mean diameter to find the interfacial area.

$$d_s = \frac{\sum_i n_i d_{bi}^3}{\sum_i n_i d_{bi}^2} \qquad 2.39$$

The gas hold-up has been shown to be a vital parameter required in predicting the mass transfer in gas - liquid systems. It has been extensively investigated, and many parameters such as the gas distributor type, the liquid velocity and direction with respect to the gas flow, have been shown to significantly effect the value of the gas hold-up.

2.7 Effect of High Gravitational Fields (Higee)

Higee is a concept that uses centrifugal force to create an artificial gravitational environment, the main advantage of which is that the magnitude of the accelerations created by the centrifugal force can far exceed the acceleration due to gravity, 9.81 m/sec^2 (see Table 2.2). Ramshaw[4] was one of the first to realise the potential implications of this to a number of two phase counter-current separation processes. The acceleration within a centrifugal field is given by :

$$g^* = \omega^2 r = ng \qquad 2.40$$

Even modest speeds of rotation can produce significant increases in applied acceleration, and Table 2.2 shows the magnitude of the acceleration at a radial depth, r, of 0.4m with varying rotational speed .

Table 2.2 Effect of Rotational Speed on Acceleration (r = 0.4 m)

Speed (rpm)	50	100	200	300	400	500	1000
g* (m/sec^2)	11	44	175	395	700	1100	4400
n (where g* = ng)	1.1	4.5	18	40	71	110	450

2.7.1 Current Commercial Applicatons

At present most chemical processes take place under a normal gravitational environment, but rotary solvent extraction units have been successfully used for quite some time. Podbielniak[46] developed the first commercially successful rotary extractor in 1944. The extractor consisted initially of a perforated spiral wrapped around a shaft, but this was later updated to concentric perforated cylinders. Around the same time two German companies developed the Luwesta extractor, a vertical multistage design basically consisting of three mixer settlers mounted on top of each other. This design has also been successful for penicillin extraction.

The need to develop rotary solvent extractors arose as a result of large scale production of penicillin during the Second World War. Rotary extractors were used to recover the penicillin from fermentation broth, and the early processes used three stages to concentrate the penicillin to the desired level. Other applications for which rotary solvent extractors are used include lubricating oils and effluent treatment. Oil mixtures produced by distillation normally contain aromatic and polar compounds that degrade under the operating conditions of most lubricants, and solvent extraction is used to remove these compounds from the oil. The treatment of effluent streams usually involves removing small concentrations of chemicals (< 0.5%), and the ability of rotary extractors to handle large throughputs, and give high mass transfer performance make them particularly suitable for this area.

2.7.2. Advantages of Increasing the Gravitational Acceleration

The advantages of using increased gravitational fields can be seen when looking at the how the hydrodynamics of a bubble column are dependant on 'g'. In sections 2.6.2 and 2.6.3 the bubble sizes and velocities were studied, and from various equations their dependency on the gravitational acceleration was seen as follows :

Bubble Formation : $d_b \propto \left(\frac{1}{g}\right)^{1/3}$ (eqn. 2.25), $d_b \propto \left(\frac{1}{g}\right)^{1/5}$ (eqn. 2.26)

Bubble Velocity : $u_t \propto g^{1/3}$ (eqn.2.32 and substituting $d_b \propto g^{-1/3}$)

The above equations show that as the gravitational field increases the bubble size will decrease, leading to a greater interfacial mass transfer area, and therefore overall mass transfer. We also observe that the bubble velocity will increase as the gravitational field is increased which

should mean an increase in hydraulic capacity. This is confirmed by the Sherwood correlation (sect.2.4.2) which relates the flowrate ratio to the quantity $u_s^2 a_t / g\varepsilon^3$. As this value is fixed for a given flow ratio, the use of high 'g' means a resulting increase in u_g. Experimental work has also been carried out on the effect of increasing the gravitational environment on the volumetric mass transfer coefficient by Keyvani and Gardner[47], and Vivian et al.[48], who report the volumetric mass transfer coefficient to increase with rotational speed to an exponent of between 0.4 - 0.7.

Table 2.3 shows what the potential of this increase can mean in practice, and compares a traditional column with a rotary machine for the de-oxygenation of 46 kg/sec of sea water from 10 ppm to 20 ppb :

Table 2.3 : Comparison of Rotary De-Aerator with Column[49]

		Rotary De-Aerator	Column
Space (m)		Area - 2 x 2 Height - 2	Area - 2x2 Height - 20 3 stages Diameter - 1.47
Residence Time (secs)		20	180
Weight (Tonnes)			
	Vessel	2.9	9.5
	Packing	0.2	1.6
	Liquid	1.8	22.3
Power	Motor	0.6	
	Vacuum		5.0
	Total	5.5	38.4

In 1992 the cost of supporting 1 Tonne of off-shore platform equipment was approximately $45,000[50]. The running costs are similar because the power requirements are comparable, and the stripping gas for the rotary machine will be natural gas which can then be used as fuel. While the potential for significant overall cost savings is clear, practical research and development work is required, which is the subject material of this thesis. Previous work carried out on a 0.5m diameter rotor with 0.1m radial depth of packing showed that 2.5 mass transfer units could be obtained to process saturated water at $18m^3/hr$[51]. In order to realise the full potential of using Higee technology for the stripping of oxygen from water, and to provide a greater understanding of the interaction between the gas bubbles and liquid, a larger 1 m diameter rotor was built to give a larger radial contact depth, and therefore further mass transfer.

The subsequent sections of this thesis detail the initial design of the rotor and its subsequent development, together with the observed hydrodynamic and mass transfer performance, and compares the experimental findings with those predicted by various theoretical equations.

CHAPTER 3. ROTOR DESIGN

3.1 History and Development

As seen in Section 2.7 the potential application of Higee technology for the process of de-oxygenating water would seem very promising. However in taking the idea from its conceptual stage through to the final full scale design requires gradual development through a number of stages.

In the initial stages of development the gas phase was the continuous phase with liquid droplets or rivulets passing through. However high energy penalties were incurred due to the liquid reaching peripheral velocities of up to 60 m/s, and also due to intense shearing of the thin liquid film as the liquid flowed radially outwards over the packing. Although the shearing of the film gave rise to improved mass transfer, the kinetic energy of the liquid as it left the periphery of the machine was lost, and for a water throughput of 500 tonnes/hr it was shown that the typical power consumption was 500 kW[52] - a power consumption that was deemed unacceptable. Further, investigation into sparingly soluble gases in liquids showed that relatively small volumes of gas are needed to carry out the stripping duty compared with that required for more soluble systems. Typically for oxygen stripping the volume ratio of inert gas (at s.t.p.) to liquid is 0.1 - 0.5. Therefore by making the liquid the continuous phase and the gas the dispersed phase the flow ratio of liquid to gas will be more acceptable, and the liquid phase can be returned to the centre of the machine and therefore most of it's kinetic energy recovered. By considering the liquid kinetic energy as it leaves the machine and the inlet gas compression needed, the power requirements of a machine with the liquid as the continuous phase would be 63 kW for a throughput of 500 tonnes/hr[52]. This is a considerable reduction in power usage compared to the cost of operating the machine with the gas as the continuous phase, and therefore led to further research along this design strategy.

The next stage was to build a small prototype machine (Mark I Rotor) with a continuous liquid phase, the design and results of which are given in Section 3.2. Work was carried out on the Mark I machine investigating the mass transfer performance for different gas and liquid flowrates. Along side this bubble studies were carried out to examine the effect of bubble sizes produced in high gravitational fields. From the culmination of this work the next stage along the line of development was to build a scaled up 1 metre diameter rotary Mark II machine, the design for which is shown in Section 3.3.1. It is the Mark II machine that the research of this thesis is based around, and it is hoped that the findings will lead to an initial full scale industrial design.

3.2 Mark I Rotor

Figure 1 shows the design of the initial prototype machine for the de-oxygenation of water. The rotor is 0.5m in diameter and incorporates a torus of packing of radial depth 10cm, initial width 5cm, capable of being rotated upto 1500 rpm and having a liquid throughput of 10 tonnes/hr. The design allowed the packing width to be reduced to 2.5cm in order to reduce the demand on gas and liquid.

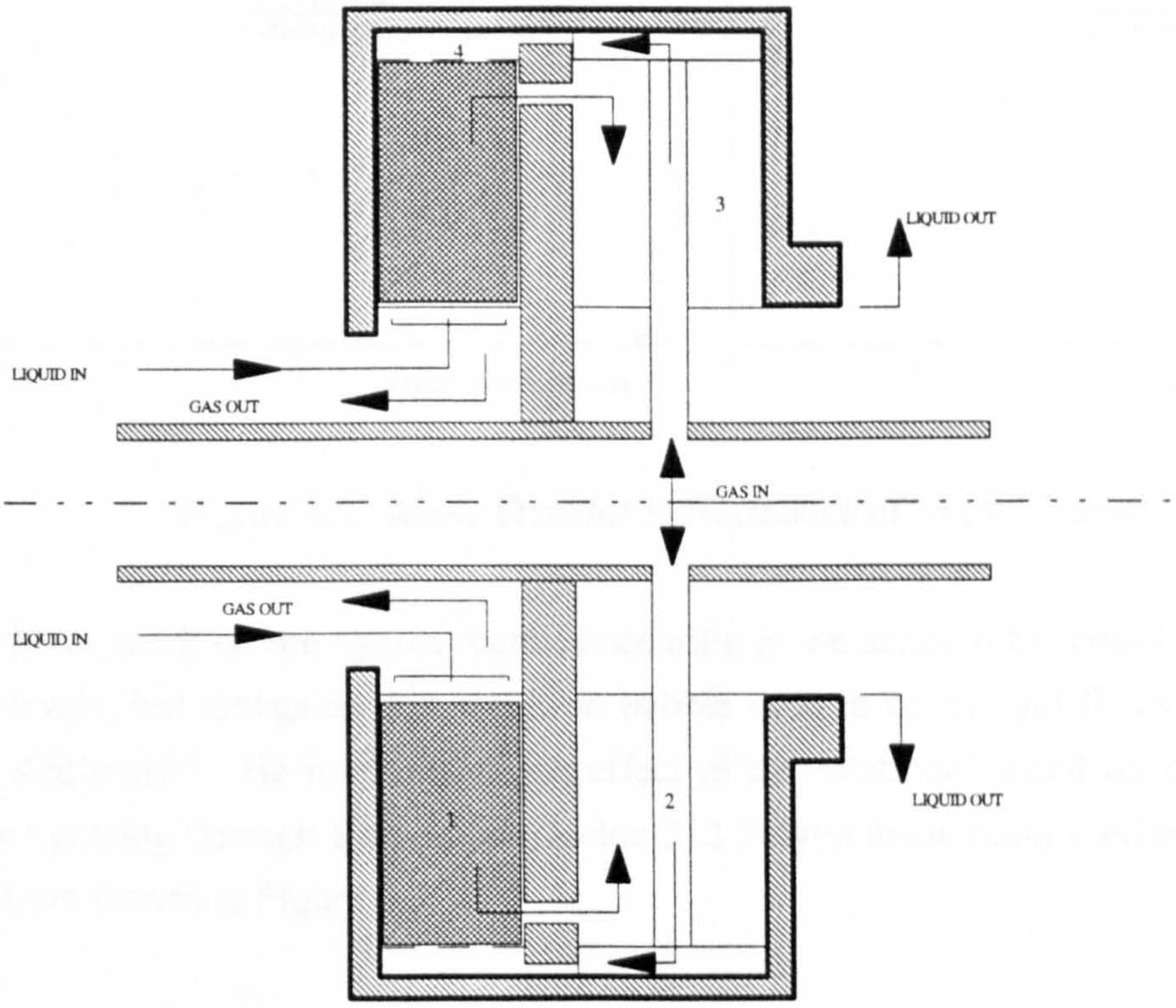

1 - DECLON 312 IMPREGNATED POLYURETHANE FOAM
INNER RADIUS 10cm
OUTER RADIUS 20cm
WIDTH 5cm
2 - RADIAL GAS TUBE
3 - RETURN CHAMBER
4 - PLENUM CHAMBER AND MEMBRANE

Figure 3.1 : Original Design Mark I Rotor

The stripping gas used was nitrogen. The gas was passed through two radial tubes (2) and then into the peripheral plenum chamber (4). The gas then passed through a porous stainless steel distributor, supporting a Permair F membrane (pore size 27 microns), into the rotating pool of liquid, and the bubbles formed migrated counter-currently through the liquid and packing (1). The liquid was sprayed via stationary nozzle distributors near to the inner liquid surface and flowed radially out. However instead of being collected at the periphery, the liquid passed into the return chamber (3) and was transferred radially inwards to the lip of the weir, where it was then recoverd. The reason for this was to recover the majority of the kinetic energy of the rotating liquid pool.

The results produced by this machine were taken by Balasundaram[51] and can be seen in Figure 3.2. They show that for the Mark I rotor machine, there is improved mass transfer as the gas flowrate is increased and a decrease in mass transfer as the liquid flowrate increases.

3.2.1 Results from Mark I Machine

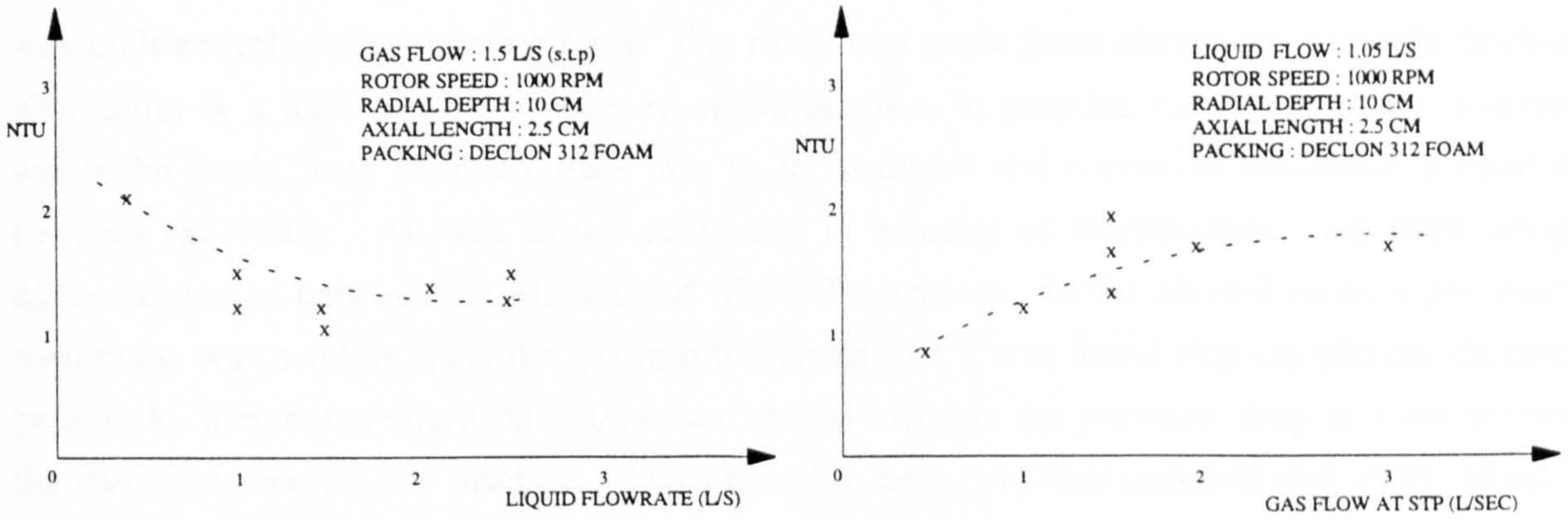

Figure 3.2 : Mass Transfer Performance of Mark I Rotor

Little work on the hydrodynamics occuring in the actual rotor could be carried out due to the design, but alongside this, work on bubble sizes in centrifugal fields was being carried out by Alshaban[7]. He investigated the effect of the rotational speed on the average bubble size after passing through 1 cm of the Declon 312 Polyurethane foam used in the rotor, and his findings are shown in Figure 3.3.

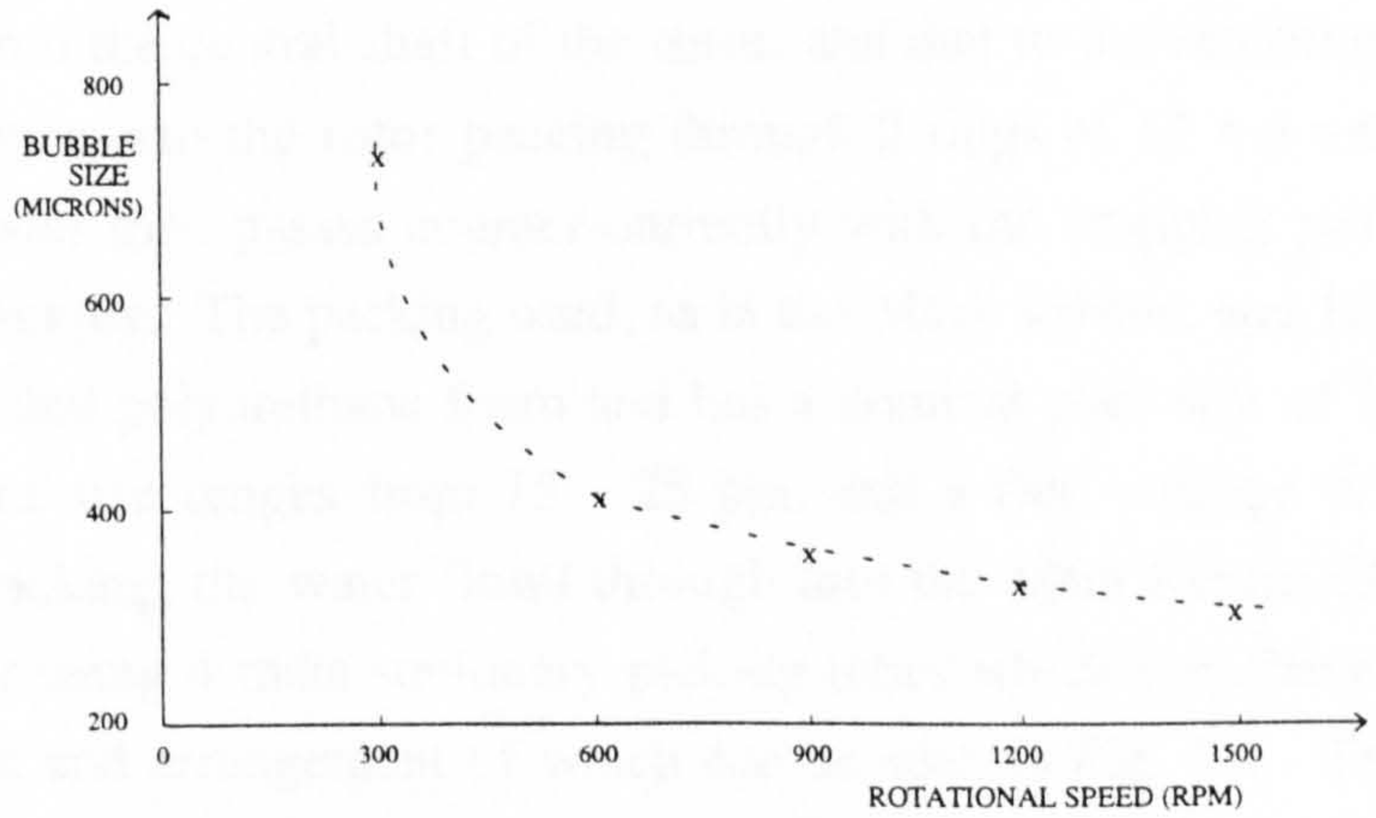

Figure 3.3 : Variation of Bubble Size with Rotational Speed

Figs. 3.2, 3.3 showed promising potential of the use of Higee Technology for the gas - liquid systems, and as a result the next stage required a scaled up rotor design to be built which could be used to investigate the mass transfer further, and to visually explore the hydrodynamics that occur between the gas and liquid in these centrifugal environments.

3.3 Mark II Rotor

3.3.1 Mechanical Design

The original design of the scaled-up Mark II rotor machine can be seen in Figs. 3.4 - 3.6. The rotor is made entirely from aluminium except for the central shaft about which it rotates, which is made from stainless steel. This is in contrast to the Mark I machine which was built entirely using stainless steel. The rotor was made from aluminium primarily because aluminium is a light metal and easy to manufacture. In practice the entire rotary machine would be made from stainless steel due to its strength and corrosive resistance properties towards salt water. As well as the difference in material of manufacture, two main design differences exist between the Mark I and Mark II machines. In the Mark I rotor, a peripheral membrane was used to inject the gas into the liquid, but it was found that the plenum chamber behind the membrane could fill with water and so increase the pressure drop or even prevent the gas from entering the machine. This proved to be a continual problem and so the Mark II machine was designed with 120 individual gas injector nozzles which if filled would easily blow out the water. The second main design difference between the two machines is the way in which the water is removed from the rotor. The Mark I machine used a weir box arrangement so that as the liquid passed into the return chamber it would migrate towards the centre and spray out over the back plate which acted as the weir. A collection box around the machine caught the liquid as it flew out of the rotor. In the Mark II machine instead of using the weir arrangement, stationary pick-up tubes are mounted near to the shaft and collect the water at the interface.

Figure 3.4 shows a cross sectional view through the rotor. Water is passed through the rotary union into the central shaft of the rotor, and due to the centrifugal force acting upon it, the water is flung into the rotor packing through 2 rings of 12 x 4 mm diameter holes in the shaft. The water then passes counter-currently with the stripping gas (in this case nitrogen) through the packing. The packing used, as in the Mark I rotor, was Declon 312 HC20, which is an impregnated polyurethane foam and has a nominal pore size of 20 pores per inch (ppi), the actual pore size ranges from 15 - 25 ppi, and a free voidage of 95%. Having passed through the packing, the water flows through into the Main Return Chamber and is removed from the rotor using 4 main stationary pick-up tubes which each have a bore size of 12 mm, and the design and arrangement of which can be seen in Fig. 3.6. The rotor also contains a smaller Sample Return Chamber the purpose of which is to collect and analyse water taken at various radial depths by 8 sample tubes. These tubes are placed at 1/5, 2/5, 3/5, and 4/5 of the radial packed length, 2 tubes at each length. Each tube in design is nominally identical and consists of a nominal bore of diameter 5.8 mm for the liquid to flow through. By separately analysing the water from this chamber it is hoped that a greater understanding in the variation of the rate of mass transfer with the radial depth may be determined. The water in the sample

return chamber is removed using two smaller pick-up tubes, each with a nominal bore size 8 mm (see Fig. 3.6).

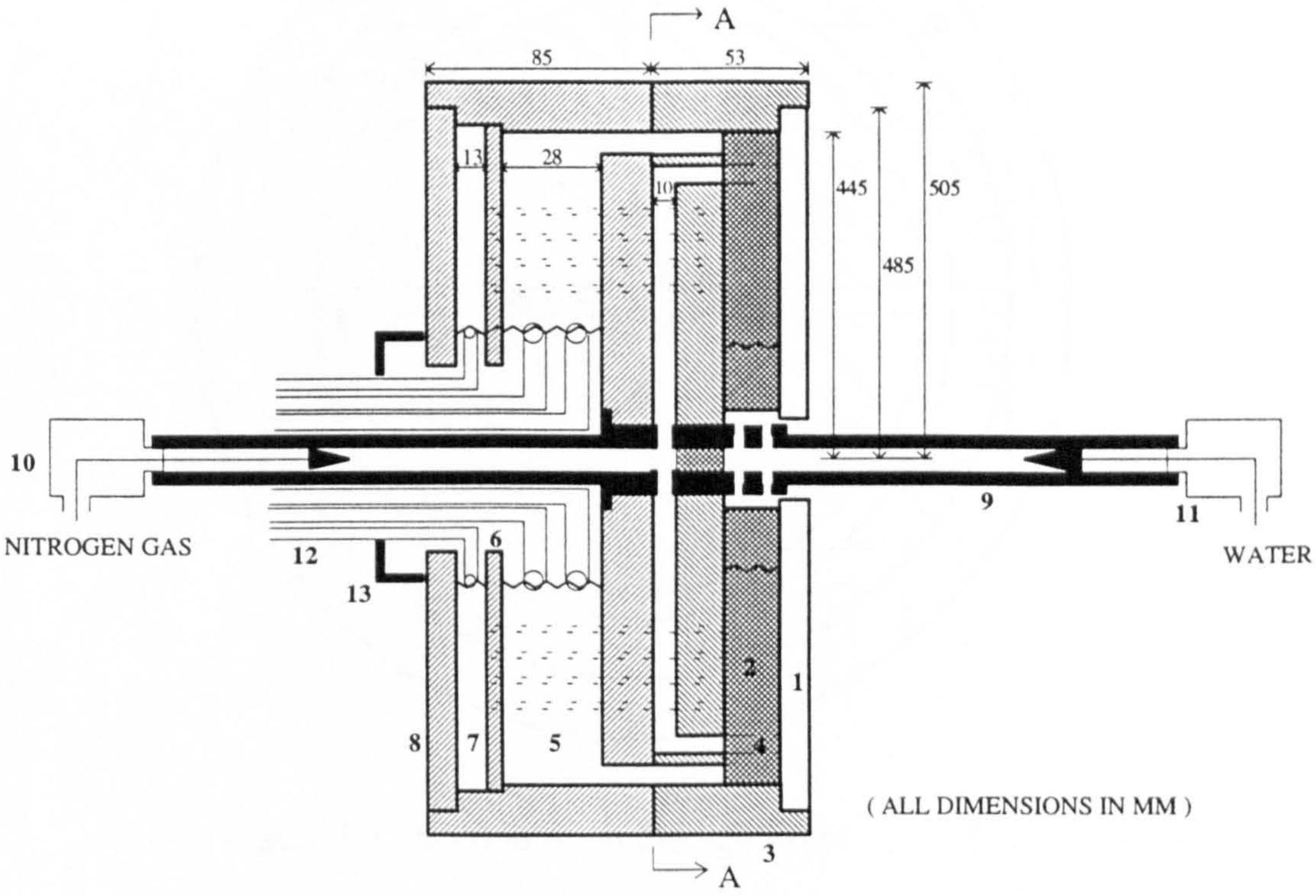

MAJOR STRUCTURAL ITEMS

1 - POLYCARBONATE WINDOW 108 mm I.D., 970 mm O.D., 10 mm width

2 - DECLON 312 HC20 PACKING : IMPREGNATED POLYURETHANE FOAM
PORE SIZE 15 - 25 ppi.

3 - MAIN CHAMBER : 60 mm THICK ALUMINIUM

4 - GAS INJECTOR NOZZLES x 120

5 - MAIN RETURN CHAMBER

6 - CHAMBER SEPARATOR PLATE : 300 mm I.D., 927 mm O.D., 10 mm width

7 - SAMPLE RETURN CHAMBER

8 - BACK PLATE : 300 mm I.D., 970 mm O.D., 13 mm width

9 - STAINLESS STEEL SHAFT : 50 mm I.D., 76 mm O.D., 1006 mm LONG

10 - GAS ROTARY UNION : DEUBLIN Model No. 2200-000-102

11 - LIQUID ROTARY UNION : DEUBLIN Model No. 525-000-055

12 - PICK-UP TUBES

13 - NITROGEN BLANKET COVER : 360 mm O.D.

Figure 3.4 : Cross Section through Mark II Rotor Machine

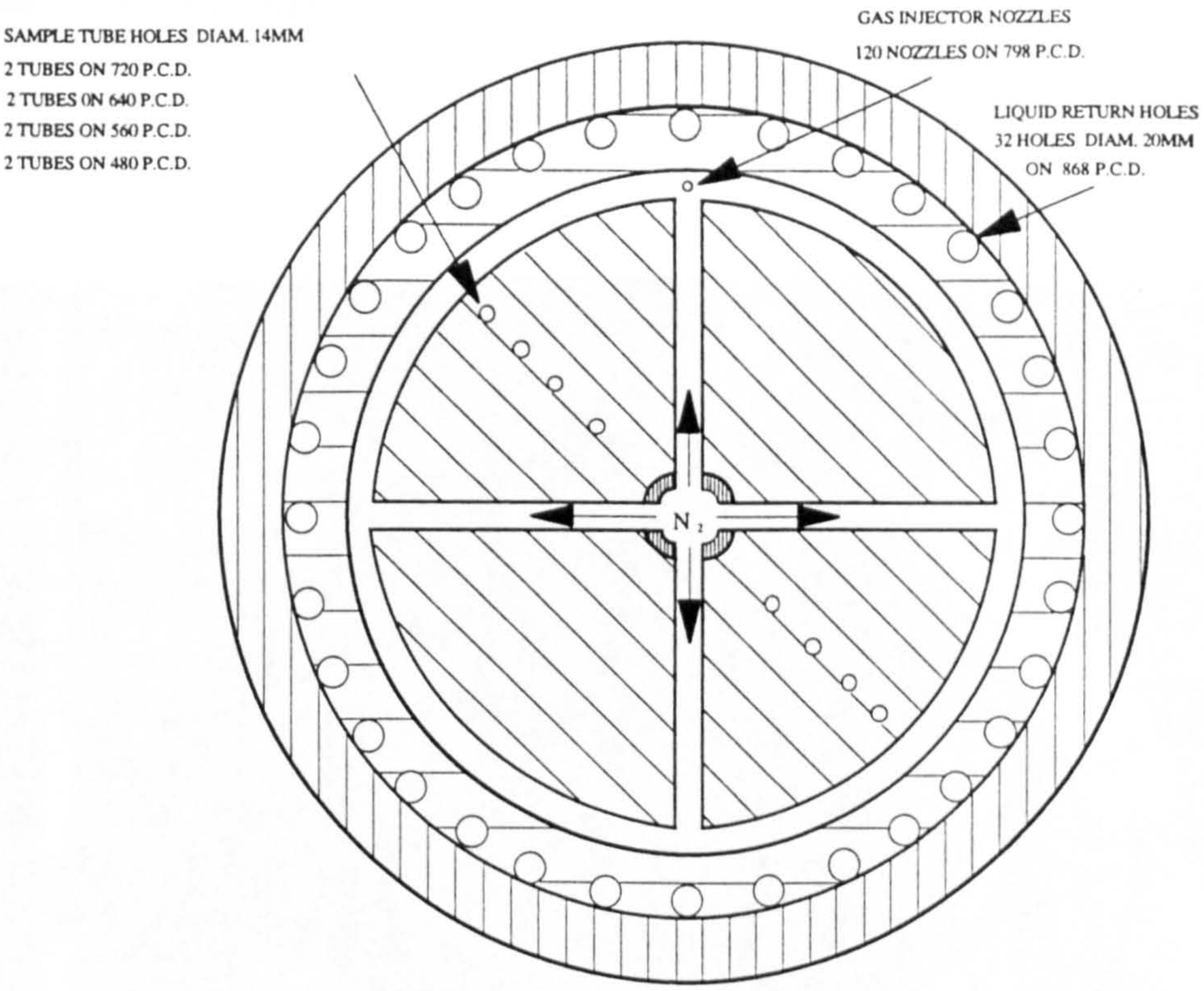

Figure 3.5 : Section A - A through Rotor

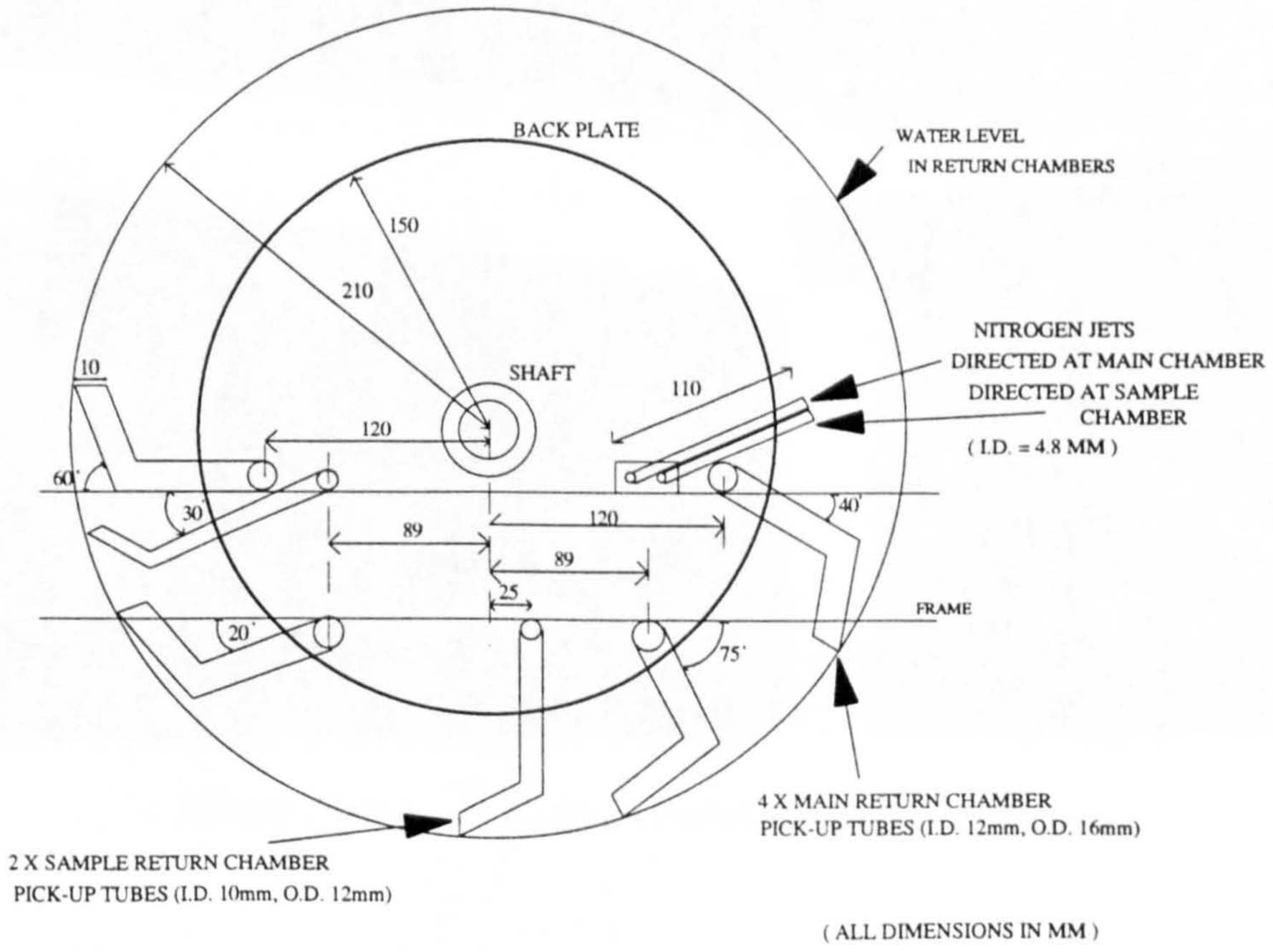

Figure 3.6 : Rotor Pick-up Tube Arrangement

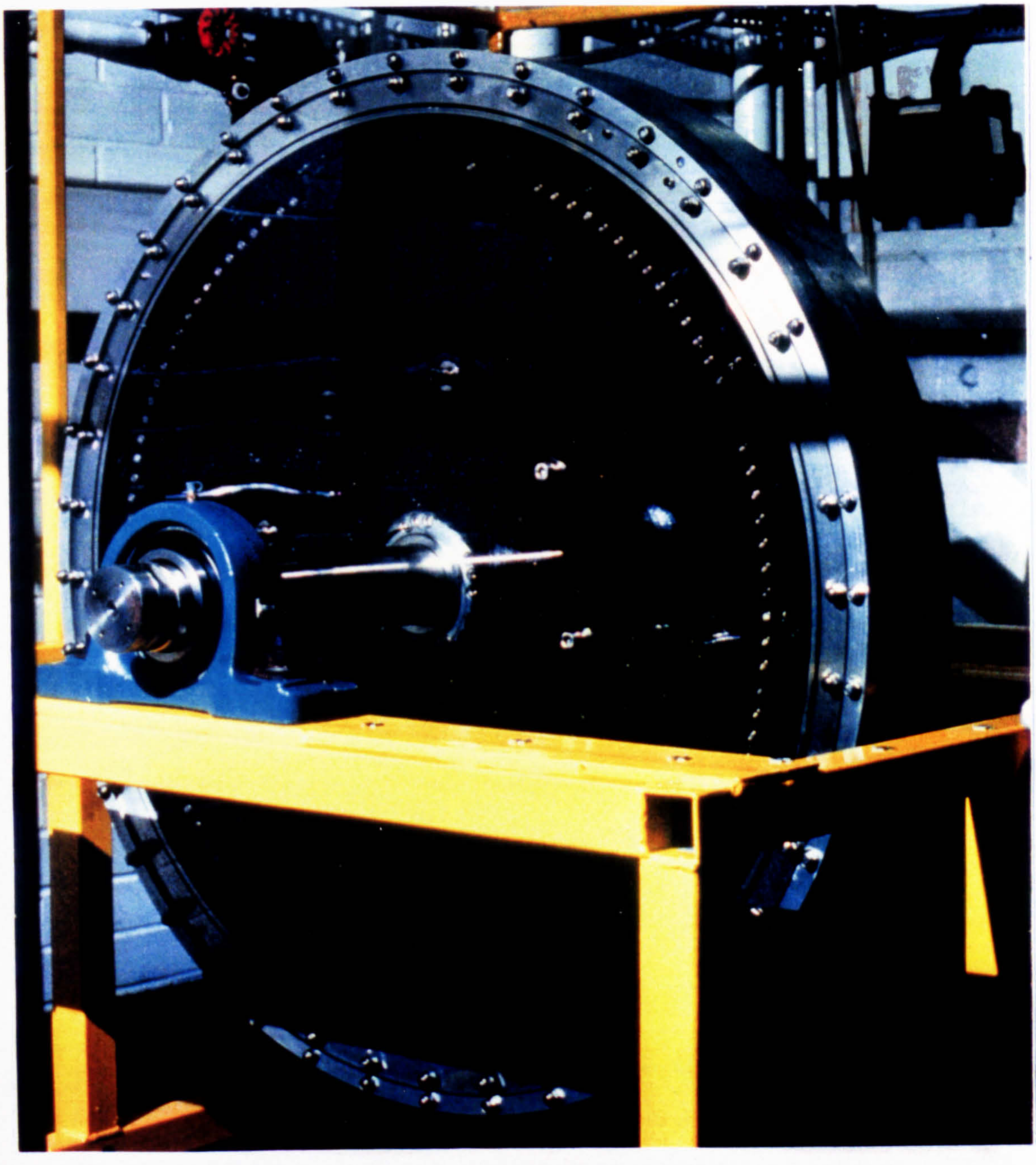

1 Metre Diameter Rotor (Front View)

The nitrogen gas is also passed via a rotary union into the shaft of the machine (the opposite end to the liquid). The gas is displaced from the shaft via 4 main radial vanes into an annular header on which the 120 gas injector nozzles are located, as shown by Fig. 3.5. The design details of the individual gas injector nozzles can be seen in Fig. 3.7. As is shown each individual nozzle contains 2 x 0.5 mm holes which are directed towards the outside of the rotor. This means that the centrifugal force should help prevent water getting into the nozzle, and make it easier to blow out if any should get in. The gas passes counter-currently to the liquid flow before leaving the rotor to the atmosphere between the shaft and packing.

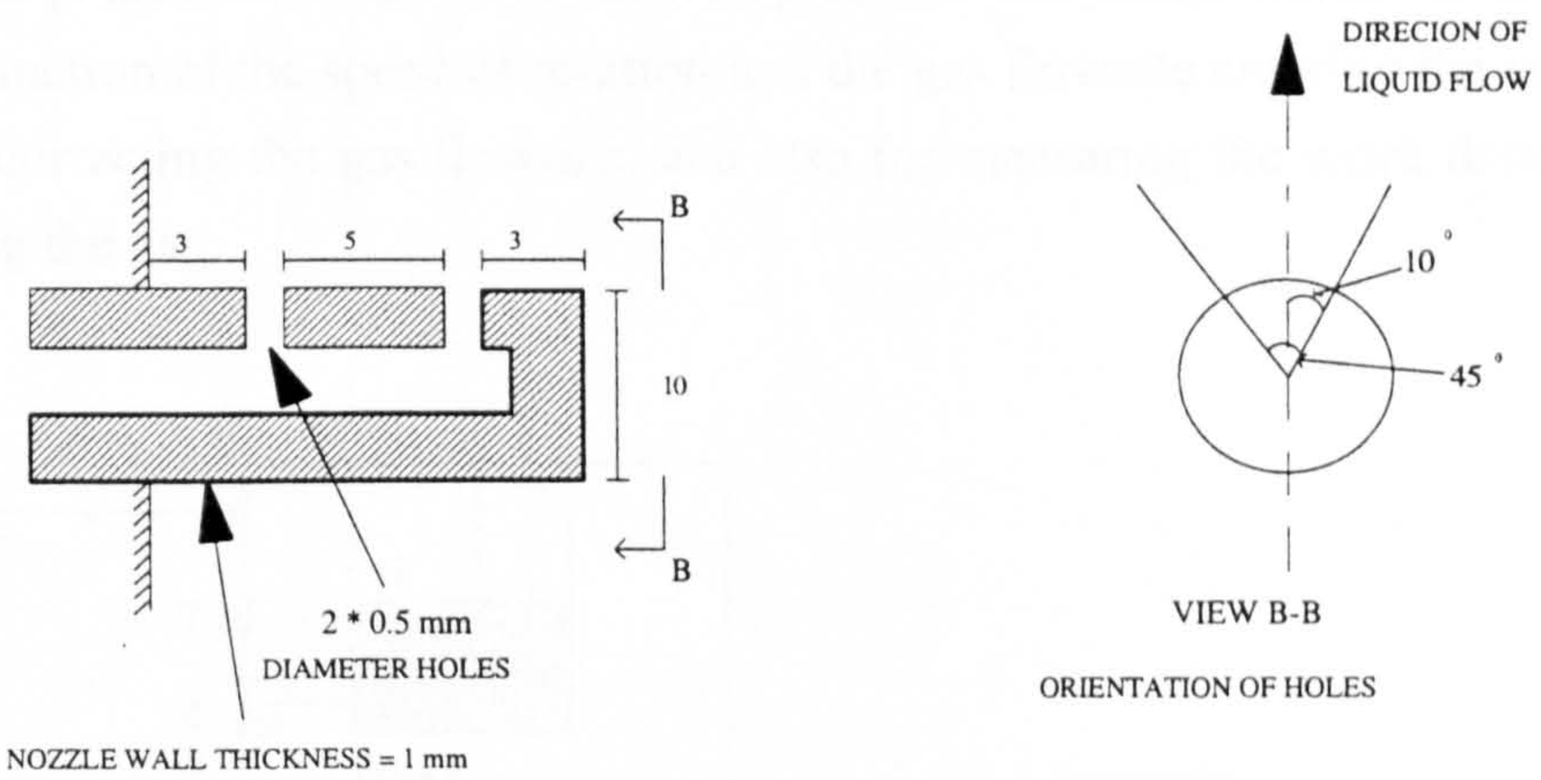

Figure 3.7 : Gas Injector Nozzle Design

Table 3.1 Range of Experimental Operating Conditions

Range of Operating Conditions for the Mark II Rotor					
Speed (rpm)		Gas Flowrate (m^3/hr) (s.t.p.)		Liquid Flowrate (l/s)	
Maximum	Minimum	Maximum	Minimum	Maximum	Minimum
500	200	4.0	0.5	0.1	0.5

The above table shows the experimental ranges of the speed, gas flow and liquid flow used in the operation of the rotor. Below a speed of 200 rpm it was found that the liquid did not couple properly with the packing and would leak out of the centre of the machine. The upper rotational speed was initially 400 rpm due to the strength of the polycarbonate window. However later the polycarbonate front was replaced with an aluminium plate, and the strength of the new plate allowed for higher rotational speed to be attained. The limits for the gas flowrate are such that there must always be gas flowing through the rotor to prevent the nozzles from filling, and usually any gas flow above the upper limit would entrain liquid out of the rotor with the gas, causing severe spraying. The liquid limit has an upper limit of 0.5 l/s which is set by the capacity of the four main pick-up tubes. Above this value, the pick-up tubes choked, and the liquid is sprayed out of the rotor.

3.3.2. Experimental Set-Up

Figure 3.8 shows the process flow diagram associated with the continuous operation of the rotor. An inventory list of the miscellaneous items can be seen found in Table 3.2. Water is pumped from the tank into the rotor, the flowrate of which is controlled by a diaphragm valve. A liquid rotameter was placed into the discharge line of the pump so that the flow of water could be measured directly. The nitrogen gas used was O.F.N., i.e. oxygen-free nitrogen. Two gas rotameters measure the gas flowrate into the rotor, and a pressure gauge records the gas pressure which varies according to the conditions inside the rotor. The gas pressure is a function of the speed of rotation and the gas flowrate entering the machine, and is important for correcting the gas flowrate, and also for measuring the work done by the rotor on compressing the gas.

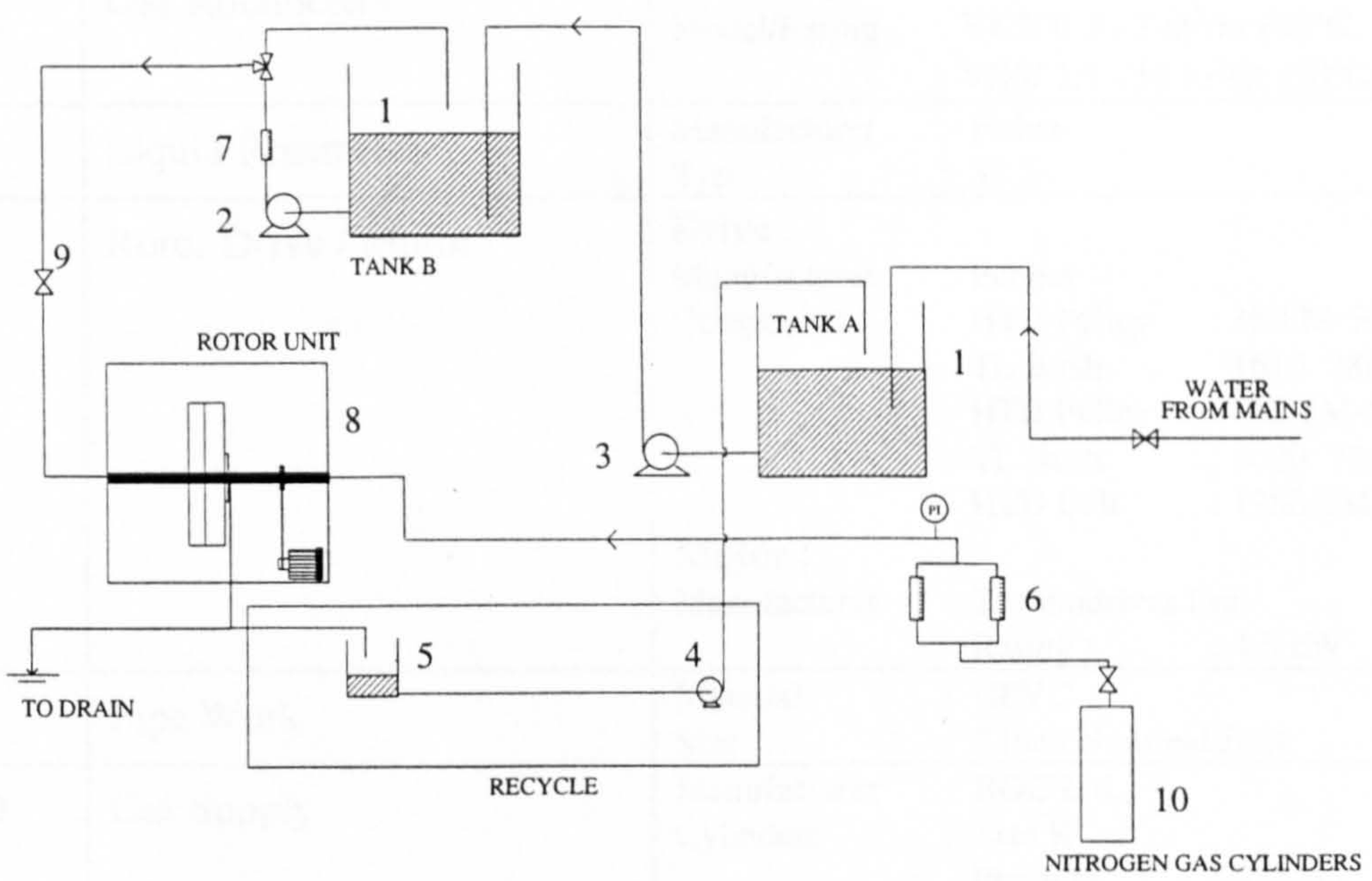

Figure 3.8 : Process Flow Diagram for Rotor

Initially the water passed through the rotor and out to drain. However as batches of salt water were required during the research programme to simulate sea water and passed through the rotor, a recycle system was introduced so that the salt water could be re-aerated and passed into Tank A before being passed back through the rotor again. The main reasons for this were the cost of the salt and the time taken to make up a batch of salt water. The recycle system consists of a stainless steel tank with three conductivity probes (upper, lower and common) mounted inside and connected to a level sensing relay. The relay activates the pump when the upper probe becomes immersed (i.e. a closed circuit exists between the upper and common probes), and cuts out the pump when the water level drops below the lower probe (i.e. an open circuit exists between the lower and common probes).

Table 3.2 : Miscellaneuos Items of Equipment associated with the Rotor

Unit No.	Description	Specifications
1	Water Tank	Material : Polyethylene Diameter : 1.33 m Capacity : 400 gallons
2 / 3	Main Water Pumps	Manufacturer : Worthington-Simpson Ltd. Model No. : 3DC25 No.A7882F / A7861F Motor : Crompton Parkinson Ltd Rating : 4 kW
4	Recycle Pump	Manufacturer : Stuart Turner Ltd Motor : Rating : 250 W
5	Recycle Tank	Material : Stainless Steel Dimensions : Height 810mm x 330mm (i.d.) Upper Probe : Height 530mm (above tank base) Lower Probe : Height 260mm (above tank base) Level Sensing Relay : RS 346-609
6	Gas Rotameters	Manufacturer : Nixon Model/Rating : VK2/ 0.3 - 3 m^3/hr (20°C, 1Bar) : VK3/ 1.8 - 18 m^3/hr (20°C, 1Bar)
7	Liquid Rotameter	Manufacturer : Fisher Type : 35 S
8	Rotor Drive / Motor	Drive : Manufacturer : Fenner Components : HTD Pulley : 36-8M-50 TL Bush : 1610 28mm HTD Pulley : 112-8M-50 TL Bush : 3020 75mm HTD Belt : 1280-8M-50 Motor : Manufacturer : Technodrives Ltd Rating : : 4.5 kW
9	Pipe Work	Material : UPVC Size : 2 inch Nominal Bore
10	Gas Supply	Manufacturer : BOC Ltd., Cylinders : Size K Pressure : 175 Bar

3.3.3 Oxygen Concentration Analysis

As the aim of this research is to investigate the level of oxygen concentration in the water as it passes through the rotor, the sampling method and analysis of the oxygen concentration is of vital importance. Section 3.3.3.1 details the oxygen probe used in measuring the oxygen concentration levels, and section 3.3.3.2 explains the original design of the sampling technique used.

3.3.3.1 Oxygen Probe

The equipment used for the oxygen analysis was the Orbisphere Model 27271 process analyser. This unit consists of a sensor (no.21152), and indicaing instrument (no.26072). Figure 3.9 shows a perspective view of the sensor.

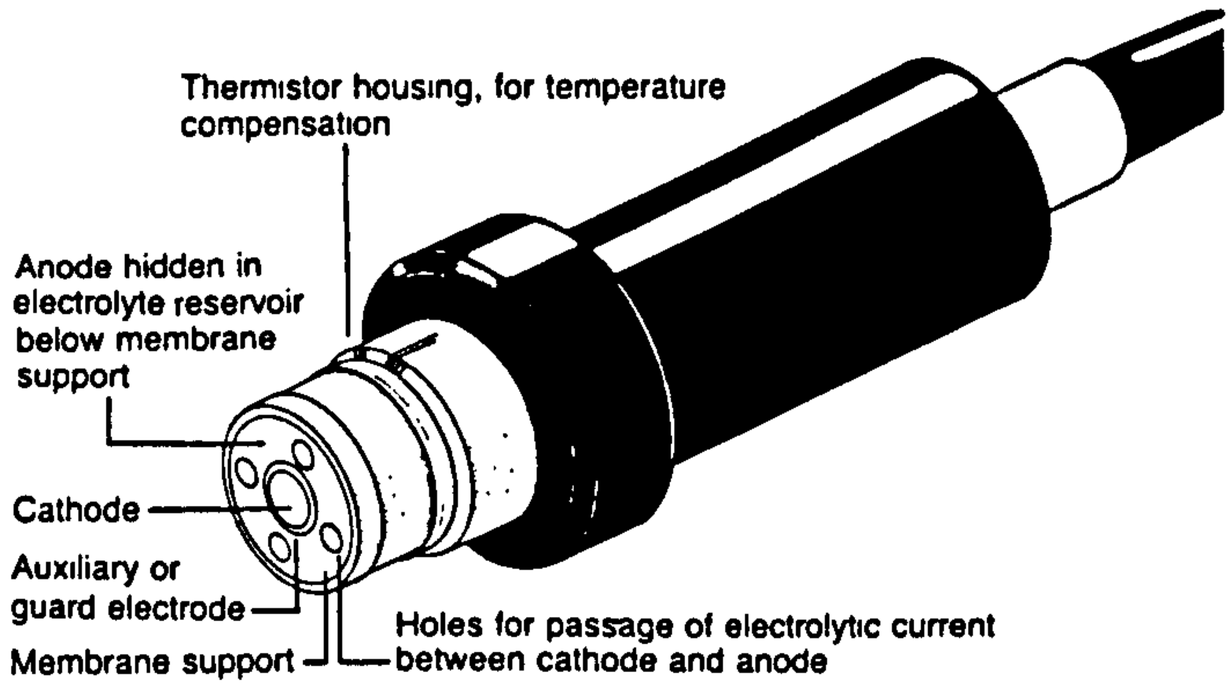

Figure 3.9 : View of Oxygen Sensor

The performance characteristics of the Orbisphere Model 27271 are shown below in Table 3.3.

Table 3.3 : Oxygen Probe Technical Data[14]

Characteristics :	In - Line
Oxygen Ranges (ppm)	0 - 1.999 0 - 19.99 0 - 199.9
Accuracy Most Sensitive Range (ppm) Drift (per month)	± 1 % 0.005 ± 0.5 %
Response Time (secs) (90% signal change at 25°C)	38
Temperature Range (°C)	0 - 100 ± 0.2
Sample Flow Range (cc/min)	50 - 250

For the sensor to function properly the flowrate of the sample water through the chamber must lie between two limits. The lower limit is set by the requirement that oxygen consumption by the sensor should be negligible compared with the flux of oxygen through the chamber, and the upper limit is the point at which the water flow becomes so turbulent that standing wave vibrations of the membrane occur with a resultant convective transport of anode products, oxygen, and impurities from within the reservoir of the sensor to the cathode region. In

practice the recommended sample flowrate of **150 cc/min** was used for all the mass transfer measurements.

3.3.3.2 Sampling Technique

The original method of sampling from the rotor took the sample liquid from both the two back chambers. One stationary sample tube, of nominal bore 3 mm, was positioned in each of the two back chambers at a depth of approximately 6 cm beneath the liquid interface, and the kinetic energy of the liquid was used to overcome the pressure drop and drive the sample through the analyser system. The nitrogen blanket which consisted of a circular metal plate of 360 mm O.D. was placed around the back of the rotor, and nitrogen gas was injected inside via two small tubes to shroud the gas-liquid interface with nitrogen gas. The purpose of this was to try and prevent any contamination of the de-oxygenated water with air which would result in false readings. A valve arrangement was used to switch between the analysis of the two back chambers. The probe was mounted into the line with a continuous flow passing across the membrane. The recommended flow of 150 cc/min was controlled using a Platon liquid rotameter graduated from 20 - 280 cc/min of water at 20°C.

3.3.4 Photograhic Equipment

A significant part of this research work has involved the use of high speed photography to examine the rotor hydrodynamics in detail. The details and layout of the photographic equipment used can be seen in Fig.3.10 :

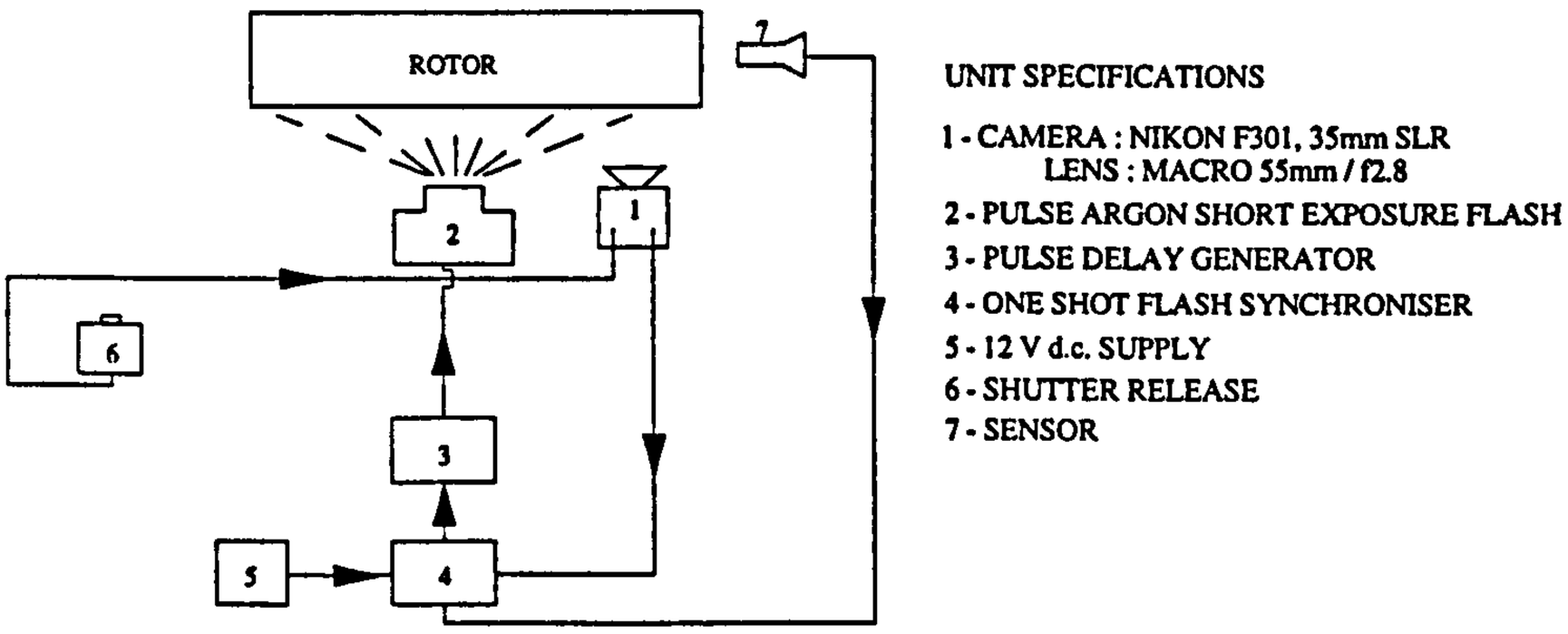

Figure 3.10 : Schematic of Rotor Photographic Assembly

The above photographic assembly was used to examine small areas of the rotor packing to determine the bubble sizes. As soon as the shutter release button is pressed, the camera shutter opens which closes the hot shoe contact and resets the one shot flash synchroniser.

The synchroniser waits until the sensor detects the white line on the rotor shaft, upon which it closes its relay thus triggering the flash delay unit. The flash delay unit then triggers the argon pulse flash unit which releases a 6 joule, 650 nanosecond spark. For the operation of the argon pulse unit a constant bleed of argon is required. Finally the camera shutter closes.

Both the argon pulse flash unit (Model No. 2-500N/2/6) and 4 channel delay generator were supplied by Pulse Photonics Ltd, and together can generate a double spark if required. For the other photographic work carried out, that being the overall rotor hydrodynamic pictures, two strobe units were used to illuminate the front of the rotor. The strobe units used were positioned above and below the rotor face, and were :

Strobosun Type 1203C, Manufacturer : Dawe Instruments Ltd

Portable Stroboscope Type 4912, Manufacturer : Bruel & Kjaer

3.3.5 Rotor Design Modifications and Extentions

As with any project in its conceptual stage, the original design is bound to have some teething problems and some of the design details need to be adjusted or removed and other items of equipment need to be added. During the course of this programme of research a number of modifications were made to the rotor, and these are outlined in this section. The main changes / additions were :

(i) Nitrogen Blanket System
(ii) Gas Injector Nozzles
(iii) Liquid Sampling System
(iv) Tracer Sensors / Equipment

3.3.5.1 Nitrogen Blanket System

The nitrogen blanketing system was the first major design problem to be encountered. As briefly mentioned earlier the purpose of the nitrogen blanketing system was to prevent recontamination of the de-oxygenated water by the air as it left the back of the rotor. At typical oxygen concentration levels in the water of 100 ppb leaving the rotor any air that could contact the water would rapidly re-dissolve into the water thereby lessening the rotor's performance. Therefore by shrouding the back of the rotor with nitrogen gas should help to prevent this.

In the original design of the blanketing system two nitrogen jets, one jet directed at each return chamber, purged the area around the pick-up tubes and liquid interface with nitrogen (see Fig. 3.6). However as the gas is blown out into the blanket in one place it is unlikely that the distribution of the gas would be even across all of the interface, and initial experimental mass transfer work showed[53] that the greater the amount of nitrogen purging the

blanket the lower the dissolved oxygen concentration in the water leaving the rotor. It was thought that this was due to the 'jetting' effect produced by the nitrogen purge jets. Calculations showed[53] that typical jet velocities ranged from 23 m/s - 50 m/s and as the jets were only centimetres from the interface in the original design, the nitrogen gas would be blowing into the interface causing increased turbulence and therefore additional mass transfer. The greater the amount of nitrogen used, the greater the jet velocity, and therefore the more turbulence and mass transfer achieved. In order to eliminate this problem the gas jets were rotated anti-clockwise from their initial position through 90° so that they were directed towards the centre of the blanket and not the interface. The ends were also plugged and 16*2 mm diameter holes were drilled in four places along the sides at 90° to each other and with a 10 mm spacing as shown by Fig. 3.11. It was hoped that this design should give a far more uniform distribution of nitrogen throughout the entire blanket, and no 'jetting' effect would occur at the interface.

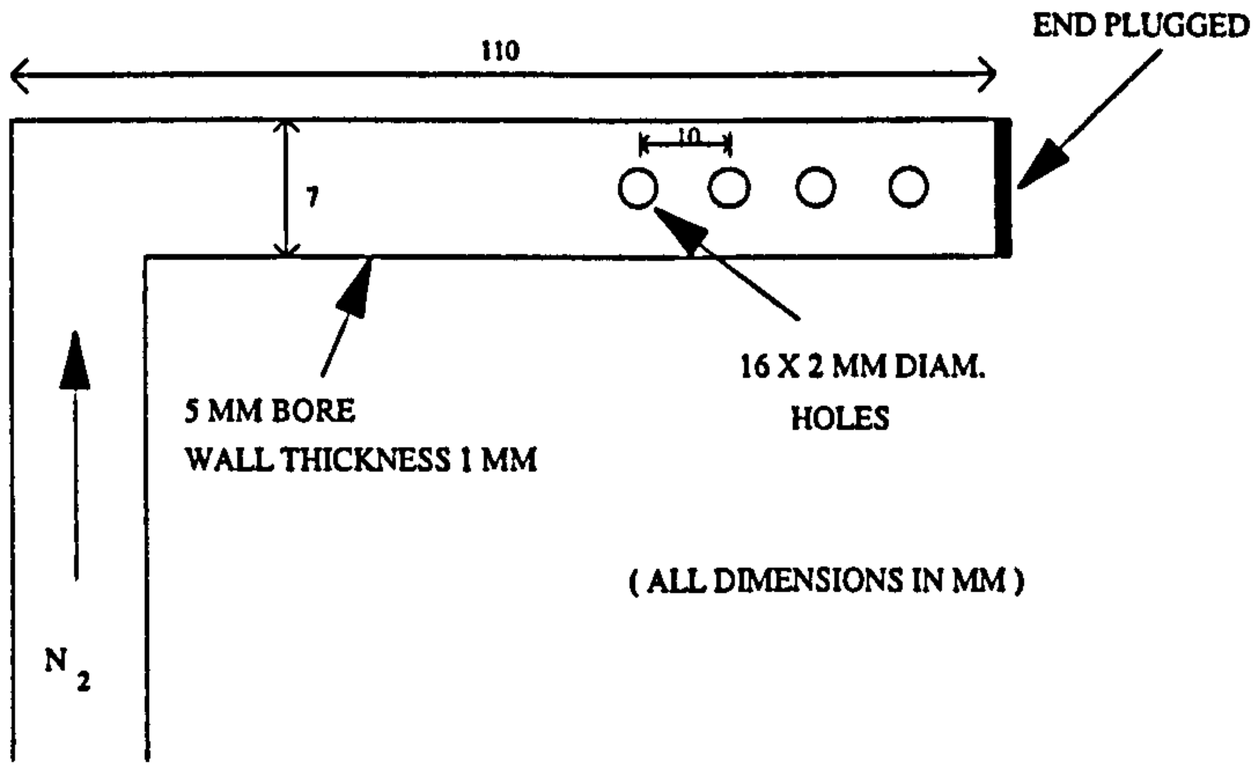

Figure 3.11 : Nitrogen Jets Design

Gas analysis of the nitrogen blanket showed the composition of the shroud to be uniform and range from 5% - 1% of oxygen by volume[53] depending on the nitrogen flowrate into the blanket. However this sampling / blanketing system was unacceptable, and therefore another gas sampling technique, as detailed in section 3.3.5.3, was later introduced.

3.3.5.2 Gas Injector Nozzles

The original design of the 120 gas injector nozzles is shown in Fig. 3.7. However when investigating the hydrodynamics of the rotor, a spiral pattern of gas and liquid was seen in the rotor (see sect. 5.2.1) which revealed a severe hydrodynamic maldistribution. The root of this problem was thought to be mainly attributed to the gas injector nozzles. As the rotor is oriented in a vertical position there will be a difference in point accelerations within the machine. While the rotor is in operation the centrifugal acceleration will be directed radially outwards whereas the earth's gravitational acceleration will always be acting in a downwards

direction. By considering one gas nozzle this means that as the nozzle passes through the bottom position of the rotor it will experience the sum of the centrifugal and gravitational accelerations, whereas as the gas nozzle moves around to the top position inside the rotor the point acceleration changes to the difference between the centrifugal and gravitational accelerations. That means that there will be an effective point acceleration difference of 2*g between the top and bottom of the rotor. As the pressure drop of the gas across the nozzles will be very small, the difference in point accelerations and therefore the pressure due to the pool of liquid is likely to cause the nozzles to fire preferentially at the top of the rotor whilst filling with liquid at the bottom of the rotor. The result of which causes a pulsing action of gas injection and therefore the observed spiral pattern.

Due to the orientation of the rotor this difference will always exist but its effect may be lessened by increasing the pressure drop across each of the individual gas nozzles. The pressure drop of the gas through the rotor is shown by equation 3.1

$$\Delta P_{GAS} = \Delta P_{NOZZLE} + \Delta P_{LIQUID} \qquad 3.1$$

With the initial design, the gas pressure drop is due to the pool of liquid as $\Delta P_{nozzle} \approx 0$. However if the pressure drop across the nozzle is increased such that $\Delta P_{gas} \approx \Delta P_{nozzle}$, then the pressure drop due to the liquid pool will become insignificant, and the point variations in the liquid pool head should become negligible. This may done by either adding a membrane across the nozzle, increasing the gas velocity through the nozzle, or by decreasing the cross sectional area of the nozzle.

The gas pressure drop due to the nozzle and liquid pool can be found from equations 3.2 and 3.3 respectively. Equation 3.2 assumes that the gas flow through nozzle is ideal, isothermal and incompressible.

$$\frac{P_2^2 - P_1^2}{2P_1 v_1} + 4\left(\frac{R}{\rho u^2}\right)\left(\frac{L}{d}\right)\left(\frac{G}{A}\right)^2 = 0 \qquad 3.2$$

$$P_{Liquid} = \rho_L \frac{\omega^2}{2}\left(r_1^2 - r_2^2\right) \qquad 3.3$$

Table 3.1 showed the range of operating conditions for the rotor. The largest ΔP_{gas} will occur at 400 rpm, 4 m^3/hr, and the smallest ΔP_{gas} will occur at 200 rpm, 0.5 m^3/hr. Substituting these values into equation 3.2 and adding on the expansion losses ($\rho u^2/2$) of the gas the theoretical pressure drop of the gas through the nozzle, ΔP_{nozzle} ranged from 21 N/m^2 - 730 N/m^2 . The pressure due to the head of the pool of liquid, ΔP_{liquid} ranged from 26 kN/m^2 - 105 kN/m^2. The actual difference in pressure due to the liquid head between the top and bottom of the rotor was 2*g, i.e. 4 kN/m^2. As mentioned earlier the above show that the pressure drop across the nozzle is insignificant to the pressure head of the pool of liquid. It would be ideal if the nozzle pressure drop could dominate and thus eliminate the variations in pressure around the rotor due to the liquid pool, but as the pressure drop through the liquid pool is approximately 1 Bar, this would mean a huge increase in the gas nozzle pressure drop

to minimise this effect which is not practical and would lead to large gas compressibility costs. However although it may not be practical to eliminate totally the pressure fluctuations, their effect may be lessened by increasing the nozzle pressure drop.

The first method tried out to increase the nozzle pressure drop was to add a membrane sleeve across each nozzle. Various materials were tried which included Polyethylene, Porvair C, Permair F and sintered bronze, these materials having a typical pore size of 15 microns. Experimentally it was found that the gas nozzle pressure drop increased to the range of 5 kN/m^2 - 35 kN/m^2 depending on the flowrate and membrane material used. This is a marked improvement although the pressure drop due to the liquid pool still dominates. The major problem with this approach is that it is impossible to ensure that all the gas travels through the membrane material and not along a path between the nozzle and membrane sleeve, and therefore that all the nozzles will have an identical pressure drop and hence gas flow.

The second and third methods tried, i.e. increasing the gas velocity and decreasing the cross sectional area, are essentially the same. The gas velocity was increased by blocking off some of the nozzles. It was decided to plug completely every other nozzle, and for the remaining nozzles plug one of the two 0.5 mm diameter holes, i.e. 3 in every 4 holes would be sealed and so increase the gas velocity by a factor of 4. As the pressure drop is proportional to the square of the velocity, a 4-fold increase should yield a 16-fold increase in pressure drop. However, the disadvantage with this approach is that large plumes of gas are produced (see sect. 5.2.2) which suggests that there is a significant volume of the packing in which the contact between the two phases is poor. This revealed itself by the fact that little improvement in the overall mass transfer performance was achieved.

The third method tried was to decrease the cross sectional area of the 0.5 mm diameter holes of the gas nozzles. Due to the way the nozzles were sealed into the machine it was not possible to remove them and make new nozzles with smaller holes. Therefore 0.4 mm diameter copper wire was threaded into the nozzles to decrease the area as shown in Appendix IX (a). By placing the wire into the holes the equivalent diameter of the holes becomes 0.3 mm, and the pressure drop range has been increased to 550 N/m^2 - 5 kN/m^2. Although the increase across the nozzles may not be as high as that generated by the other methods, the design is simple, giving a better visual distribution of gas (see sect. 5.2.3) and leading to an improvement in mass transfer performance (see ch.6). Therefore it is this design that was thought to be the most satisfactory.

3.3.5.3 Liquid Sampling System

Section 3.3.3 described the method in which the mass transfer analysis took place from the rotor. However, due to the break down in the mathematical method and reliability of the mass transfer results taken, it was decided to design a new sampling system to take the sample directly out of the packing of the machine, as shown in Figs. 3.12 - 3.14 and Appendix IX (b).

The new method takes the liquid sample from the rotor without any contact with the air to avoid any possibility of re-contamination. As shown in Fig. 3.12, there are 4 sampling tubes that run inside the packing and are fixed to the inner aluminium plate of the rotor. These tubes take a liquid sample from 4 different positions and radial depths (1/4, 1/2, 3/4, and full radial packed length). Each tube has a clamp valve so that only one sample can be taken at any one time, and the sample flows down the hypodermic tube into a boss mounted on the centre axis of the rotor and then through a tube that runs inside the rotor shaft (Fig. 3.13). A collection chamber (Fig. 3.14) mounted onto the liquid rotary union collects the sample, which then proceeds through the oxygen analyser and out to the drain. As the sampling tubes are rotating with the machine, there is no kinetic energy of the liquid to drive the sample through. Therefore a vacuum pump (Charles Austen Pumps Ltd., Model : Capex L2) was fitted into the line to provide the driving force required, capable of pulling a vacuum of upto 0.5 Bar(a). However it was found that as the 3/4, 1/2, and 1/4 sample tubes were immersed in the gas-liquid contact area of packing, then when sampling at these positions gas entrainment with the sample occurred which caused fluctuations in the readings from the analyser, and no steady state result could be attained. It was thought that if the liquid velocity into the sample tubes was decreased thereby causing less drag on the bubbles in the immediate vicinity, the problem could be solved. This was done by placing diffusers on the ends of the sample tubes.(Fig.3.15)

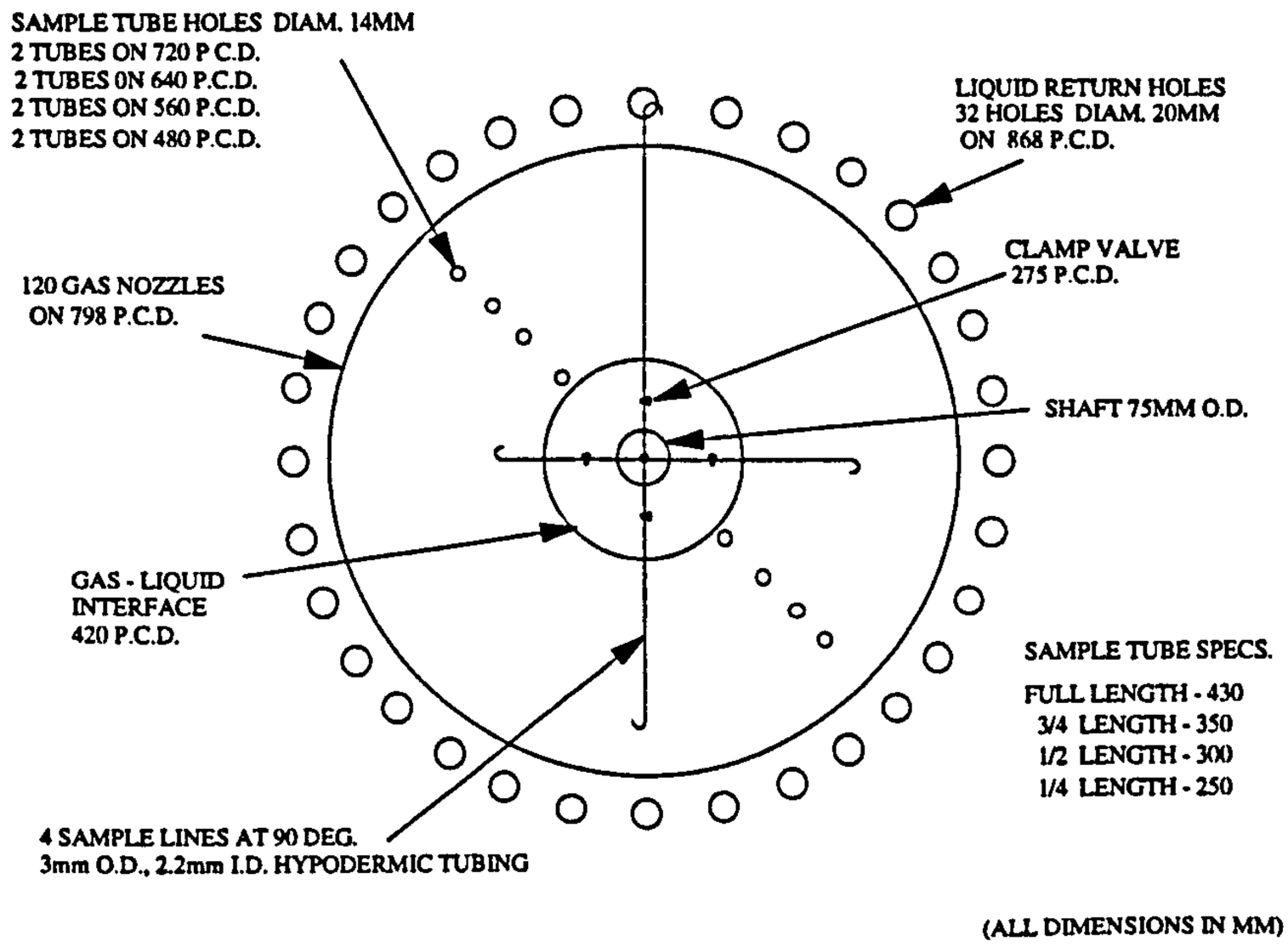

Figure 3.12 : New Sample Tube Arrangement (Front View)

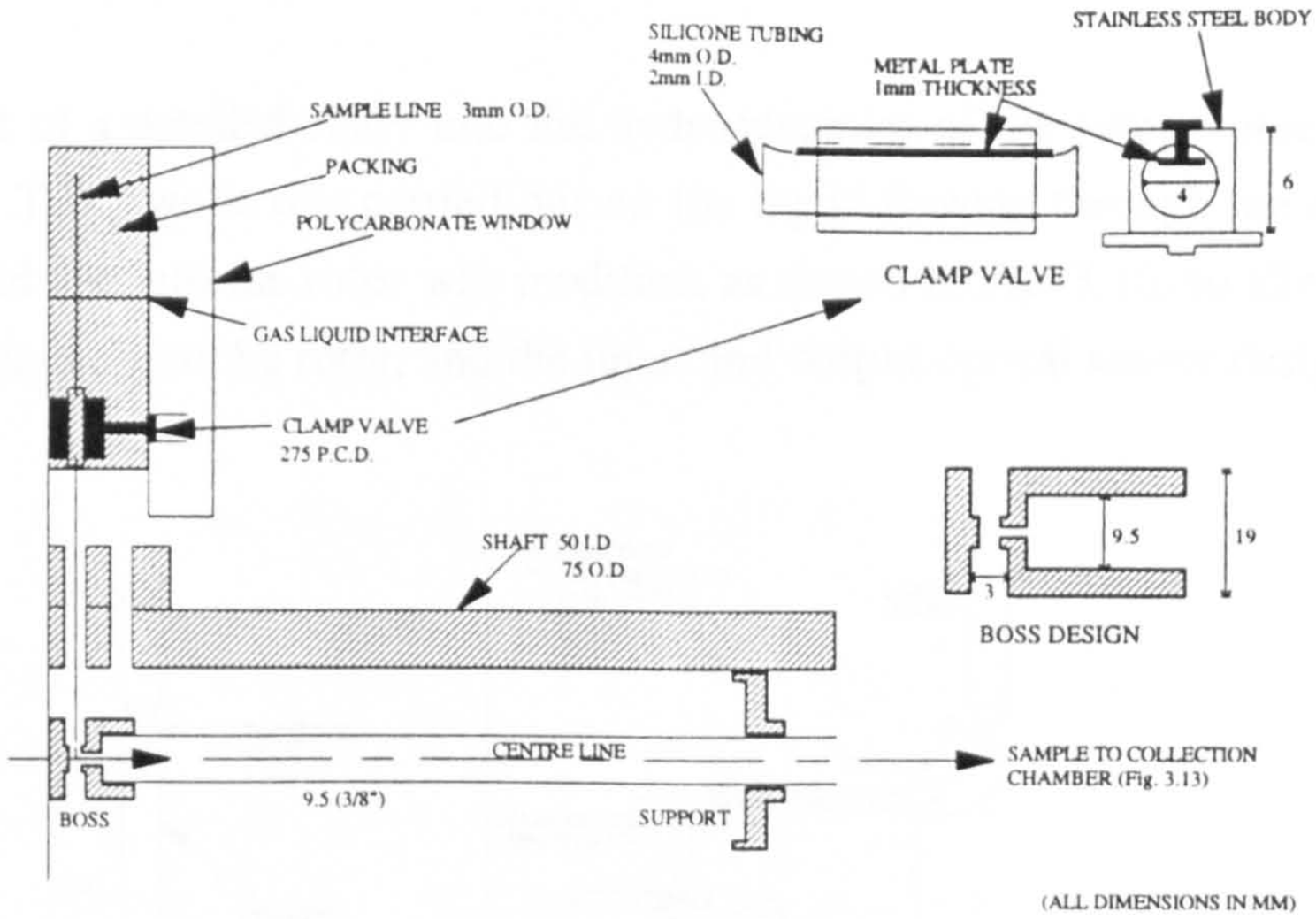

Figure 3.13 : Sample Line out of Rotor (Side View)

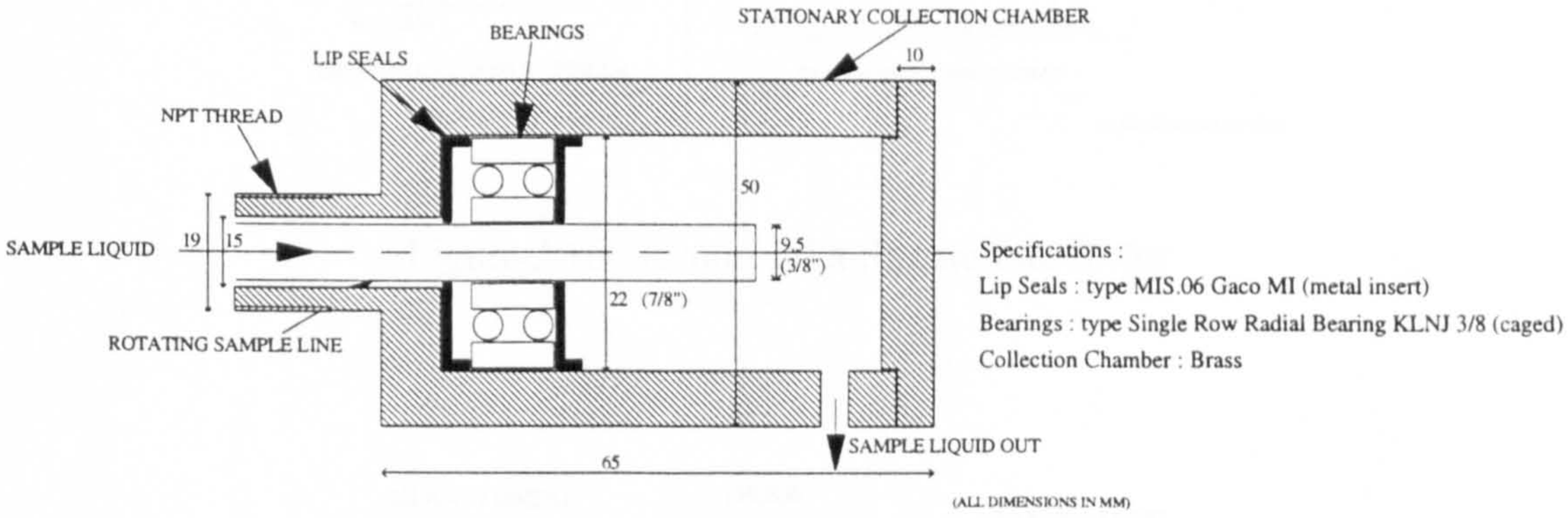

Figure 3.14 : Sample Liquid Collection Chamber

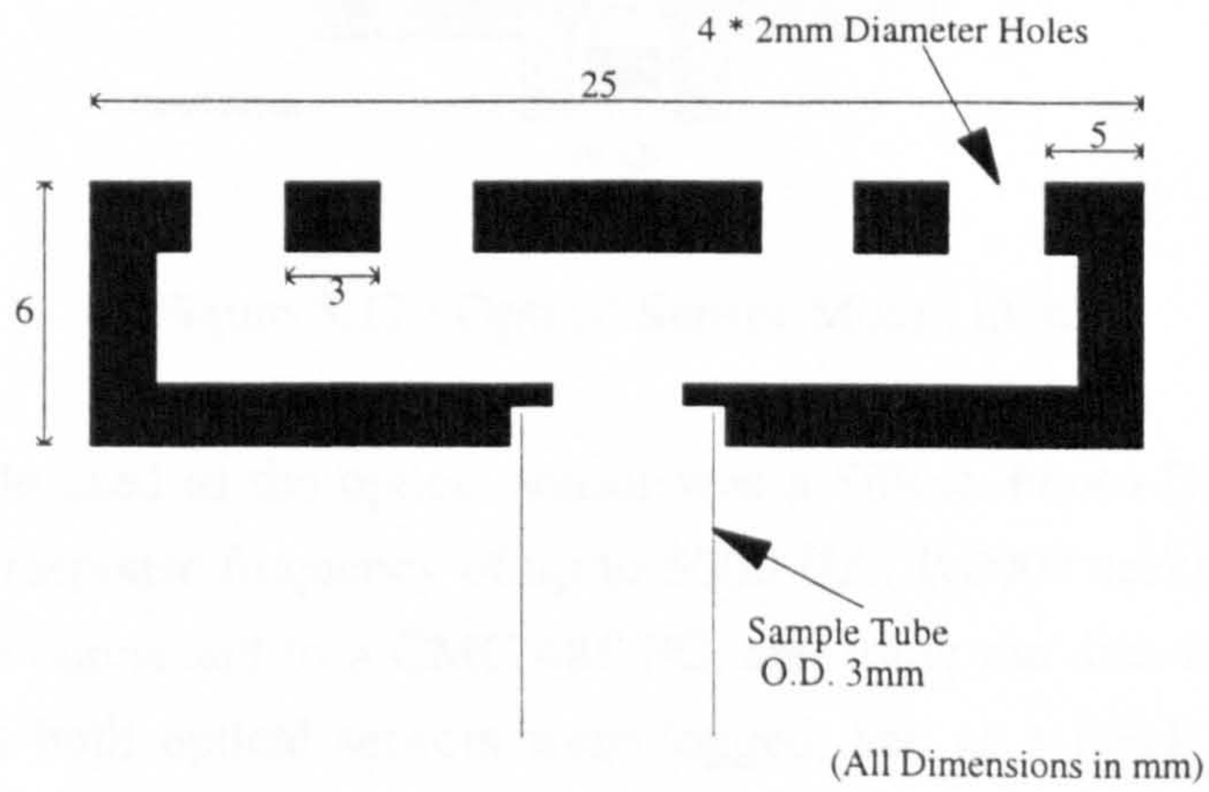

Figure 3.15 : Sample Tube Diffusers

3.3.5.4 Tracer Sensors/Equipment

As part of a detailed study into the hydrodynamics of the rotor, some residence time distribution (R.T.D.) work was carried out on the liquid flowing through the rotor (see Sect. 5.3). The liquid line into the rotor was modified, as shown in Fig. 3.16, to allow for a plug of tracer to be inputted into the rotor, and the input and output optical sensor design is detailed in Fig. 3.17.

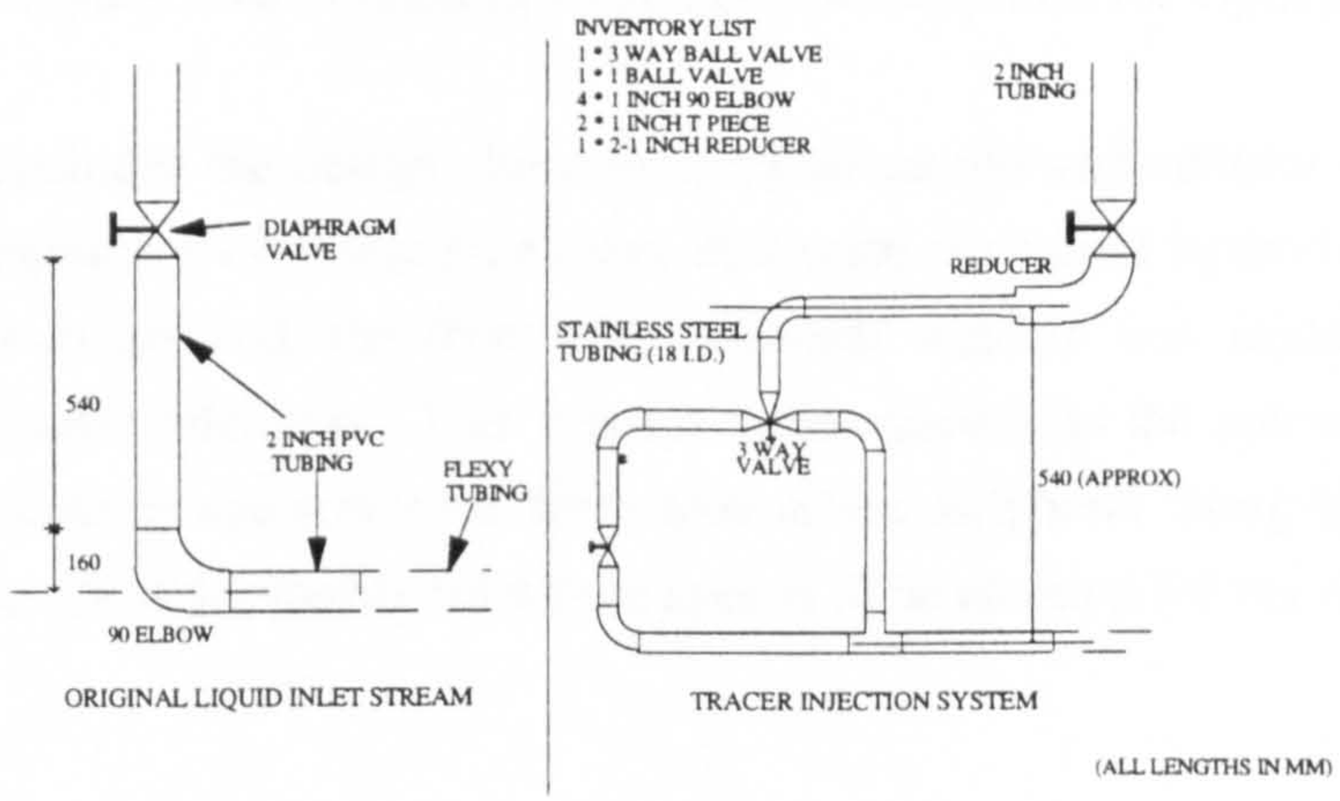

Figure 3.16 : Liquid Inlet Stream into Rotor

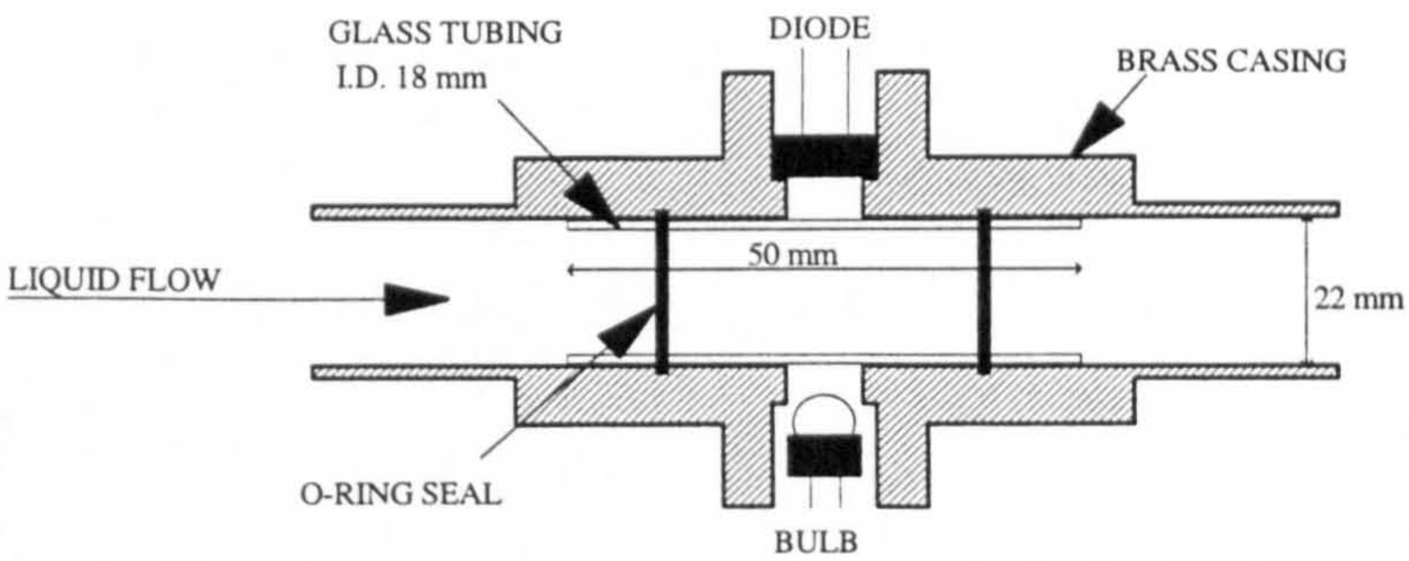

Figure 3.17 : Optical Sensor Mount Design

The diode used as the optical sensor was a Silicon Photo-Diode (RS 308-067) which has an accurate response frequency of up to 5000 Hz (0.0002 secs) as shown in Figure 3.18. The diodes were connected to a CMC 486 PC, and using the data-logger software Dash 300, the ouputs from both optical sensors were logged, and as a result the liquid residence time distributions characterised.

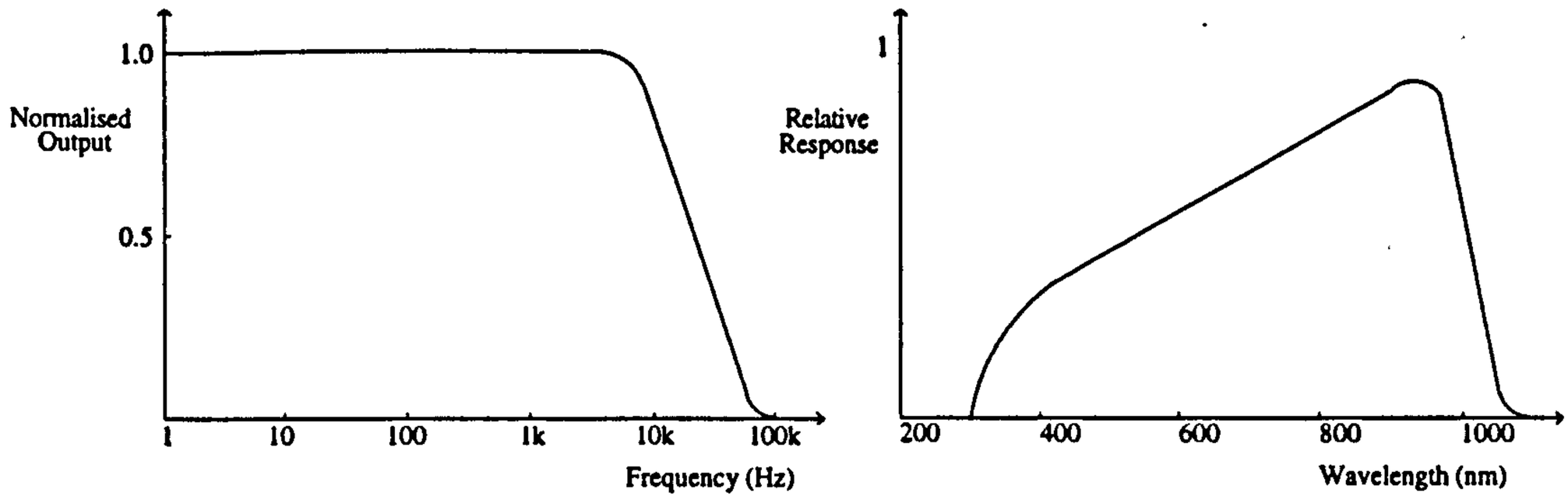

Figure 3.18 : Frequency and Spectral Response for Optical Diode

This concludes the design alterations, modifications and additions to the Mark II rotor during this programme of research, except that once the visual hydrodynamic studies on the rotor had been completed, the front polycarbonate window was replaced by an aluminium window of the same thickness. This was for safety reasons as the polycarbonate window was showing some crazing and stress fractures around the peripheral fixing bolts (see Appendix IX (c)), and to also allow for higher rotational speeds to be attained for the mass transfer studies.

CHAPTER 4 : MODELLING a PACKED ROTATING GAS - LIQUID CONTACTOR

The following chapter investigates the possibilities of accurately modelling the mass transfer and hydrodynamic performance of the 1m diameter rotor. In order to model the rotor, the best line of approach would seem to be to use existing equations for gas-liquid behaviour under normal gravitational acceleration and replace 'g' with the centrifugal acceleration, $\omega^2 r$, where applicable. Therefore a detailed current knowledge on gas-liquid stripping systems (described in chapter 2), together with the mechanical design of the rotor (detailed in chapter 3) needs to be combined in order to predict the overall hydrodynamic and mass transfer performance between gas and liquid in this Higee environment. The purpose of the model is to see the effect of various parameters such as gas and liquid flowrate, rotational speed, packing depth, and packing size on the overall performance of the machine, and to be able to predict the rotor performance under conditions that are not possible to attain experimentally.

The first section looks at the modelling of the hydrodynamics of the system, i.e. the gas bubble size, hold-up and gas and liquid velocity, in 'high g' environments. The subsequent sections explore the applicability of various mass transfer coefficient correlations to the stripping of oxygen from water in a 'high g' system, and finally the actual computer model of the 1 m diameter rotor is detailed.

4.1 Rotor Hydrodynamics

4.1.1 Gas Hold-up

Section 2.6.4. detailed various methods and correlations to find the gas hold-up in gas-liquid systems, which is strongly dependant on the superficial gas velocity. In conventional systems the gas and liquid superficial velocities will remain fairly constant throughout the column, whereas for the rotor this will not be the case as the cross sectional area through the packing in the rotor varies with the radial depth (see Fig 4.1), and therefore the gas and liquid superficial velocities will constantly change.

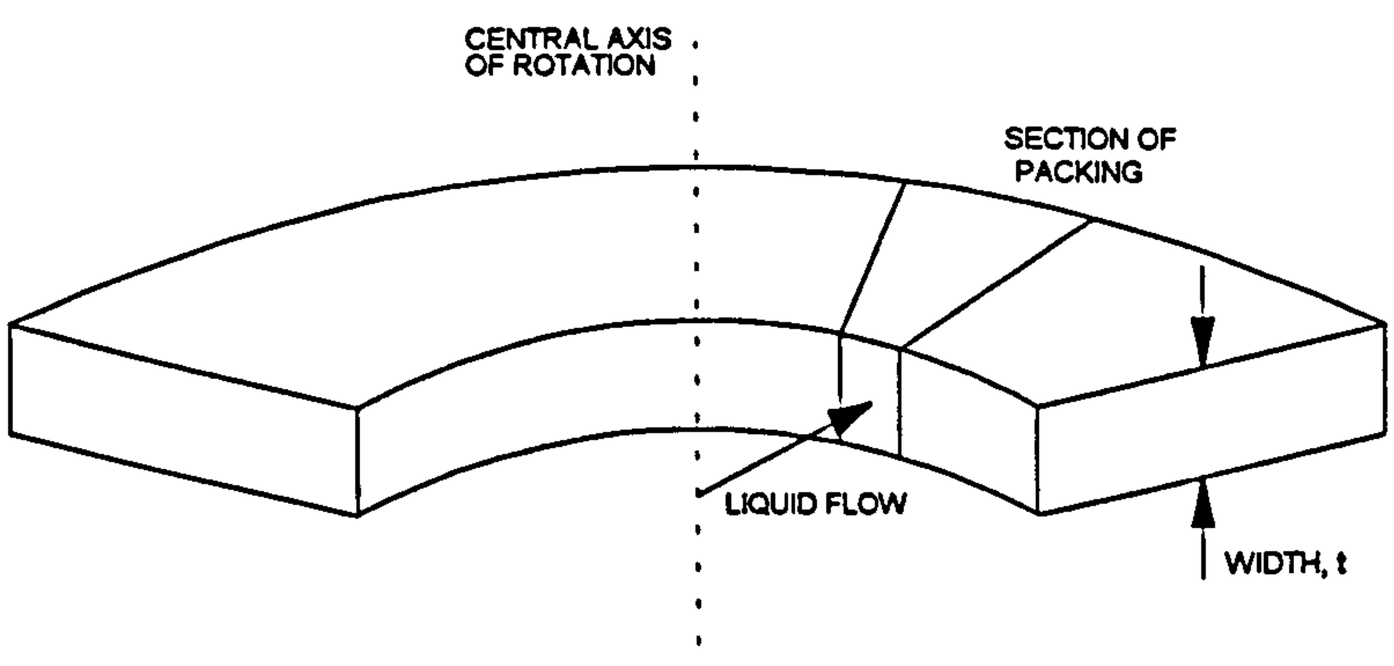

Figure 4.1 : Cross Section through Section of Packing

One approach for determining the gas hold-up is to compare the position of the gas-liquid interface in the rotor during operation, and by carrying out an overall pressure balance between the liquid pool in the packed section and the liquid pool in the return chamber (see Fig. 4.2) the gas hold-up may be calculated.

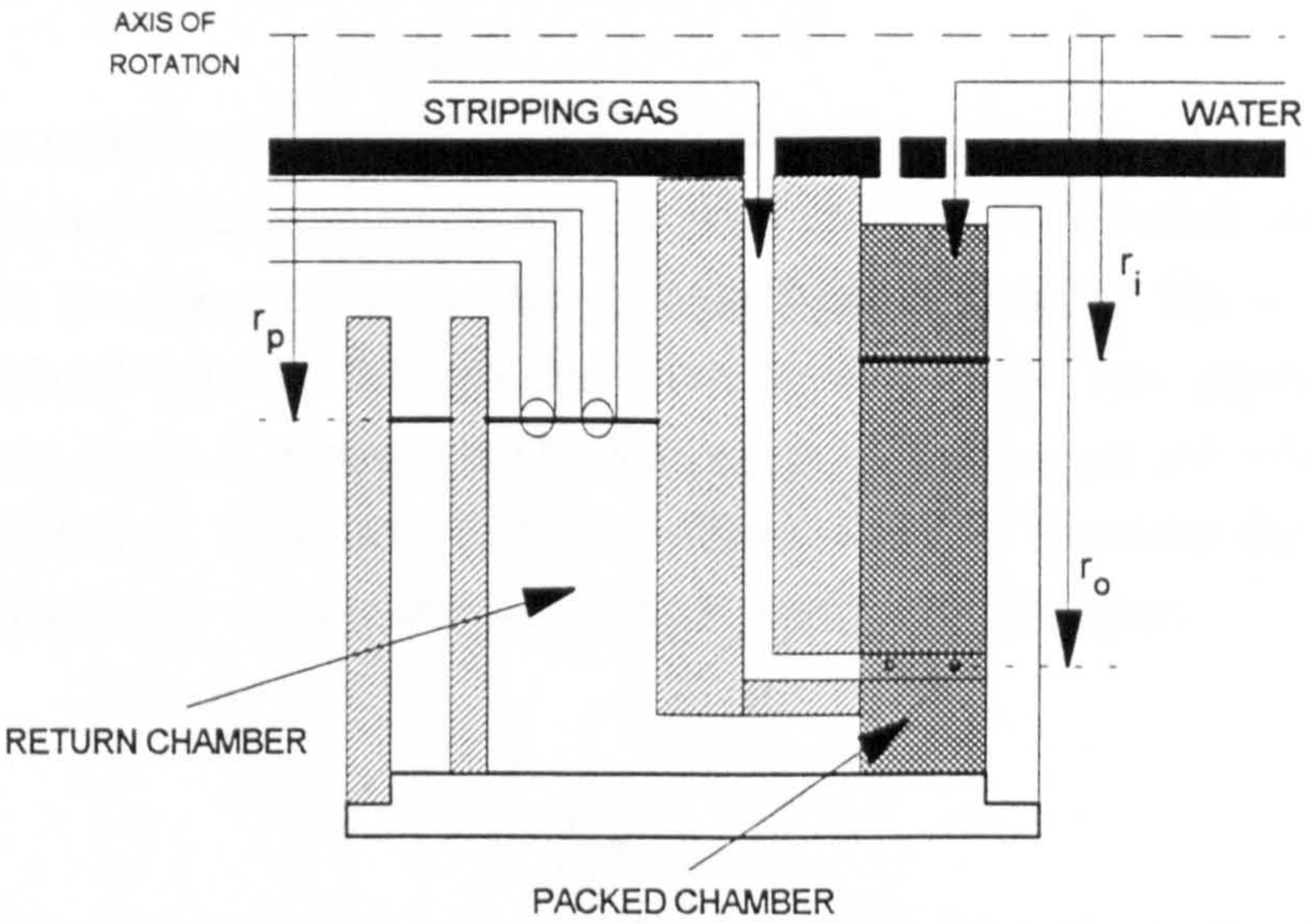

Figure 4.2 : Half Section of Rotor

Carrying out a pressure balance on the rotor, and assuming no frictional losses encountered by the liquid :

Liquid Pressure Head in Return Chamber = Liquid Pressure Head in Packed Section

Pressure, dP, due to a head of liquid, dr, is given by :

$$dP = \rho g h = \rho \omega^2 r dr \qquad 4.1$$

To find the pressure in the rotor due to the rotating liquid pool at any radial depth, r, equation 4.1 must be integrated between the interface and r to give :

$$\int_0^P dP = \rho\omega^2 \int_{r_i}^{r} r dr = \frac{\rho\omega^2}{2}\left(r^2 - r_i^2\right) \qquad 4.2$$

Applying equation 4.2 to both the Packed chamber and Return chamber (see Fig.4.2) :

$$\left(\rho_l(1-\phi)\frac{\omega^2}{2} + \rho_g\phi\frac{\omega^2}{2}\right)\left(r_0^2 - r_i^2\right) = \rho_l\frac{\omega^2}{2}\left(r_0^2 - r_p^2\right)$$

which when rearranged can be used to solve for ϕ, the average gas hold-up.

$$\phi = \frac{\rho_l}{\rho_l - \rho_g}\left(\frac{r_p^2 - r_i^2}{r_0^2 - r_i^2}\right)$$

As $\rho_l >> \rho_g$ then $\rho_l/(\rho_l-\rho_g) \approx 1$ and the overall gas hold-up may be approximated to :

$$\phi \approx \left(\frac{r_p^2 - r_i^2}{r_0^2 - r_i^2}\right) \qquad 4.3.$$

However, the hold-up will vary along the radial depth decreasing as the radial depth increases. For predicting the mass transfer performance of the rotor along the radial axis, it is therefore important to be able to predict how the gas hold-up varies. The correlation chosen to predict the gas hold-up depends on the value of the liquid superficial velocity. The cross sectional area through the packing at a radial depth r is :

$$A = 2\pi rt$$

and therefore the superficial liquid velocity at this point is $u_l = V_l/2\pi rt$. The liquid velocity will be at a maximum at the gas-liquid interface and when the liquid volumetric flow is high, and at a minimum at the gas injector nozzles and when the liquid volumetric flow is low. Calculating the liquid superficial velocity through the rotor between these two points gives a liquid superficial velocity range of between **0.33 - 3.2 cm/sec.** *Therefore as the velocity is relatively low and as the Schugerl, Lucke and Oels correlation (eqn.2.37) contains the parameter 'g', it is the most applicable for calculating the hold-up variation in the rotor.*

$$\phi_g = 0.91\left(\frac{u_g}{\sqrt{gd_s}}\right)^{1.19} \qquad 4.4$$

The gas velocity in equation 4.4 will vary with the gravitational acceleration, and for the purpose of the model is taken to be equivalent to the bubble terminal velocity as calculated in section 4.1.4.

4.1.2. Gas Bubble Formation

Gas bubbles are produced in the rotor through 120 gas injector nozzles (Fig. 3.7), the theoretical formation of which are detailed in Section 2.6.2.1. In order to best describe the bubble formation at the nozzles in the rotor, the Reynolds Number, based on the flow through the orifice, needs to be determined.

$$\mathrm{Re}_{or} = \frac{\rho_l u_{or} D_{or}}{\mu_l} \qquad 4.5$$

The nominal gas flow varies in the rotor from 0.5 - 4 m^3/hr which, when divided by the 120 gas nozzles each containing 2*0.5 mm diameter orifices, gives an orifice velocity range of 3 - 24 m/sec and Reynolds number between 1200 - 9800. This shows that the bubble formation will occur mainly in the *jet regime,* although at the low gas flowrates (0.5 m^3/hr) formation will occur in the *intermediate regime*. As described earlier in section 2.6.2.1. much discrepancy in the findings occurred in the jet regime, and all the qualitative analysis was made for systems operating under a 1-g environment. Therefore it seems at present that it is not possible to accurately predict the sizes of the gas bubbles as they are formed at the orifices of the nozzles. Equation 2.26 may be applicable for estimating the bubble size of formation at a low gas flowrate and the predicted results can be seen below in Table 4.1. However the disadvantage

with this equation is that it does not take into account the diameter of the orifice at which the bubble forms.

Table 4.1 : Predicted Bubble Size of Formation using Equation 2.26

Total Gas Flow (m^3/hr)	Re_{or}	Rotational Speed (rpm)	Predicted Bubble Size of Formation (mm)
0.5	1228	200	1.57
0.5	1228	300	1.34
0.5	1228	400	1.19

However, as the nozzles are immersed in the packed section of the rotor, the need to accurately predict the bubble size of formation may not be significant in the determination of the overall mass transfer as the bubbles will immediately collide with the packing filaments. The bubble size through the gas-liquid contact region is therefore only likely to be determined by the packing pore size and gravitational acceleration.

4.1.3. Gas Bubble Size

The packing size, rotational speed, gas and liquid flowrates and properties may all play their part in determining the size of the gas bubbles through a packing material in a Higee environment. Section 2.6.2.2. examined the work done on bubble collisions and introduced the concept of the critical bubble size, the size below which a bubble will not split on colliding with a stationary baffle. For gas-liquid systems the critical bubble diameter can be found by re-arranging eqn. 2.29.

$$d_c = \frac{-u_t^2(\rho_g + \rho_l/2) \pm \sqrt{\left(u_t^2(\rho_g + \rho_l/2)\right)^2 + 4*1.8\Delta\rho g*3.12\sigma}}{2*1.8\Delta\rho g} \qquad 4.6$$

As can be seen from equation 4.6, the critical bubble size is dependant upon the bubble terminal velocity, and can not be determined until the terminal velocity of the gas bubbles is found. However the above equation does not account for how a particular packing material will effect the bubble size, and in order to predict the packing's effect, the number of bubble collisions and the probability of the bubble splitting need to be determined.

Alshaban[7] proposed a model based on probability for determining whether a bubble would break up or not. The model considers bubble splitting to occur as a result of the product of the probability of a bubble hitting the packing and the probability of the bubble actually splitting. The model assumes that there is no relative tangential velocity between the bubble and the packing, and therefore the model equations are based on geometric factors

alone. The probability of a bubble hitting an obstacle is taken as the ratio of the cross sectional areas of the bubble to the pore and gives :

$$\Pr(hit) = \left(\frac{d_b}{d_p}\right)^2 \qquad d_b \leq d_p$$

$$\Pr(\text{hit}) = 1 \qquad d_b > d_p$$

The probability of the bubble splitting on impact is dependant on two terms, the filament thickness and the critical droplet size. Considering the filament thickness, t_f, then as t_f must be less than $d_p/2$ and the closer t_f gets to zero the greater the probability of the bubble splitting :

$$\Pr(Split) = \left(1 - \frac{2t_f}{d_p}\right) \qquad 0 < t_f < \frac{d_p}{2}$$

Since the bubble will not break-up when it reaches the critical diameter the second term was shown to be :

$$\Pr(Split) = \left(\frac{d_b - d_c}{d_p}\right) \qquad d_b > d_c$$

However, Lee[44] extended this idea for droplets and said that if a bubble was above the critical size it will split if it hits an obstacle and if it is below its critical size it will not split, and so simplified the second term :

$$\Pr(Split) = \psi(d_b - d_c)$$

where $\psi(\ )$ is the unit step function. Combining all these ideas for bubbles, the overall probability of a bubble hitting the packing and splitting is given by :

$$\Pr(Hit\&Split) = \left(\frac{d_b}{d_p}\right)^2 \left(1 - \frac{2t_f}{d_p}\right)\psi(d_b - d_c) \qquad d_b \leq d_p \qquad 4.7$$

$$\Pr(Hit\&Split) = 1 \qquad d_b > d_p$$

Equation 4.7 will vary with the rotational speed and radial position since the critical bubble diameter is dependant on these parameters. It's value is zero until the critical bubble diameter is reached, and continues to rise with the bubble diameter until it becomes one, at which point the bubble diameter has reached the packing pore size. The Declon 312 HC20 packing used in the rotor has a nominal specification of 20 pores per inch or average pore size 1.3 mm. As seen in Table 4.1 the predicted bubble formation size is greater at 200 and 300 rpm than the packing pore size, and therefore these bubbles will be immediately broken up by the packing. The limitations with the above model are that it relies on geometric factors alone, makes no account for any possible bubble coalescence within the packing, assumes no relative tangential velocity between the bubble and the packing, and the probability of a bubble splitting is independent of the bubble velocity.

4.1.4 Gas Velocity

The terminal 'free' rise velocity of a bubble is dependant upon the drag coefficient (see eqn. 2.32) which in turn is dependant on the bubble Reynolds number ($\rho_l u_r d_b/\mu_l$), and as can be seen this is dependant upon the bubble size and relative velocity. Therefore, as the bubble relative velocity, Reynolds number, and diameter are all intrinsically linked to one another, an iterative procedure has to be followed, as shown in Figure 4.3, based initially on the bubble size as predicted in Table 4.1, and a drag coefficient of 0.44.

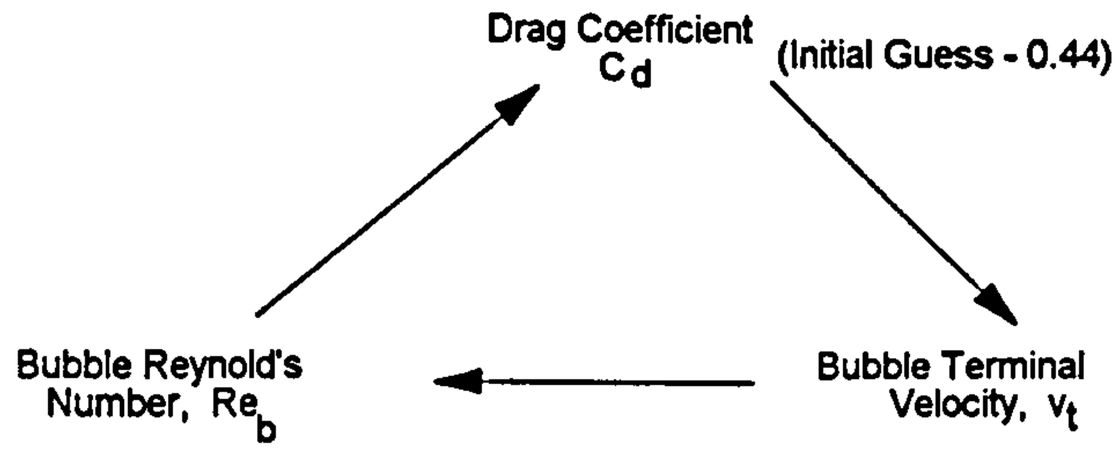

Figure 4.3 : Iterative Procedure for Calculating the Bubble Terminal Velocity

Table 4.2 shows some typical values predicted for the bubble terminal velocity in the rotor at the gas injector nozzles.

Table 4.2 : Bubble Terminal Velocity Prediction

Rotational Speed (rpm)	Total Gas Flow (m^3/hr)	Drag Coeff. Cd	Bubble Size (mm)	Terminal Velocity (m/s)	Bubble Reynolds No.
200	0.5	0.44	1.57	0.91	1195
300	0.5	0.44	1.34	1.27	1420
400	0.5	0.44	1.19	1.59	1580

The major observation that can be seen from Table 4.2, is that the bubble Reynolds number is much greater than 500 in all cases (see section 2.6.3), which means the drag coefficient guess of 0.44 seems reasonable. Although the effect of liquid flow through the rotor has not been taken into account, the only part this would play is in the calculation of the relative gas velocity to find the bubble Reynolds number. As the liquid velocity is negligible compared with the bubble velocity at the gas injector nozzles it has been ignored, but if included, would only result in increasing the Reynolds number which is already well in excess of 500 and therefore confirming the value of 0.44 for the drag coefficient.

4.2 Rotor Liquid Mass Transfer Coefficients

Section 2.5 detailed the various theories and correlations for trying to predict the overall mass transfer in gas-liquid systems in which the gas is sparingly soluble in the liquid. This whole area has been extensively investigated, and equations 2.8 - 2.18 have been used to predict the liquid side mass transfer coefficient in various systems. The choice of correlation used will depend on whether the gas or the liquid is the continuous phase, and as shown in section 3, the rotor has been designed with the liquid as the continuous phase with the gas phase dispersed throughout. Some work has been done on the effect of gravity on the mass transfer coefficients for systems in which the liquid behaves as the dispersed phase. Tung and Mah[54] used the Penetration theory to model the effect of gravity on the mass transfer coefficient, where $k_l \propto g^{1/6}$, and using data obtained by Ramshaw & Mallinson for air and de-oxygenated water, found that the penetration theory was still capable of describing the liquid mass transfer behaviour in Higee processes fairly well. Vivian, Brian & Krukonis[48] examined the process of desorption of carbon dioxide from water and found that $k_l a \propto g^b$ where the exponent b varied from 0.41 - 0.48. Penetration theory predicted k_l to vary with gravity to the power 1/6, and they suggested that this discrepancy may be accounted for by the probable rise in interfacial area with gravity.

However, little work has been done on predicting the effect of increasing the gravitational environment on the liquid film coefficient for systems in which the liquid becomes the continuous phase. Therefore the equations that are applicable for cases where the liquid is the continuous phase, and include the gravitational acceleration term will be used to try and predict the coefficient, and hence overall mass transfer performance. Theoretically derived equations 2.9, 2.10, 2.13, and empirical equations 2.16 - 2.18 will be used to model the liquid side coefficient for the stripping of oxygen from water in the rotor. Figure 4.4 shows how the liquid side mass transfer coefficient, as predicted by the various equations for the rotor, varies as a function of the radial packed length. Typical values for the liquid film coefficient under normal gravity can be seen in Fig. 2.9 which shows the value of k_l to vary for air and water between 0.01 - 0.05 cm/s. The overall mass transfer results based on the differing liquid film coefficient predictions are compared with the experimental results (see Figs. 4.12, 13) to try and determine which equation is the best at modelling the liquid film coefficient for nitrogen and water in high gravitational systems.

As can be seen from Figure 4.4 the general trend with all predictions is that the liquid mass transfer coefficient will increase as the radial depth, and therefore gravitational acceleration, increases. The increase in the mass transfer coefficient, and therefore decrease in the liquid film resistance, is what is expected under Higee conditions. Under the operating conditions of Figure 4.4, the acceleration experienced by the gas and liquid ranges from 20 - 40 times normal gravity which is a fairly narrow range, and the resulting increase in the predicted mass transfer coefficient is also small.

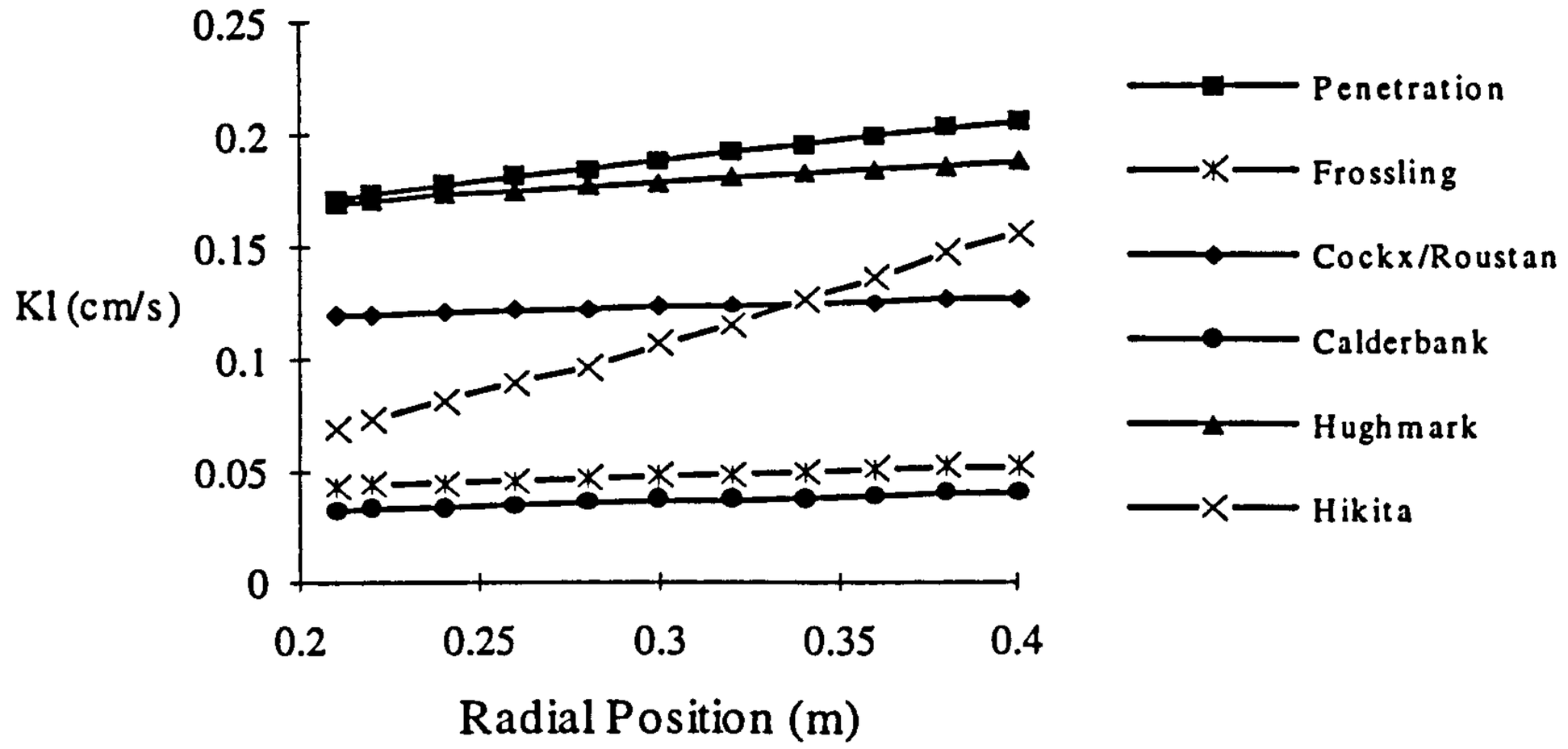

Figure 4.4 : Theoretical Liquid Film Coefficients at 300 rpm,
Gas and Liquid Flow 0.5 l/sec

Hikita's correlation shows the most significant increase over this range which may be explained by the fact that it is the only correlation to predict the volumetric mass transfer coefficient, and therefore to find the liquid film coefficient the prediction must be divided by the estimated interfacial area. There is also a large discrepancy between some of the predictions, the Penetration model predicting the coefficient around 0.18 cm/s compared with the Calderbank model that predicts the coefficient to be around 0.04 cm/s. There is a factor of 4 -5 times difference between the highest and lowest predictions which will therefore lead to a large difference in the overall predicted mass transfer performance of the rotor.

4.3 Computer Model of Rotor

This section combines the above sections 4.1 and 4.2 and details the actual computer program used to model the 1 m diameter rotor. A previous attempt at modelling a small rotor[55] has been proposed but on detailed examination it was found that this model was basic, inaccurate, and also in some places in error. In modelling the rotor a number of assumptions have to be made :

(1) The volume of the packing inside the rotor is negligible (porosity = 0.95)

(2) The gas bubbles are spherical and at their critical bubble diameter in the rotor

(3) The gas bubbles move through the packing at their terminal 'free' rise velocity

(4) There is no relative tangential velocity between the bubbles and the packing

(5) There is no bubble-bubble interaction, i.e. coalescence

(6) Liquid Pressure Drop through the Rotor is negligible

The above assumptions are made in order to calculate the bubble size, velocity, and hold-up in rotating packed beds. Assumption (1) seems reasonable, assumption (2) and, therefore (4) and (5), have been shown by Alshaban[7] and confirmed experimentally (Section 5.4) to best describe bubble sizes in centrifugal fields, and assumption (6) is valid especially at the lower liquid flowrates. Assumption (3) is made, as at present there is no other way of estimating the bubble velocity, but its validity is not known.

Figure 4.5 shows the model flowsheet used in determining the theoretical predictions of the hydrodynamic and mass transfer performance of the 1m diameter rotor. The program was written in Fortran and compiled using a Fortran77 compiler, and the full program code listing can be found in Appendix 1. The rectangles in the above figure thus represent the subroutines used in the fortran listing, and the diamonds represent the tolerances that need to be met before the program may proceed further.

The main program, **Model,** starts by calling the introductory subroutines **Intro**, **Specs** and **Operate,** which introduces the program, lists the design specifications of the rotor and the physical property data of the gas and liquid, and allows the user to input the operating conditions, i.e. range of rotational speed, gas and liquid flowrates and initial oxygen concentration in the water. Once the inputs have been read in, an output file, 'rotor.dat', is set up before the main calculations begin. As many of the parameters such as gravitational acceleration, superficial phase velocities, and pressure, that determine the characteristics of the rotor are constantly changing with radial position, the equations used to predict the performance characteristics would need to be integrated along the entire radial length of the machine. This is not mathematically possible and so the radial length is divided into 100 sections, and the parameters used in determining the rotor characteristics i.e. bubble size, velocity, hold-up and mass transfer coefficients, are taken as constant for each section. The results for the mass transfer and hold-up for each section can be summed, and the bubble size and velocity averaged, to give accurate overall rotor performance predictions.

The first calculation subroutine called by the program is **Gravity**, which divides the radial length into 100 sections, the outer radius at the gas nozzles (0.4 m) and the *initial* inner radius at the pickup tube radius (0.21 m), and calculates the gravitational acceleration (Eqn. 2.40) at the beginning of each section. The pressure in the rotor due to the head of liquid is also calculated at this point (Eqn. 4.2) so that the local gas density can be determined from equation 4.8.

$$\rho_g = \frac{nP_g}{RT} \qquad 4.8$$

where n is the relative molecular mass of the gas (r.m.m. of Nitrogen = 28). The program then moves on to first calculating the hydrodynamics of the rotor i.e. the gas bubble size, velocity and hold-up. Subroutine **Bubble** is called, and at the gas nozzle radial depth, calculates the bubble size of formation using Davidson's equation (Eqn. 2.26). As the nozzles themselves are immersed in the packing then the size of formation of the bubbles must be less than or equal to the packing pore size based on assumption (4). Therefore once the calculated bubble size is

found the value is checked to see that this condition is satisfied otherwise the size is set to equal the packing pore size. For the subsequent sections, the equilibrium bubble size equation (Eqn. 4.6) is used to determine the bubble size, and this value is continually checked against the packing pore size. Within subroutine **Bubble**, once the bubble size has been calculated, subroutines **Holdup** and **Velocity** are called in turn. Equation 4.4 was used to determine the gas hold-up in each section through the rotor, and then the velocity is found using the iterative procedure as detailed in section 4.1.4. Having calculated the hold-up in each section the individual values can be summed to give a value for the total gas hold-up in the rotor which is performed in subroutine **Tothold**. Having calculated the total hold-up the program checks this value to ensure that the rotor is not flooding so that the calculations may proceed. The rotor will flood if the gas-liquid interface reaches the inside diameter of the polycarbonate window, 108 mm (See Fig. 3.4). Using equation 4.3 and substituting a value of 0.054 m for the radial position of the interface yields a gas hold-up of 0.26. Therefore if the total hold-up is greater than 26% the program tells the user the rotor is flooding and terminates the calculations. However, if the hold-up is less than the critical value the program proceeds calling subroutine **Interface**, and again using equation 4.3 the new position of the gas-liquid interface is determined. The program then returns to subroutine **Gravity** and re-calculates the radial sections, gas density, bubble size, hold-up, velocity and total hold-up in the rotor until the position of the gas-liquid interface converges and the tolerance of 0.001 m is satisfied. Once the tolerance is met the program outputs the hold-up, average gas velocity and bubble size, and the position of the gas-liquid interface. This completes the hydrodynamic modelling of the rotor.

The program then proceeds to predict the mass transfer performance of the rotor. The first subroutine then to be called is **Mtcoeff** which calculates the liquid side mass transfer coefficient for each of the radial sections. As seen in section 4.2 a number of different correlations were tried in predicting the mass transfer coefficient and Fig. 4.4 shows how the predicted coefficient varies along the radial length. Once the coefficient has been determined for each section, subroutine **Height** is called which calculates the height of a transfer unit using equation 2.5, and therefore the number of mass transfer units attained in each radial section. This is then summed by the main program **Model** to give the overall total number of transfer units achieved in the rotor. Finally **Outlet** is called which simply calculates the final oxygen concentration (in ppm) in the water as it leaves the rotor using equation 2.7. As seen in section 2.4.1. the equilibrium constant is given by Henry's Law, and values for Henry's constant are shown in Table 4.3.

Table 4.3 : Henry's Constant for Oxygen[17]

Temperature (°C)	0	5	10	15	20
Henry's Const., H (atm)	25500	29100	32700	36400	40100

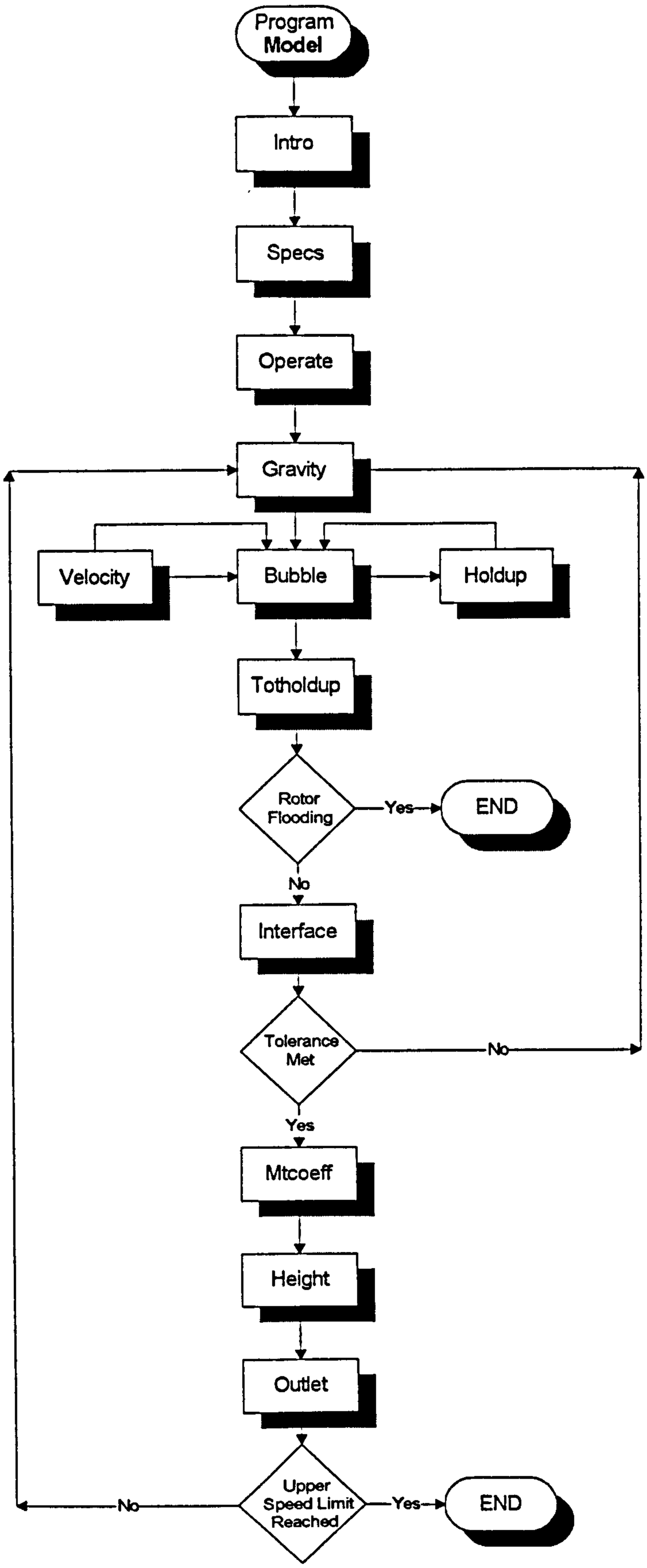

Figure 4.5 : Computer Model Flowsheet

A value of 32700 atm for Henry's constant was chosen for the rotor calculations as 10°C is an average value for the experimental water temperature. This value was divided by the local gas pressure, converted into atmospheres, to give the equilibrium constant for each section from which the outlet concentration could be calculated. The outlet concentration from the n^{th} section was then used as the inlet concentration for the $(n+1)^{th}$ section and this process repeated until the final section was completed, the outlet concentration of which gave the final outlet concentration from the rotor. This completes the mass transfer performance prediction for the rotor, and the program then increases the speed by the inputted increment and repeats all the calculations at the new speed. This process continues until the upper rotational speed is reached at which point the program terminates. Once the program has terminated, the mass transfer results which have been sent to the output file 'rotor.dat' are then displayed graphically using the software package *xgraph*, so that the variation in the overall mass transfer performance of the rotor with the rotational speed can be seen.

4.4 Model Output Results

The following section examines the rotor performance as predicted by the model, and looks at the effect of the speed, radial position, and the flowrates on the gas hold-up, bubble size and velocity, and overall mass transfer performance in the rotor.

4.4.1 Gas Hold-up

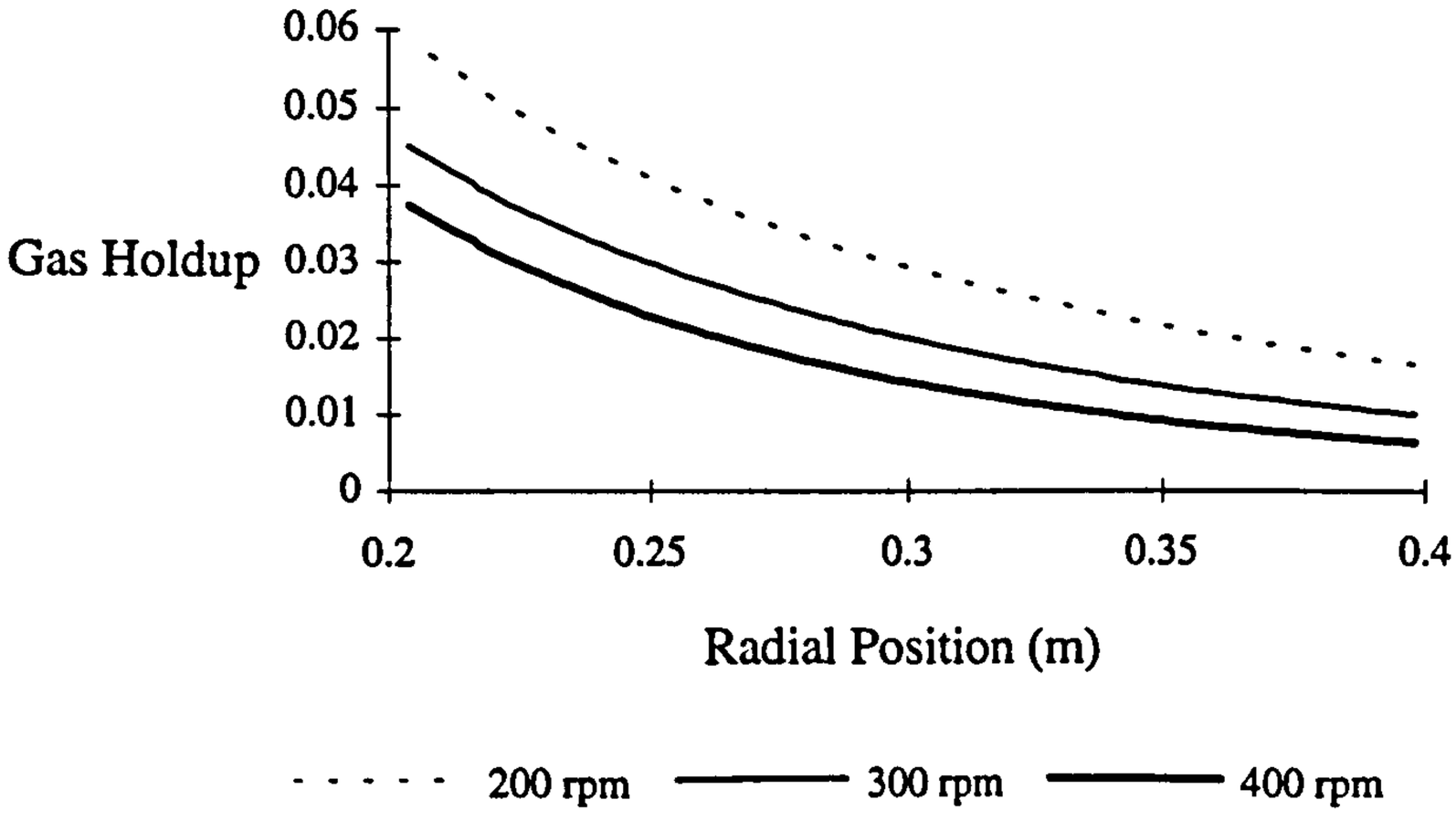

Figure 4.6 : Variation in Gas Hold-up through the rotor at Increasing Rotational Speeds at a Gas and Liquid Flowrate of 0.5 l/sec

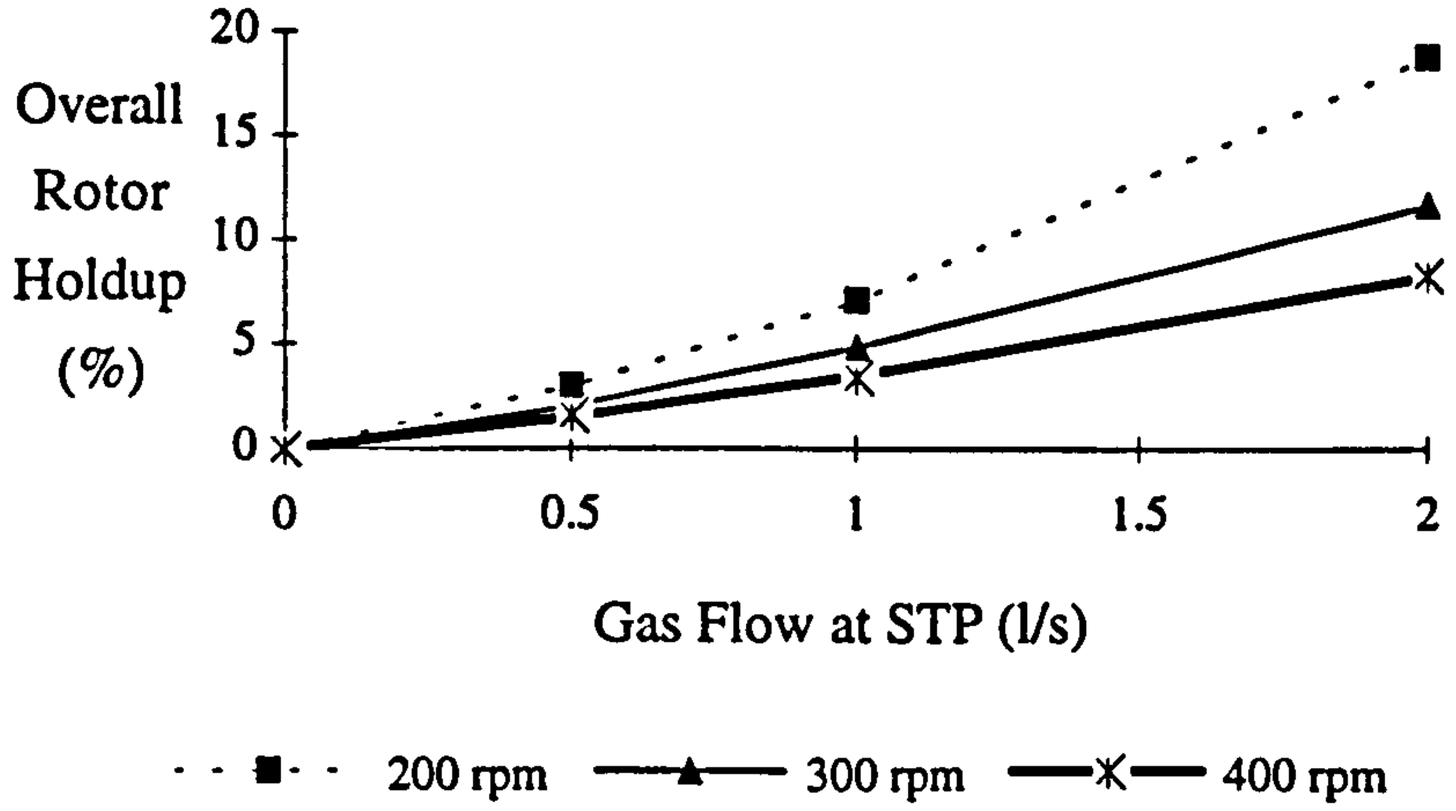

Figure 4.7 : Variation of the Overall Gas Hold-up in the Rotor with Gas Flow at Increasing Speed and a Liquid Flowrate of 0.5 l/sec

Fig. 4.6 shows that the gas hold-up in the rotor decreases as the radial depth increases. This can be explained by the increase in the cross sectional area of the rotor and also an increase in the gravitational acceleration leading to smaller bubbles. For a given gas flowrate, as the rotational speed is increased the gas hold-up decreases which is as a result of the increase in pressure of the liquid in the rotor leading to an increase in the gas density and therefore a decrease in the average gas bubble size. As expected Fig. 4.7 shows that as the gas flowrate is increased the gas hold-up will increase.

4.4.2 Gas Bubble Size

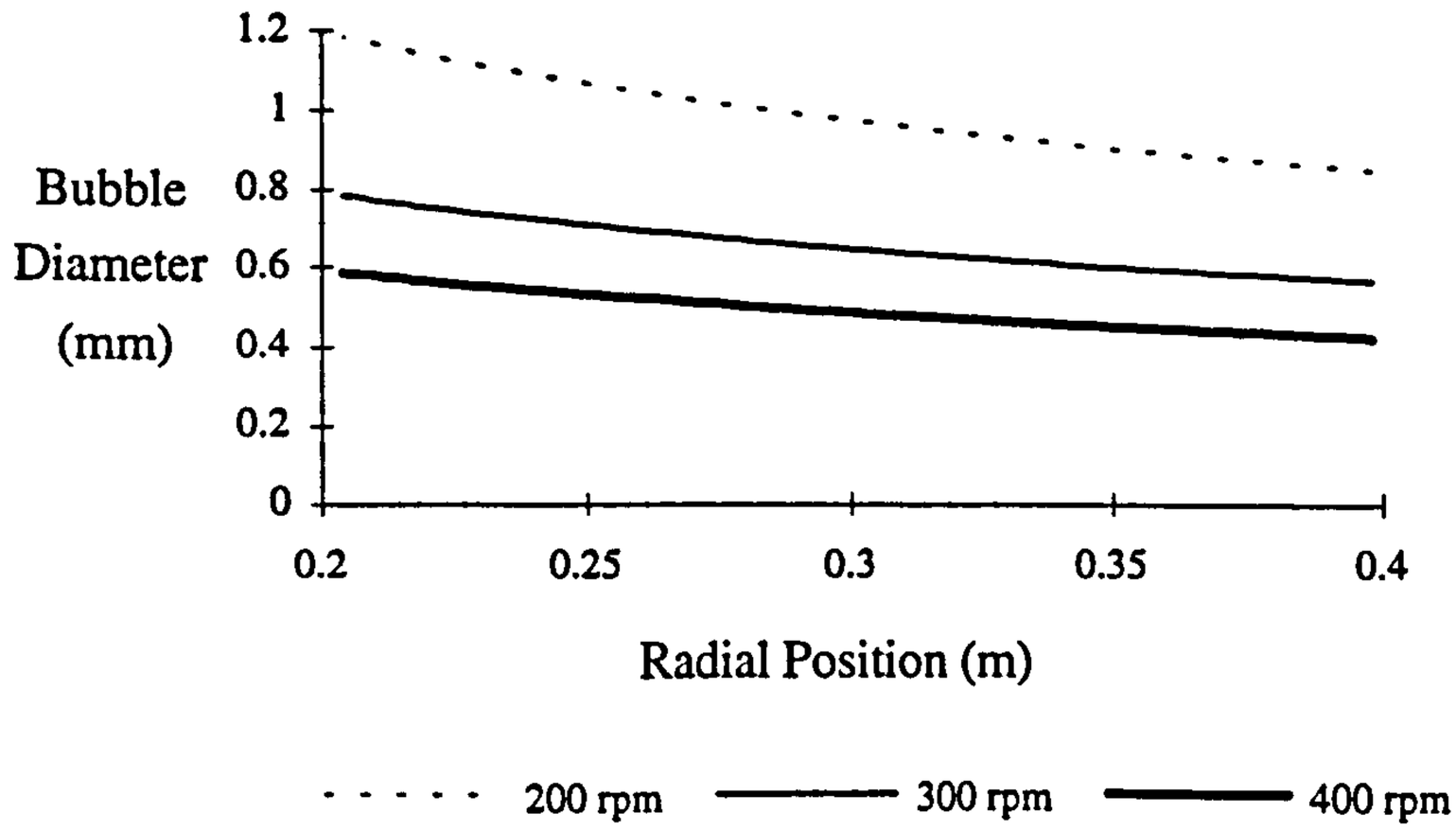

Figure 4.8: Variation of Gas Bubble Size with Radial Position and Increasing Speed at a Gas and Liquid Flowrate of 0.5 l/sec

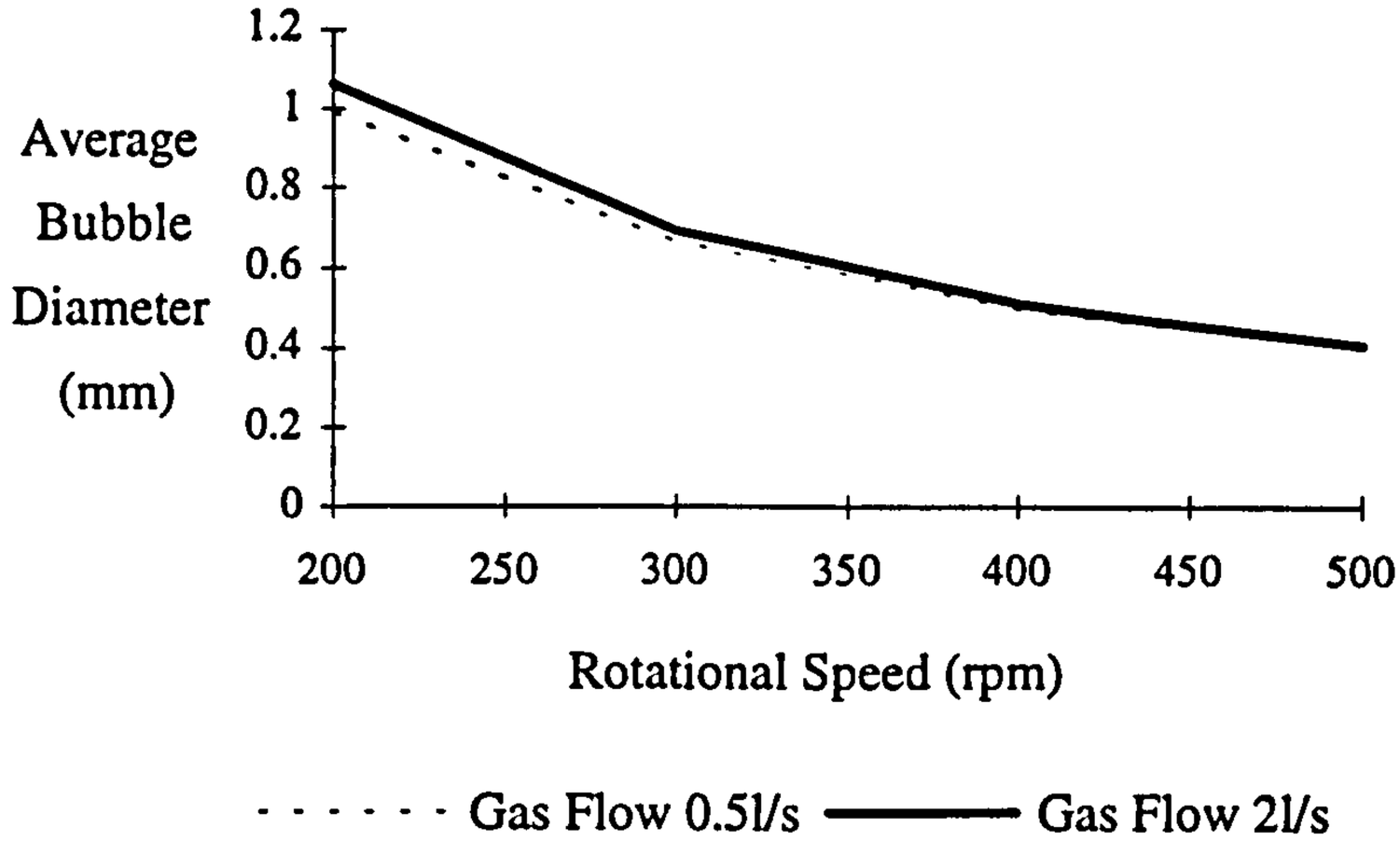

Figure 4.9 : Variation of Average Bubble Size with Rotational Speed at High and Low Gas Flows and Liquid Flow 0.5 l/sec.

Fig. 4.8 shows how the equilibrium bubble size varies through the rotor packing. In all cases the equilibrium bubble size is less than the packing pore size of the Declon HC20 packing, and seems to be fairly constant along the entire radial length. A doubling of the rotational speed decreases the average equilibrium bubble size by up to 50%. As shown in Fig. 4.9 the gas flowrate seems to have little effect on the bubble size. A comparison of the above predicted bubble size with that found experimentally can be found in Table 5.3 (Sect. 5.4) of this thesis.

4.4.3 Gas Velocity

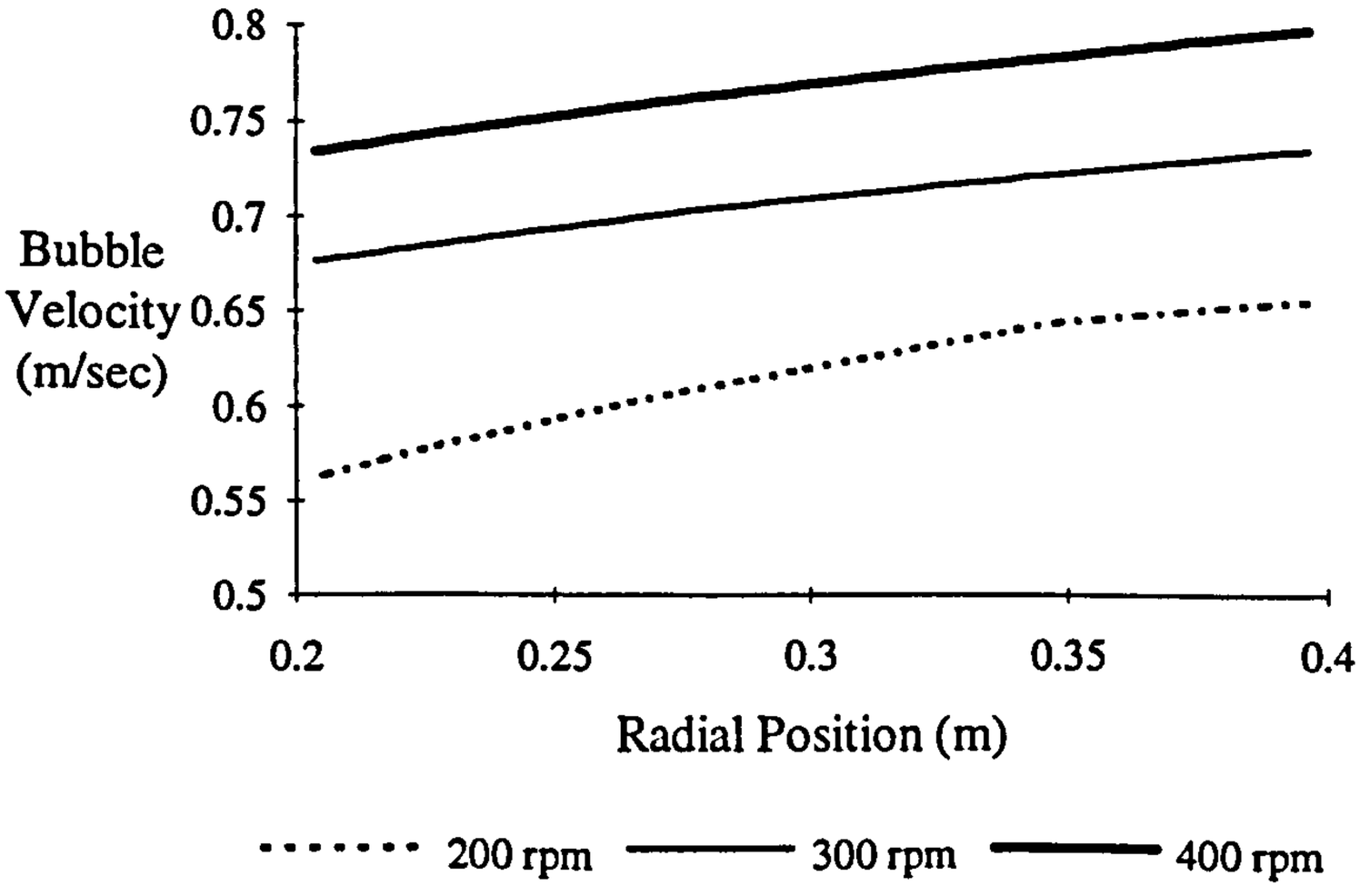

Figure 4.10 : Variation of Gas Terminal Velocity through the Rotor with Increasing Rotational Speed and Gas and Liquid Flow 0.5l/sec

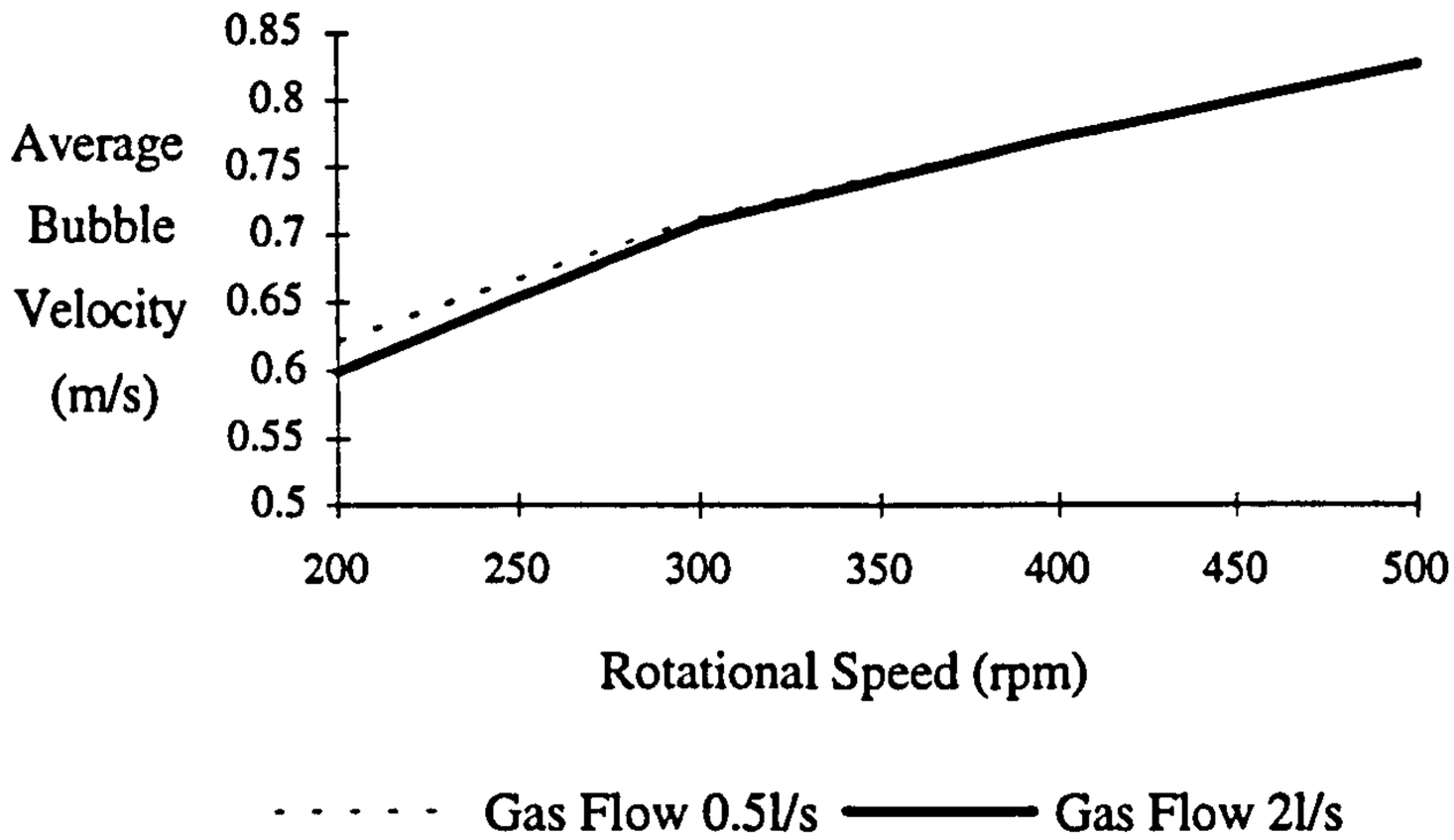

Figure 4.11 : Variation in Average Bubble Velocity in Rotor at High and Low Gas Flows and Liquid Flow 0.5l/sec

Fig. 4.10 shows how the bubble terminal velocity varies through the rotor. Equation 2.32 showed the bubble velocity to be proportional to the gravitational acceleration with an exponent of 1/2 which is why the bubble velocity through the rotor will increase with the rotational speed. Perhaps surprisingly, as shown in Fig. 4.11, the gas flowrate has little influence on the predicted bubble velocity.

4.4.4 Mass Transfer Performance

Figures 4.12 - 15 show the predicted overall mass transfer between the gas and liquid in the rotor for the six equations used in predicting the liquid side film coefficient. The mass transfer is displayed in numbers of transfer units as this is an easy and convenient method of displaying the mass transfer for sparingly soluble systems (see Sect. 6.1). Figs. 4.12,13 show the predicted mass transfer performance of the rotor against the rotational speed for a gas to liquid flowrate ratio of 1:1 and 2:1, using the original Declon HC20 packing. As can be seen by comparing the predicted mass transfer with the experimental data, it would seem that the best correlation to fit the data points at the 1:1 gas to liquid flowrate ratio is the Hughmark correlation, whereas at the higher gas to liquid flowrate ratio of 2:1, no correlation fits the experimental data, with the actual rotor performance falling somewhere in between the mass transfer prediction based on the correlations of Cockx / Roustan and Hikita. The Cockx / Roustan prediction would be chosen in preference to Hikita's correlation as it displays the same performance characteristics as the experimental data over the rotational speed range 200 - 400 rpm.

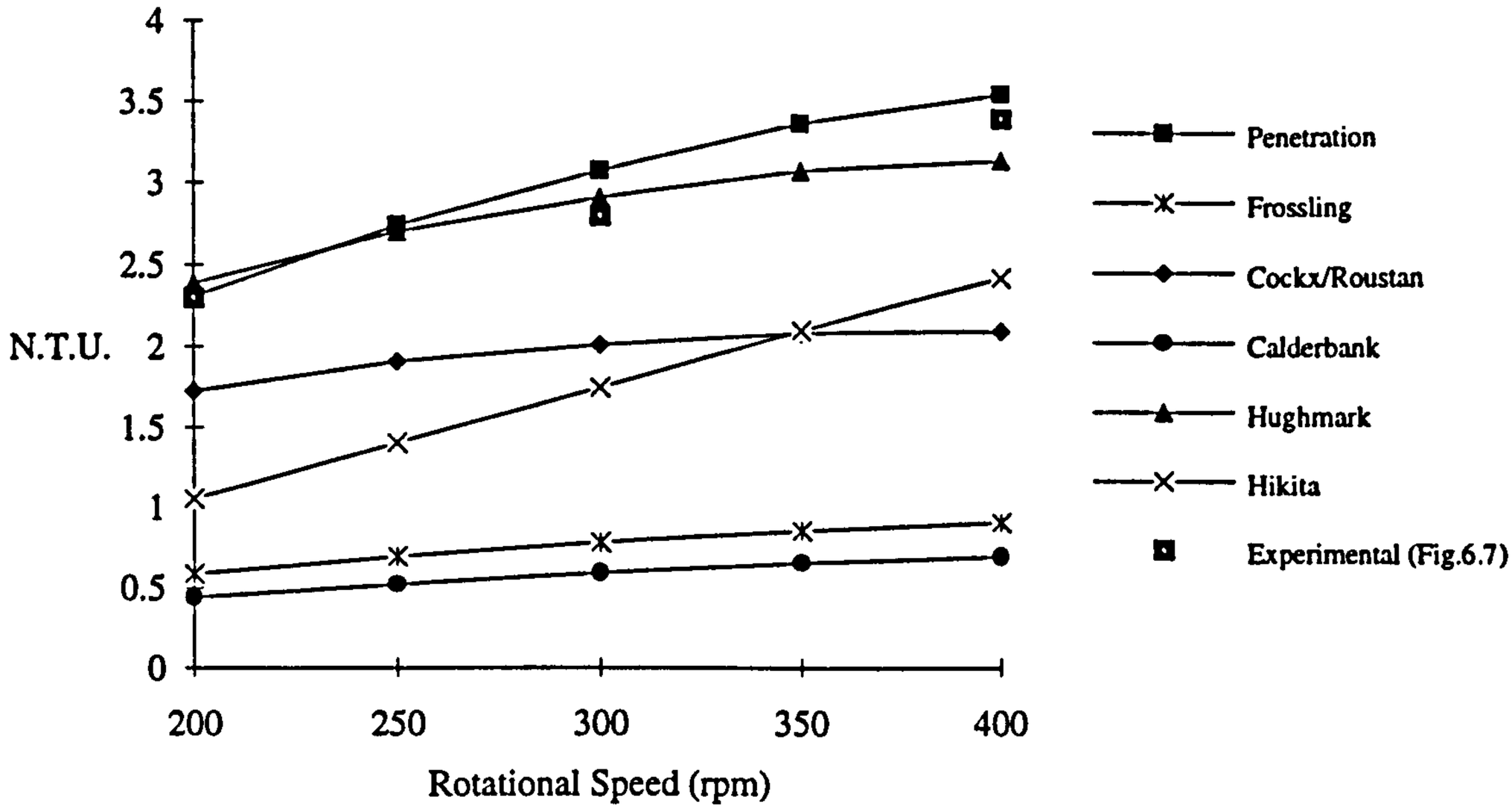

Figure 4.12 : Predicted Mass Transfer Performance of the Rotor for a Gas and Liquid Flowrate of 0.5 l/sec using Declon HC20 Packing

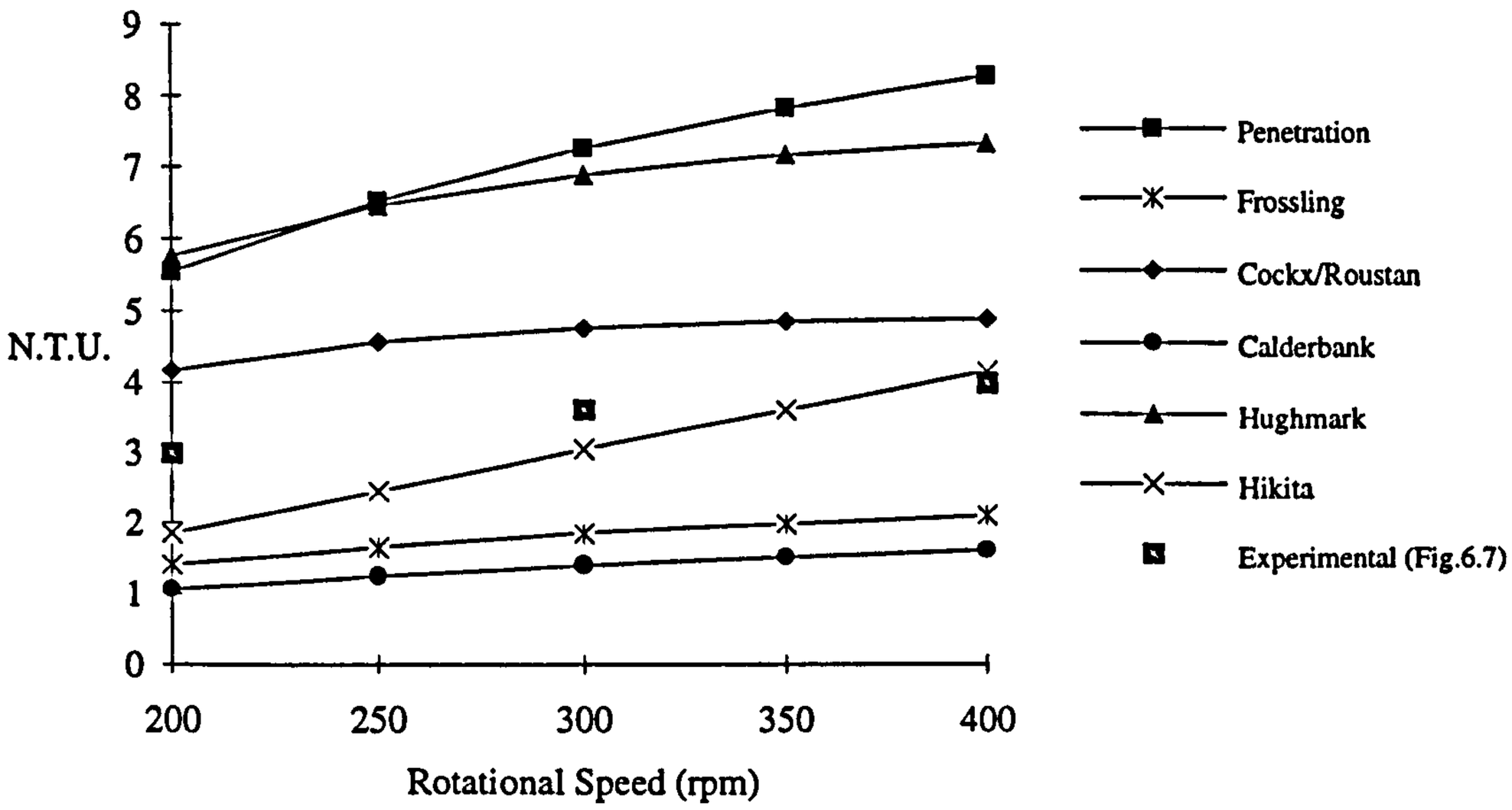

Figure 4.13 : Predicted Mass Transfer Performance of the Rotor for Gas Flow of 1.0 l/sec and Liquid Flow 0.5 l/sec using Declon HC20 Packing

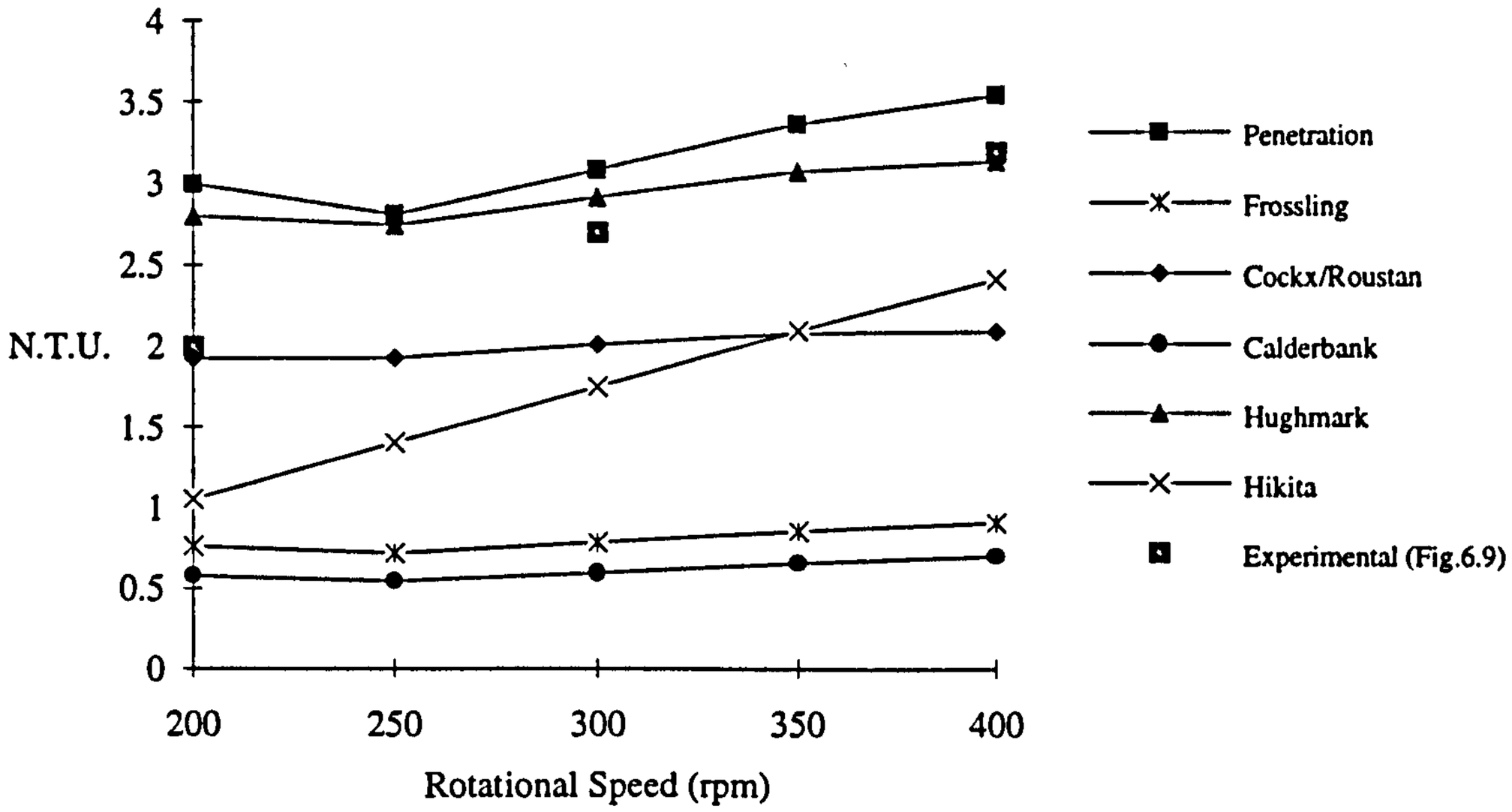

Figure 4.14 : Predicted Mass Transfer Performance of the Rotor for a Gas and Liquid Flowrate of 0.5 l/s using the more Porous Declon HC30 Packing

Fig. 4.14 shows the predicted performance of the rotor at a 1:1 gas to liquid ratio with the finer Declon HC30 packing, which has an average pore size of 0.85 mm. The main points of interest are that the model predicts a noticeable increase in mass transfer performance of the rotor at the lower speed of 200 rpm compared with the regular HC20 packing, which is thought is attributed to the fact that at 200 rpm the average bubble size is about 1 mm in diameter (see Fig. 4.9) and so as the pore size is less than this the bubbles will be broken up leading to a greater interfacial area. The only correlation not to display this increase at 200 rpm is Hikita's correlation, which predicts the mass transfer with the new packing to be identical to that of the original packing. This is because the correlation predicts the volumetric mass transfer coefficient and therefore the change in interfacial area does not affect the mass transfer prediction. The experimental data from the rotor does not display this increase in mass transfer at the higher speeds and again at the lower gas flow Hughmark's correlation seems to model the mass transfer of the rotor most accurately.

Fig. 4.15 shows the model predictions for the mass transfer achieved in the rotor along half of the packed length. Comparing the predicted rotor mass transfer at the half radial length with that shown in Fig. 4.12 it can be seen that the predicted mass transfer is nearly proportional to the radial length, i.e. approximately half of the mass transfer is achieved along the first half of the radial length, in all cases. However this is certainly not the case experimentally as there is only a slight difference between the results obtained at the full and half radial lengths, and therefore as can be seen from Fig. 4.15 all of the predictions considerably under estimate the mass transfer.

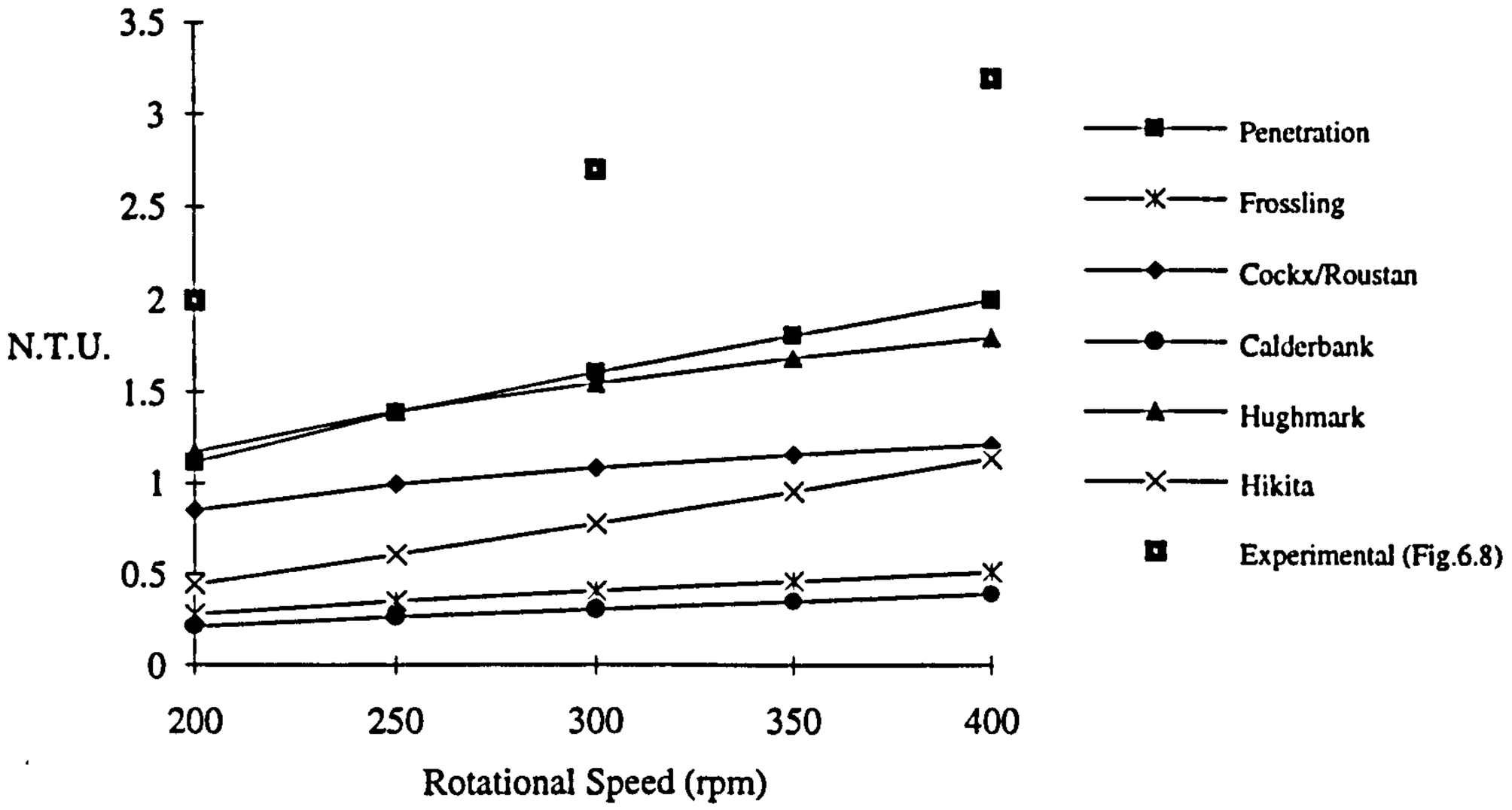

Figure 4.15 : Predicted Mass Transfer Performance for **Half** the Packed Length of the Rotor for a Gas and Liquid Flow of 0.5 l/s using Declon HC20 Packing

4.5 Discussion

The above model, although fairly detailed, has its limitations in its applicability to modelling all the rotor characteristics. The assumptions made in section 4.3 simplify the true picture of the gas and liquid behaviour in the rotor packing, and therefore are not all valid. In modelling the hydrodynamics of the rotor, Figs. 4.8, 4.9 show that the predicted bubble sizes in the rotor, which it assumes to be the critical bubble size, are higher than the experimentally measured values (see Sect. 5.4, Table 5.3). There is also at present no correlation able to predict the bubble size at formation for the rotor, and the bubble size at any point throughout the packing will vary over a range due to splitting and coalescence rather that the single value assumed by the model. Alshaban[7] in his work on bubbles in centrifugal fields found the range of bubble sizes to be Gaussian in their distribution and his main observations showed the standard deviation of the bubble sizes to decrease as the rotational speed and gas flow increased. The bubble velocity will be effected by collisions with packing filaments and other bubbles, and the liquid velocity in the rotor, as seen in section 5.3, is complicated in itself with varying degrees of backmixing and general maldistribution occurring.

The modelling of the mass transfer is somewhat varied in its success. Figs. 4.12, 4.14 show that the Hughmark correlation is generally applicable in the prediction of the rotor mass transfer at low gas to liquid ratios, but as this ratio increases then Hughmark's correlation tends to over estimate the overall mass transfer, and other correlations such as that proposed by Cockx / Roustan are more accurate. One possible explanation for this is the maldistribution in liquid flow through the rotor which is not accounted for in the model. The correlations

proposed by Calderbank and Frossling significantly under estimate the mass transfer performance and are therefore generally not applicable to the modelling of the mass transfer in the rotor. The reasons for this are that Calderbank's correlation is only valid for small bubbles only ($d_b < 0.5$ mm), whereas as can be seen from Fig. 4.8 the bubble sizes are in the range of 0.6 - 1.2 mm. Frossling's equation is based on bubbles that are completely rigid which assumes no internal circulation, and as seen in Fig. 2.9, rigid behaviour occurs at bubble diameters of around 0.2 mm which is clearly not applicable in this case. Hikita's correlation does not show the same mass transfer curve characteristics in the experimental range due to the correlation predicting the volumetric coefficient, and therefore not accounting for the increase in interfacial area that will occur in 'high g' environments. Therefore the applicability of Hikita's equation to modelling Higee processes is questionable.

Due to the complexity of the rotor, possible ways forward in improving the accuracy and robustness of the model are difficult. Clearly the assumptions made do not reveal the entire picture. One improvement to the model may be to use the probabilistic model detailed in section 4.1.3. to produce a bubble size distribution through the packing. However applying this model would be complicated and the probability of a collision is calculated on geometric factors alone, and assumes no relative tangential velocity between the bubbles and packing surface, which again is an over simplification of the actual situation. The liquid flow through the rotor has been modelled using a multi-parameter tanks-in-series model (Sect. 5.3) which may be possible to include in the overall rotor model but again the model is complicated and may be difficult to implement in the program. However these are possible ways forward in the development of an accurate and robust Higee model, and have been recommended as future research to be undertaken.

CHAPTER 5 : HYDRODYNAMIC CHARACTERISTICS OF ROTOR

5.1 Introduction

The hydrodynamics of the rotor is a collective term used to describe the gas and liquid flow characteristics through the machine. As explained in previous chapters, various parameters are used to characterise the rotor hydrodynamics, and these are terms such as the type of flow, gas bubble size and velocity, and the hold-up. The hydrodynamics of the rotor are inseparably linked with the mass transfer that occurs between the two phases, and so a detailed understanding of the rotor hydrodynamics should lead to design and operation strategies for the improvement in the overall mass transfer performance of a Higee rotor.

For much of the hydrodynamic work, high speed photography was used (see Sect. 3.3.4) due to the high speeds of rotation of the machine. The initial design of the rotor allowed a polycarbonate window to be fitted to the front of the rotor so that the gas and liquid hydrodynamics could be seen. However due to the strength of the polycarbonate material, the speed of rotation was limited to speeds of under 400 rpm, and even at modest speeds (300 - 400 rpm) significant bowing of the polycarbonate window could be noticed. This led to crazing and eventually some stress fractures appeared around the peripheral fixing bolts (see Appendix IX (c)), and this was later replaced by an aluminium front plate. Inside the packing area, small sections of the packing material were cut out at different radial positions to make windows so that the gas bubble sizes could be examined (see Sect. 5.4).

The following sections examine how the operating conditions affect the liquid phase and gas phase hydrodynamics through the rotor, focusing specifically on the overall visual rotor hydrodynamics, the characterisation of the liquid flow through the packing using a pulse input tracer technique, and the gas bubble sizes as the bubbles migrate through the packing pores to the centre of the rotor.

5.2 Overall Rotor Hydrodynamics

As part of a detailed examination into the way the liquid and gas pass through the rotor much photographic work was taken through the various stages of development of the rotor. All the photographs taken for the overall rotor hydrodynamics used the two stroboscope units placed above and below the rotor face, and the photographs were taken using a high speed 400 a.s.a. film with an exposure time of 0.5 seconds and a camera aperture setting of 2.8. The following subsections show the visual effect of the nozzle design on the gas and liquid flow in the rotor packing for varying operating conditions, until eventually a nozzle design was found in which the general hydrodynamics gave the appearance of a uniform hydrodynamic distribution throughout.

5.2.1 Original Gas Injector Nozzles

The initial hydrodynamic studies of the rotor in the investigation of the gas and liquid flow patterns involved taking photographs of the machine at different operating conditions. The entire rotor face was illuminated using two strobe units placed above and below that were synchronised with each other. As can be seen from photographs 1 - 4 the initial observations were quite unexpected. It can be seen that :

1. A *spiralling* pattern was produced in the rotor between the gas and liquid phase, and this effect becomes more pronounced as the speed of rotation and gas flowrate are increased.

2. Gas plumes can be seen coming from the injector nozzles around the top and down the left side of the rotor, but not at the base and the right side of the rotor face.

3. As the gas flowrate increases, the gas liquid interface in the rotor moves towards the centre of the rotor. This will be due to the increase in the gas hold-up in the machine.

It was decided that as the *position* of a nozzle rather than the actual nozzle itself determined whether gas would fire from it's orifices, there was not a design fault with some of the nozzles, but rather a pressure difference in the machine. This could only logically be explained by considering the vertical orientation in which the rotor operates, and therefore the effect of natural gravity causing slight differences in the pressure head on the gas nozzles due to the rotating pool of liquid. Although this difference will always exist while the rotor operates in a vertical orientation, it's influence may be lessened by increasing the pressure drop over the individual nozzles, thereby lessening the fraction of the total pressure in the rotor due to the liquid pool. This has been detailed and explained in full in section 3.3.5.2. The obvious step would be to replace the nozzles themselves with nozzles of a different design, but due to the actual assembly design of the rotor, it was not possible to remove the existing nozzles. Therefore different methods were tested to increase the pressure drop on the existing nozzles, which included placing membranes across the nozzles, plugging some nozzles to increase the gas flow through the remaining ones, and decreasing the cross sectional area of the orifices.

GAS INJECTOR NOZZLES

GAS - LIQUID INTERFACE

DECLON HC20 PACKING

ROTOR

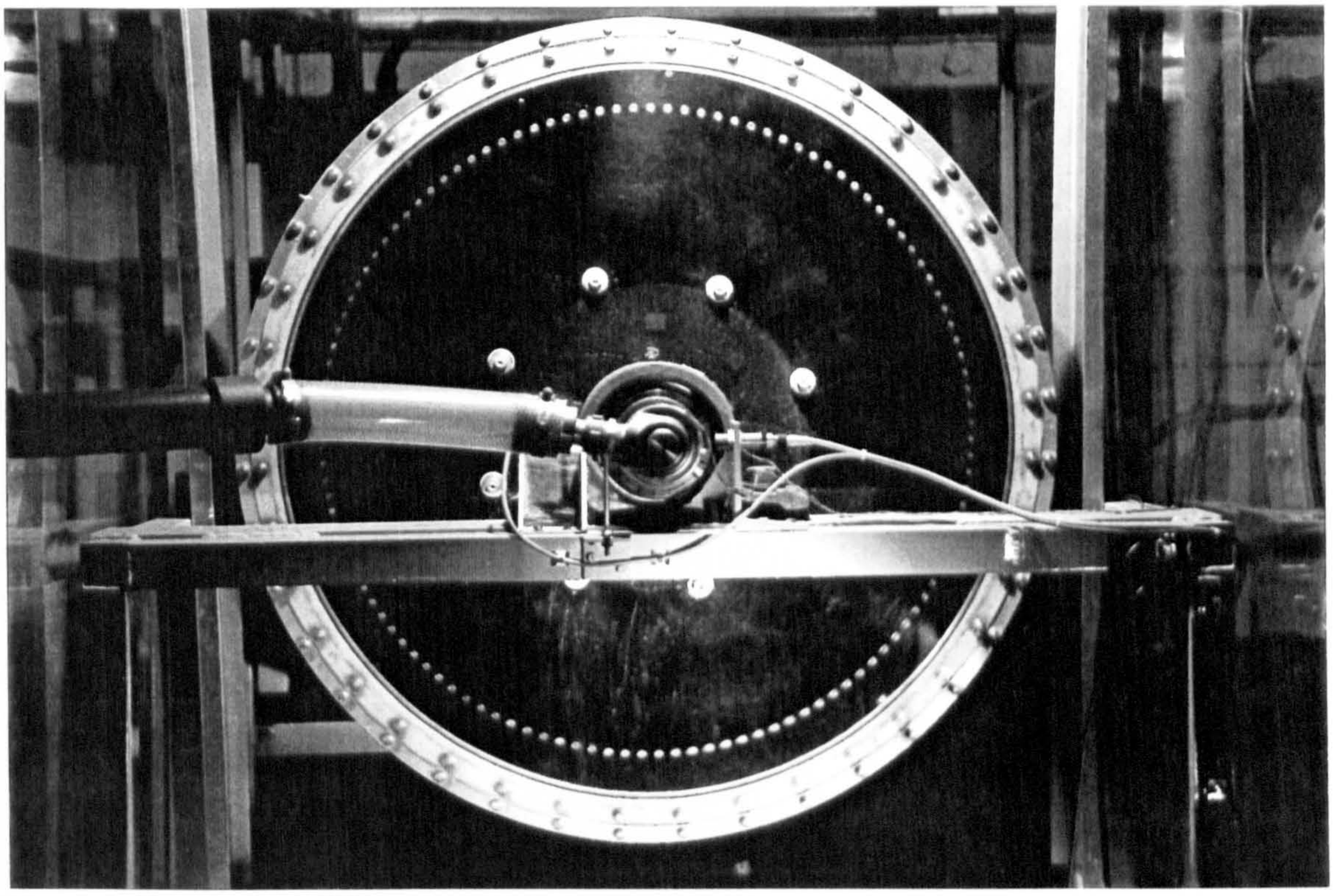

Photograph No.1 : *Overall Rotor Hydrodynamics with Original 120 Gas Nozzles*
Speed 200 rpm, Liquid Flow 0.1 l/sec, Gas Flow (stp) 0.3 l/sec

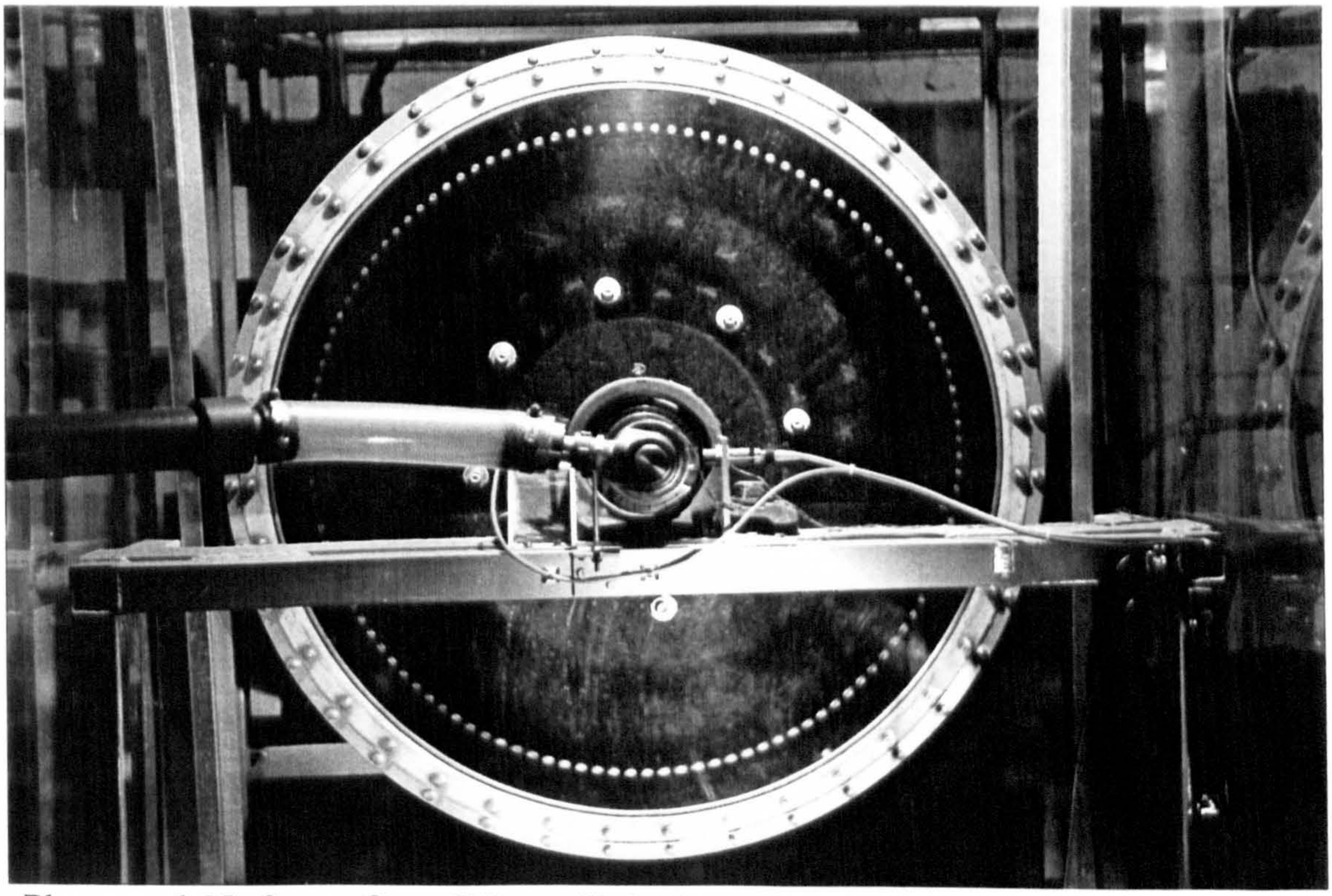

Photograph No.2 : *Overall Rotor Hydrodynamics with Original 120 Gas Nozzles*
Speed 200 rpm, Liquid Flow 0.1 l/sec, Gas Flow (stp) 1.0 l/sec

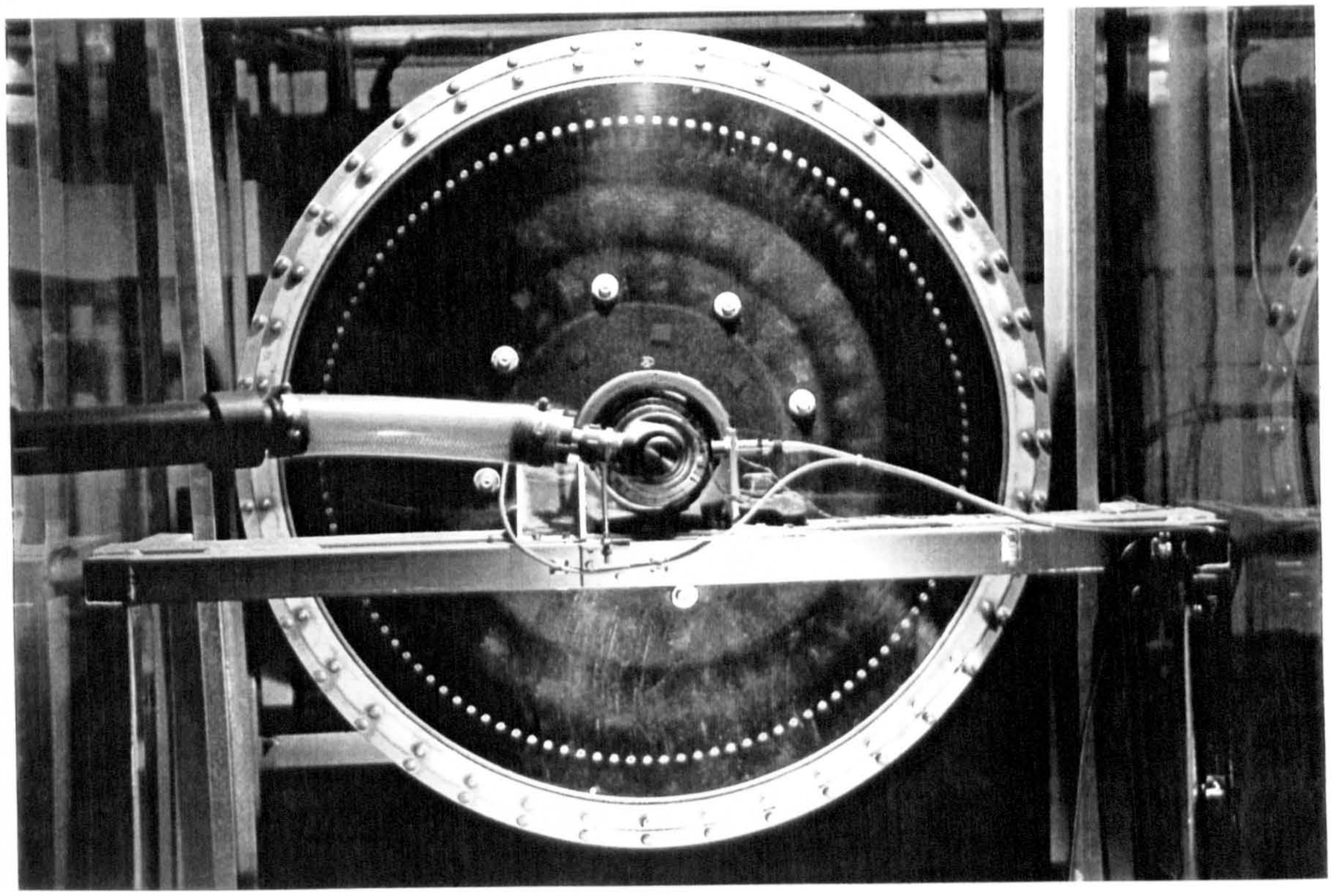

Photograph No.3 : *Overall Rotor Hydrodynamics with Original 120 Gas Nozzles*
Speed 300 rpm, Liquid Flow 0.1 l/sec, Gas Flow (stp) 1.1 l/sec

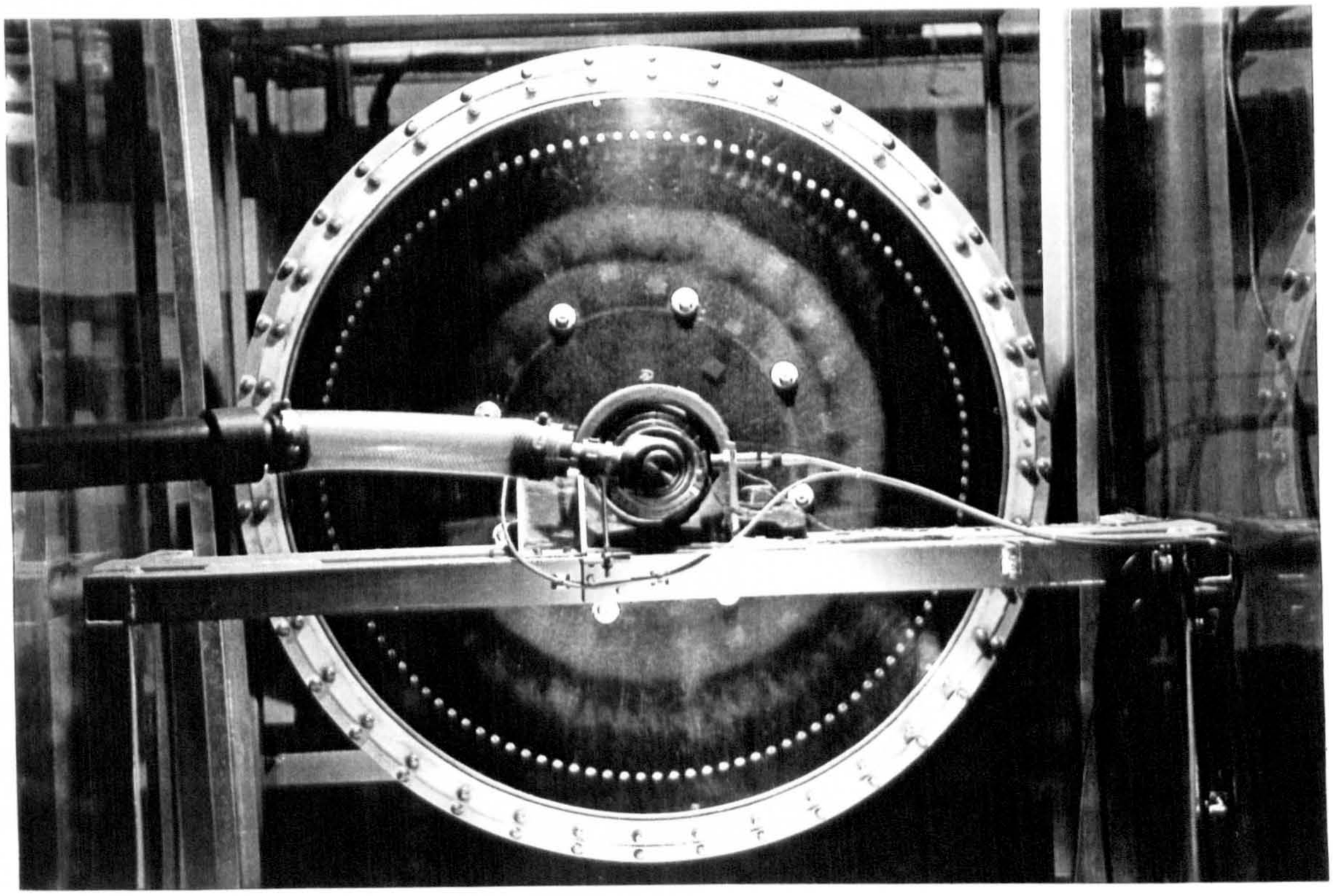

Photograph No.4 : *Overall Rotor Hydrodynamics with Original 120 Gas Nozzles*
Speed 400 rpm, Liquid Flow 0.1 l/sec, Gas Flow (stp) 1.2 l/sec

5.2.2 Modified Gas Nozzles (Increased Gas Velocity)

One method adopted to increase the gas pressure drop across the nozzles was to increase the flow and hence velocity through the nozzles. To achieve this 3 in every 4 holes were completely plugged so that the resulting mass flowrate through each nozzle orifice should increase four-fold, and the resulting overall hydrodynamics can be seen in photographs 5 - 6. From these the following observations and conclusions were made :

1. The nozzles seem to fire at all positions around the rotor, which has prevented them from filling with water at the bottom of the rotor, and as a result the spiralling pattern seen with the original design has disappeared.
2. Large gas plumes are now produced due the high gas velocities leaving the gas nozzles. Typical gas velocities are now in the region of 10 - 95 m/sec. However there is a substantial region of the packing that now has poor mixing between the gas liquid, and is therefore not being utilised.

The above method may have helped to reduce the spiralling effect in the rotor, but with the ineffective utilisation of much of the packing material, there is little improvement in the overall hydrodynamics of the rotor, and one problem seems to have been replaced by another. Therefore there was no reason for pursuing this method.

5.2.3 Modified Gas Nozzles (Reduced Orifice Diameter)

The initial orifice diameter of the gas nozzles was 0.5 mm, and another means of increasing the pressure drop across the nozzles is to reduce the cross sectional area, and hence the orifice diameter. Possibly the simplest way of doing this was by inserting 0.4 mm gauge copper wire through the nozzle orifices, thus effectively reducing the orifice bore to 0.3 mm. (see also Sect. 3.3.5.2) Photographs 7 - 8 show the overall hydrodynamics for the rotor using the copper wire with 60 nozzles, and 60 nozzles still plugged, although this was subsequently modified further so that all 120 nozzles containing the copper wire were in operation. As can be seen :

1. All the nozzles in operation are firing regardless of their position in the rotor, giving visually a uniform distribution throughout.
2. A much higher proportion of the packing is being effective in the contacting of the gas and liquid, which in turn should provide a much greater interfacial area for mass transfer.

The above approach seems to be the easiest to implement with the existing nozzles and yields what visually seems to be a much improved uniform distribution throughout the rotor. However a visual analysis can not reveal much, and a more detailed analysis of the liquid flow through the rotor was carried out using a tracer technique. (Sect. 5.3)

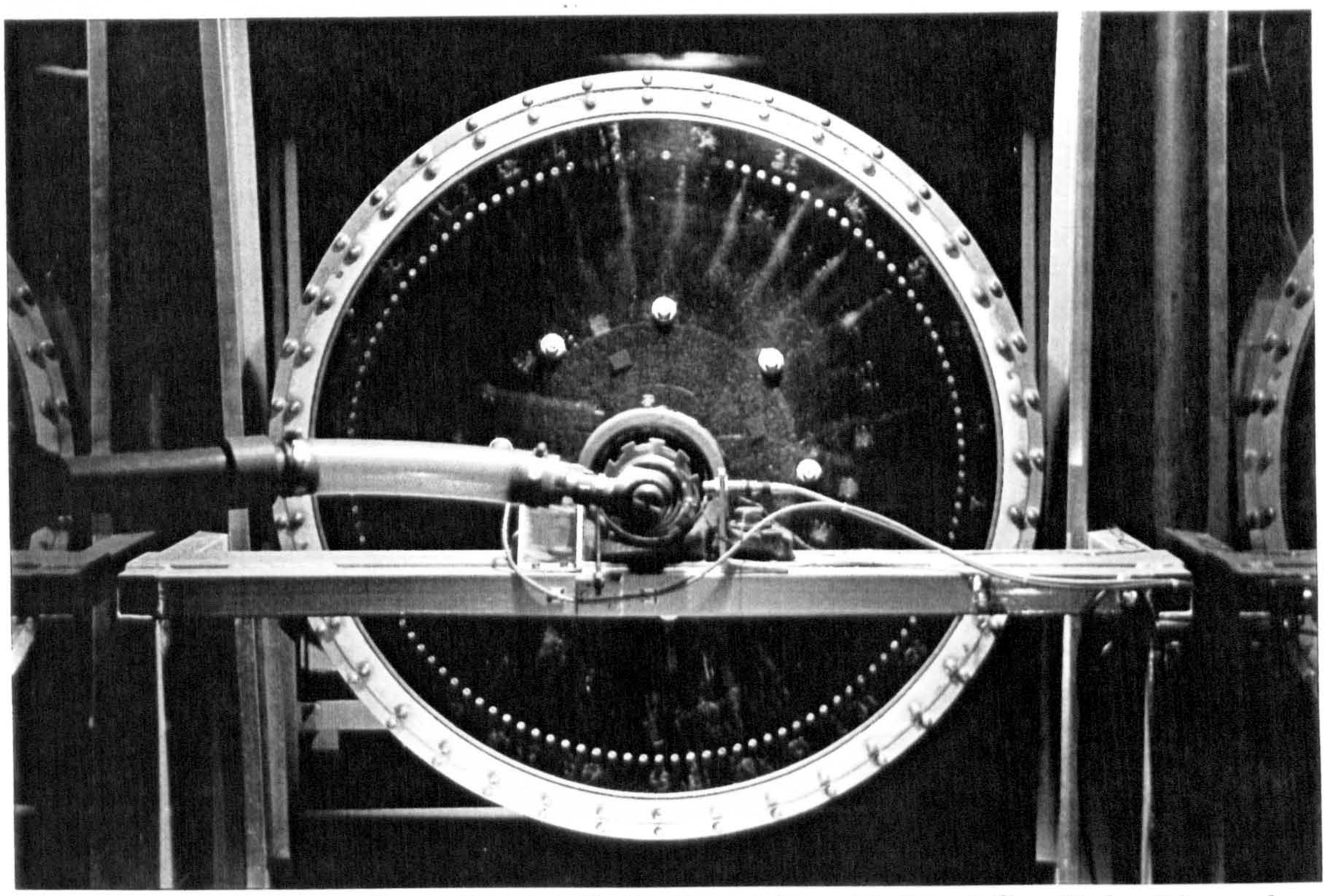

Photograph No.5 : *Overall Rotor Hydrodynamics with 3 in 4 Gas Holes Plugged*
Speed 250 rpm, Liquid Flow 0.1 l/sec, Gas Flow (stp) 1.1 l/sec

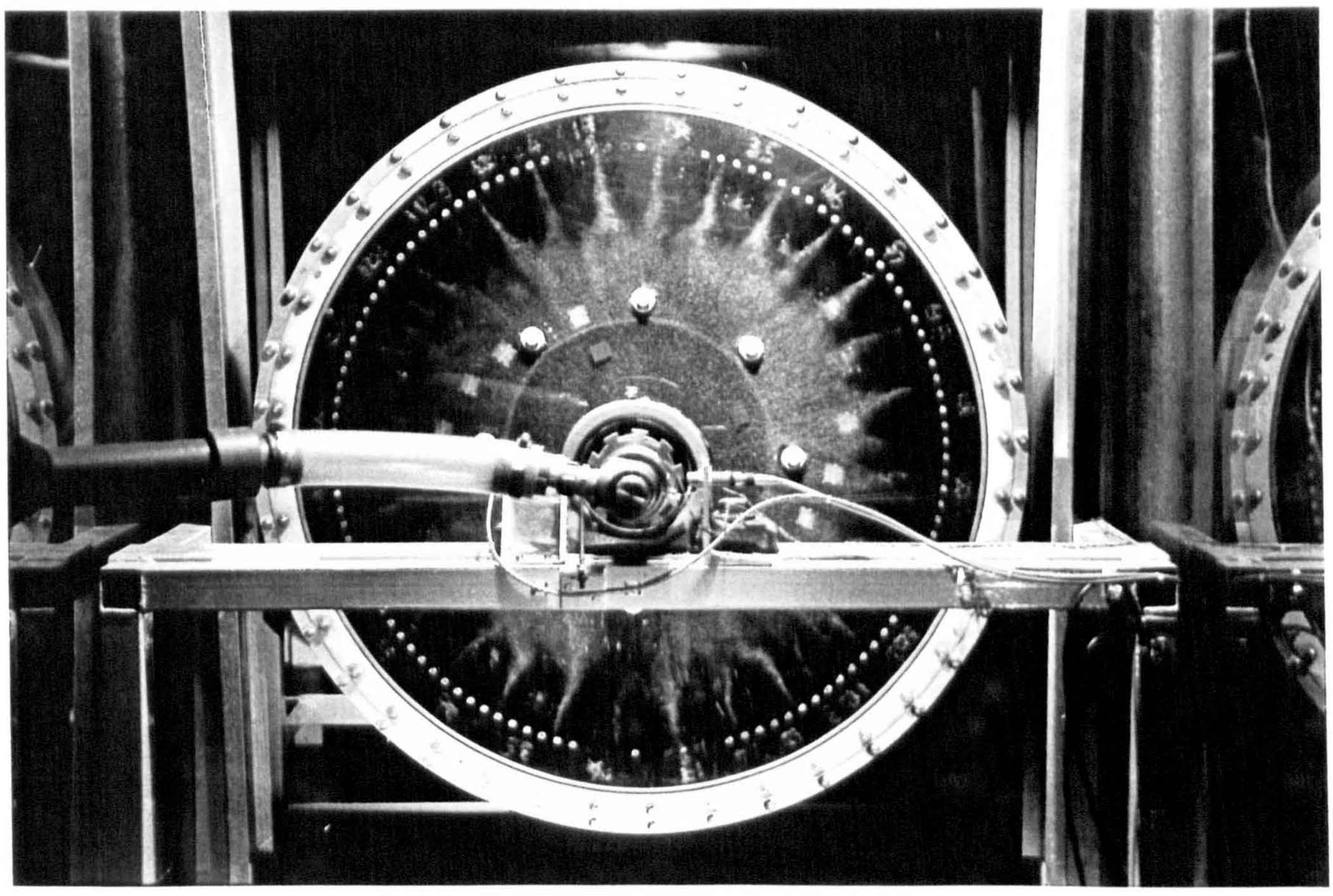

Photograph No.6 : *Overall Rotor Hydrodynamics with 3 in 4 Gas Holes Plugged*
Speed 350 rpm, Liquid Flow 0.1 l/sec, Gas Flow (stp) 2.0 l/sec

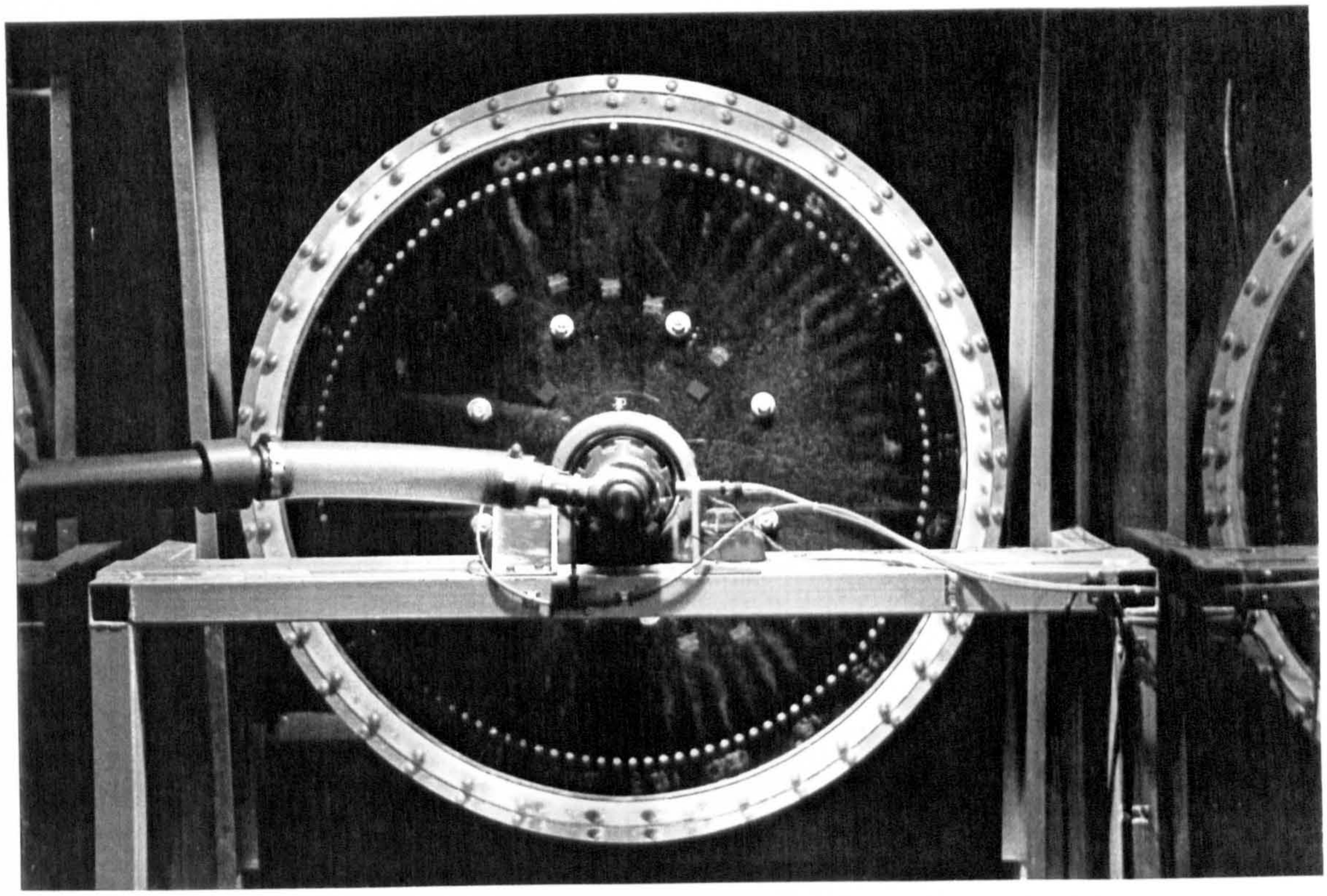

Photograph No.7 : *Overall Rotor Hydrodynamics with 60 Nozzles Plugged, & 60 Nozzles with 4mm Copper Wire*
Speed 200 rpm, Liquid Flow 0.2 l/sec, Gas Flow (stp) 1.6 l/sec

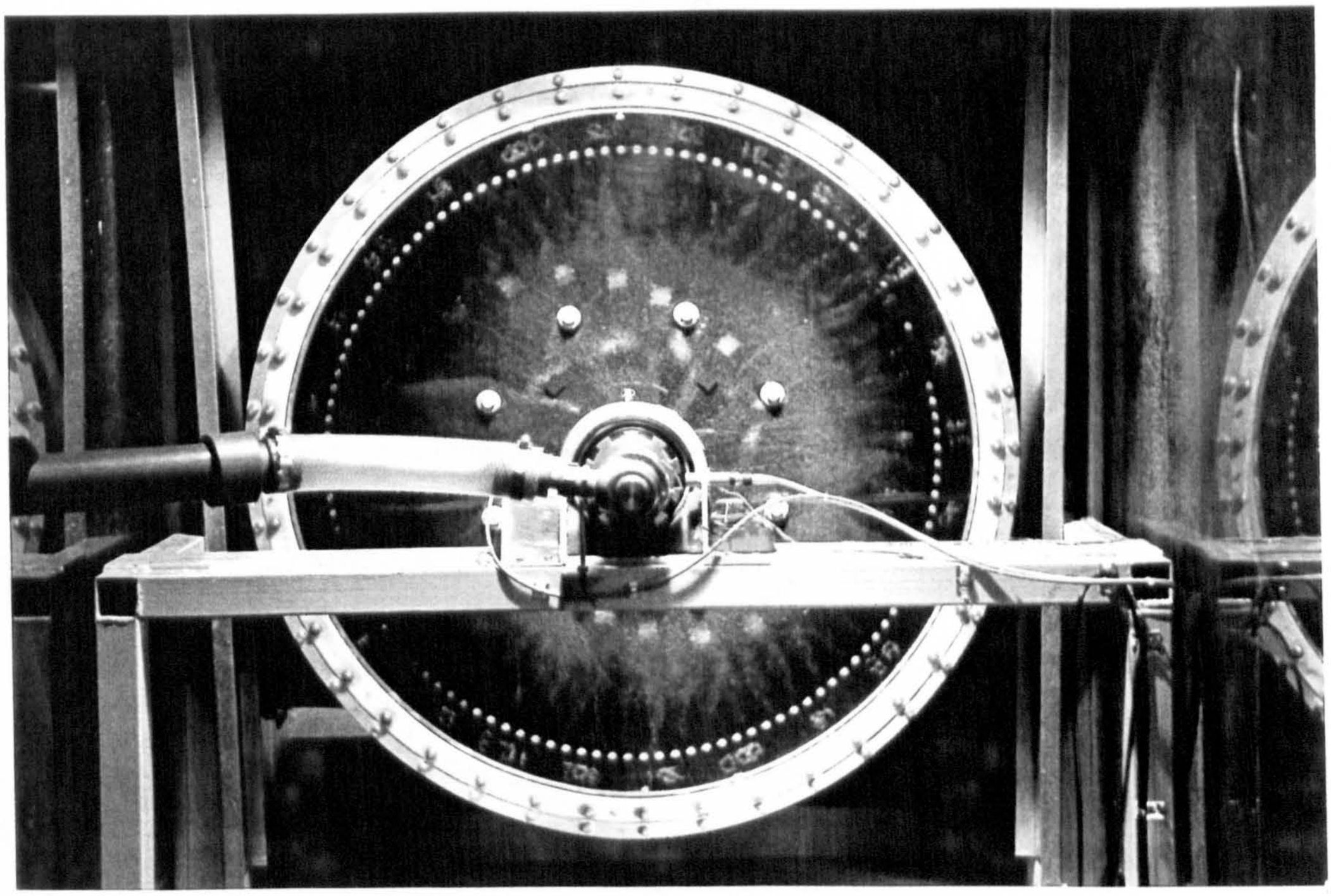

Photograph No.8 : *Overall Rotor Hydrodynamics with 60 Nozzles Plugged, & 60 Nozzles with 4mm Copper Wire*
Speed 400 rpm, Liquid Flow 0.6 l/sec, Gas Flow (stp) 1.9 l/sec

5.3 Liquid Phase Hydrodynamics

Section 2.6.1 focused on fluid flow, detailing the two ideal types of flow and how in reality the actual fluid flow through process equipment will deviate to varying degrees from the two ideal scenarios. In rotating contactors the ideal liquid flow through the packing would be plug flow, as any backmixing will lead to a drop in the overall mass transfer performance, but as demonstrated by the experimental findings the mass transfer results at the half and full packed lengths are not consistent with plug flow (Sect. 6.5), and therefore the assumption of plug flow needs to be examined. A common technique used in the characterisation of flow through process equipment is inject a tracer in a known manner, i.e. step change, pulse, sinusoidal wave etc., and by recording the tracer leaving the system (see Fig. 5.1), the nature of the actual flow may be described by comparison of the output to the input wave.

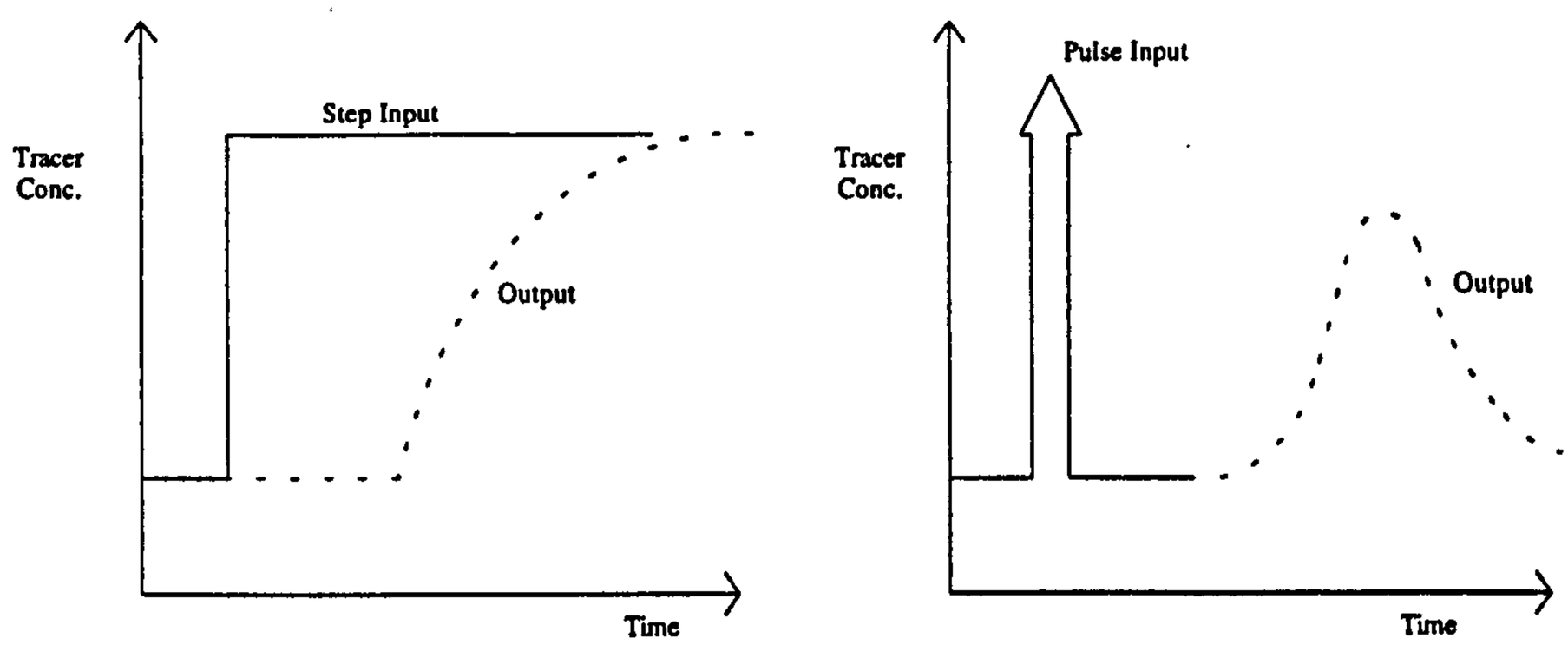

Figure 5.1 : Typical Tracer Response to varying Input Signals

A convenient method used in the analysis of the output of the tracer from the vessel is the exit age distribution of the elements of tracer fluid. This age distribution is commonly known as the Residence Time Distribution (R.T.D.), and is expressed such that the area under the curve is equal to 1. This procedure is called *normalising* the distribution.

The tracer is a fluid that has a property different to that of the actual fluid passing through the system, and typical properties that are used are pH value, conductivity, and optical attenuation. Both a pH meter and conductivity probe were tested, but the typical response time of the pH probe was in the order of seconds due to the diffusive mechanism that takes place across the probe membrane, and although the conductivity probe had a faster response time it was not sensitive enough and little output registered on the plotter. Also the use of an acid or salt solution in the rotor was impractical as the rotor is made from aluminium and would therefore be susceptible to corrosive attack. As the required response needs to be fast and sensitive, it was decided that a dye and optical sensor would be the most suitable tracer method to use.

The design details and specifications for the equipment used in the tracer work have been described in section 3.3.5.4. Due to the light sensitivity of the diode, the diode and light

source have to be enclosed and mounted so that their positions are fixed, and that the diode receives a constant light intensity (see Fig. 3.17). Figure 3.18 shows the response characteristics for the silicon photo diode used, and as can be seen the diode can accurately respond at frequencies up to 5000 Hz (0.0002 sec). The dye used in the work is of critical importance and a number of commonly used dyes such as methyl blue and potassium permanganate were tried although it was found that the diode only gave response for a narrow range of concentrations. Nigrosine, a water soluble black dye was tried which gave a response for a much larger range of concentrations especially at very dilute concentrations, and this dye was chosen for the tracer experimental work.

5.3.1 Calibration of Optical Diode

Having built the sensors and found a suitable dye, the sensors had to be calibrated using the nigrosine dye. Figure 5.2 shows the calibration curve for the sensors, which was found operating the light source from a 12V d.c. supply. The zero threshold of the diode was set at the point at which ordinary water produced an output response from the diode just on the zero limit, and this point set the light intensity of the bulb. The maximum output from the diode was found to be 10.15V which occurred when the light from the bulb source was no longer able to penetrate the dye.

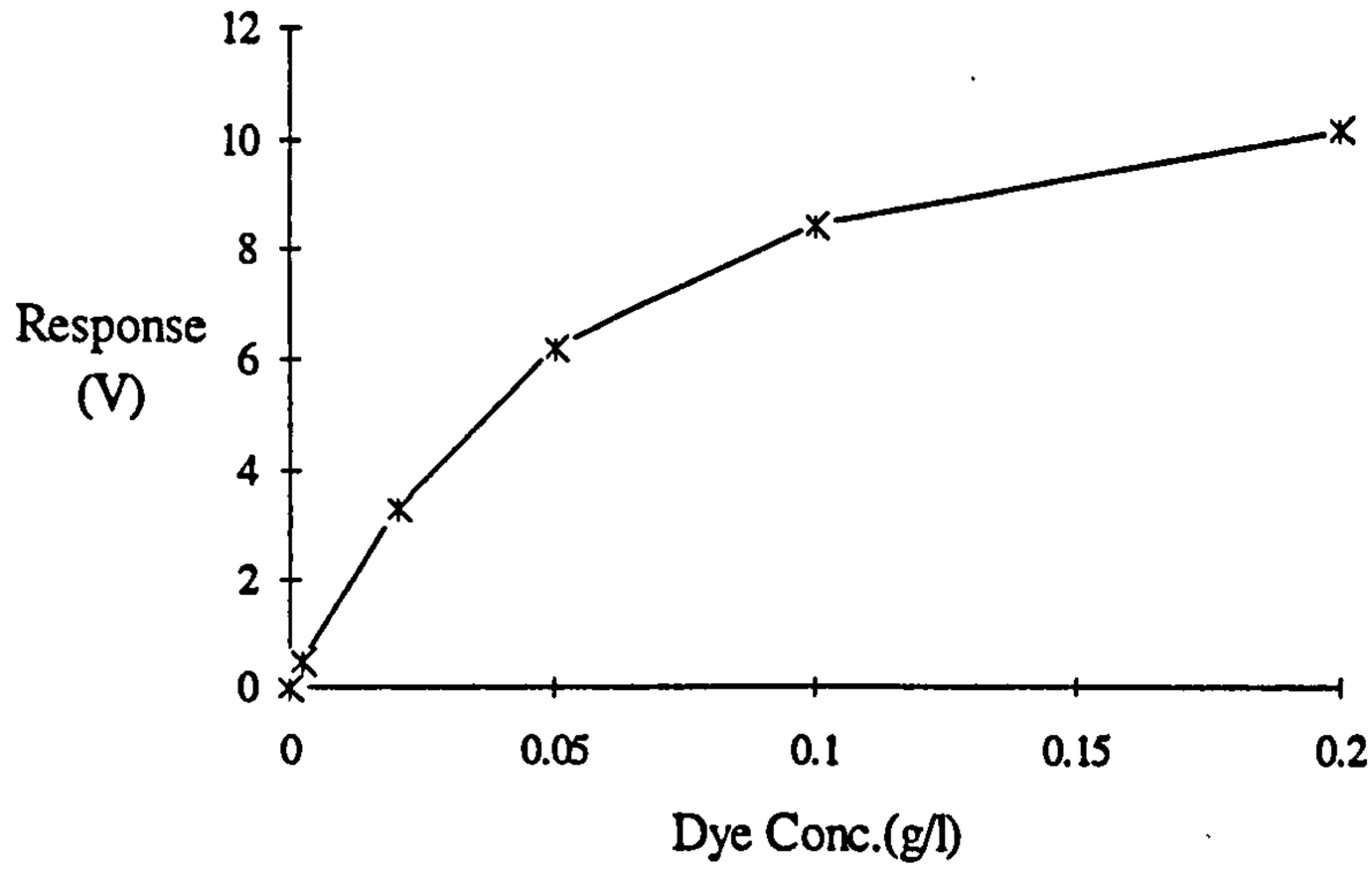

Figure 5.2 : Sensor Calibration Curve using Nigrosine Dye

5.3.2 Data Processing and Analysis

The output from the diodes were recorded and logged using the Amplicon DASH300 software package Windows version 2.1. This data logger was able to deal with a maximum of 15 input channels, record up to 16000 data points, and have a minimum sample interval of 0.0005 sec. For all the tracer runs carried out on the rotor two channels were used, one to log the input tracer signal and the other to log the output response. 8000 data points for each channel were recorded at 0.015 sec intervals and so the total time for each run was 4 minutes.

However, the output data is in millivolts, and so the data needs to be converted back into units of concentration (g/l). In order to re-convert 16,000 data points from millivolts to grams/litre, the calibration curve x-y co-ordinates need to be switched around and the curve mapped by a mathematical equation. Using a mathematical software package MATLAB, the curve was found to be accurately mapped by the following polynomial of degree 5 :

$$y=(48.43\times10^{-4})x-(6.81\times10^{-4})x^2+(5.90\times10^{-4})x^3-(1.06\times10^{-4})x^4+(6.79\times10^{-6})x^5 \quad 5.1$$

The input / output data sets were then evaluated using equation 5.1 in Matlab so that the data was transformed from millivolts into grams/litre. Finally as each sample was taken at 0.015 sec intervals a time scale can be found from the sample number. It should be noted that all the output results displayed in subsequent sections have had the time scale adjusted so that for each run the input tracer entered the rotor at time = 0.

5.3.3 Experimental Results

The input optical sensor was mounted in-line immediately before the liquid rotary union joining the stationary input line to the rotating shaft of the rotor. The response tracer was taken from the rotor using the sampling system detailed in sect. 3.3.5.3, with the optical sensor mounted after the sample collection chamber. The aim of the work is to determine the liquid hydrodynamics in the packing of the rotor, but due to the rotating machinery and the position of the sensors being outside of the rotor, the resulting output tracer response will also include any mixing that may take place along the rotor shaft or in the sample line. The first task was therefore to try and quantify these "end effects", so that the amount of backmixing actually occurring in the packed section of the rotor can be determined.

5.3.3.1 End Effects

Experimental liquid volumetric flows through the rotor range from 0.1 - 0.5 l/sec which therefore gives a range of residence times of the liquid in the shaft of the rotor of between 1.1 - 5.5 secs, assuming that the shaft runs full of liquid. There is no way of quantifying the amount of mixing that will take place in the shaft, although as the residence time is very short especially at the higher liquid flowrates, the amount of mixing taking place in the shaft compared with the overall mixing in the rotor itself can justifiably be assumed negligible.

The sampling system also had to be examined to see if any further mixing of the tracer took place between the packed section and the output optical sensor. In order to do this, two different sampling rates of 150 cc/min and 300 cc/min were used for an identical run, i.e. the same input tracer and rotor operating conditions. If the residence time distributions from these two samples are identical then it can be assumed that plug flow exists in the sampling line at

these flowrates, and therefore any mixing takes place in the rotor packing. Figure 5.3 shows the two outputs from the rotor at the two sample flowrates.

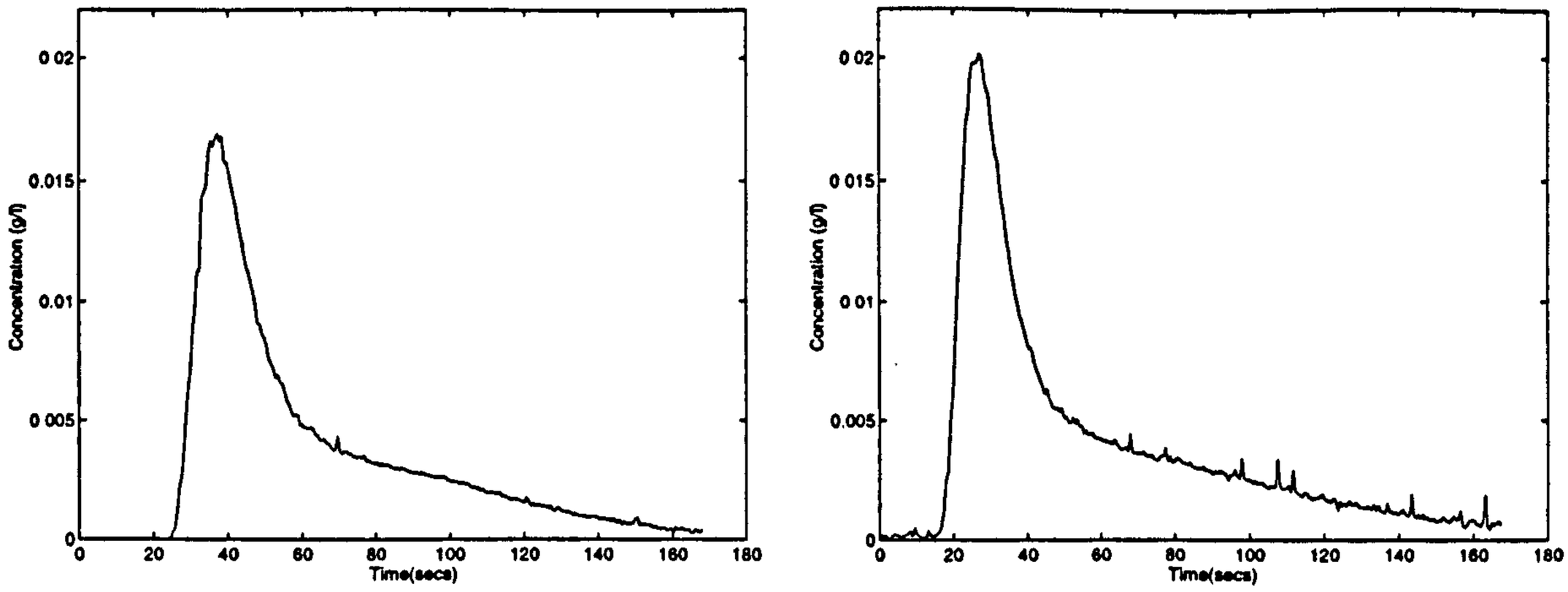

(i) Sample Flow - 150 cc/min (ii) Sample Flow - 300 cc/min

Figure 5.3 : Tracer Outputs from Rotor using Different Sampling Rates

Figures 5.3(i) and (ii) are not directly comparable as they sample at different rates, and therefore more tracer will be pulled through the sensor at the higher flow. This was confirmed using a mathematical software package, MathCad, which found the areas under graphs (i) and (ii) to be 0.554 and 0.645 respectively. In order to directly compare the curves, they need to be converted into Residence Time Distribution curves which is achieved by normalising the outputs, i.e. dividing the output by the area under the graph (Figure 5.4(i)). Due to the sample flowrate difference, the residence time in the sample line will vary and hence this accounts for the faster response of curve 5.3(ii). By shifting the normalised response curves over one another the curves can be directly compared as shown in Figure 5.4(ii).

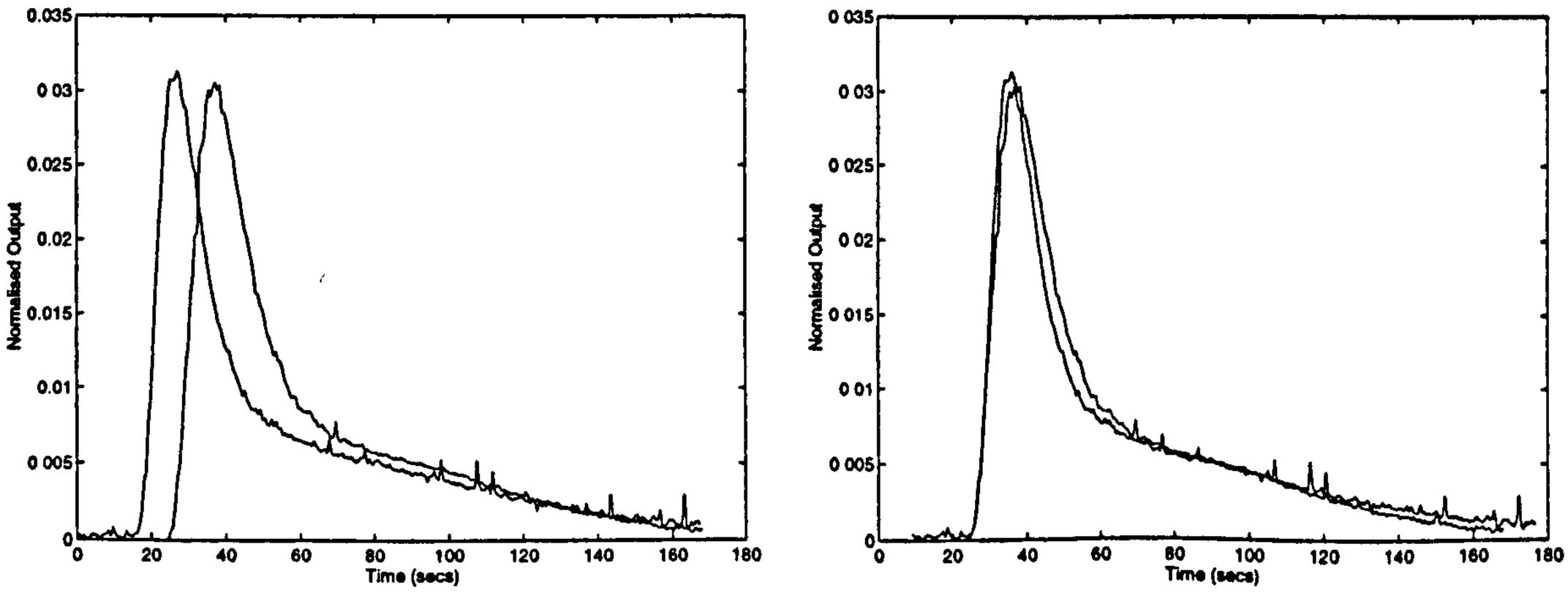

(i) Normalised Response (ii) Curves Mapped on One Another

Figure 5.4 : Normalised Response of Tracer

From Figure 5.4(ii) it can be concluded that the sampling rate has minimal effect on the R.T.D. of the tracer in the rotor, and therefore any further mixing in the sample line is very small. It can be concluded that the "end effects" are negligible and can be assumed negligible compared with the mixing in the rotor packing. An arbitrary sample flow of **200 cc/min** was chosen for all the tracer experimental work.

5.3.3.2 Tracer Input Signal

The experimental set-up for inputting the tracer into the rotor has been detailed in section 3.3.5.4. Fig. 3.15. The system is designed so that a 40 ml pulse of dye can be injected into the rotor. The inlet line to the rotor has a 3-way valve so that the bypass line can be filled with the dye, and at a given time the water flow diverted through the bypass line so that the 40 ml of dye is injected as a plug into the rotor. The concentration of the nigrosine dye used in all the experimental work was 2 g/l, which gave good output responses for all experiments. The input signal should therefore typically be a square wave, and figure 5.5 shows the recorded input tracer signal of the dye into the rotor.

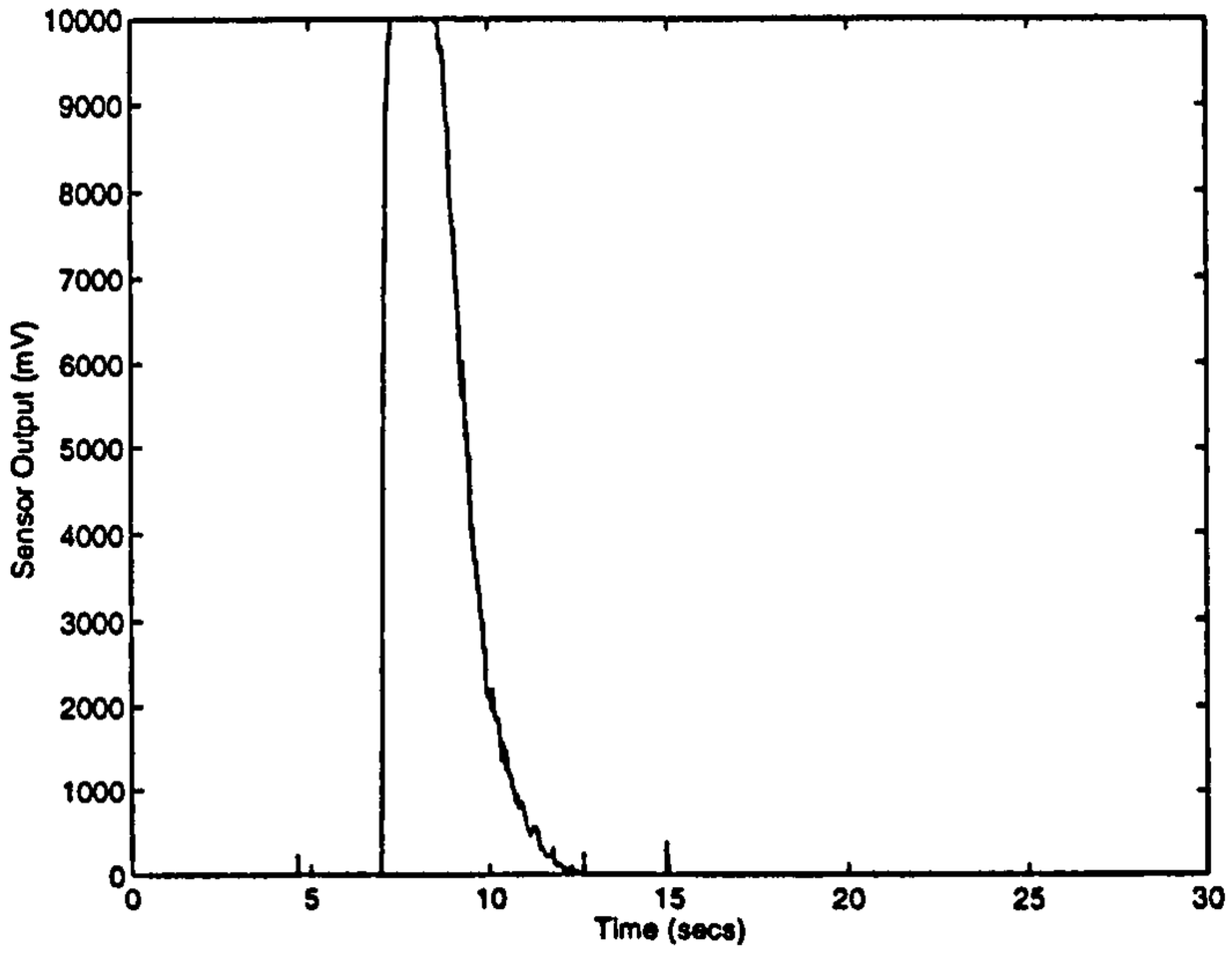

Figure 5.5 : Recorded Input Tracer Signal into the Rotor

The input signal is close to that of a square / pulse wave and this input signal is used in all the tracer work, from which all of the output responses seen in following sections are produced. The output has been left displayed in millivolts as the concentration of the input dye exceeds the calibration curve range.

5.3.3.3 Initial Tracer Output Response

The initial tracer output results were taken with the sampling system described in section 3.3.5.3., and therefore are taken at single points within the packing at the full, 3/4, 1/2, and 1/4 radial packed lengths. Figure 5.6 shows the initial tracer output responses from the rotor using the Declon HC20 packing, with operating conditions of 300 rpm, liquid flow 0.1 l/sec, and a gas flow of 1 m^3/hr nominal (or 0.4 l/sec at s.t.p.). All of the graphs are displayed with a time scale such that the input tracer into the rotor entered at a time, t = 0.

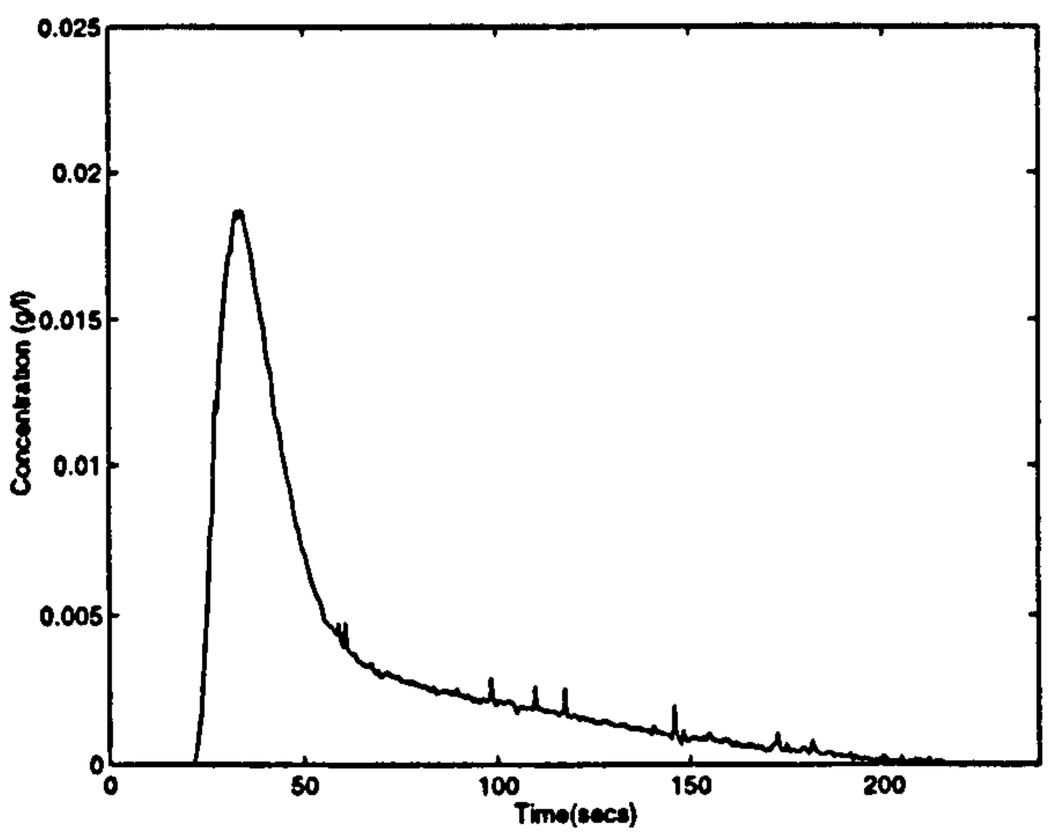

(i) Full Radial Length

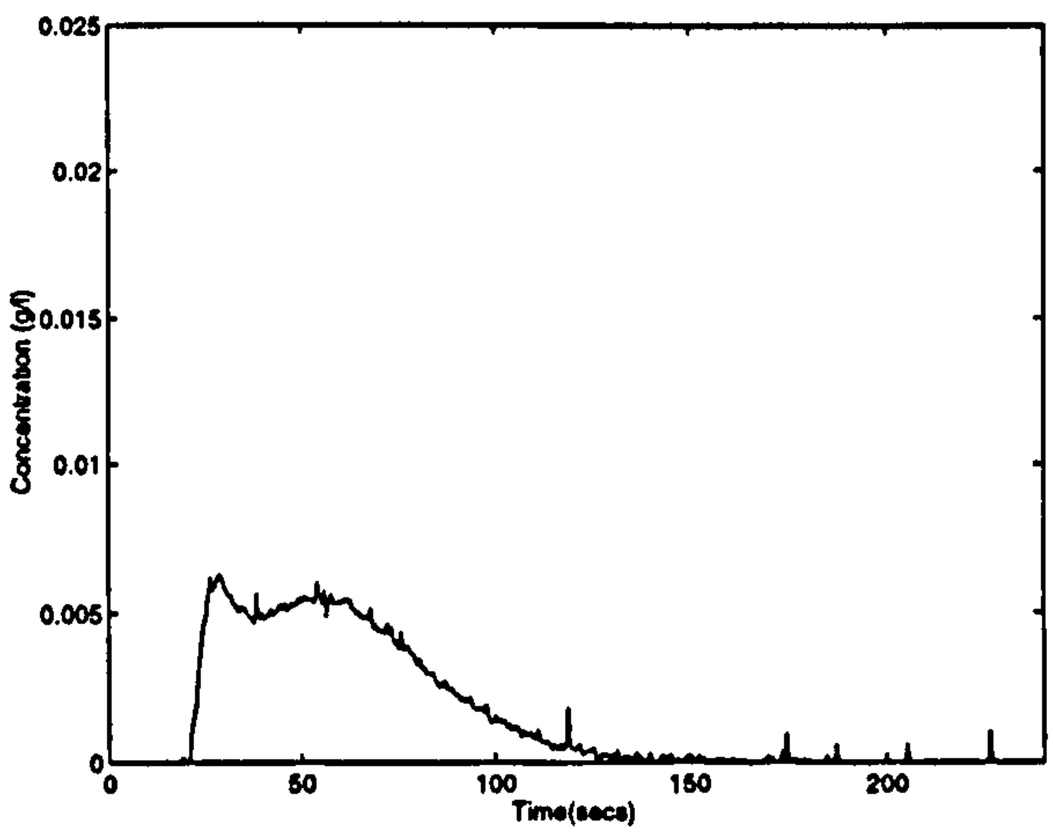

(ii) 3/4 Radial Length

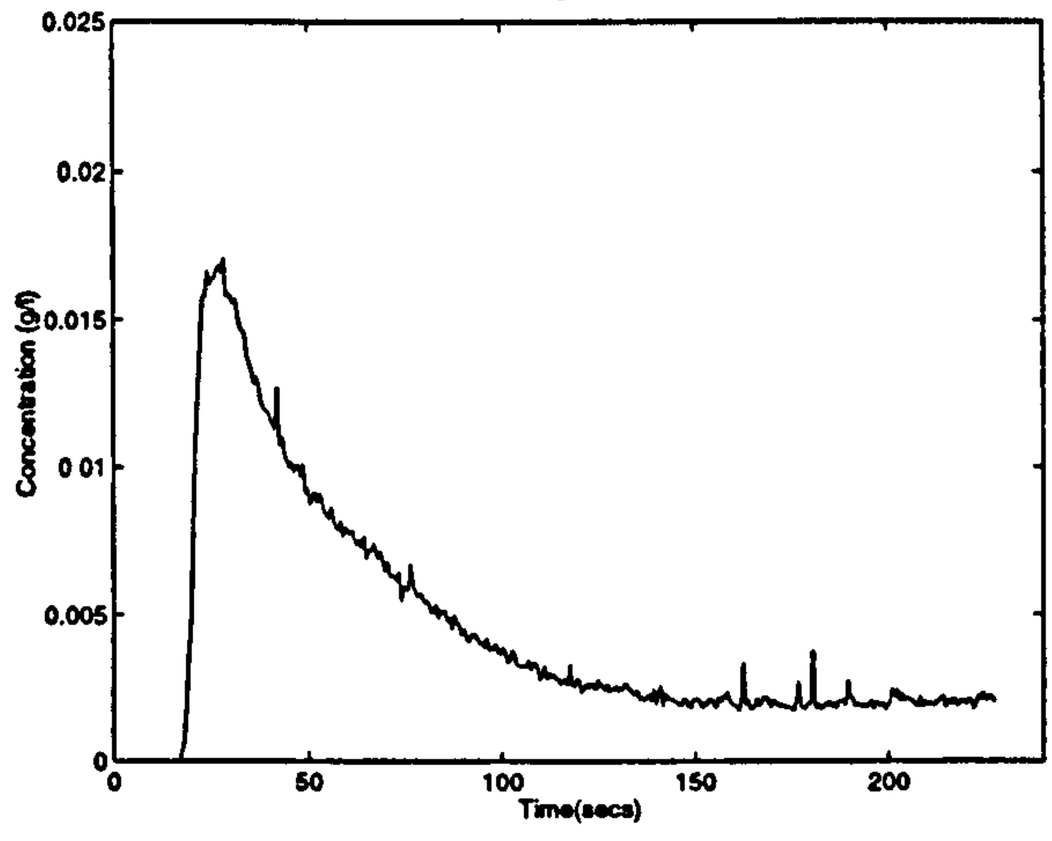

(iii) 1/2 radial Length

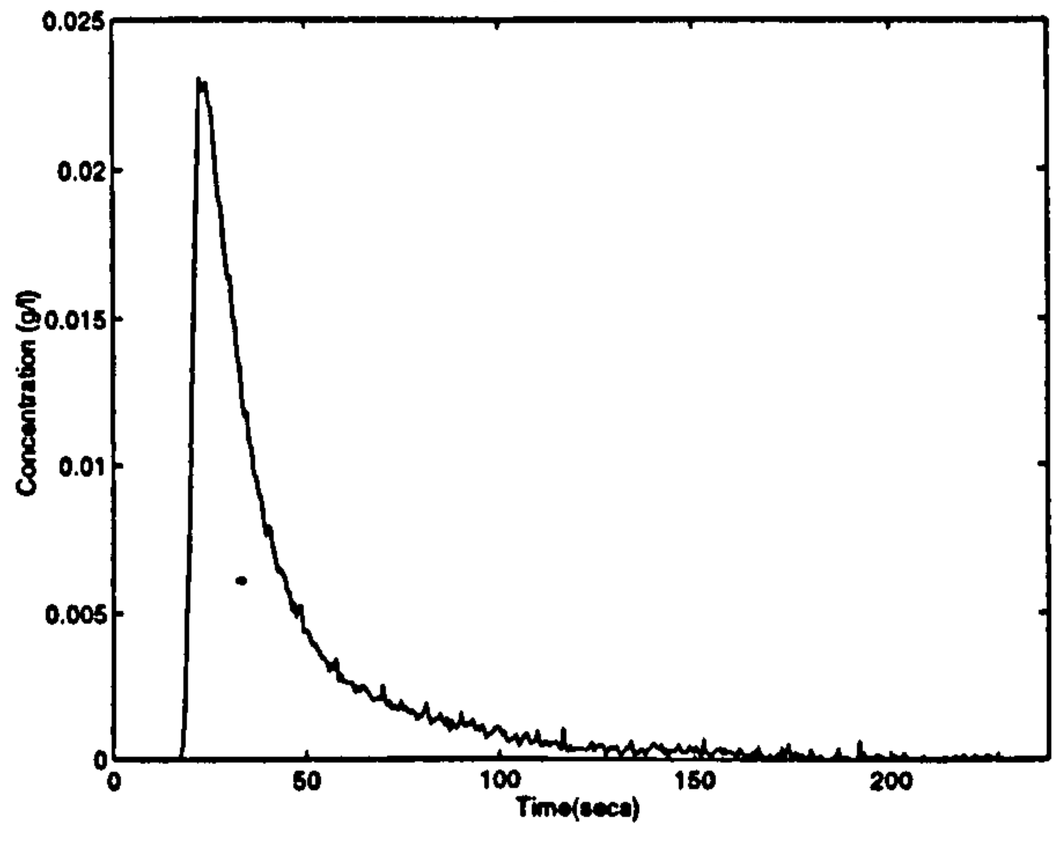

(iv) 1/4 Radial Length

Figure 5.6 : Tracer Output from Different Radial Positions within the Rotor

As can be seen from Figure 5.6, the response curves vary considerably and no obvious pattern can be seen relating the response to the packed length. Therefore this would suggest significant maldistribution of the liquid flow throughout the rotor packing. It may also be likely that sampling at the one circumferential point at each radial depth may not be representative of the entire radial depth.

5.3.3.4. Output Tracer Response at Full Packed Length

Having showed the variations in the liquid flow through the rotor, and that sampling at any singular point will not give an accurate picture of the complete rotor, the sample positions were modified so that the 4 sample tubes *all sampled at the same radial length* and at 90° to each other. Figures 5.7, 5.8 show the variations in the tracer response around the machine all sampled at the full radial packed length, and examines specifically the effect of the liquid flowrate through the machine on the response. Again all graphs can be directly compared as the response is shown for the tracer entering the rotor at a time, t = 0.

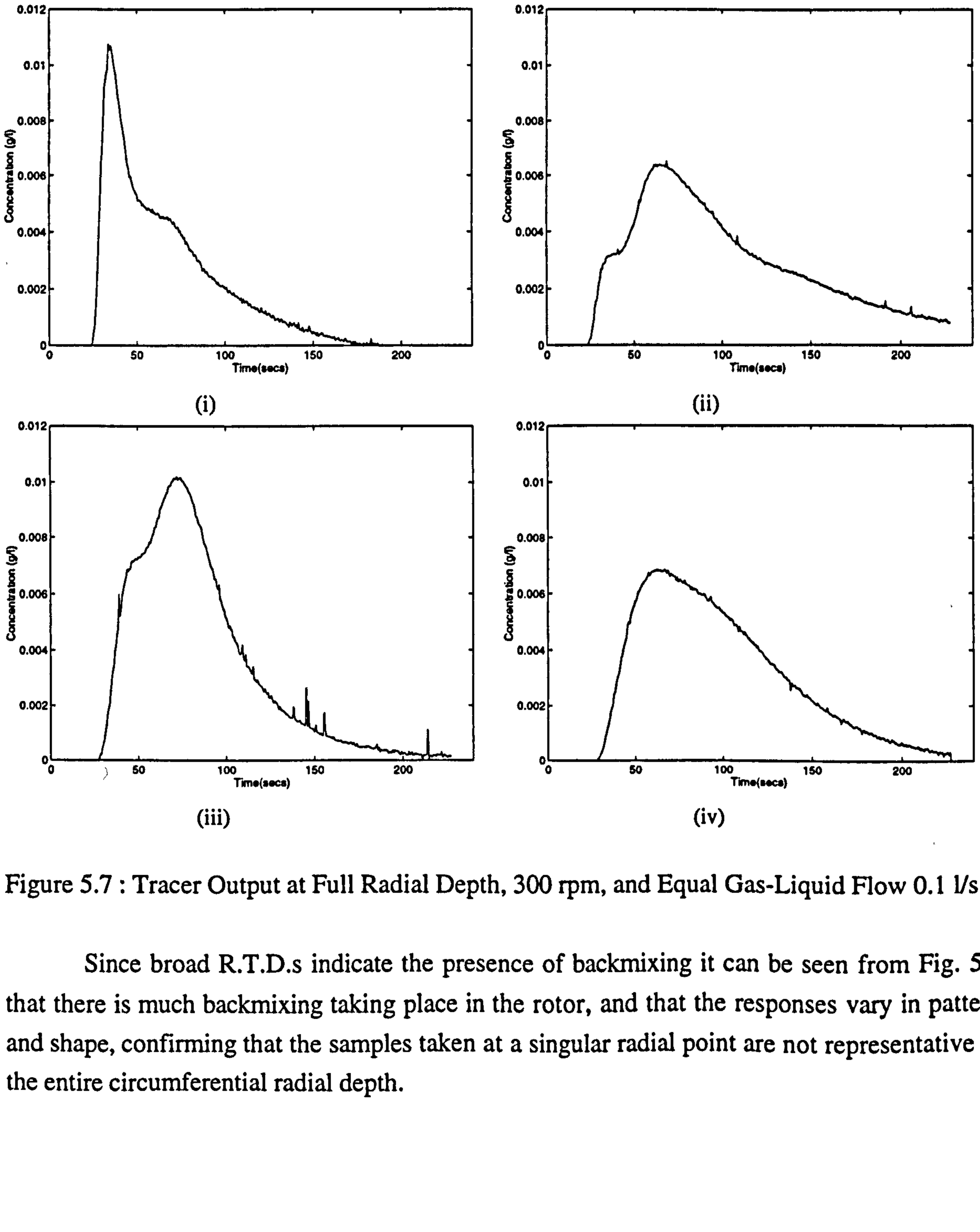

Figure 5.7 : Tracer Output at Full Radial Depth, 300 rpm, and Equal Gas-Liquid Flow 0.1 l/s

Since broad R.T.D.s indicate the presence of backmixing it can be seen from Fig. 5.7 that there is much backmixing taking place in the rotor, and that the responses vary in pattern and shape, confirming that the samples taken at a singular radial point are not representative of the entire circumferential radial depth.

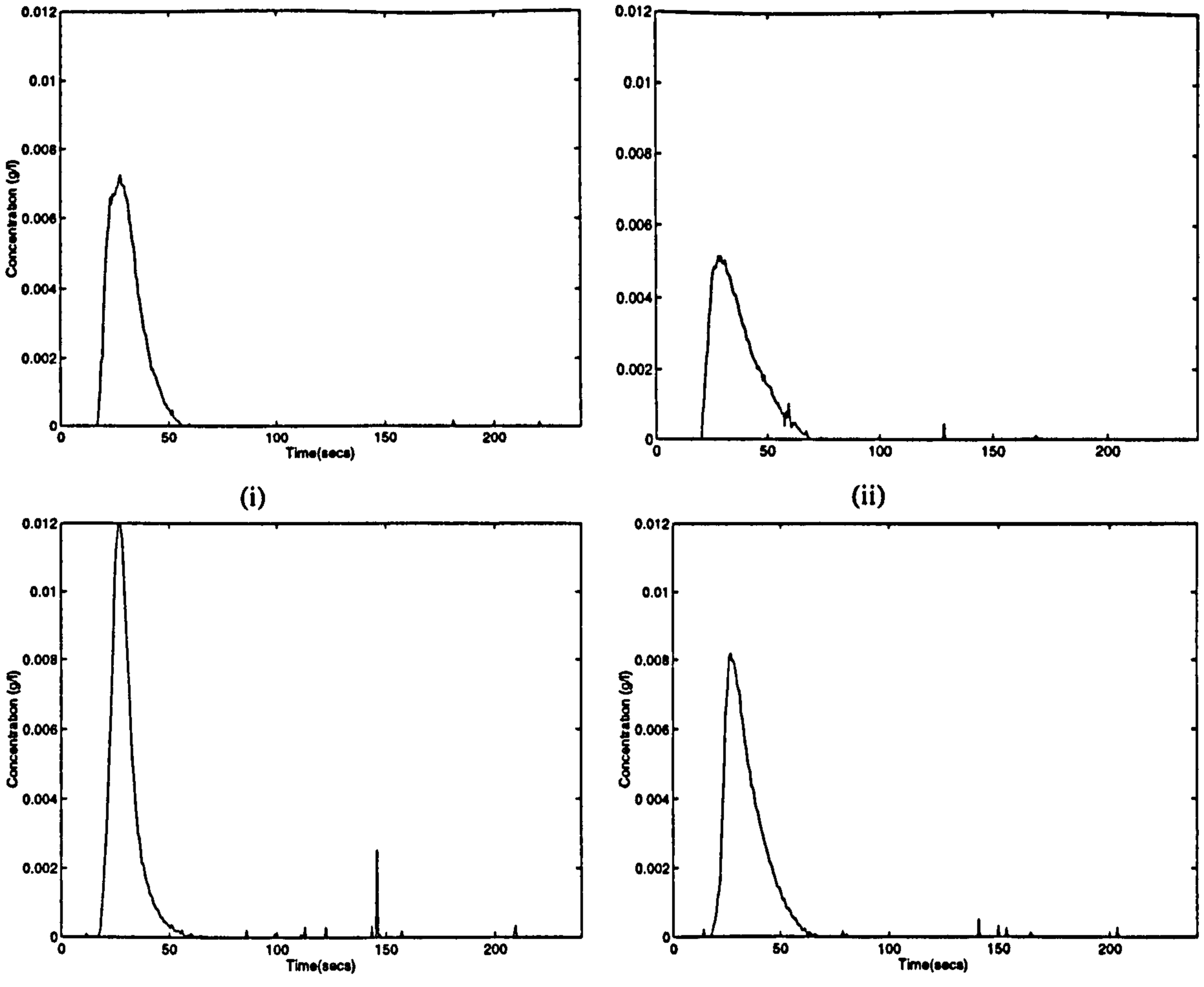

Figure 5.8 : Tracer Output at Full Radial Depth, 300 rpm, and Equal Gas-Liquid Flow 0.5 l/s

Figure 5.8, in contrast to Figure 5.7, shows a much more regular pattern in the responses around the machine for equal gas to liquid flowrate ratios, with the graphs at the 0.5 l/sec flowrate showing significantly reduced backmixing, and a flow pattern much closer to that of plug flow. It can therefore be concluded that at higher liquid throughputs, the liquid flow approaches a much more uniform distribution throughout the rotor, and exhibits liquid hydrodynamic characteristics closer to true pug flow.

However improved the distribution at the higher liquid flowrates is, it would be more representative as a whole to sample the tracer at all 4 positions around the radial depth simultaneously. The graphs displayed in Figure 5.9 for the denser Declon packing, are a representative sample of the rotor as a whole (i.e. sampled simultaneously from all 4 positions), and show the effect of rotational speed, liquid and gas flowrate on the output tracer response of the rotor.

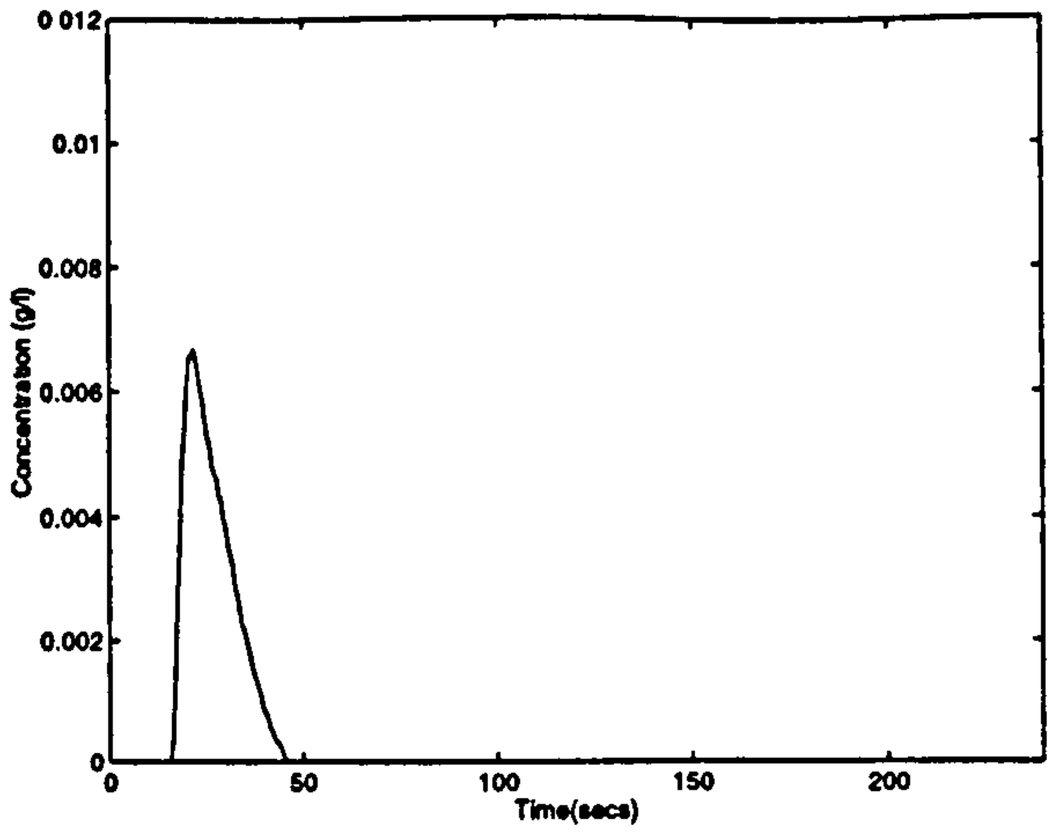

(i) Speed 300rpm, Liquid Flow 0.5 l/s, Gas Flow 0.4 l/s

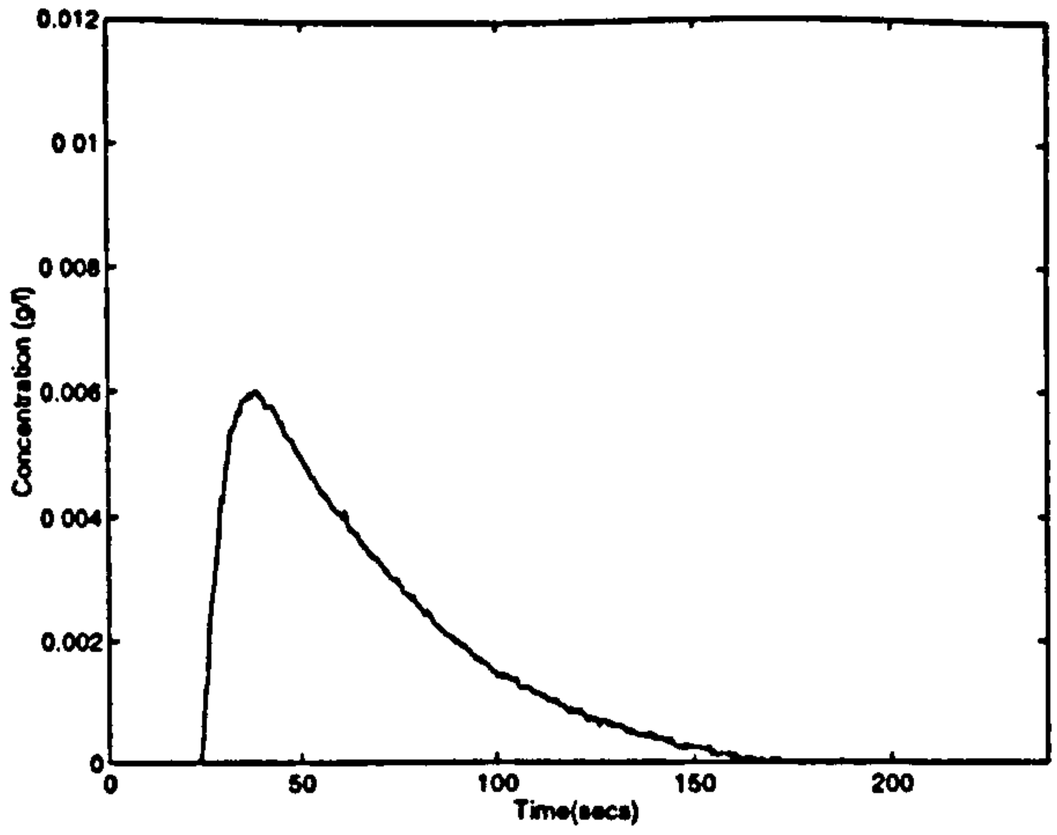

(ii) Speed 300rpm, Liquid Flow 0.1 l/s, Gas Flow 0.4 l/s

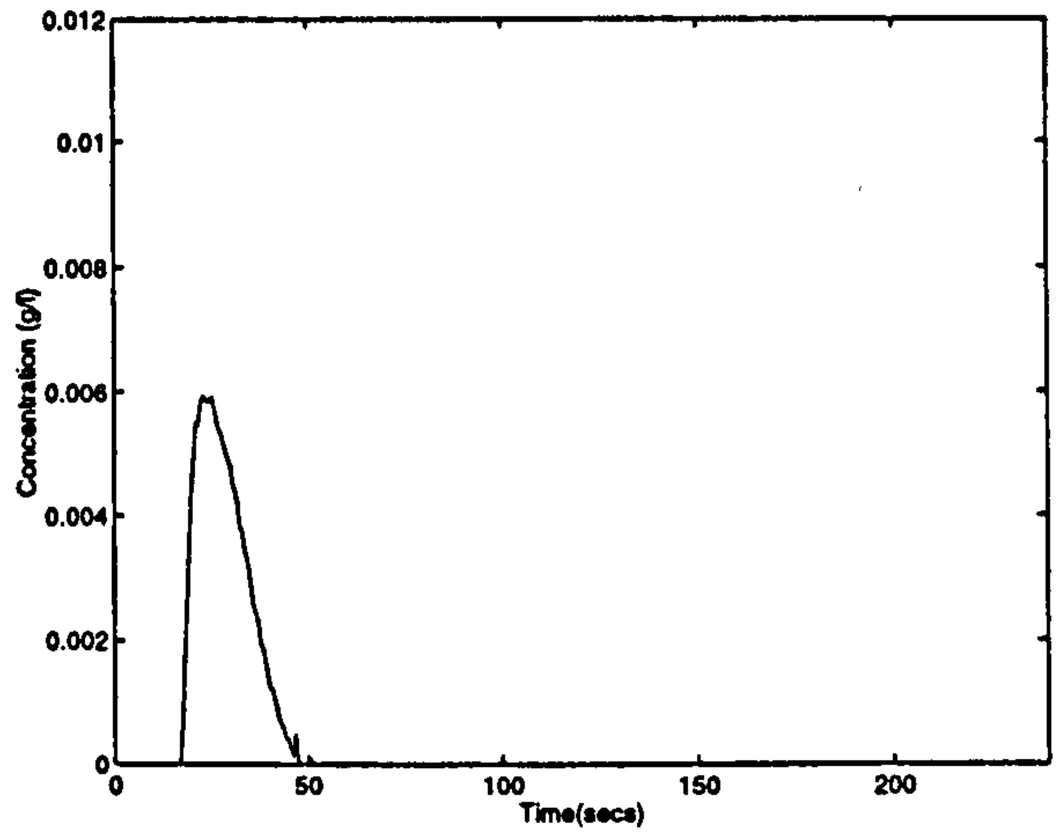

(iii) Speed 400rpm, Liquid Flow 0.5 l/s, Gas Flow 0.4 l/s

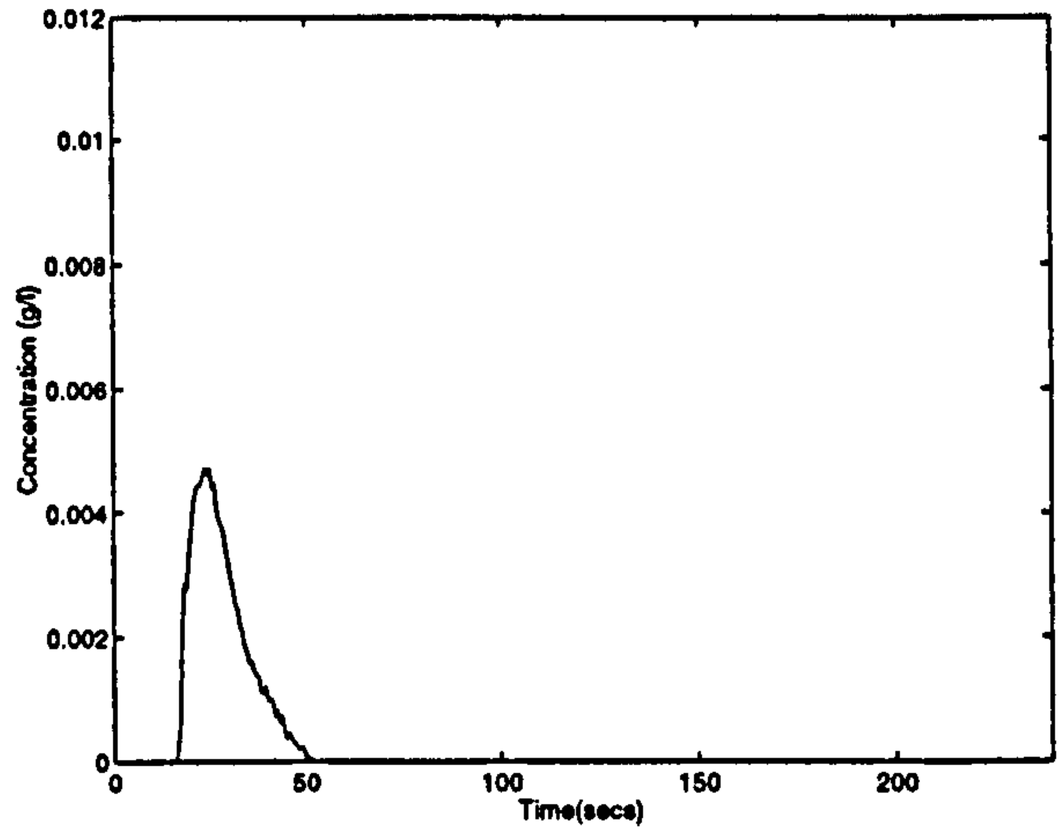

(iv) Speed 300rpm, Liquid Flow 0.5 l/s, Gas Flow 1.9 l/s

Figure 5.9 : Effect of Rotational Speed, Liquid and Gas Flow on Tracer Output, using Declon HC30 Packing

Graph(ii) stands out among the others, showing that for the rotor the liquid flowrate is the singularly most influential parameter on the liquid hydrodynamics. The speed of rotation seemed to have little observable effect although it was only increased from 300 to 400 rpm, which does not cover a wide range. The gas flowrate seems to only have small effect, and from observation appears to slightly extend the tail of the distribution. To quantify the effects of rotational speed, gas and liquid flow further, the above graphs have been converted into R.T.D. curves and mathematically modelled in section 5.3.4 using a multi parameter tanks-in-series model.

5.3.3.5 Output Tracer Response at 1/2 Packed Length

As well as the full packed length, 4 sampling points were then placed at the 1/2 packed length so as to compare the the tracer response at the 1/2 length with the full length. The graphs shown in Figure 5.10 are identical to those displayed in Figure 5.9, but are sampled at the 1/2 radial packed length rather that the full radial packed length.

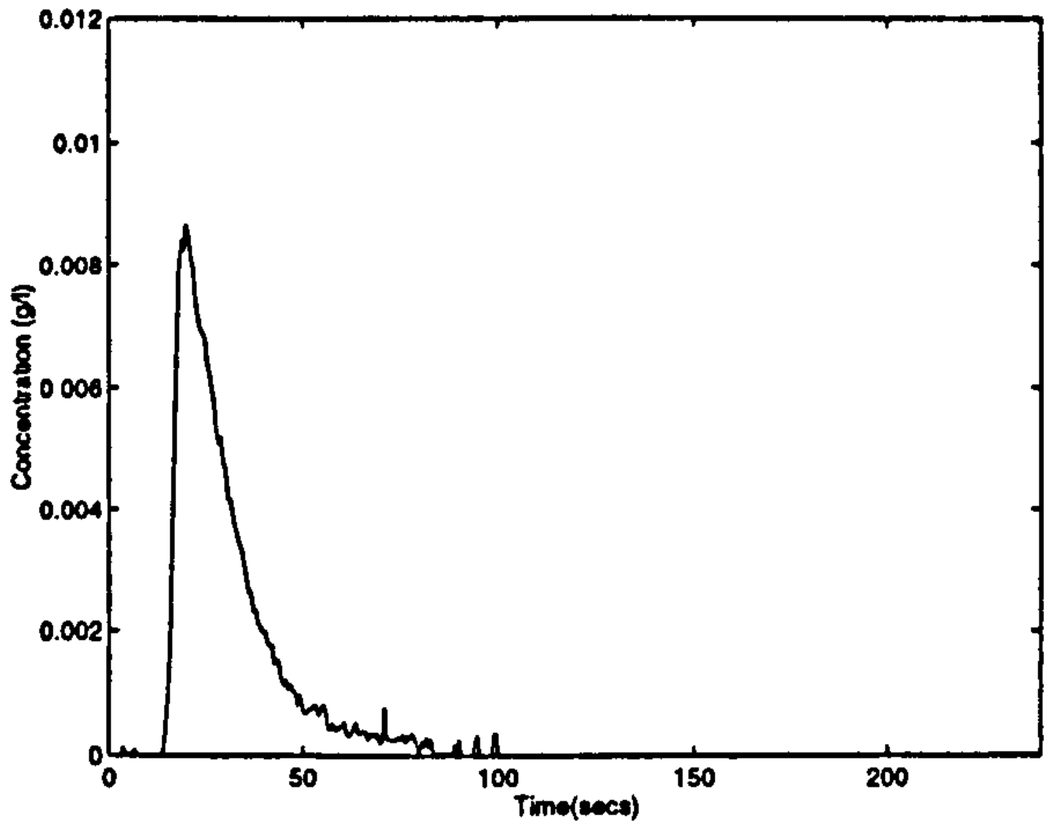

(i) Speed 300rpm, Liquid Flow 0.5 l/s, Gas Flow 0.4 l/s

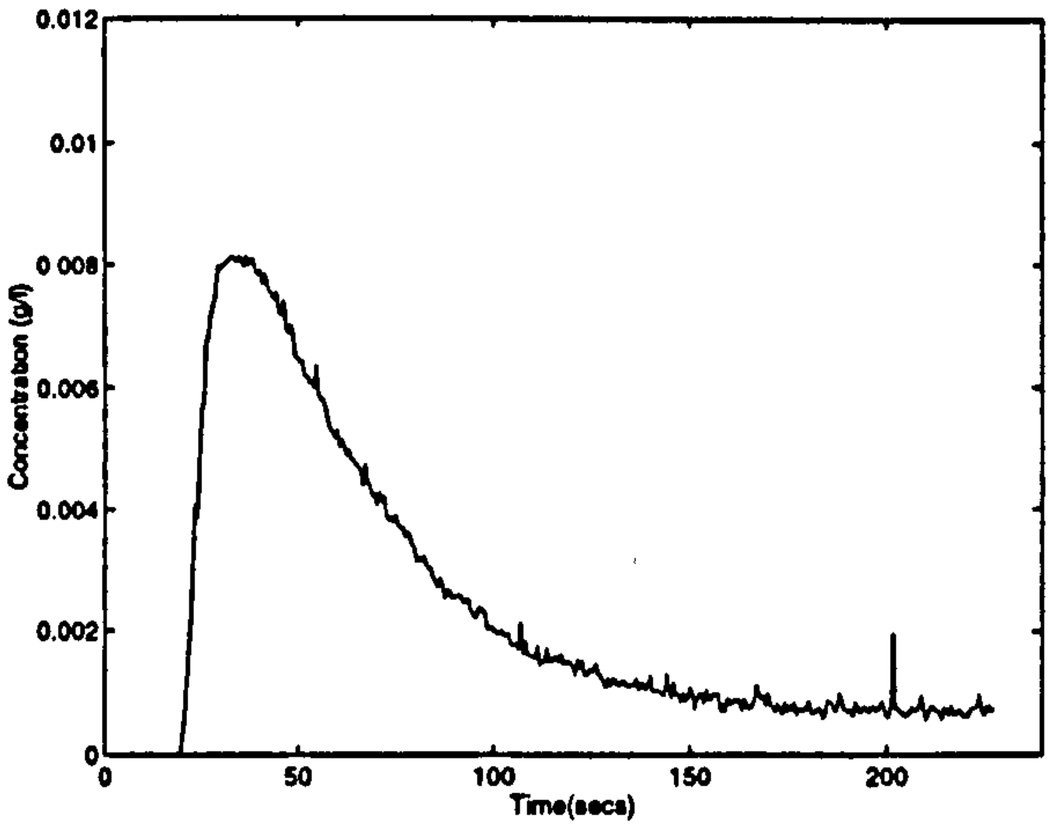

(ii) Speed 300rpm, Liquid Flow 0.1 l/s, Gas Flow 0.4 l/s

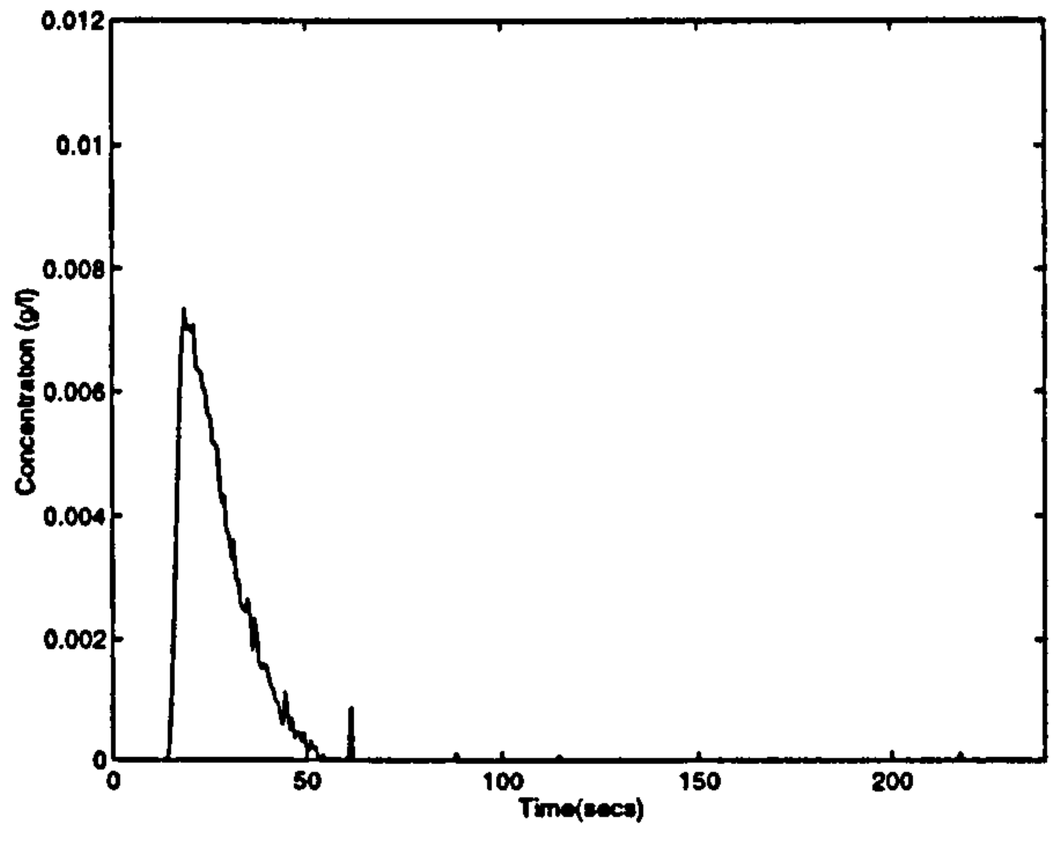

(iii) Speed 400rpm, Liquid Flow 0.5 l/s, Gas Flow 0.4 l/s

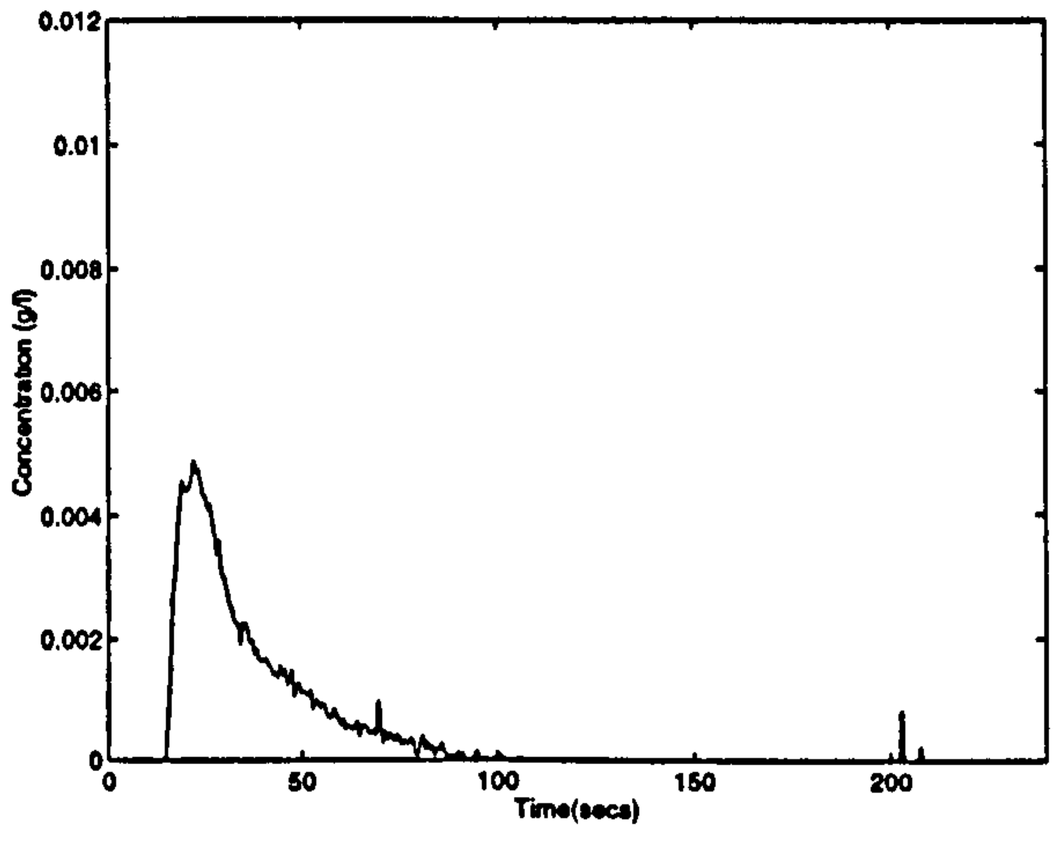

(iv) Speed 300rpm, Liquid Flow 0.5 l/s, Gas Flow 1.9 l/s

Figure 5.10 : Effect of Rotational Speed, Liquid and Gas Flow on Tracer Output, using Declon HC30 Packing

As one might expect, the patterns displayed in Figure 5.10 resemble very closely those of Figure 5.9. The response in graph(ii) does not fall to zero, and it is thought that this is likely to be attributed to a bubble attaching itself to the glass tubing in front of the sensor causing an offset. However the general response characteristics are very similar to those seen in 5.9(ii). The effect of the gas flow is more pronounced 5.10(iv), and although for the full packed length

it was thought to have extended the tail of the distribution, this is more clearly seen at the 1/2 packed length.

5.3.4 Mathematical Modelling

Although much can be observed from the experimental work shown in section 5.3.3., it would be helpful to quantify rather than just qualify the effects of the operating conditions of the rotor on the liquid hydrodynamics. In order to do this a mathematical model needs to be found to generally describe the output tracer response from the rotor, and various parameters of the model changed to fit the individual cases. The values of these parameters can then be used to quantify the effects of the rotational speed, gas and liquid flowrate.

Section 2.6.1 described in full the two ideal types of flow for items of equipment and models used to describe "real life" situations which deviate to greater and lesser extents from the ideal cases. The most commonly used models used to describe "real life" cases are the one parameter models such as the axial dispersion model and the tanks-in-series model, but when modelling the tracer outputs from the rotor using MathCad these models were found not to satisfactorily model the liquid phase hydrodynamics for all the range of operating conditions. Therefore a more complicated multi-parameter model was required, and the model described in section 2.6.1.2.3 (Fig. 2.14), which considers the liquid flow to behave as a series of CSTRs each with a deadwater region associated with it, was found to be a more accurate fit for the experimental data.

Equation 2.24 showed that for distributions for which most of the fluid is not delayed then the R.T.D. can be simplified to :

$$E(t) = f_0 E_{N(active)} + f_1\left(E_{N(active)} * E_{1(delay)}\right)$$

for which the R.T.D. for the active and deadwater regions, $E_{N(active)}$ and $E_{1(delay)}$ can be found from equation 2.22 :

$$E(t) = \frac{1}{\bar{t}}\left(\frac{t}{\bar{t}}\right)^{N-1} \frac{1}{(N-1)!} e^{-\left(\frac{t}{\bar{t}}\right)}$$

Substituting the active and deadwater residence times into the model leads to the following model equation for predicting the liquid phase residence time distribution in the rotor :

$$E(t) = f_0\left(\frac{1}{t_a}\left(\frac{t}{t_a}\right)^{N-1} \frac{1}{(N-1)!} e\left(\frac{-t}{t_a}\right)\right) + f_1 \int_0^t \left(\frac{1}{t_a}\left(\frac{\tau}{t_a}\right)^{N-1} \frac{1}{(N-1)!} \exp\left(\frac{-\tau}{t_a}\right)\right)\left(\frac{1}{t_d}\exp\left(\frac{-(t-\tau)}{t_d}\right)\right) d\tau \quad 5.2$$

where t_a and t_d are the mean residence times for the active and deadwater regions respectively, and τ a dummy variable over which the convolution between the active and deadwater regions

is evaluated. The tracer output responses shown in Figure 5.9 were taken, normalised to give the R.T.D. curve, and modelled by equation 5.2, the predicted results of which are shown in Table 5.1. The MathCad program used for the modelling of the tracer R.T.D. in the rotor can be seen in Appendix II, which shows the model to accurately map the experimental data points.

Table 5.1 : Model Predictions for Liquid Phase Hydrodynamics

Rotor Operating Conditions			Model Parameter Predictions					
Speed (rpm)	Gas Flow (l./sec)	Liquid Flow (l/s)	N	t_a	t_d	f_1	Nt_a	Nt_a^2
300	0.4	0.5	48	0.426	7.784	0.811	20.45	8.71
300	0.4	0.1	43	0.724	38.697	0.964	31.13	22.54
400	0.4	0.5	48	0.450	8.216	0.917	21.60	9.72
300	1.9	0.5	46	0.481	8.397	0.775	22.13	10.64

The model predicts the number of stirred tanks in series, N, the fraction of fluid that is delayed, f_1, and the mean residence times per tank in the active and deadwater regions, t_a and t_d respectively. As can be seen from Table 5.1, the value in each case for N is large, and therefore the approximation of the distribution as a Gaussian curve with exponential curve first proposed by Levich is valid (see Fig. 5.11). Therefore from the model parameters, the total mean residence time of the liquid through the active region, Nt_a, the variance of the liquid through the active region, Nt_a^2, the residence time of liquid delayed, Nt_a+t_d can be found. The average residence time of the liquid in the rotor could then be found from :

$$\bar{t}_{rotor} = (1-f_1)Nt_a + f_1(Nt_a + t_d) \qquad 5.3$$

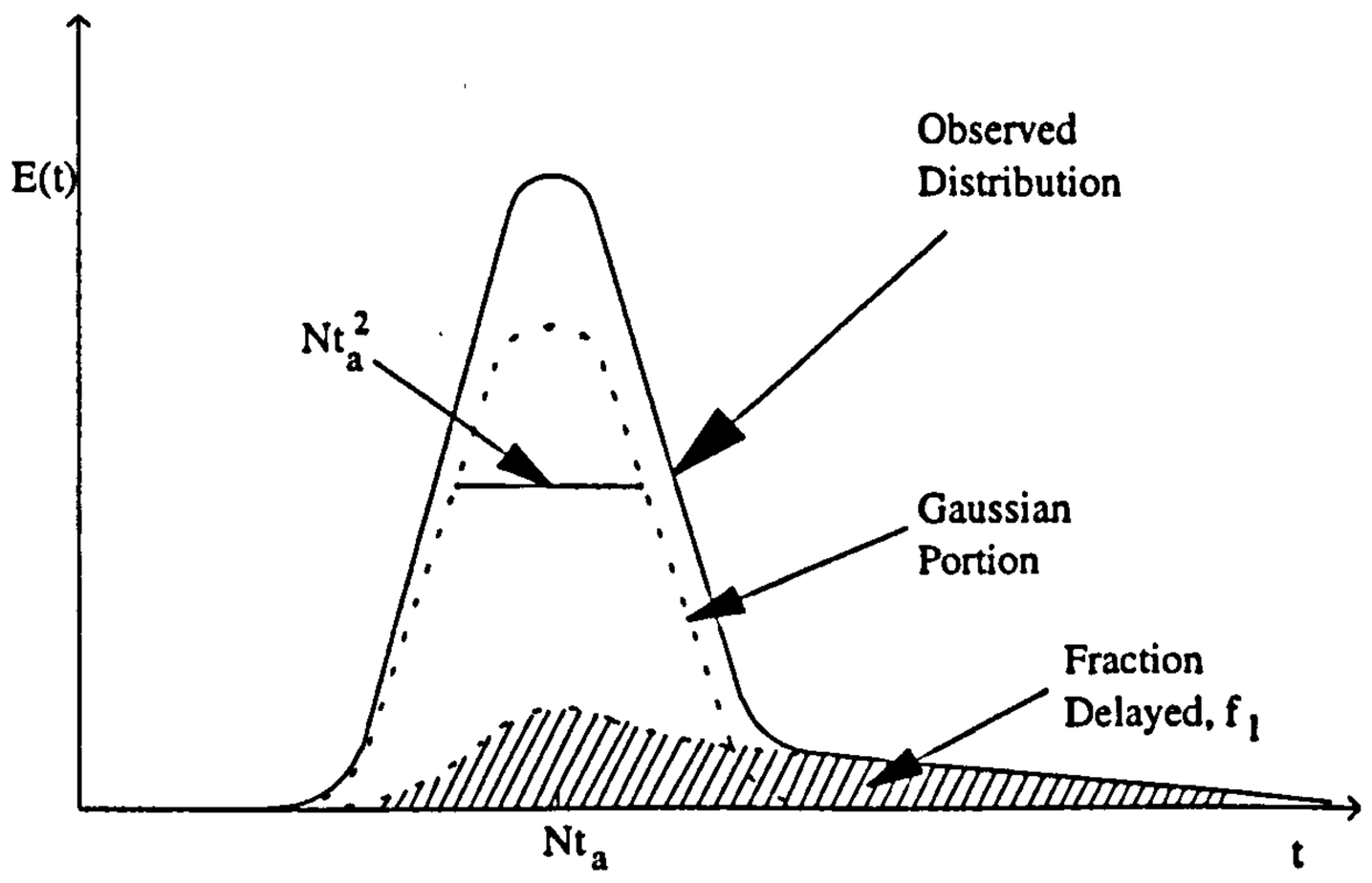

Figure 5.11 : Approximation of Observed Distribution by Gaussian Distribution with Exponential Decay Curve

The following conclusions about the effects of the various operating parameters on the liquid flow through the rotor can be found from Table 5.1 :

1. In all cases, N is large and Levich's approximation is valid and the model is able to describe each situation well.
2. The effect of the rotational speed and gas flow seem slight, although the increase in the gas flow marginally increases the values of t_a and t_d.
3. The liquid flowrate is the dominating parameter, as t_a, t_d, and Nt_a^2 are significantly higher at the low liquid flow of 0.1 l/s than for all other cases. Since Nt_a^2 measures the spread of the Gaussian part of the distribution and is related to the degree of backmixing, it can be seen that at lower liquid flowrates the degree of backmixing has been increased.
4. The fraction delayed, f_1, in all cases is higher than that probably expected, although at the high liquid flow the mean delay time, t_d, is significantly lower (approx. 8 secs) than that at the low liquid flow (approx. 38 secs).
5. From eqn. 5.3 the *average* residence time of the liquid in the rotor at the high liquid flow is around 28 secs, whereas at the lower flowrate it is 68 secs.

5.4 Gas Phase Hydrodynamics

As mentioned in the introduction to this chapter, a number of physical parameters are used to describe the phase hydrodynamics, the previous section detailing the type of flow that the liquid phase exhibits as it flows through the packing. This section looks at the gas phase, and the parameter concentrated upon in describing the hydrodynamics of the gas phase is the gas bubble size. Other parameters such as the gas bubble velocity and hold-up are intrinsically linked with the gas bubble diameter (see Sects. 2.6.3, 2.6.4), and hence this is the reason for focusing the experimental work on the gas bubble diameter.

Figure 5.12 shows the positions of the packing windows, which are small areas of the packing cut out for the specific purpose of examining the gas bubble size generated through the packed section of the rotor. Photographs 9 - 16 examine the bubble size generated from the original design of gas nozzles, through various radial positions in the packing (window nos. 2, 4, 9, and 12), looking at how the various rotor parameters effect the gas bubble size, and how the bubble size changes as the bubbles migrate through the packing towards the centre of the machine. Photographs 17 - 20 look at the bubble sizes produced using the modified gas nozzle design so as to be able to compare the effect of the new gas nozzle design with the original design on the average bubble size.

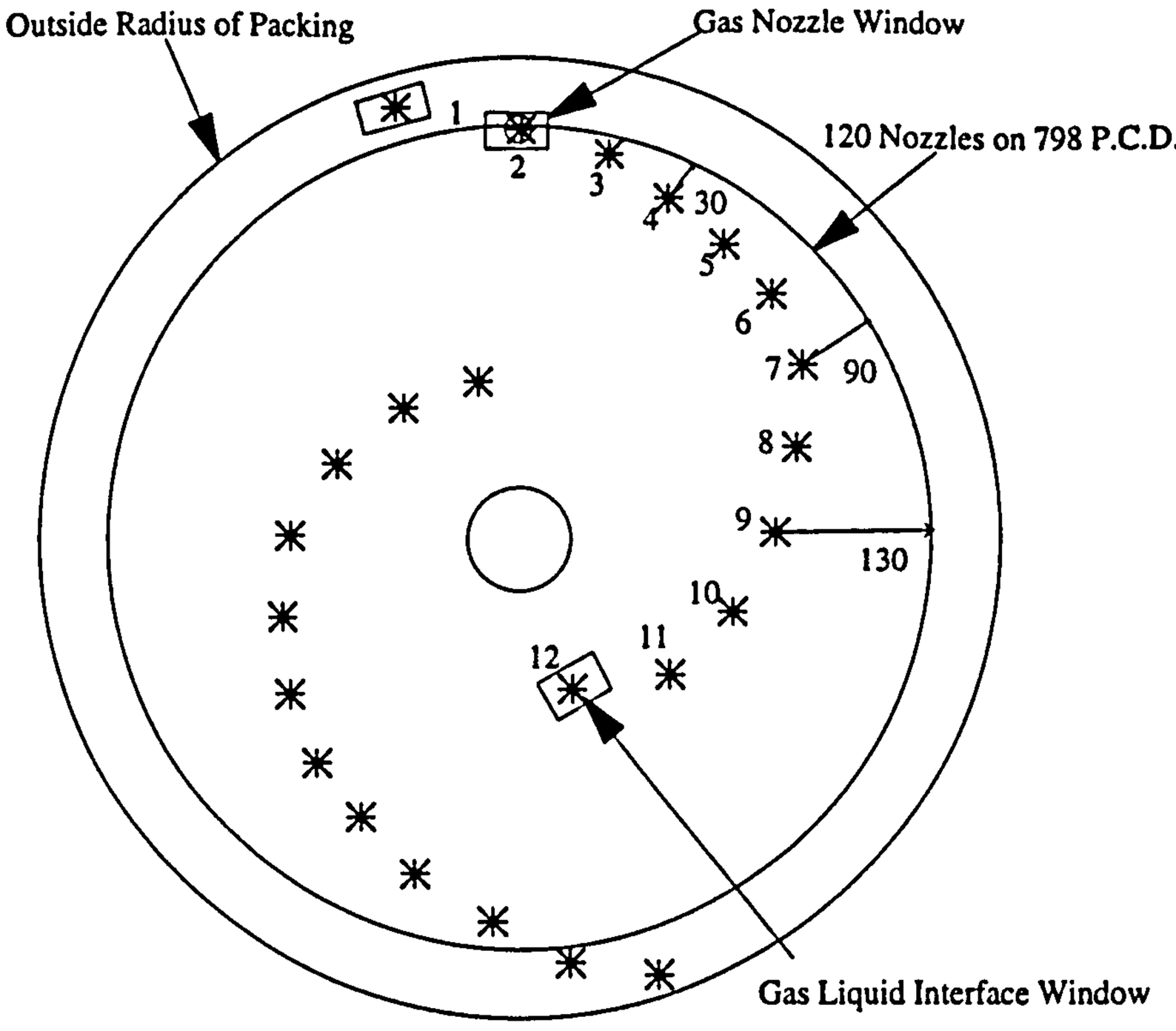

✳ - Position of Windows in Rotor Packing (Dimensions in mm)

Figure 5.12 : Diagram to show Positions of Packing Windows

Table 5.2 shows the approximate average values for the bubble sizes shown in photographs 9 - 20. An average sized bubble is chosen and the size measured by ruler and divided by the magnification, which is found from knowing the actual dimensions of the windows shown. The ratio of the actual length to the measured length in the photograph gives a value for the magnification. A rough estimate may also be found from the packing pore size, as the photographs are all taken with the Declon HC20 packing which has a nominal pore size of 1.27 mm.

Table 5.2 : Average Bubble Sizes produced in the Declon HC20 Packing

Photograph No.	9	10	11	12	13	14
Window No.	2	4	9	9	9	12
Average Bubble Size (mm)	-	-	0.5	0.7	0.9	0.5

Photograph No.	15	16	17	18	19	20
Window No.	12	12	4	9	9	12
Average Bubble Size (mm)	0.7	0.9	0.3	0.6	0.4/0.5	0.8

GAS NOZZLES

WINDOW

GAS BUBBLES

WINDOW

PACKING

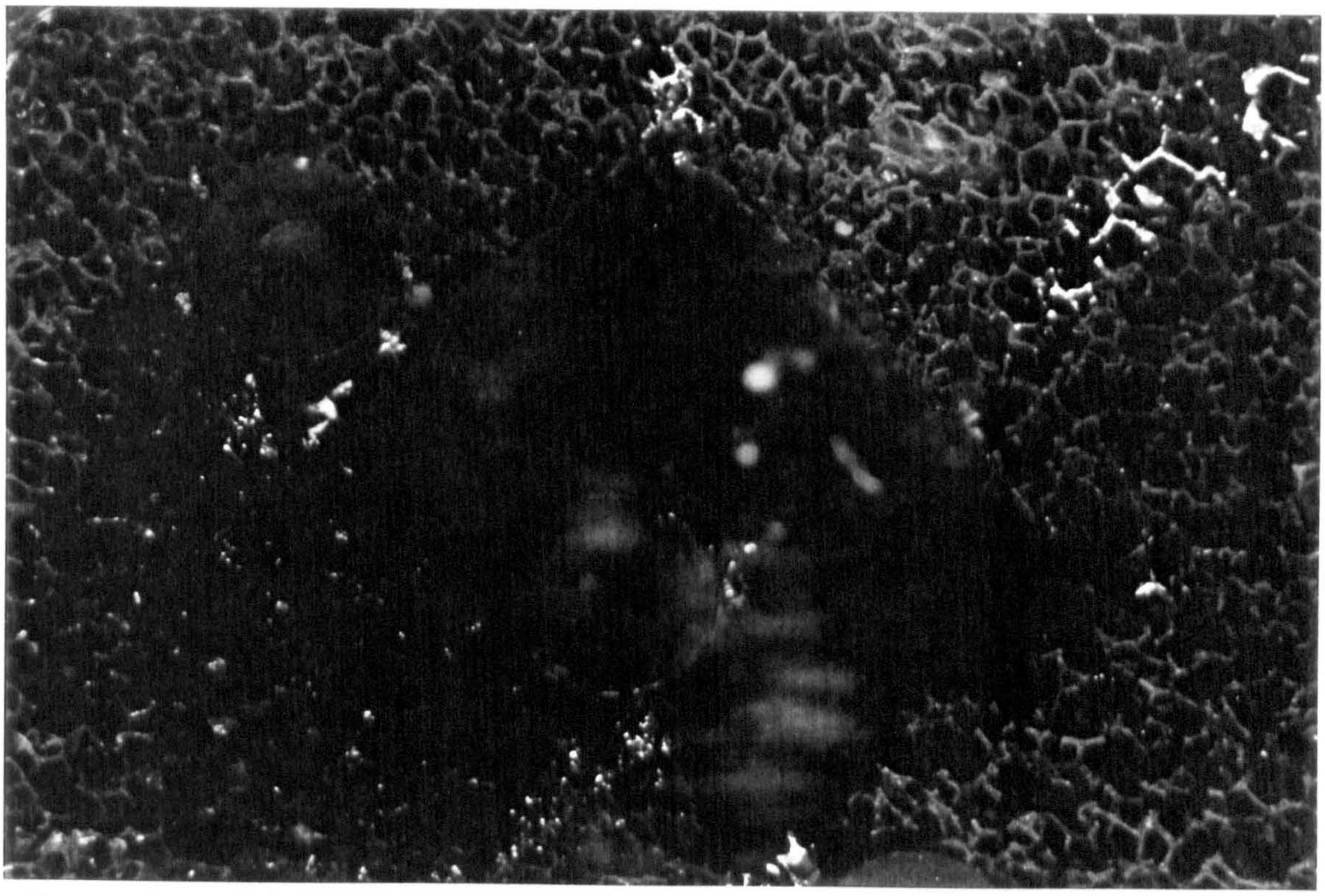

Photograph No.9 : Window No.2 : *Gas Injector Nozzle*
Speed 300 rpm, Liquid Flow 0.1 l/sec, Gas Flow (stp) 1.0 l/sec

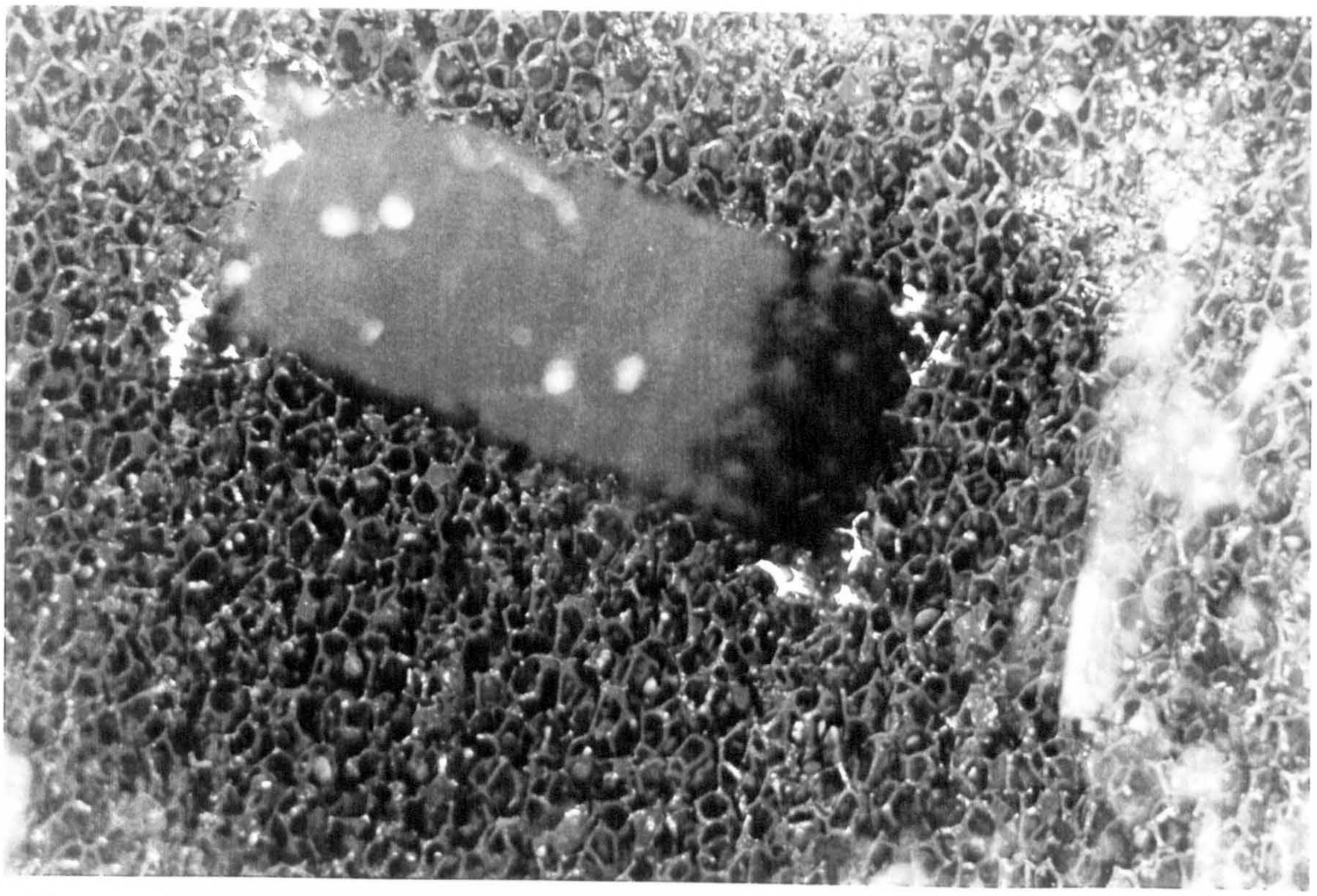

Photograph No.10 : Window No.4 : *Gas Maldistribution*
Speed 300 rpm, Liquid Flow 0.1 l/sec, Gas Flow (stp) 1.0 l/sec

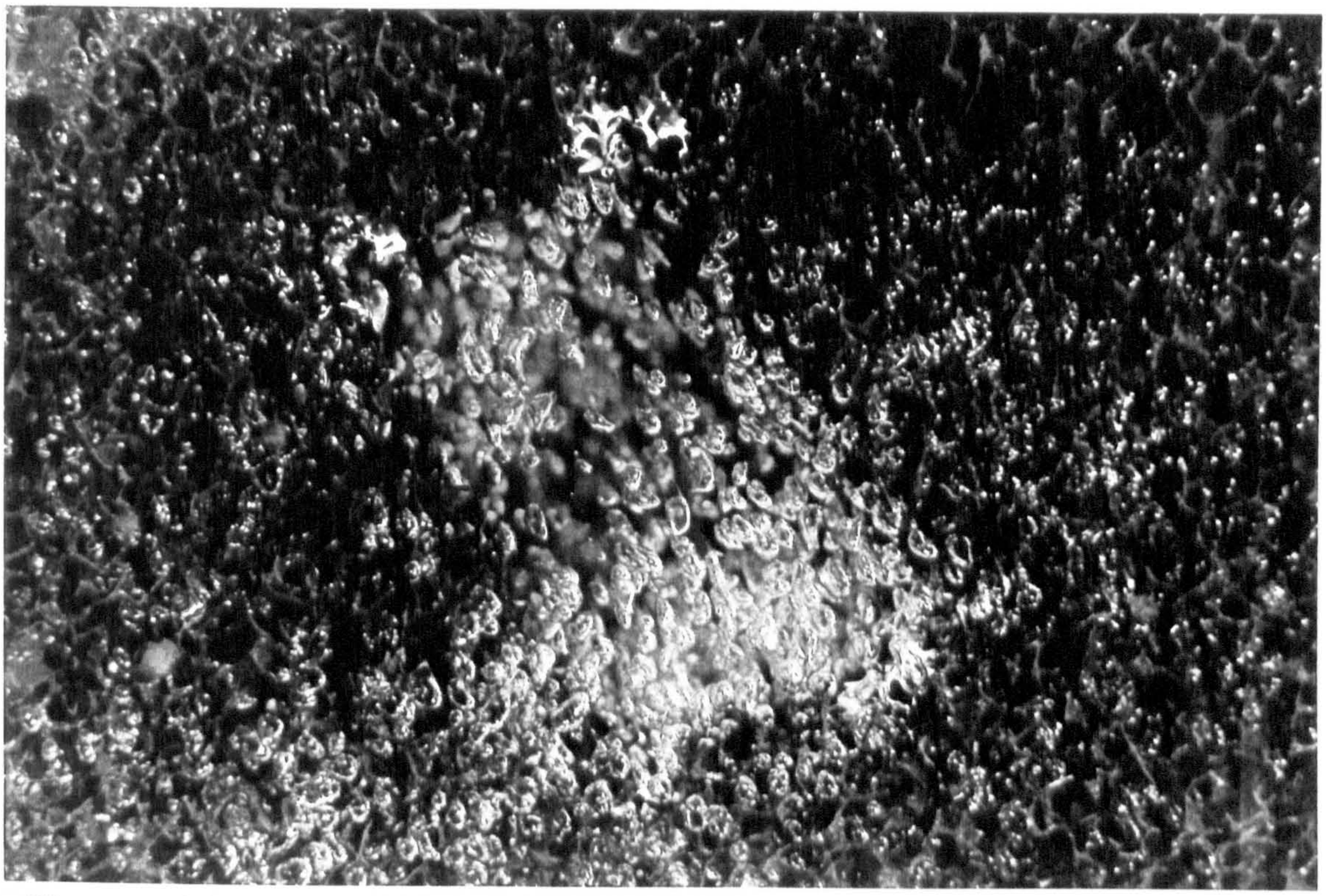

Photograph No.11 : Window 9 : *Effect of Speed*
Speed 300 rpm, Liquid Flow 0.1 l/sec, Gas Flow (stp) 1.0 l/sec

Photograph No.12 : Window 9 : *Effect of Speed*
Speed 250 rpm, Liquid Flow 0.1 l/sec, Gas Flow (stp) 1.0 l/sec

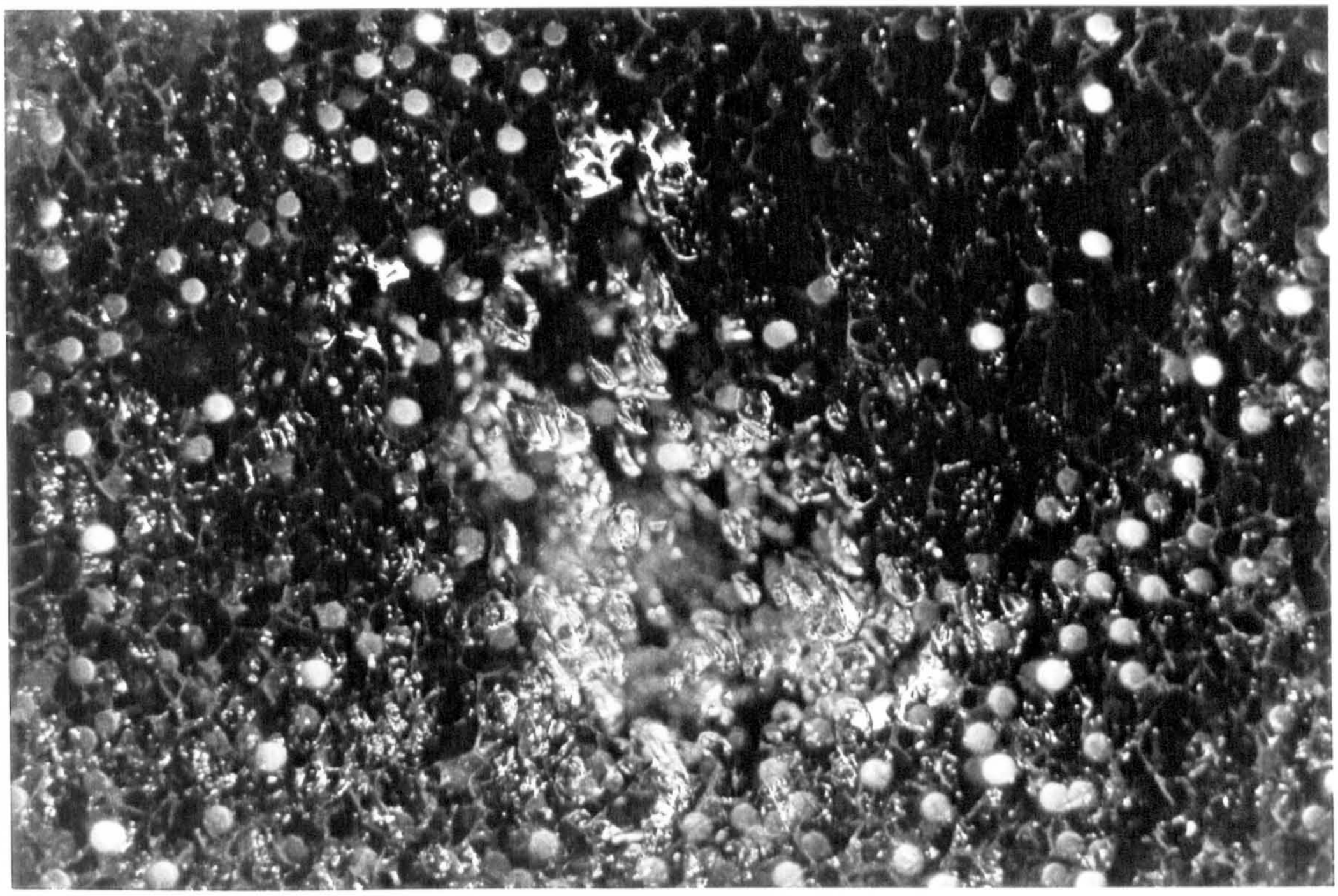

Photograph No.13 : Window 9 : *Effect of Speed*
Speed 200 rpm, Liquid Flow 0.1 l/sec, Gas Flow (stp) 1.0 l/sec

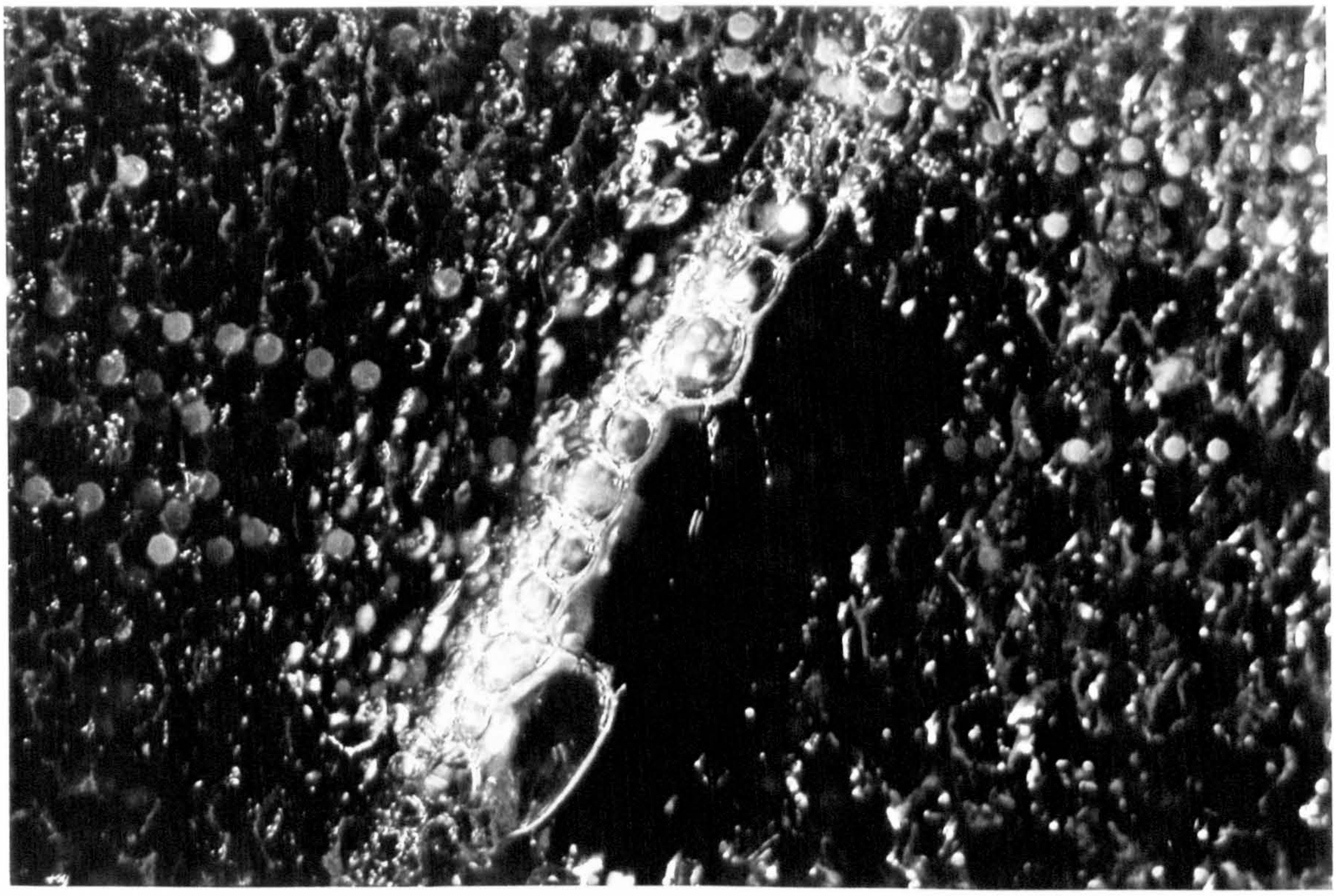

Photograph No.14 : Window 12 : *Gas - Liquid Interface*
Speed 300 rpm, Liquid Flow 0.1 l/sec, Gas Flow (stp) 1.0 l/sec

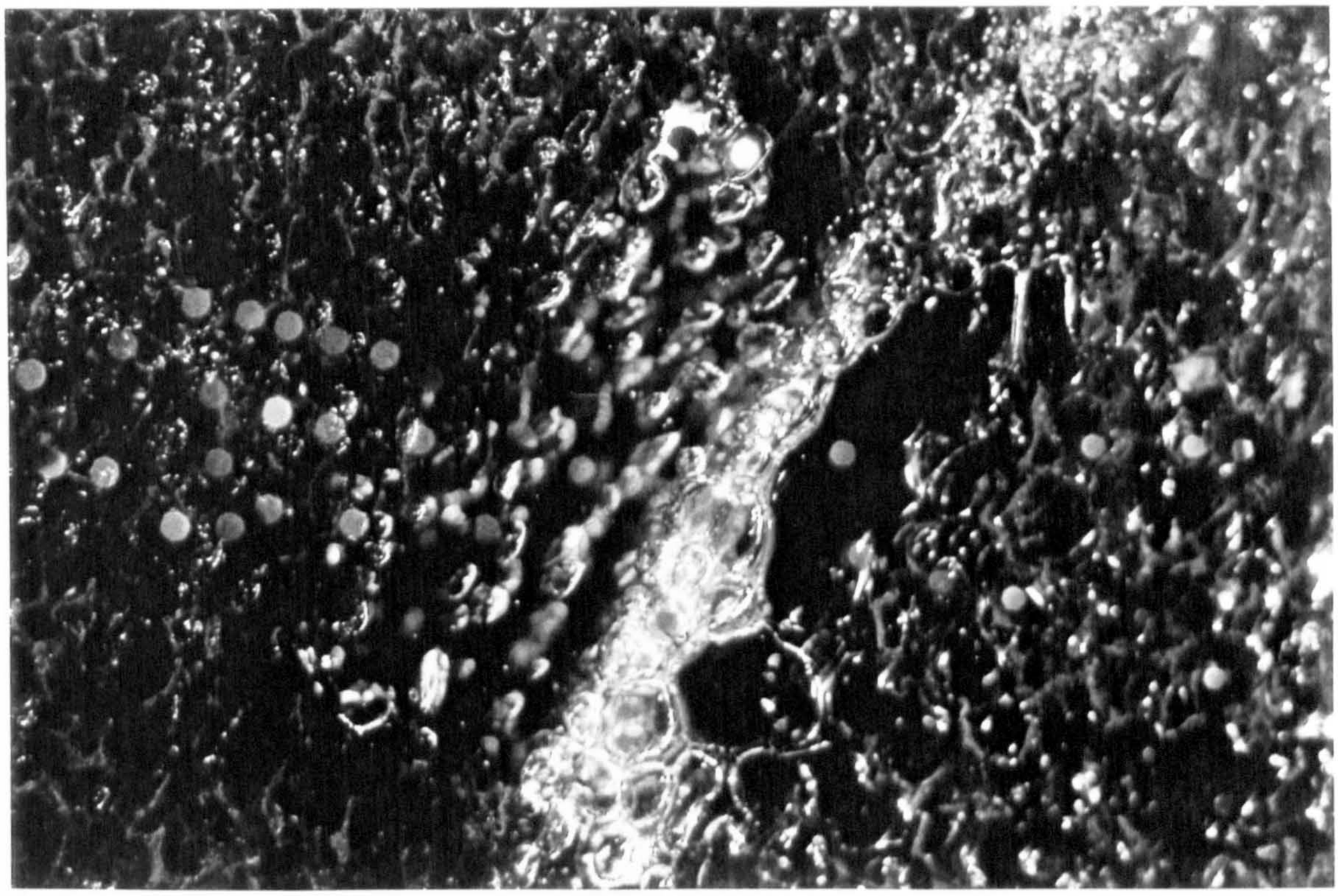

Photograph No.15 : Window 12 : *Gas - Liquid Interface*
Speed 250 rpm, Liquid Flow 0.1 l/sec, Gas Flow (stp) 1.0 l/sec

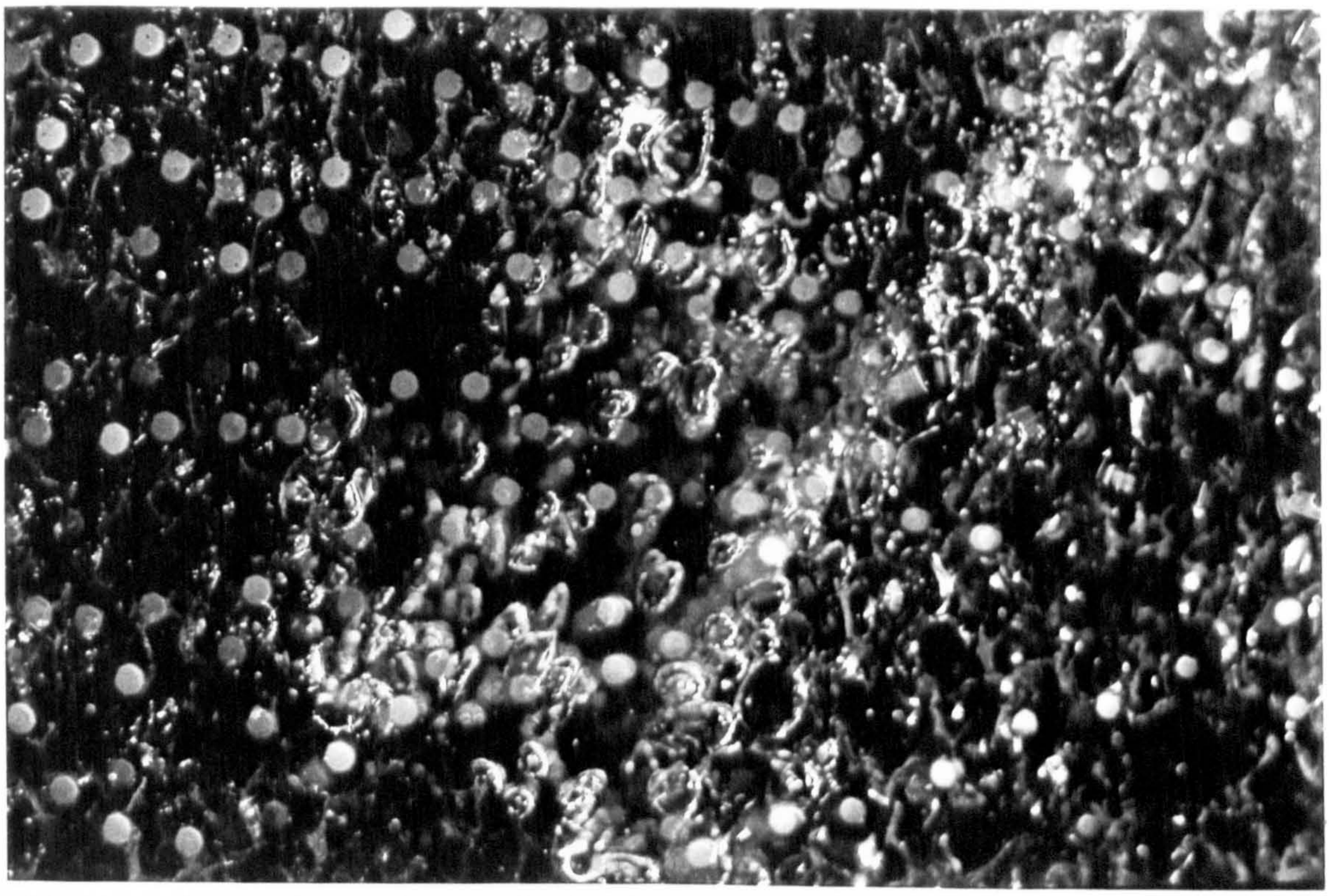

Photograph No.16 : Window 12 : *Gas - Liquid Interface*
Speed 200 rpm, Liquid Flow 0.1 l/sec, Gas Flow (stp) 1.0 l/sec

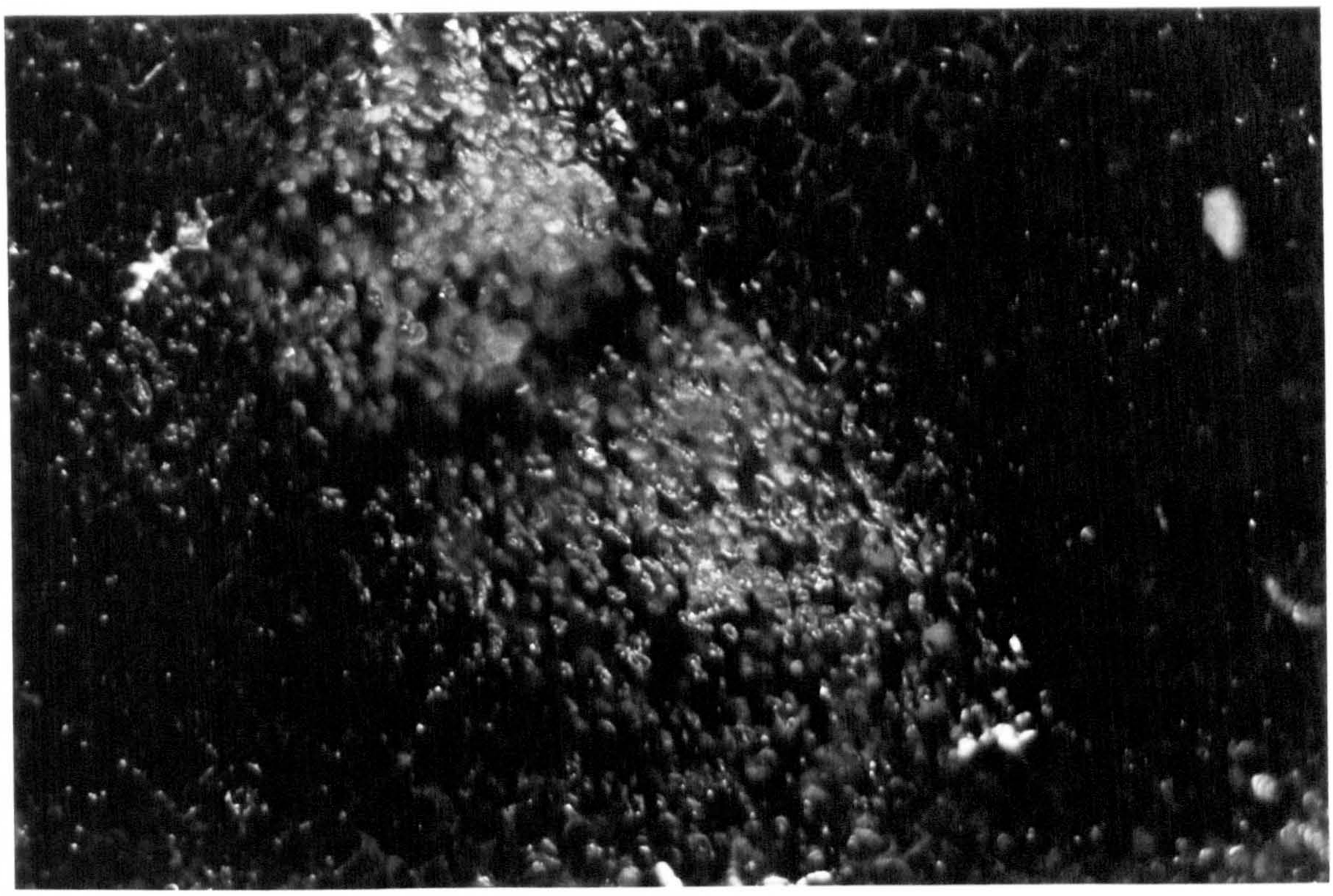

Photograph No.17 : Window 4 : *Modified Gas Nozzles*
Speed 350 rpm, Liquid Flow 0.1 l/sec, Gas Flow (stp) 1.2 l/sec

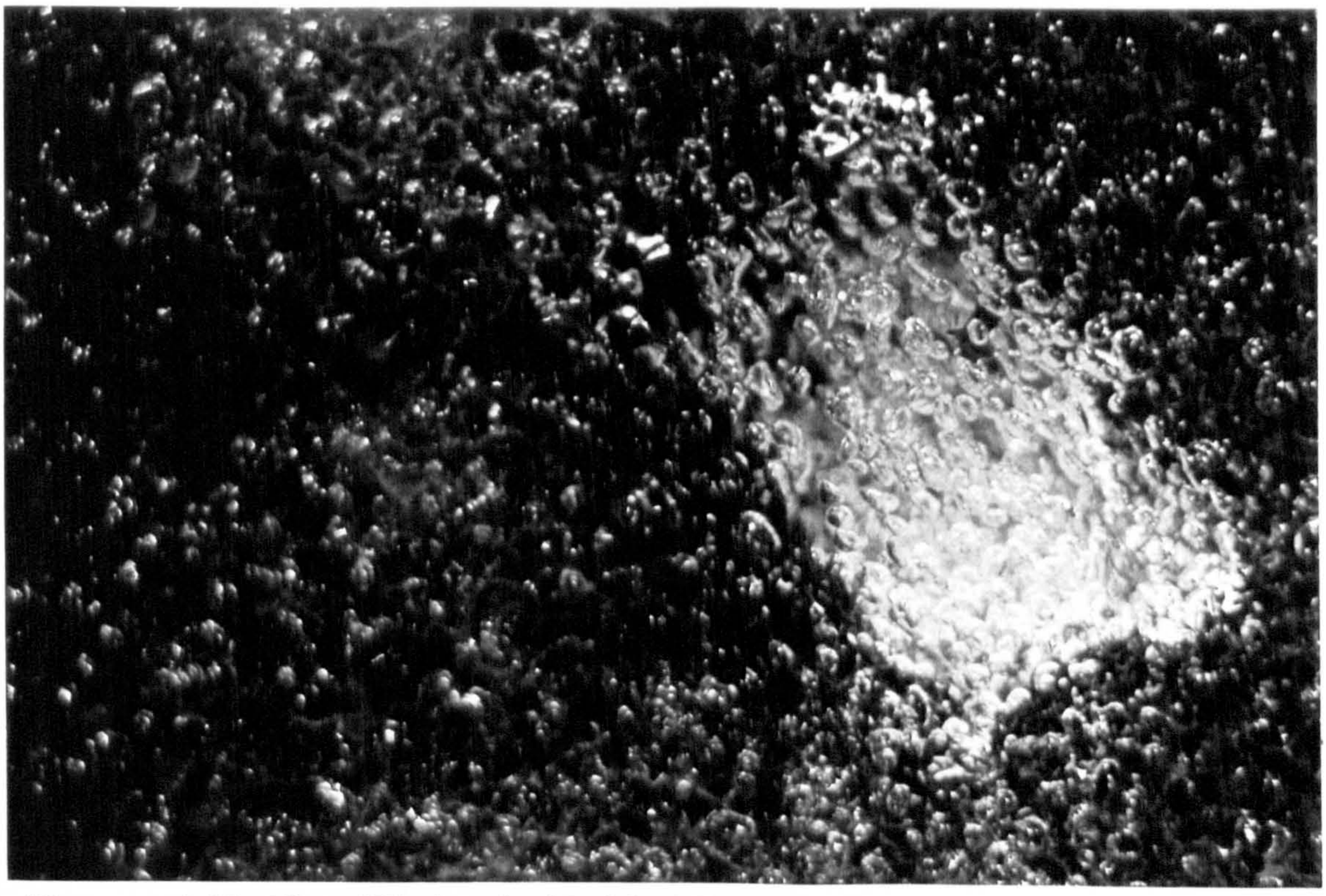

Photograph No.18 : Window 9 : *Modified Gas Nozzles*
Speed 250 rpm, Liquid Flow 0.1 l/sec, Gas Flow (stp) 1.1 l/sec

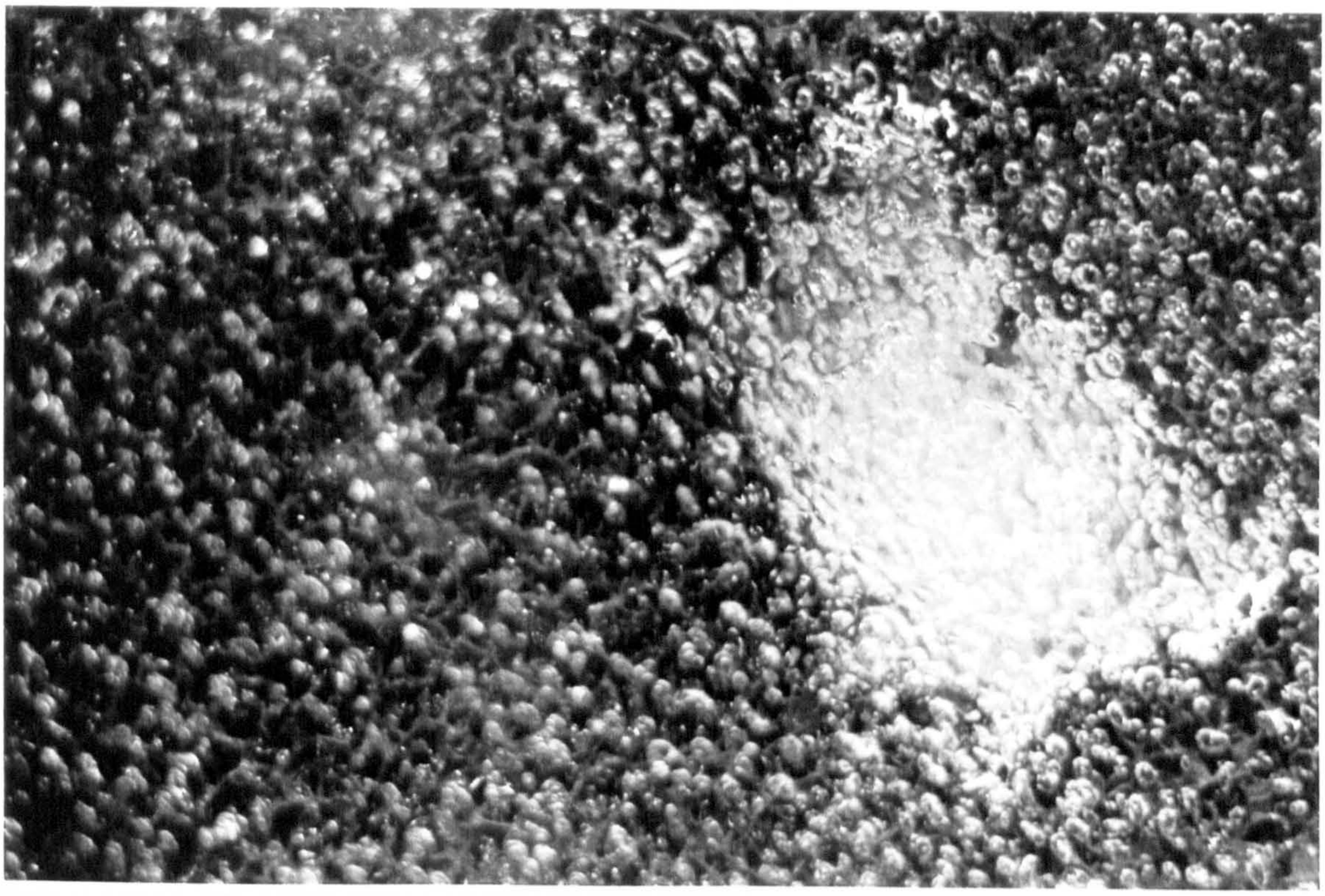

Photograph No.19 : Window 9 : *Modified Gas Nozzles*
Speed 350 rpm, Liquid Flow 0.1 l/sec, Gas Flow (stp) 1.2 l/sec

Photograph No.20 : Window 12 : *Modified Gas Nozzles*
Speed 250 rpm, Liquid Flow 0.1 l/sec, Gas Flow (stp) 1.1 l/sec

From the photographs 9 - 20 and Table 5.2 the following observations can be made about the gas hydrodynamics within the Declon HC20 packing in the rotor :

1. It is impossible to determine the bubble size at formation at the gas injector nozzles, although gas can be seen coming from the nozzle (photograph no.9)
2. Window no.4 is shown in photograph nos. 10 and 17. The significance of photograph 10 is that bubbles can be seen in the packing at the top right of the photograph, but there are no bubbles in the window itself. This confirms the maldistribution of gas as seen in photograph nos. 1 - 4 with the original gas nozzle design. Photograph 17 is the same window except that the modified nozzle design is in operation, and as can be seen the window now contains gas bubbles confirming the improved distribution of gas in the packing with the modified gas nozzles.
3. The effect of the rotational speed on the bubble size is shown in photographs 11 - 13. As can be seen the average bubble size changes from approximately 0.9 mm in diameter at 200 rpm down to about 0.5 mm at 300 rpm.
4. Photographs 14 - 16 show the the gas-liquid interface, and as seen the position of the interface moves towards the centre of the rotor as the rotational speed decreases confirming that the gas hold-up in the rotor, for a constant gas and liquid flowrate, increases as the rotational speed decreases.
5. Photographs 17 - 20 show the bubbles through the packing produced using the modified nozzle design. Comparing these photographs it is clear that the average bubble size increases as the bubbles migrate through the packing towards the centre of the rotor.

A comparison of the experimental bubble sizes produced in the rotor with the bubble size predicted by the model (i.e. critical bubble diameter) and with those found experimentally by Alshaban[7] is given below in Table 5.3. The predicted bubble sizes were taken from Fig. 4.8, and as can be seen the experimentally found values are consistently lower than the predicted values, although correspond closely with those found by Alshaban. The predicted values are found to increase in size as the bubbles approach the gas liquid interface due to the change in gravitational acceleration, whereas from the photographic work little increase in bubble size was observed between the bubble sizes obtained from windows 9 and 12.

Table 5.3 : Comparison of Experimental Bubble Size with the Predicted Bubble Size

Photograph No.	11	13	14	16
Rotational Speed (rpm)	300	200	300	200
Experimental Value (mm)	0.5	0.9	0.6	0.9
Predicted Value (mm)	0.7	1.0	0.8	1.2
Alshaban's[7] Value (mm)	0.5	-	0.5(5)	-

5.5 Salt Water

Up until now little mention has been made about salt water, and all the previous experimental work and modelling has been concentrated around ordinary water. In many industrial cases, sea water would be readily available, and so the performance characteristics of sea water in a Higee rotor would need to be determined before this technology could be applied in the off-shore industry. In order to simulate sea water, a salt solution of 3% by weight (0.75 gmol/l) was made, and due to cost and time involved in making a batch, the de-oxygenated salt water from the rotor was re-aerated and recycled back into Tank A (see Fig. 3.8). However, due to the corrosive nature of salt water on aluminium, limited experimental work was carried out on the hydrodynamics of salt water through the rotor in order to minimise any corrosive attack. As seen in Appendix IX (d), even using salt water sparingly has a detrimental effect on the rotor as salt deposits soon built up on the gas injector nozzles.

Photographs 21 - 24 show some of the hydrodynamic findings using salt water. The following observations on the hydrodynamic behaviour of salt water in the rotor using the Declon HC20 packing can be made :

1. Photographs 21, 22 show that as the gas flow through the rotor is increased a substantial amount of foaming is seen and as seen in photograph 22 this tends to be irregular.
2. The maximum gas flowrate through the rotor is greatly reduced as a result of (1), and at 250 rpm the rotor started to flood at a gas flow at s.t.p. of only 0.6 l/sec.
3. Photographs 23, 24 show that the bubble sizes through the rotor are significantly reduced, an average bubble size of approximately 0.1 - 0.3 mm in diameter, whereas at the same speed of rotation the average bubble size produced with ordinary water was 0.7 mm.
4. Photograph 24 shows the window at the gas-liquid interface, and as can be seen from the bottom of the photograph there is substantial foaming produced with salt water.

A foam occurs when bubbles rise to the surface of the liquid and persist for a while without coalescence or rupture from the liquid into the gas phase. Section 2.6.2.3 stated a number of factors that influenced coalescence such as the resistance of the separating film to drainage, the critical film thickness and the ultimate strength of the final film. Gravitational force causes bubbles to rise to the liquid surface and the liquid in the walls of the foam to drain down to the main body of the liquid. The viscosity of the liquid in a film opposes the drainage of the film and its displacement from approaching bubbles. Therefore the higher the viscosity, the slower the film thinning process, and if the viscosity increases as the film thins, as in many cases, the process becomes self-retarding.

GAS LIQUID

INTERFACE

(with some mild foaming)

FOAMING REGION

(severe foaming causing flooding)

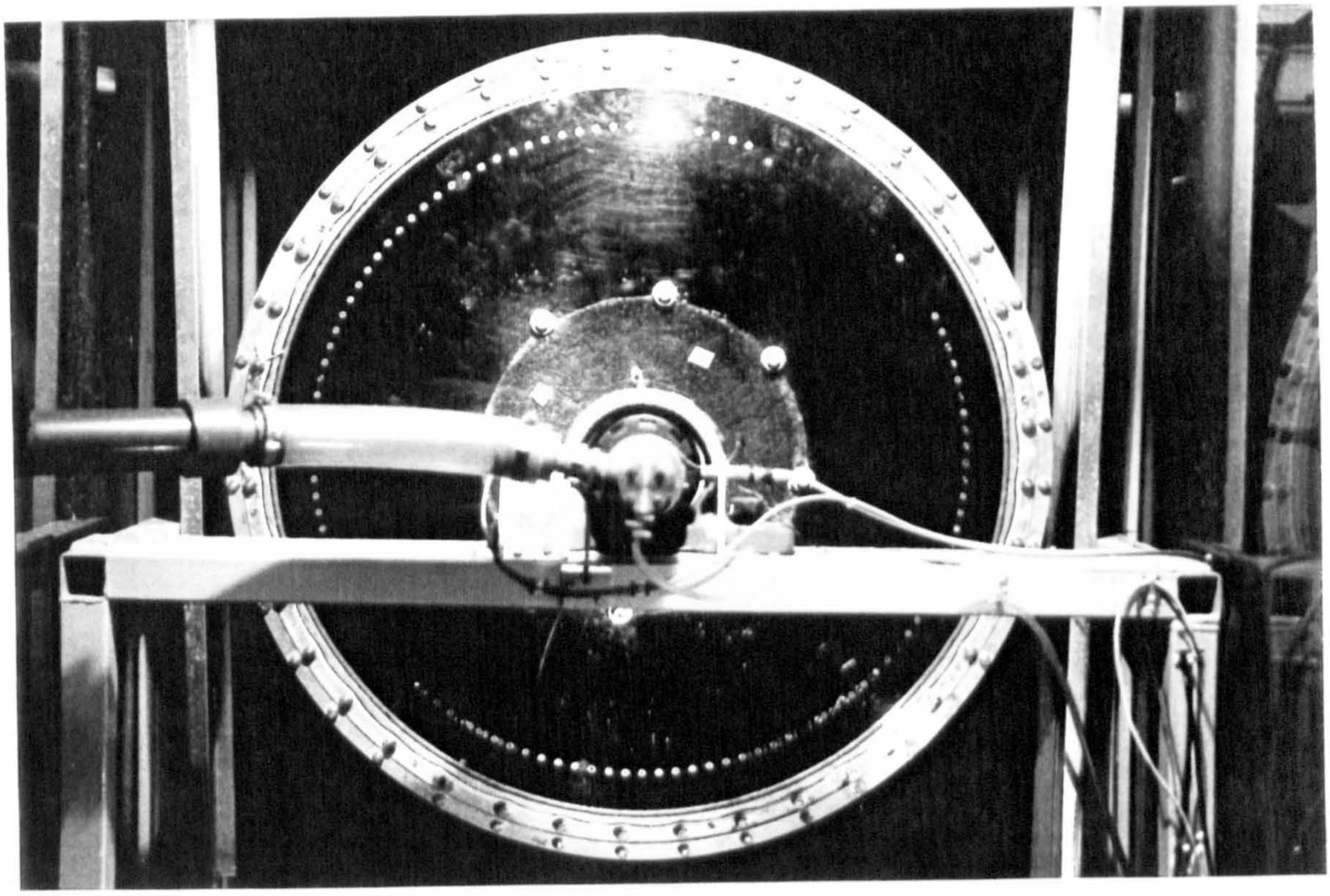

Photograph No.21 : *Overall Rotor Hydrodynamics with Salt Water*
Speed 250 rpm, Liquid Flow 0.1 l/sec, Gas Flow (stp) 0.2 l/sec

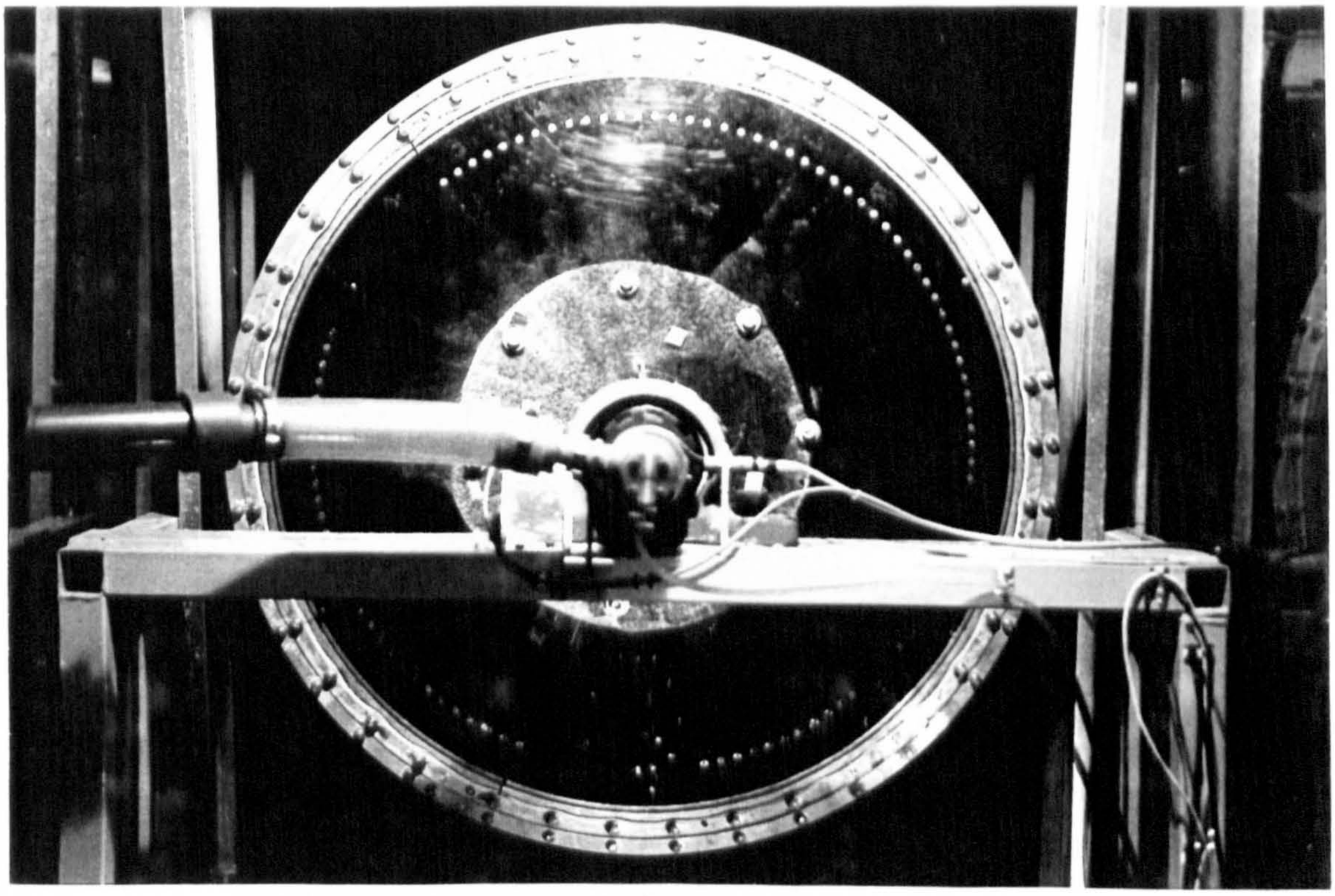

Photograph No.22 : *Overall Rotor Hydrodynamics with Salt Water*
Speed 250 rpm, Liquid Flow 0.1 l/sec, Gas Flow (stp) 0.6 l/sec

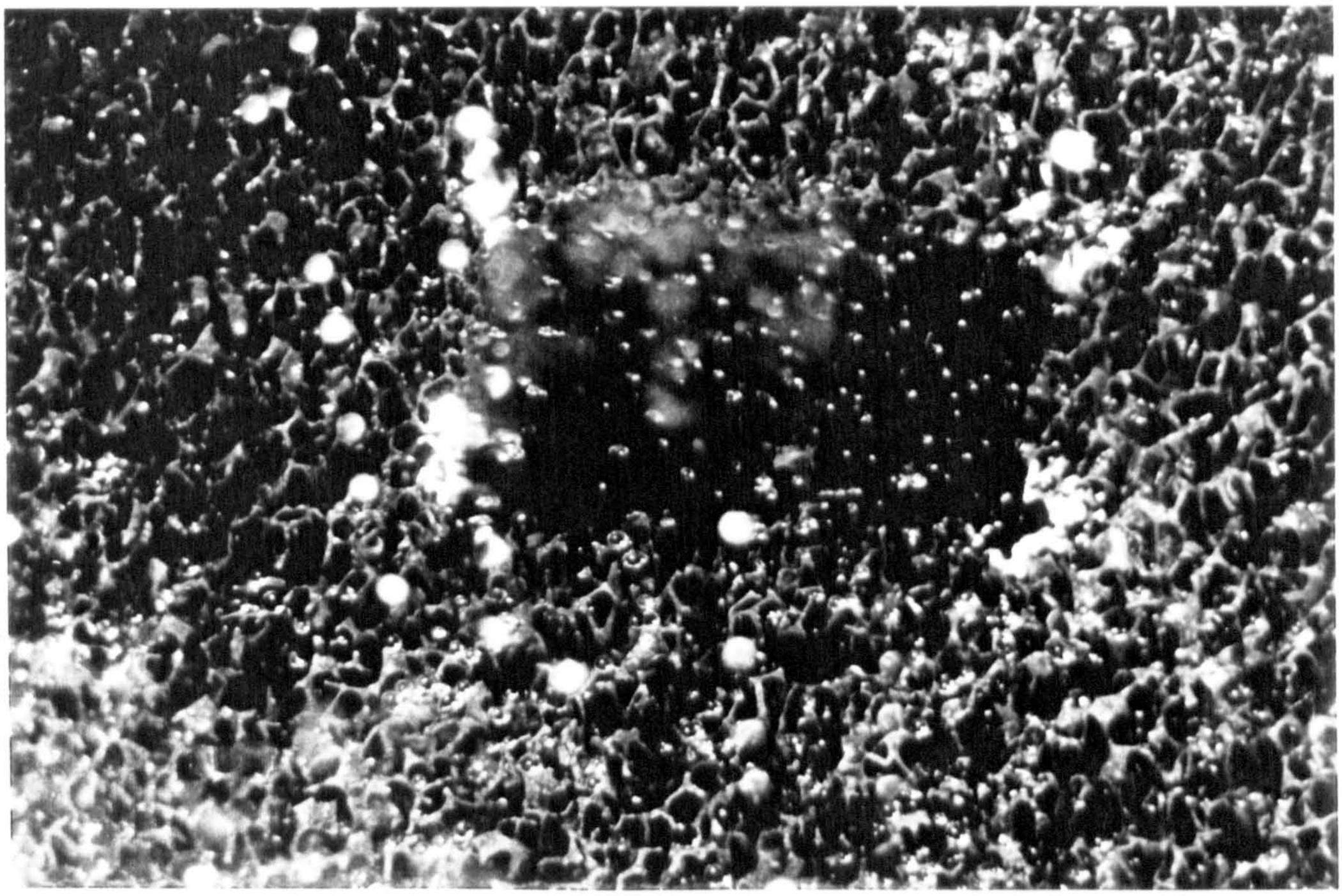

Photograph No.23 : Window 9 : *Gas Bubbles in Salt Water*
Speed 250 rpm, Liquid Flow 0.3 l/sec, Gas Flow (stp) 0.2 l/sec

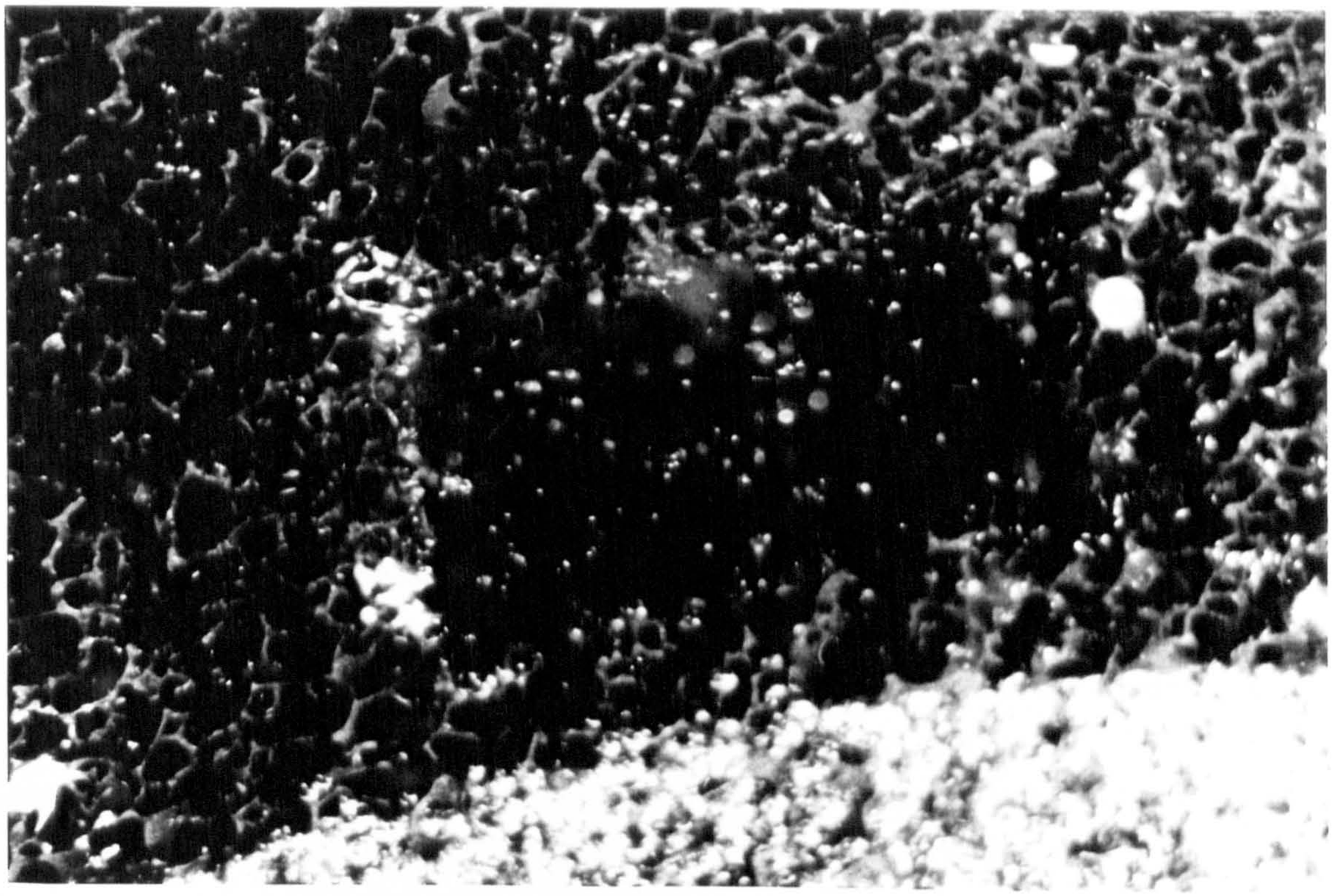

Photograph No.24 : Window 12 : *Gas Bubbles in Salt Water*
Speed 250 rpm, Liquid Flow 0.3 l/sec, Gas Flow (stp) 0.2 l/sec

A popular theory held was that the foam life was proportional to the viscosity and inversely proportional to the surface tension. However experimental analysis has shown that pure liquids do not foam whatever their viscosity, and Bickerman[56] said that the foaming characteristics of a system are strong when the rate of change of surface tension with concentration ($d\sigma/dc$) is high which has been qualitatively confirmed by experiment. However this only describes part of the overall picture, and other physical parameters such as the gravitational force, viscosity, and film thickness, all play a role in determining the foam stability.

Berkman and Egloff[17] explain some additives increase the flexibility or toughness of the bubble walls, rather than their viscosity, to make them more durable. The increased stability with ionic additives is probably due to electrostatic repulsion between charged nearly parallel surfaces of liquid film which acts to prevent draining and hence rupture.

5.6 Discussion

This completes the hydrodynamic work that was carried out on the rotor during this course of research. The principle findings of the hydrodynamic study was the recognition of the gas injector nozzle design and the liquid flowrate as the two principle parameters for good gas and liquid distribution through the rotor, and therefore these are the key parameters to improving the overall mass transfer of the Higee rotor.

Although the gas flow has not been characterised through the rotor, the overall visual photographs show how influential the gas distributor design is, and even if a uniform peripheral distribution from the nozzles is attained, then the effective use of the packing needs to be examined as this can be relatively poor as in the cases shown in photographs 5 and 6. Although the insertion of copper wire into the gas nozzle holes in order to reduce the cross sectional area leads to a greatly improved visual distribution of the gas throughout the rotor, at present it is unknown how the gas flows through the rotor packing, and how much of the packing is being utilised in the contacting of the gas and liquid. The photographic work taken of the bubbles helped to confirm the maldistribution of gas in the rotor as well as being able to estimate typical sizes of bubbles produced in high gravitational fields. As seen, the bubbles cover a range of sizes in each photo and therefore only rough estimates of the average bubble size can be made. The sizes correspond closely with those predicted using the critical bubble size equation, and as shown in theory, the average bubble size decreases as the rotational speed increases. The improved distribution of the gas through the rotor with the modified gas nozzles was also confirmed from the bubble photographic work (c.f. photographs 10 and 17), and the bubbles showed an increase in gas hold-up and a slight increase in size as they migrated towards the centre of the rotor, again confirming theoretically predicted behaviour.

From the experimental work carried out on the liquid flow characterisation using an optical tracer technique, the liquid flow through the rotor showed severe maldistribution and mixing at low flowrates (Fig. 5.7), but as the liquid flow was increased the distribution around the periphery became more uniform and closer to a plug flow response (Fig. 5.8). A multi parameter model was used to describe and characterise the liquid flow through the packing, and the model was found to be able to accurately describe each case. From the model, the value for N (the number of tanks in series) in each case was large, and therefore the residence time distribution can be approximated to a Gaussian curve with exponential decay. The change in gas flow and rotational speed showed slight effects on the output response, whereas the liquid flow was seen to be the dominating parameter with the exponential delay time, t_d, being significantly reduced at the higher liquid throughputs. It can therefore be concluded that the rotor should be run with as higher liquid throughput as possible, which at present is limited to around 0.5 l/sec in order to achieve the most uniform distribution and minimal delay time. The maximum flowrate however can be improved by either increasing the width of the packing inside the rotor or by re-designing the way in which the water is removed, and possible methods of achieving this are detailed further in Chapter 8.

The difference between the hydrodynamic characteristics of salt water to that of ordinary water is significant due to the presence of the dissolved salt inhibiting bubble coalescence, and therefore creating substantial foaming at the interface as discussed in section 5.5. As mentioned, gravitational forces aid with the film drainage and therefore a high gravitational environment should reduce the average foam life. However the increase in gravitational field does no prevent the system from foaming as many factors are involved, and this is clearly seen in photographs 22 and 24, and as a result, the threshold of the system at which flooding takes place is lowered. As seen from the bubble photographic study, the average bubble size produced in salt water is much smaller than the equivalent bubble size formed in ordinary water which will lead to a greater interfacial area. This finding is consistent with that of Alshaban[7] who attributed the smaller bubble size to the change in coalescence properties between salt and ordinary water. However, as the gas flow range is substantially reduced, the system becomes more limited and the increase in interfacial surface area may not necessarily result in an overall improvement in the performance of the rotor.

CHAPTER 6 : MASS TRANSFER PERFORMANCE OF ROTOR

6.1 Introduction

The mass transfer performance of the rotor is ultimately the single most important characteristic of the rotor. As mentioned in Chapter 1 of this thesis, the required industrial mass transfer performance for the de-oxygenation of water is to reduce the oxygen concentration from 9 ppm down to 20 ppb, and whatever the improvement in the gas and liquid hydrodynamics may be under Higee, unless the mass transfer target is achieved then the application of Higee technology to this process is futile.

As oxygen is sparingly soluble in water then, as seen in Table 4.3, the value for Henry's constant is high which means the equilibrium constant is high, and therefore the term $\frac{L_m}{mG_m}$ approximates to zero. As a result, equation 2.7 reduces to the number of transfer units being simply equal to the natural log ratio of the inlet to outlet concentration of the dissolved oxygen in the water. The number of transfer units therefore provides a convenient way of expressing the mass transfer performance of the rotor, and is the parameter used throughout the chapter.

This chapter follows the development of the mass transfer performance of the rotor beginning with the initial rotor design and sampling technique, through to the final performance assessed using the new sampling design. The effect of the rotational speed, gas flowrate, liquid flowrate are examined for two types of packing : Declon HC20; and Declon HC30, and the mass transfer at different radial positions is examined in order to gain a greater understanding of how the mass transfer is taking place.

6.2 Initial Mass Transfer Findings

The initial sampling technique from the rotor took the sample from the back chamber just below the liquid surface. The kinetic energy of the liquid in the rotor was able to overcome the pressure head through the sampling line and drive the liquid sample through the analyser. However due to the strong possibilities of recontamination of the de-oxygenated water with the atmosphere a nitrogen blanket was placed around the pick-up tubes at the back of the machine to prevent any recontamination, the details and modifications of which were discussed in section 3.3.5.1. The initial method of calculating the *inferred* mass transfer taking place in the packed section of the rotor together with the tables of results can be seen in Appendix IV. The initial mass transfer findings are displayed in Fig. 6.1.

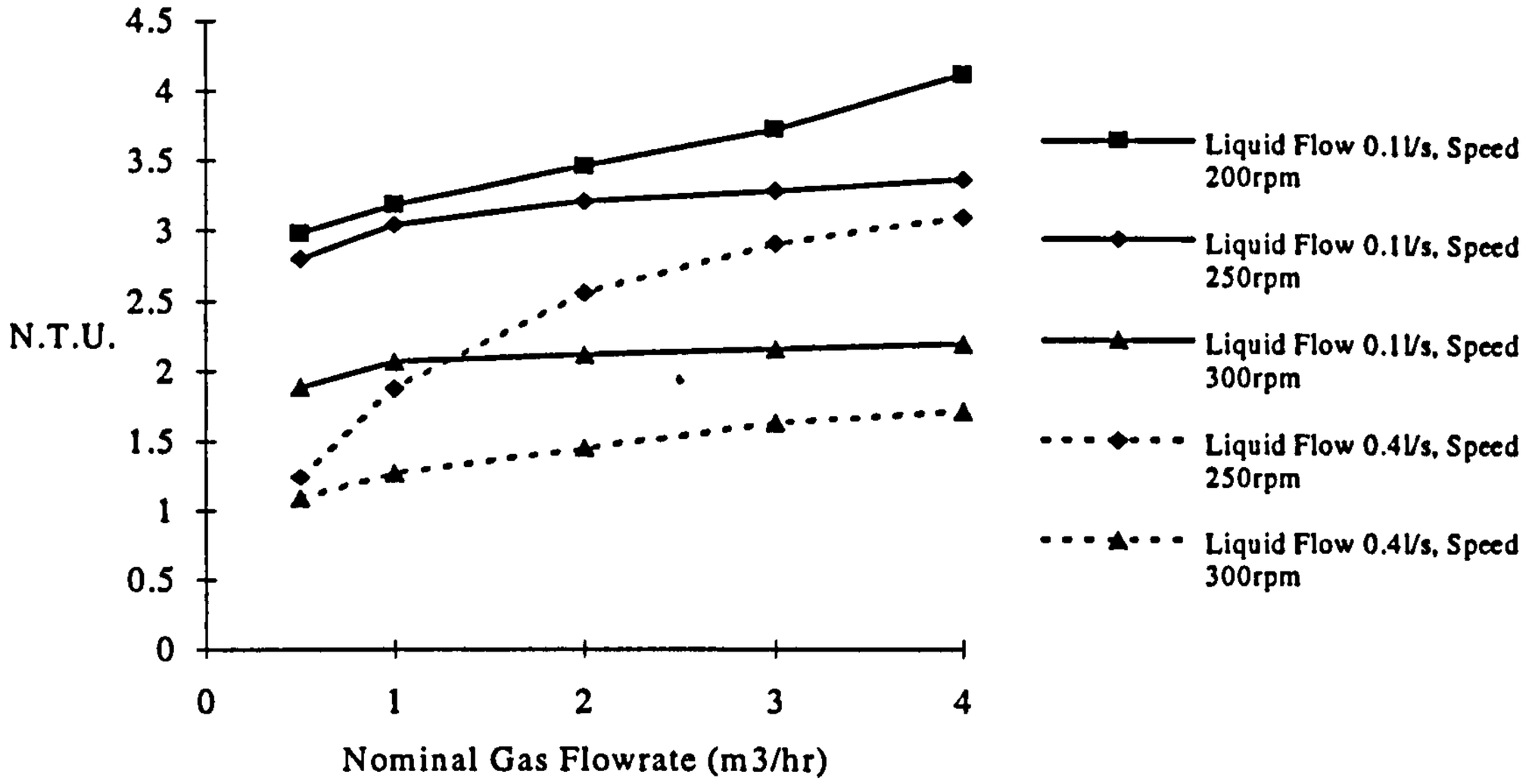

Figure 6.1 : Initial Rotor Mass Transfer Results with Declon HC20 Packing

Fig. 6.1 shows how the number of mass transfer units varies with the gas flowrate. For ease of display, the *nominal gas flowrate*, i.e. the rotameter reading, was chosen as the independent variable, but the procedure for calculating the corrected gas flow at s.t.p. can be found in Appendix III. The following main observations were made :

1. As the gas flowrate increased for a given speed and liquid flowrate, the overall mass transfer in the rotor increased, although as the gas flowrate continued to rise, the rate of increase in mass transfer fell.
2. As the liquid flowrate increased for a given speed and flowrate, the overall mass transfer in the rotor fell, and this fall was more pronounced at the lower gas flows.
3. As the rotational speed of the rotor rose over the range from 200 - 300 rpm, then for a constant gas and liquid flow, the mass overall mass transfer achieved fell.

Observations 1 and 2 above were consistent with the expected findings. However the final observation was surprising and not what had been expected. It was thought that the hydrodynamics must be accountable for this finding, and as seen in section 5.2 the overall maldistribution between the gas and liquid seems to become more pronounced at the higher rotational speeds. The next logical step seemed to be to try and eliminate this maldistribution and improve the mass transfer, but there still remained the problem with the sample analysis, not knowing the effect the nitrogen blanket was having on the dissolved oxygen concentration in the water while it was in the return chamber of the rotor. Therefore a new sampling system was designed which has been detailed in Section 3.3.5.3, so that the mass transfer in the

packed section of the rotor could be measured directly with a much greater degree of confidence in the results.

6.3 Mass Transfer Analysis with Modified Sampling System

Having increased the pressure drop across each individual nozzle (see Sect. 3.3.5.2, and Appendix V, Table (a)) in order to minimise the gas maldistribution in the rotor, re-designed the liquid sampling technique (see Sect. 3.3.5.3) to produce reliable and credible results which can be accepted with a high degree of confidence, and replaced the polycarbonate window with an aluminium plate for safety reasons and to allow for higher rotational speeds to be attained, the following mass transfer results were taken to determine the performance of the rotor. With the new sampling system, it was hoped to attain the mass transfer performance at the full, 3/4, 1/2, and 1/4 radial packed depths, and Figs. 6.2 - 6.4 show the initial findings. The mass transfer data for these graphs can be found in Appendix V.

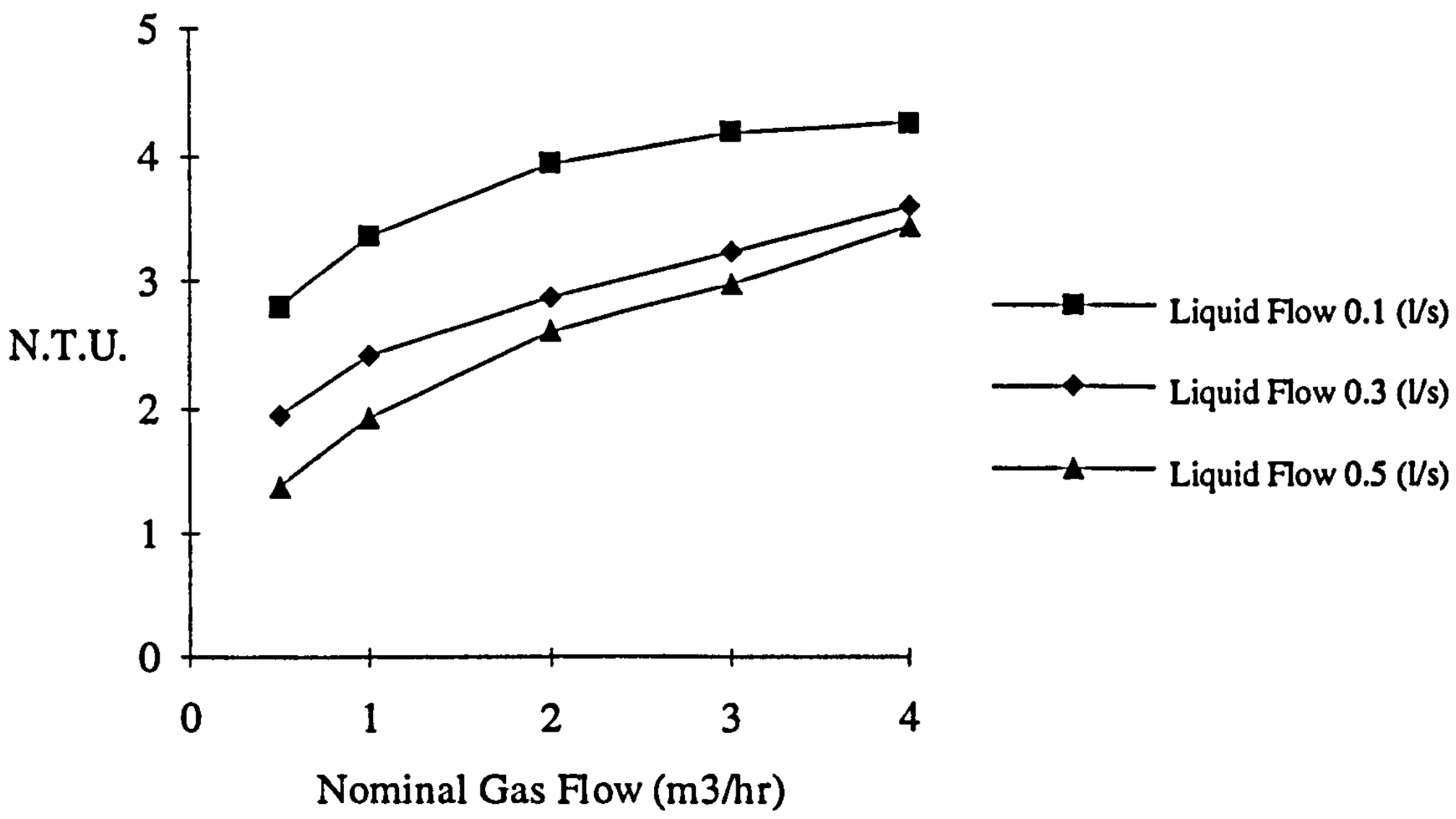

Figure 6.2 : Mass Transfer at the Full Radial Depth at a Rotational Speed 300 rpm
Declon HC20 Packing

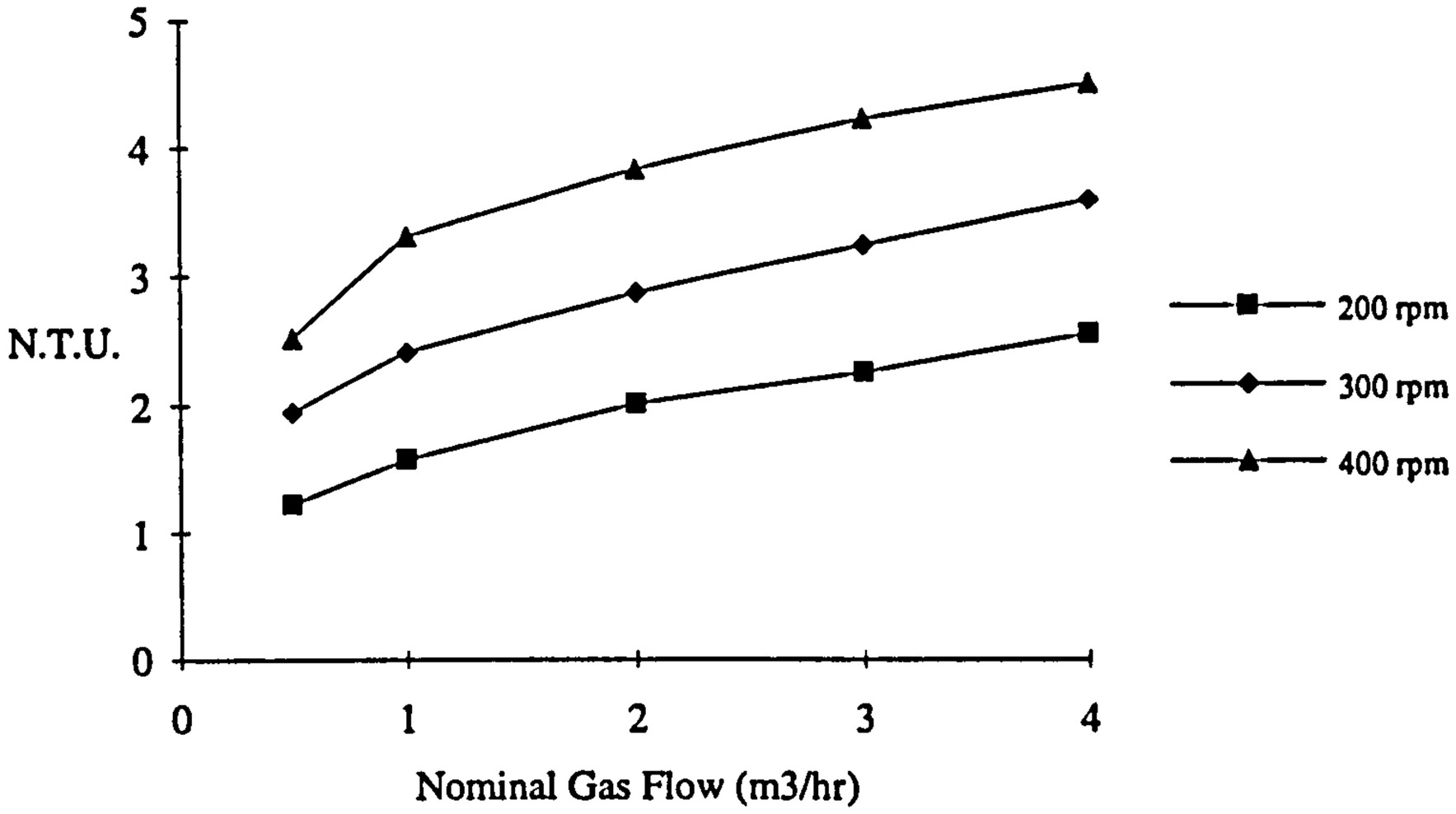

Figure 6.3 : Mass Transfer at Full Radial Depth and Liquid Flow 0.3 l/sec
Declon HC20 Packing

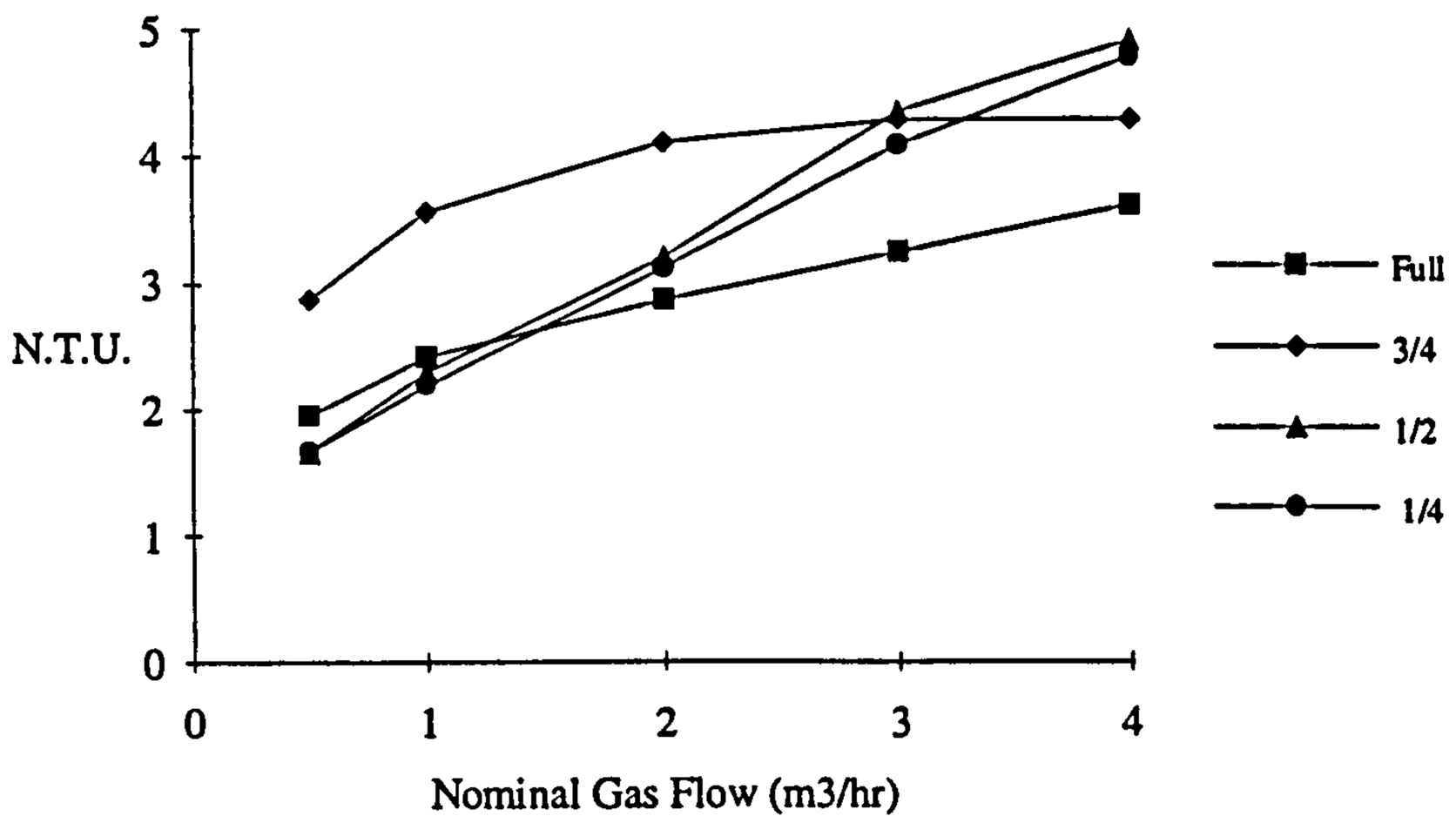

Figure 6.4 : Mass Transfer at the Different Radial Depths at 300 rpm
Liquid Flow 0.3 l/sec, Declon HC20 Packing

The following observations can be made from Figs. 6.2 - 6.4 :

1. As the liquid flowrate rises through the rotor, the mass transfer at the Full radial packed length for a given speed and gas flow falls. (Fig. 6.2)
2. As the rotational speed of the rotor increases, the mass transfer at the Full radial packed length for a constant gas and liquid flow rises. (Fig. 6.3)
3. As the gas flow through the rotor increases, the mass transfer at the Full radial packed length for a given speed and liquid flow increases.

4. There seems to be no logical pattern linking the mass transfer performance of the rotor with the radial packed length in the rotor. (Fig. 6.4)

Findings (1), (3) show trends that were consistent with the initial mass transfer results shown in Section 6.2. However (2) now reveals the trend that the mass transfer increases with the rotational speed which is consistent with theory, and therefore shows that the re-design of the gas injector nozzles has significantly improved the gas distribution throughout the rotor. One might have expected the mass transfer to be related to the radial depth but as clearly seen in Fig. 6.4 the findings are surprising and no pattern can be seen. At this stage the only explanation for this is the complicated hydrodynamic mixing patterns that must still be apparent in the rotor.

The ideal liquid flow characteristics desired in the rotor is plug flow. It seems obvious that there is a high degree backmixing of the liquid taking place in the rotor, so to improve the liquid hydrodynamics through the machine the backmixing needs to be suppressed. One way of trying to accomplish this was to put radial vanes into the rotor as detailed in the following section.

6.4 Mass Transfer Analysis using Radial Vanes

Initially 24 vanes were inserted into the packed section of the rotor up to the periphery as shown in Fig. 6.5. Each vane was made from brass sheet of thickness 0.1 mm, with a length of 300 mm and depth 11.5 mm. However as little or even a negative effect in the mass transfer performance of the rotor was seen, the number of vanes was then increased to 48. The complete mass transfer data for the radial vanes can be found in Appendix VI, and the results are displayed in Figs. 6.6 - 6.7.

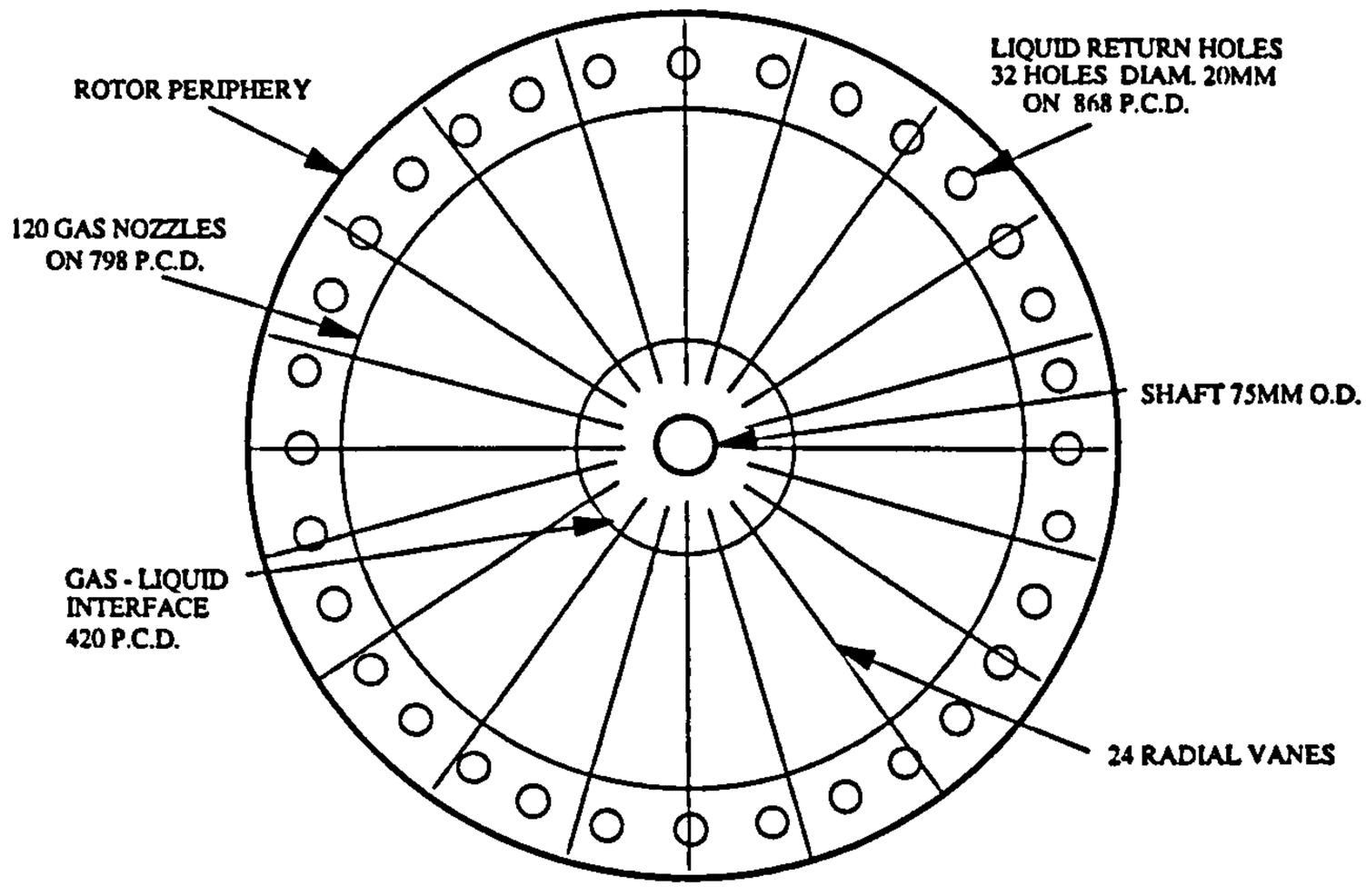

Figure 6.5 : Packed Section of Rotor with 24 Radial Vanes

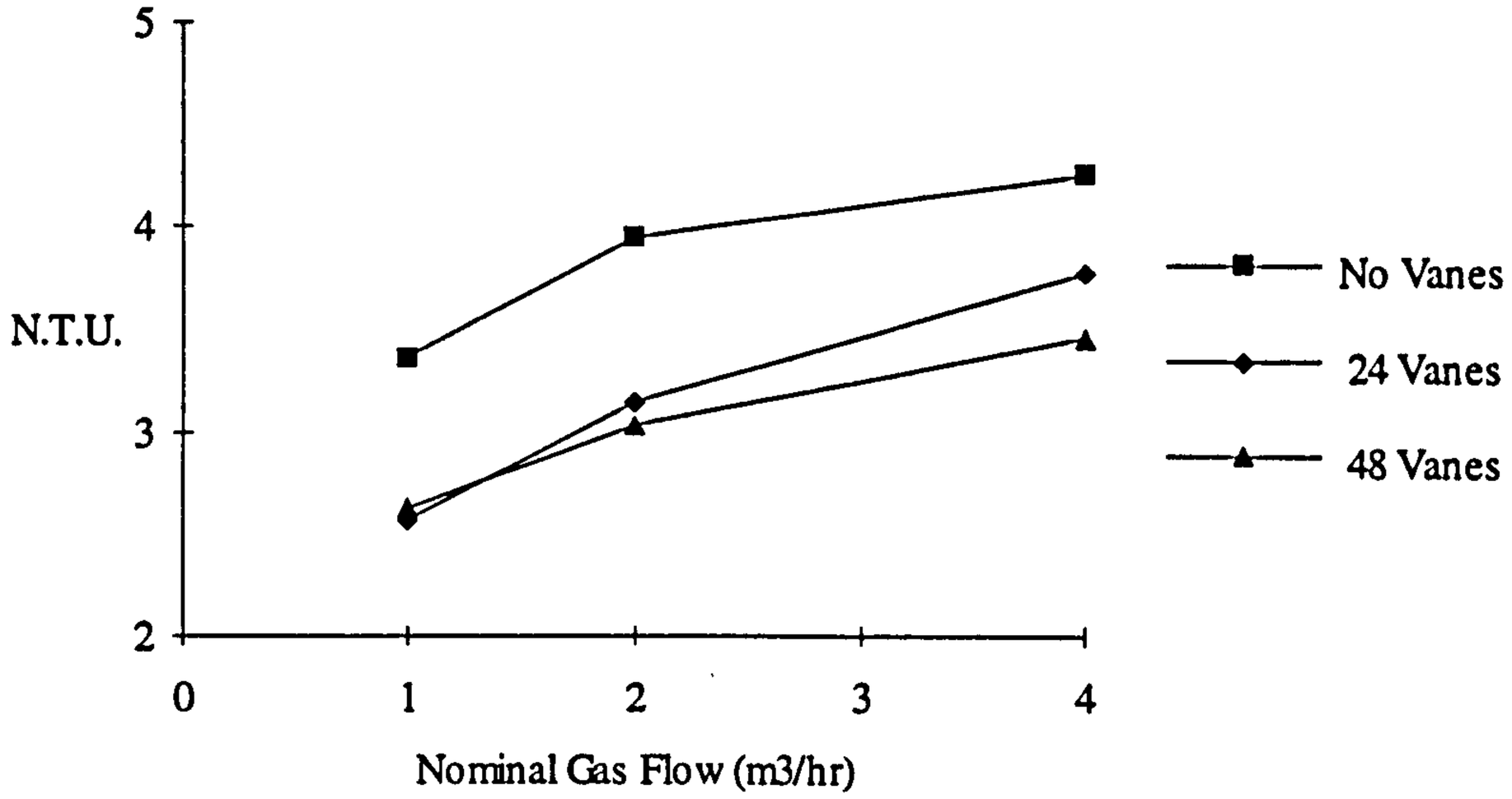

Figure 6.6 : Comparison of Mass Transfer at Full Radial Depth, 300 rpm, Liquid Flow 0.1 l/s Declon HC20 Packing with / without Radial Vanes

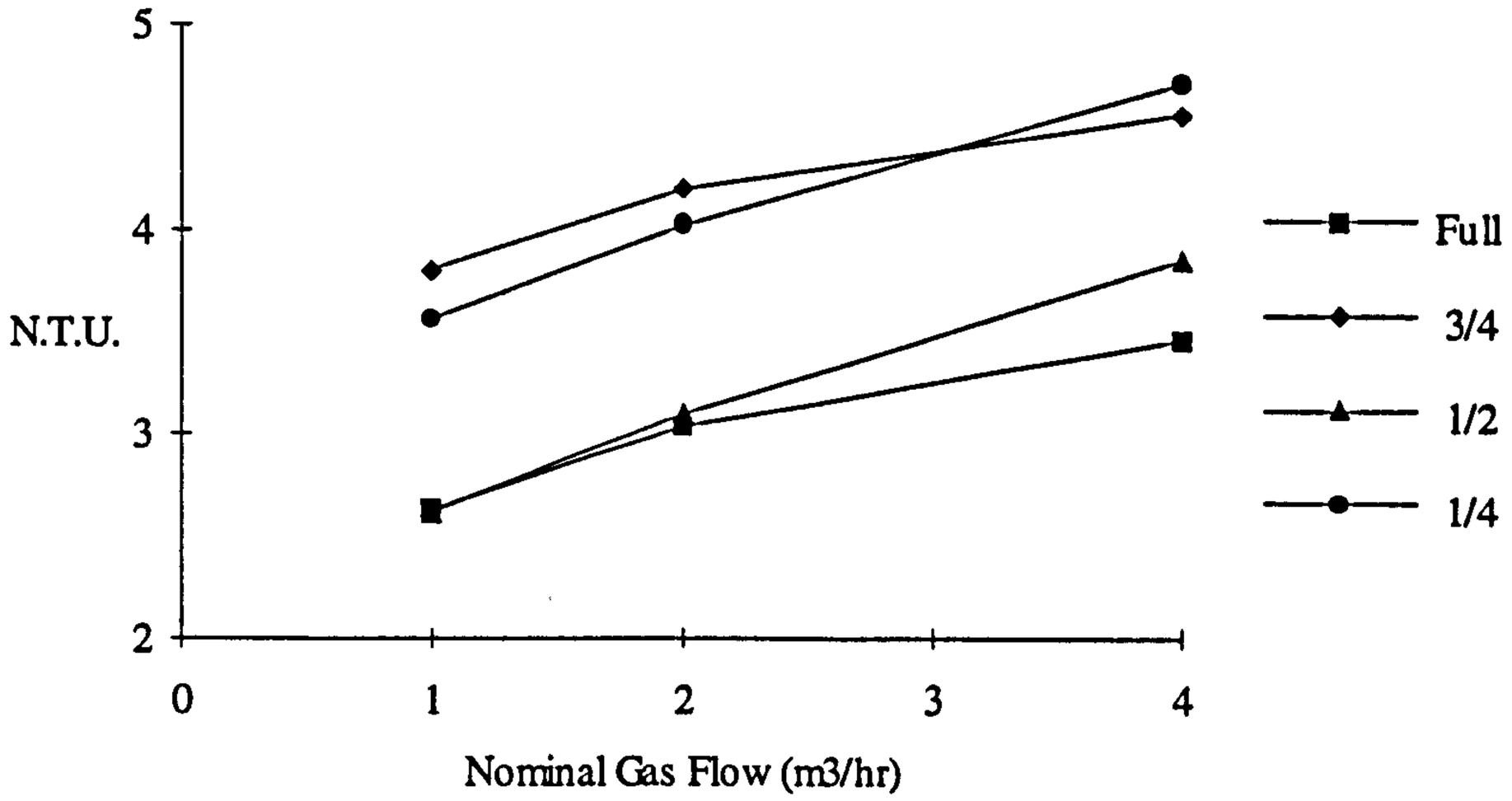

Figure 6.7 : Mass Transfer at Different Radial Depths at 300 rpm Liquid Flow 0.1l/s and using 48 Radial Vanes

From Figs. 6.6 - 6.7 it can be seen that :

1. There is a drop in mass transfer performance with the addition of the radial vanes

2. There seems to be no improvement in the liquid hydrodynamics in the rotor as a result of the addition of the radial vanes.

The explanation for the drop in mass transfer performance with the addition of the radial vanes may be attributed to 'wall effects'. In packed columns it has been known for a long time and shown that there is a tendency for liquid to accumulate at the walls and form wall flow[57]. Baker et al.[58] investigated the wall effects in packed columns for a number of different sized columns and packings. Their findings concluded that in sufficiently wide packed towers, the tendency was not for the liquid flow to concentrate near the walls, whereas for smaller columns with coarse packing the maldistribution at the walls was quite significant. They also concluded that the gas velocity has minimal effect, although an increase in the liquid flow led to increased flow in the wall region. In a more rigorous mathematical approach, Gunn[59] proposed that the preferential flow of liquid to the wall be interpreted as the difference in permeability between the wall and bulk regions of the packing, and that the potential for liquid re-distribution be derived from experimental work of two phase flow in a porous media and the widely accepted relationship between the radial velocity and radial gradient of the axial velocity in packed columns. His analysis showed that if the liquid is distributed uniformly at the top of the packing, and if the wall caused an increase in permeability of the packing next to the wall, the liquid flow will move into the wall region, with 90% of the change in distribution occurring at one column radius from the top, and 99% of the re-distribution occurring at one column diameter. It is thought that although the radial vanes may be preventing some of the liquid backmixing, they may be behaving like a series of walls, and therefore causing a lot of the liquid to wall flow through the packing. Figure 6.6 helps to confirm this theory as it shows that by increasing the number of vanes, a further drop in mass transfer is seen.

6.5 Overall Rotor Mass Transfer Results

For the liquid sample at any radial point in the rotor to be truly representative of that entire radial depth then uniform plug flow of the liquid would need to exist, but as seen from Fig. 6.4 and the tracer work Fig. 5.7, there is significant maldistribution of gas and liquid in the rotor. As the new sampling system takes the liquid sample from just one point in the machine for each radial depth, it is fair to say that this sample will not be representative of the entire rotor. Therefore the findings displayed in Figs. 6.2 - 6.4 may be misleading, and so it was decided to make all the four sample tubes of equal length so that the liquid sample could come from four points on the same radius at 90° to each other. The result would be an average, and hopefully much more representative, of the overall mass transfer performance achieved by the rotor.

6.5.1. Declon HC20 Packing

The following Figures 6.8, 6.9 show the *average mass transfer performance* of the rotor at the Full and 1/2 radial lengths for the Declon HC20 packing. The experimental data may be found in Appendix VII.

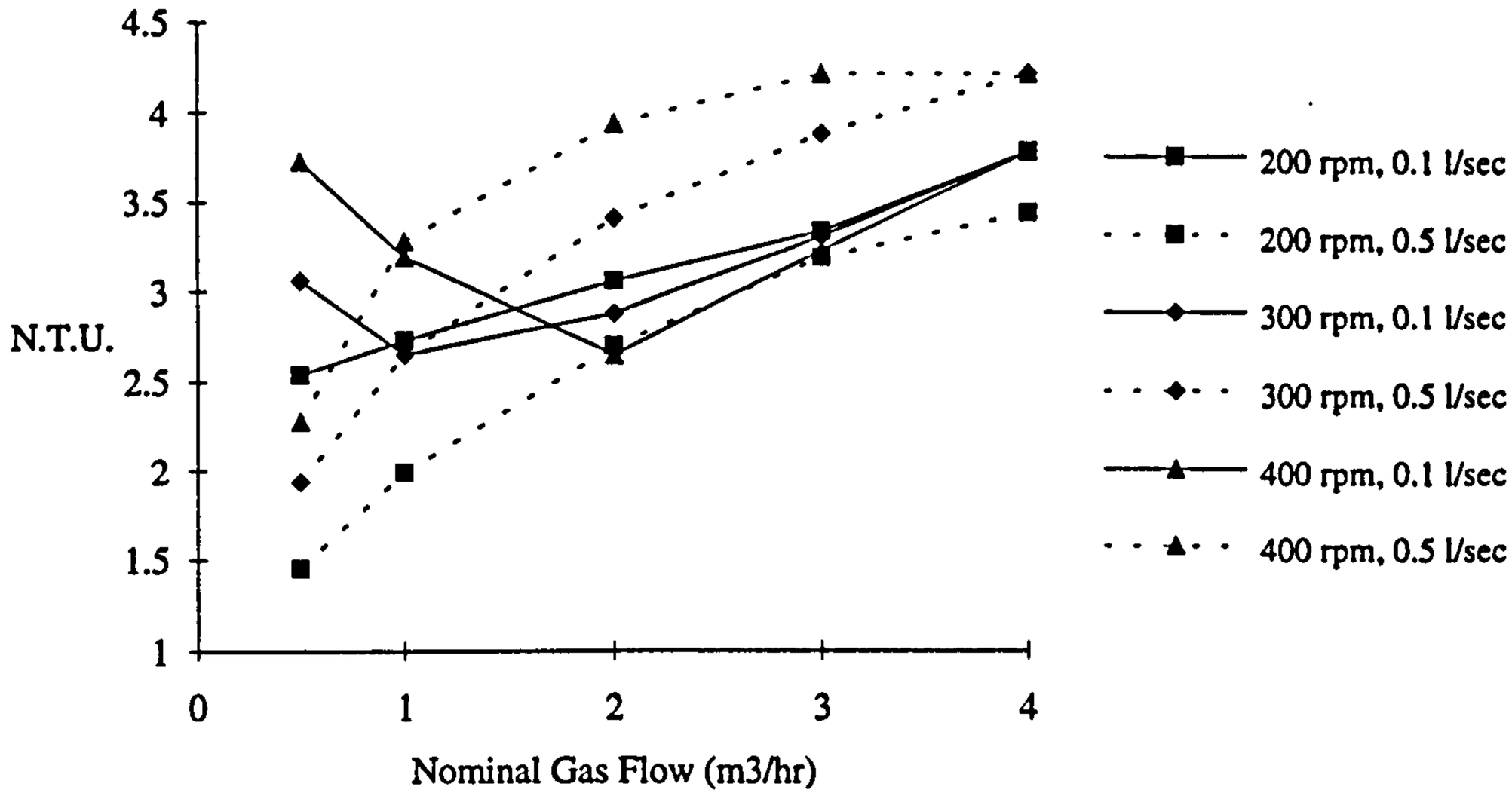

Figure 6.8 : Mass Transfer Results at Full Radial Length, Declon HC20 Packing
(average of 4 sampling points)

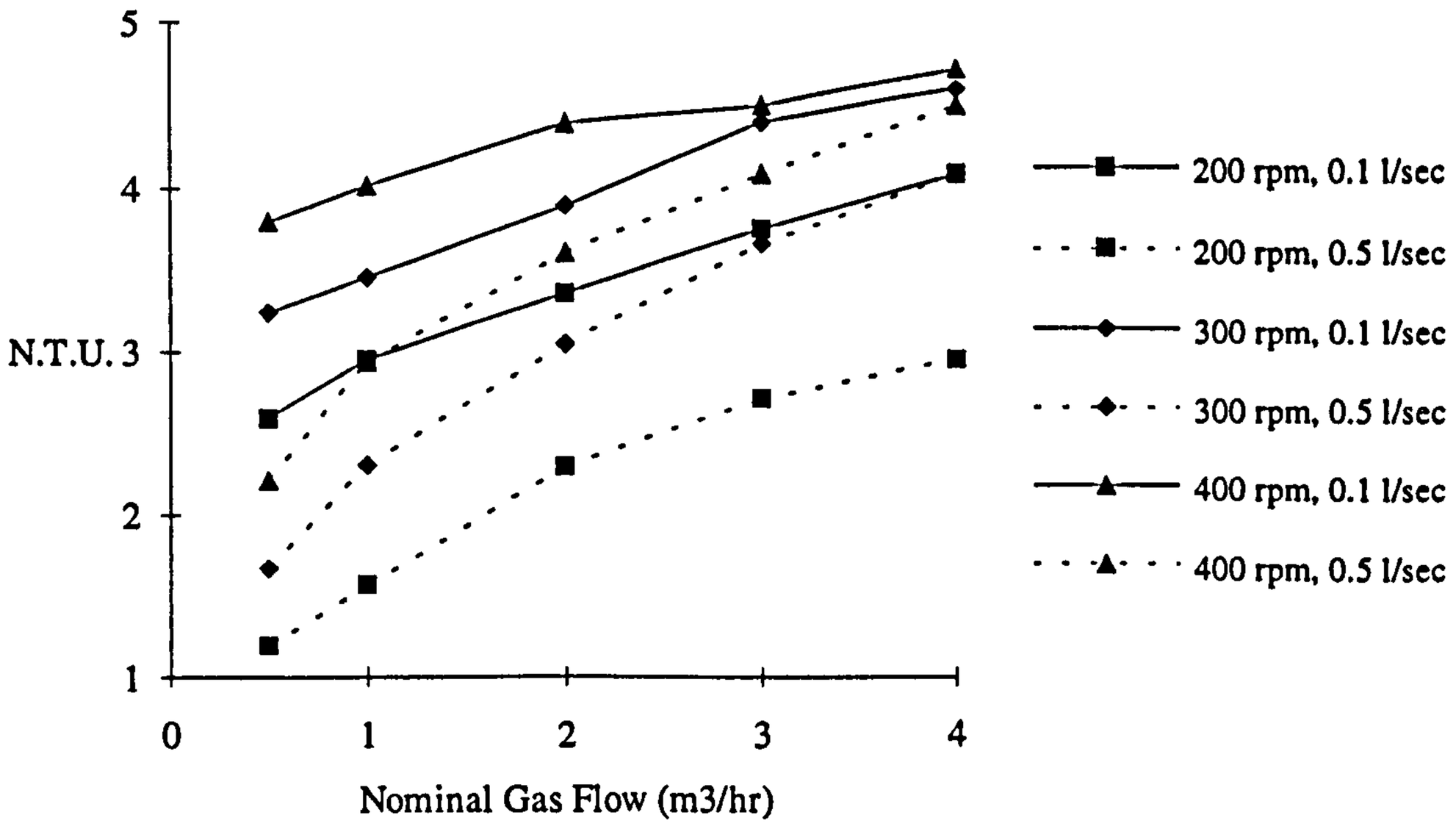

Figure 6.9 : Mass Transfer Results at 1/2 Radial Length, Declon HC20 Packing
(average of 4 sampling points)

6.5.2 Declon HC30 Packing

Figures 6.10, 6.11 show the mass transfer performance of the rotor at the same radial positions using the finer Declon HC30 packing type. The experimental data for these is found in Appendix VII.

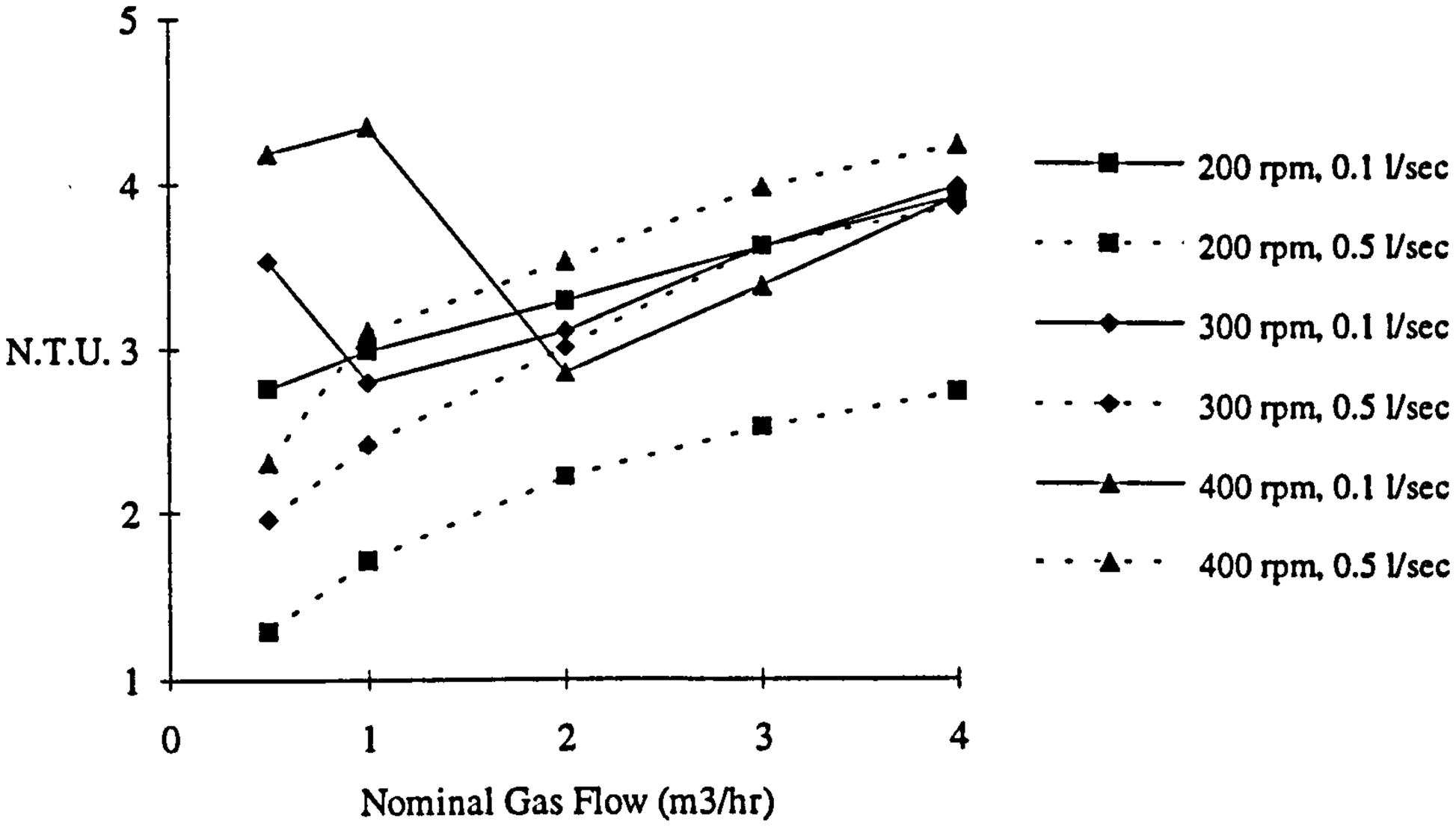

Figure 6.10 : Mass Transfer Results at Full Radial Length, Declon HC30 Packing
(average of 4 sampling points)

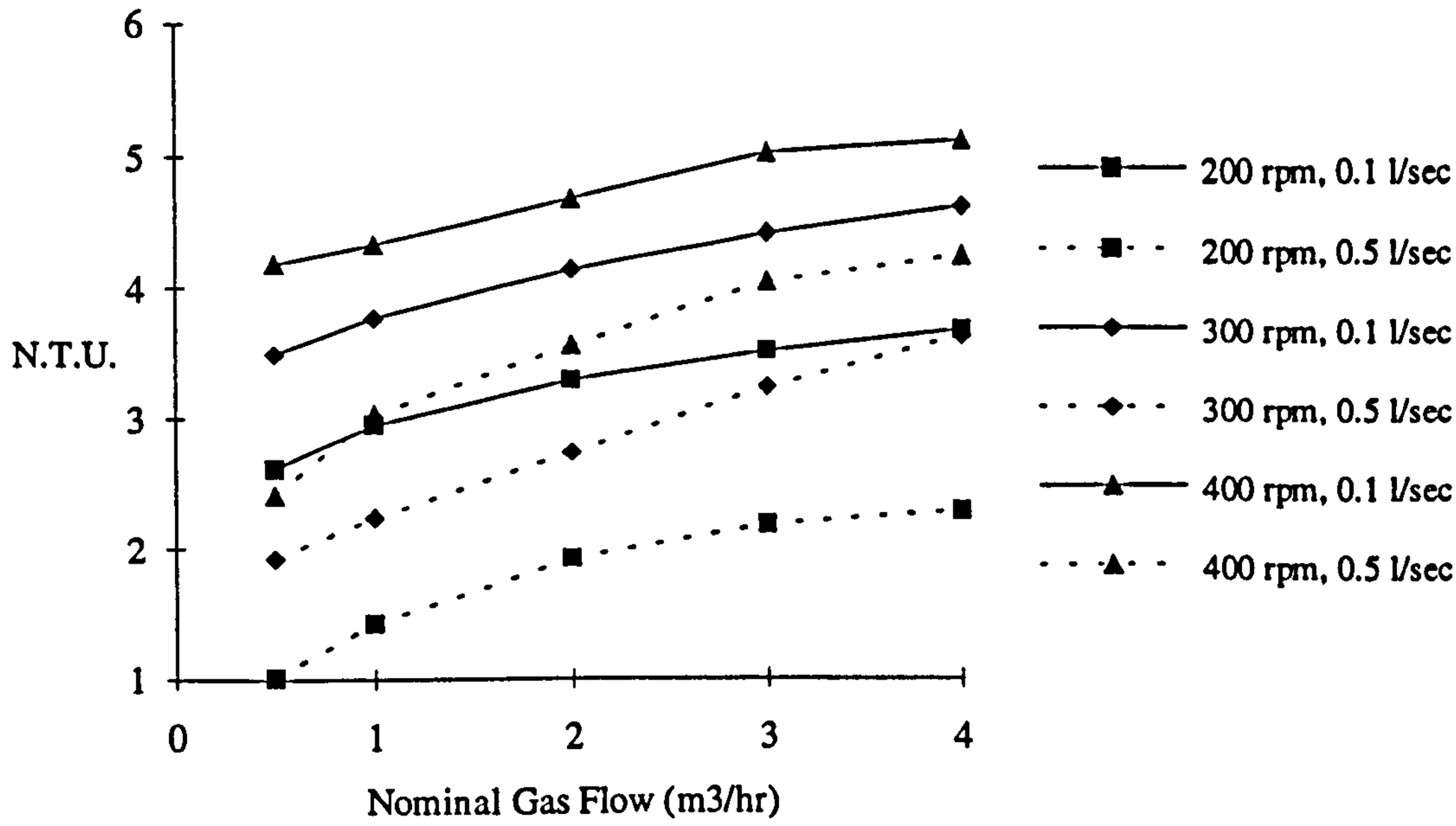

Figure 6.11 : Mass Transfer Results at 1/2 Radial Length, Declon HC30 Packing
(average of 4 sampling points)

Comparing the above findings, the following graph shows the effect of packing type and radial length on the mass transfer performance of the rotor :

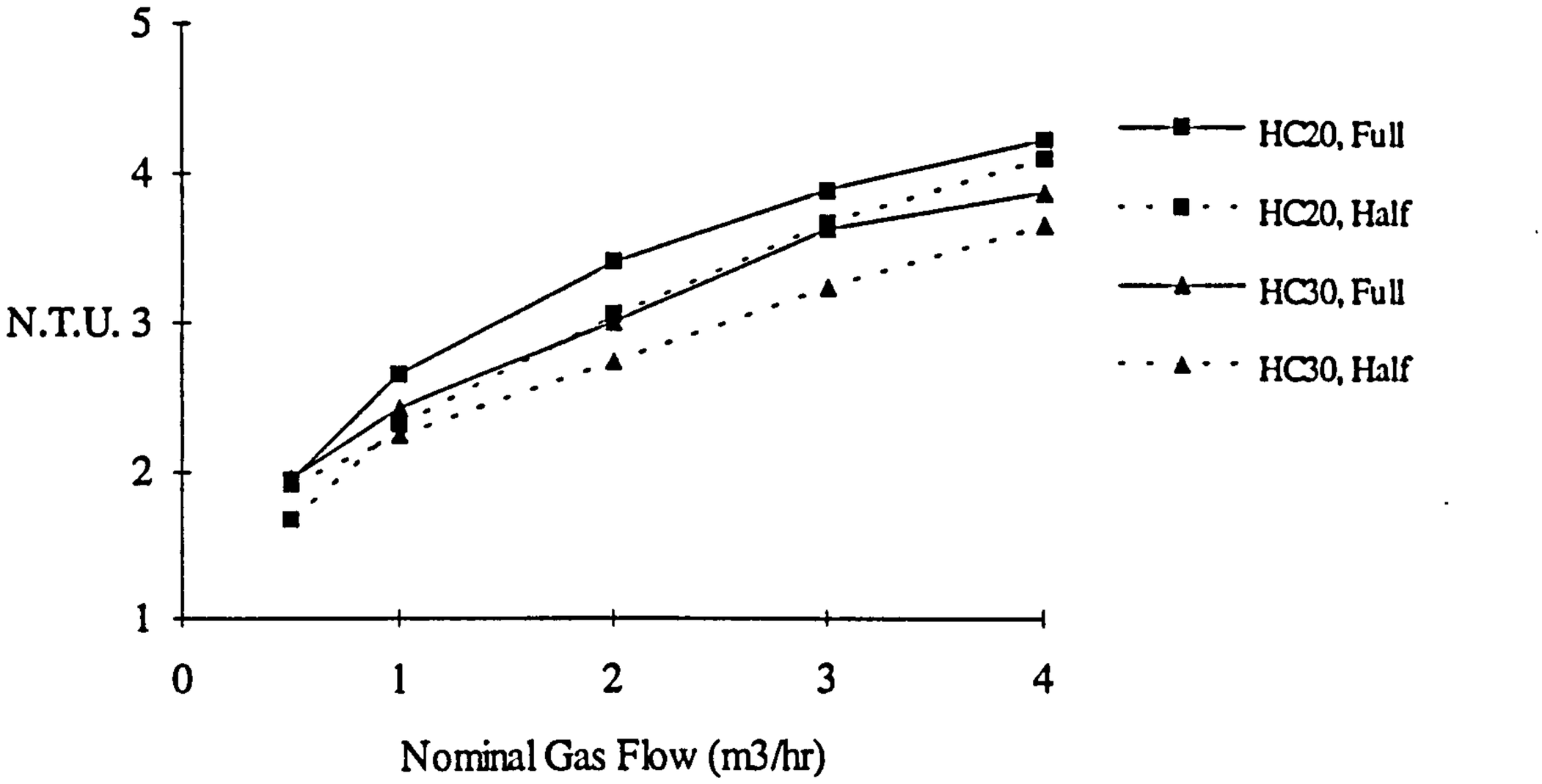

Figure 6.12 : Effect of Packing Type and Radial Depth on Overall Rotor Mass Transfer at a Liquid Flowrate of 0.5 l/sec, and Speed 300 rpm

6.5.3 Conclusions

The following conclusions can be made from the above graphs about the overall mass transfer performance of the rotor :

1. At the low liquid flowrate Figures 6.8, 6.10 show the mass transfer to fall and then rise as the gas flow increases. This confirms that there is still significant maldistribution and backmixing of liquid in the rotor. Increasing the rotational speed appears to exacerbate this effect.
2. For higher liquid throughputs the mass transfer performance of the rotor shows regular trends, i.e. increasing speed and gas flow, increases the mass transfer achieved. A much improved liquid distribution throughout the rotor therefore would seem to exist. This observation is consistent with the tracer findings in section 5.3.3.4.
3. The mass transfer at the 1/2 radial length *does not equal* 1/2 of the mass transfer at the full radial length as shown in Figure 6.12. Generally, for the high liquid flowrate, the mass transfer at the 1/2 radial depth is less than that of the full radial length but not significantly, and no fixed pattern linking the mass transfer and the radial depth can be seen.
4. Figure 6.12 also shows that the finer Declon HC30 packing produces similar results to that of the HC20 packing, and there is no improvement, and possibly even a decrease, in the overall mass transfer performance of the rotor.

6.6 Salt Water

Section 5.5 showed the preliminary hydrodynamic findings in terms of bubble size using salt water instead of ordinary water through the 1 m diameter rotor. As previously reported in that section, limited work was carried out due to the corrosive nature of the salt water on the aluminium rotor, and therefore the following mass transfer results are only the initial findings. The mass transfer data was taken at the *Full radial packed depth* using the new sampling system as used in section 6.3, i.e. only one sample point at each circumferential position. Therefore it is only possible to compare the mass transfer data taken for the salt water with that of ordinary water taken using the exact same sampling method, i.e. the full packed length data displayed in section 6.3. The data for the salt water performance can be found in Appendix V Table (f), and Figure 6.13 displays these preliminary findings.

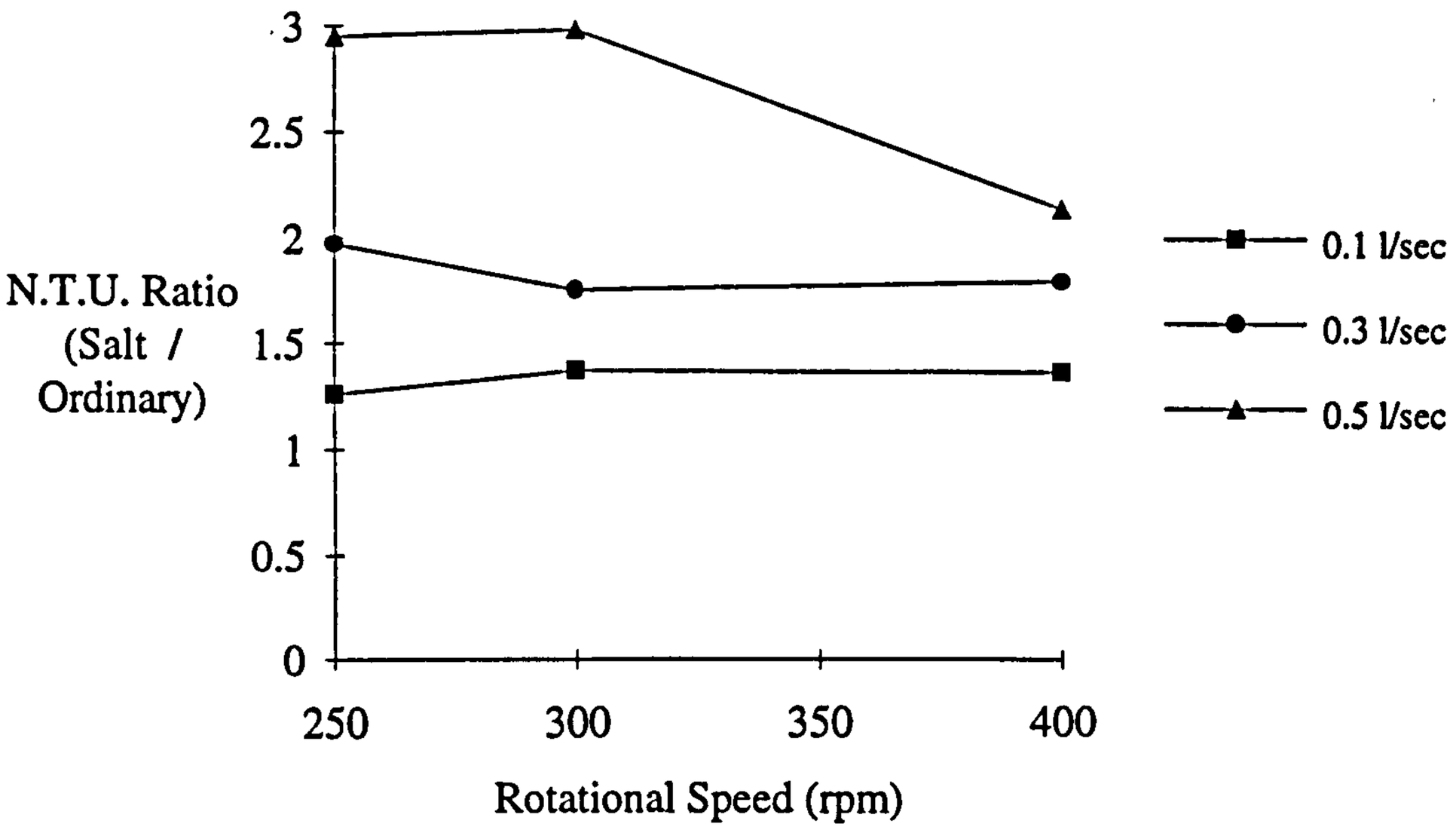

Figure 6.13 : Mass Transfer Performance of Salt to Ordinary Water at 3 Liquid Flows, and Nominal Gas Flow 0.5 m^3/hr,

Clearly the results are not as reliable as if *average sample values* had been found. However the following conclusions may be drawn from the above graph :

1. The mass transfer performance with salt water is better than that attained with ordinary water as the ratio is greater than 1 for all the experimental conditions. This is especially the case at the high liquid flowrate where the ratio is as high as 3.
2. There is no fixed ratio between the performance of salt water to ordinary water, although as the liquid flowrate increases the mass transfer ratio also increases at all the above operating speeds.

3. The above results are preliminary findings and are by no means comprehensive, and therefore should be treated with some degree of caution.

The above findings are consistent with work previously cited by Hikita[30] (p.19), and by Balasundaram et al.[51] who concluded that, from work carried out on the 0.5 m diameter prototype machine, simulated sea water gave approximately twice the mass transfer performance as that produced by ordinary water.

6.7 Discussion

This completes the mass transfer work done on the rotor. It has been a long process reaching the point of being able to produce results with a high degree of confidence and consistency, but as Figure 6.14 demonstrates, the tolerance of the mass transfer data from the rotor should be within a range of ± 15%. Appendix VIII contains some of the repeated mass transfer results to verify this.

The actual findings of section 6.5.3 show that the mass transfer results at low liquid throughputs show irregularities implying that there exists significant maldistribution of liquid flow in the rotor. However, at the high liquid throughput of 0.5 l/s a more regular pattern in the overall mass transfer performance curve of the rotor is seen, suggesting that the liquid flow through the packing is not as disturbed. Another significant finding seems to be that there is no apparent link between the mass transfer achieved and the radial length, with the performance results obtained at the half length showing little difference to those obtained at the full radial length. This would tend to imply that the vast majority of the mass transfer between the gas and liquid must take place from the moment the liquid is sprayed into the packing and reaches half way along the liquid filled packed length. This may be an important finding for design purposes and needs to be explored further. The comparison between the Declon HC20 and HC30 packings shows little change in the overall mass transfer performance of the rotor. The introduction of the HC30 packing meant that the packing pore size fell from 1.27 mm to 0.85 mm on average, but as the gas bubble sizes observed are smaller than both these values it is likely that packing will have little effect in increasing the interfacial area and therefore the overall mass transfer. The primary role of the packing is therefore to promote a more uniform gas and liquid distribution throughout the entire rotor.

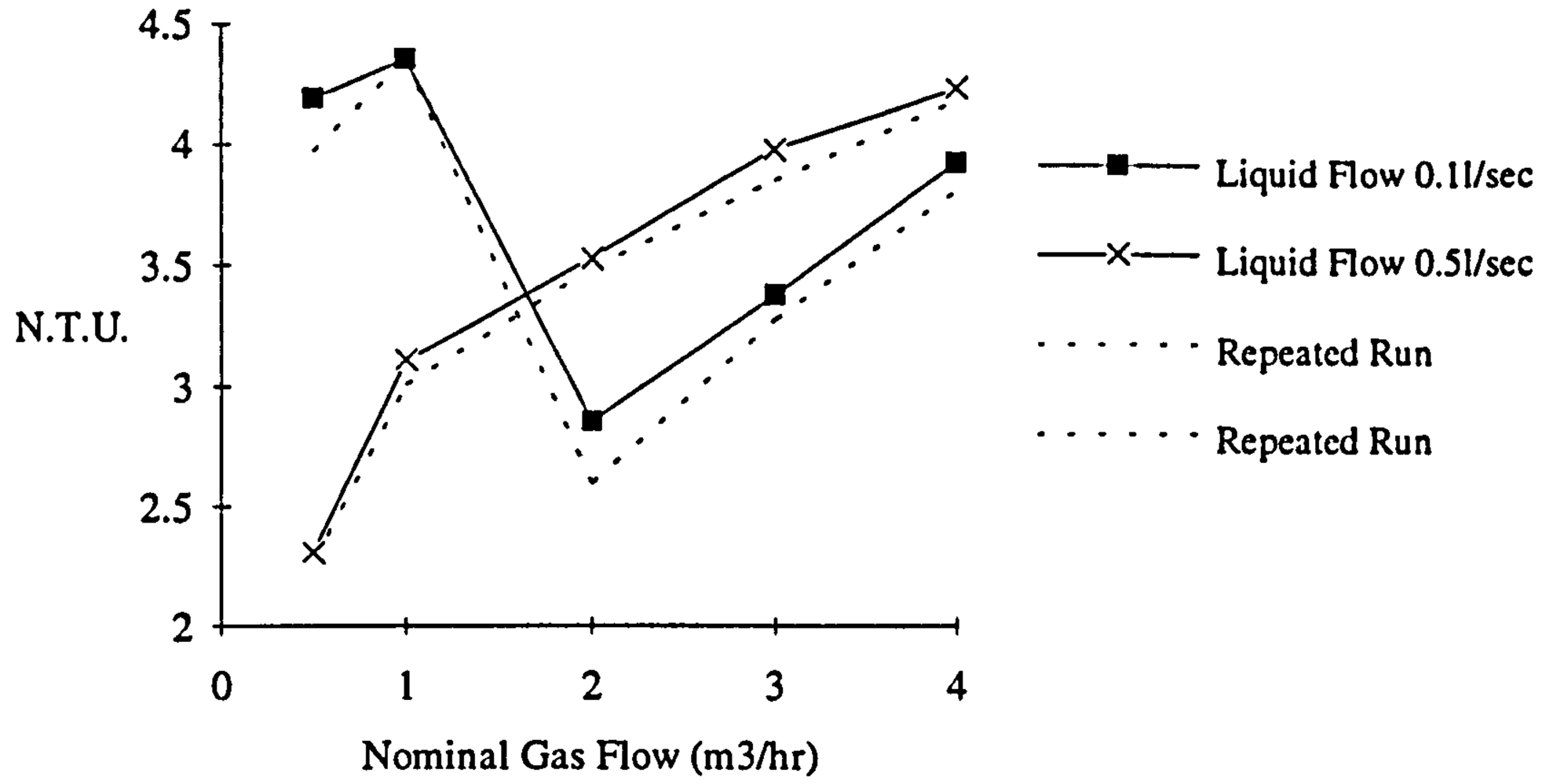

Figure 6.14 : Repeated Rotor Results at 400 rpm, Declon HC30 Packing

The actual industrial required mass transfer performance of a rotor should be 6 - 7 transfer units, i.e. a reduction from 9 ppm to 20 ppb. Traditional industrial stripping towers operate around equal gas to liquid volumetric ratios at s.t.p. to achieve this performance, and Table 6.1 below shows the experimental rotor performance under these operating conditions. The results shown are taken from Fig. 6.8, and in order to find the mass transfer at equal gas to liquid volumetric flowrates the nominal gas flow has to be guessed, the gas operating pressure then found from Table (a) Appendix V, and finally the adjusted gas flow at s.t.p. is calculated using the method described in Appendix III.

Table 6.1 : Rotor Mass Transfer Results for Equal Gas to Liquid Ratio (0.5 l/sec)

Nominal Gas Flow (m^3/hr)	Rotational Speed (rpm)	Gas Pressure (Bar a)	Adjusted Flowrate at s.t.p. (l/sec)	Rotor Results N.T.U.
1.4	200	1.60	0.52	2.3
1.2	300	1.85	0.48	2.8
1.1	400	2.35	0.50	3.4

The above results are encouraging showing that at 400 rpm approximately half of the required mass transfer is achieved in a packed length of 20 cm, corresponding to an average height of a transfer unit of 5.9 cm. The operating range of the rotor is very small, and although at the current stage the liquid throughput is low, this can be improved in a number of ways by increasing the axial width of the packing, the rotational speed, and re-designing the method for the liquid removal. The liquid removal method is mentioned in the 'Recommendations for

Future Work' (chapter 8), and being able to increase the liquid flowrate through the rotor is certainly the way forward for this program of research.

Finally the preliminary investigations into the performance of salt water in the rotor revealed that the mass transfer for salt water was greater than that for ordinary water under the same operating conditions although no fixed ratio performance between the two could be found. However as shown in section 5.5 the gas flowrate through the rotor was severely limited due to the foaming that occurred, and so the range of operation when using salt water is noticeably reduced. This area needs further investigation which would need to be carried out in a stainless steel rotary machine, and again has been recommended as future work to be undertaken.

CHAPTER 7 : CONCLUSIONS

The research in this thesis on using a 1 metre diameter rotor to generate high centrifugal acceleration in which to perform the stripping of oxygen from water can be divided into three main areas, those being the modelling of the process, the hydrodynamics of the gas and liquid in the rotor packing, and the mass transfer achieved between the two phases. From this work the following conclusions were made :

7.1 Rotor Model (Ch. 4)

1. The model of the continuous liquid phase rotor shows some success in accurately predicting the mass transfer performance at low gas to liquid ratios (typically 1 : 1) using Hughmark's correlation (Eqn. 2.17), although as this ratio increases the model trend is to over predict the amount of mass transfer that is achieved in the rotor. Other correlations could be used to predict the mass transfer more accurately at these higher ratios, but it would be useful in finding just one correlation that would satisfy all operating conditions.

2. The assumption of the model that the bubbles will migrate through the packing at their critical bubble size seems reasonable as the predicted bubble sizes corresponded reasonably well with those found experimentally (as shown in Table 5.3).

3. The model is an over-simplification of the 'real life' picture and does not take into account many phenomena that are known to be taking place inside the packing. Bubble collisions leading to splitting or coalescence produce a range of bubble sizes at any one point in the rotor rather than the single size predicted by the model, and the size distributions in high gravitational accelerations have been shown to be Gaussian in nature[7]. The liquid flow through the rotor is also complicated with significant back mixing and maldistribution occurring especially at high gas to liquid ratios. This is not taken into account by the model and may be the reason why the model tends to over predict the mass transfer performance of the rotor at these higher ratios.

7.2 Rotor Hydrodynamics (Ch. 5)

4. From the extensive hydrodynamic research carried out on the rotor the gas injector nozzle design, in particular the pressure drop, and the liquid flowrate were the two key parameters for achieving good gas and liquid distribution throughout the packing inside the rotor.

5. By increasing the pressure drop across the gas nozzles the fraction of the overall pressure drop due to the liquid pool pressure becomes smaller and therefore the difference in liquid head around the rotor becomes less significant resulting in a more uniform peripheral distribution of gas from the nozzles.

6. Using a tracer technique, the output responses showed the liquid flow through the rotor to contain severe maldistribution and back mixing which are detrimental to the overall performance of the rotor. The maldistribution was more pronounced at low liquid flowrates, typically 0.1 l/sec, and high gas to liquid ratios, but as the liquid flow was increased to its maximum throughput value of 0.5 l/sec, the distribution around the periphery of the machine became more uniform.

7. A multi-parameter tanks-in-series model was found to be able to accurately describe the residence time distribution curves from the rotor for all the experimental conditions chosen. The results from this model in all cases showed the number of tanks in series to be large, typically 40 - 50, with the effects of both the gas flow and rotational speed being small. However the range of rotational speed analysed was small, and its effect may be more pronounced if a larger range of speeds were chosen. The liquid flow showed itself to be the dominating parameter, and both the average times in the active and delay regions of the model were significantly higher at the lower flowrate. The result of this shows a shift in the position of the peak and an elongation in the exponential tail of the distribution.

8. The gas bubble analysis confirmed the gas maldistribution in the rotor that was seen with the original gas injector design. The photographic analysis for any one point in the packing showed the bubbles to cover a range of sizes with an approximate average size estimated from visual analysis. These bubble sizes corresponded very well with those found by Alshaban[7] in his experimental work. As mentioned earlier in (2), the experimental sizes also corresponded fairly closely to the critical bubble size predicted in the model, although the actual experimental size was consistently less than the predicted size. The effect of the rotational speed was to decrease the average bubble size, and typical values show the average size at 200 rpm to be 0.9 mm whereas at 300 rpm the size is 0.5 mm.

9. As the bubble stream from the gas nozzles could not be seen clearly, it is impossible to determine the effect of the orifice diameter on the bubble size of formation. However photographic analysis of the bubbles with the modified nozzles helped to confirm the improved gas distribution through the rotor. The bubble size showed a slight increase as the bubbles migrated towards the centre of the rotor, with a definite increase in the gas hold-up being seen.

10. The hydrodynamic characteristics of the rotor differ considerably when using salt water to simulate sea water instead of ordinary water. The gas bubble sizes produced are smaller but substantial foaming is seen at the interface, thus lowering the operating threshold of the rotor at which flooding starts to take place.

7.3 Rotor Mass Transfer (Ch. 6)

11. The maldistribution of the gas and liquid through the rotor was reflected in the initial mass transfer findings, which showed better mass transfer at the lower rotational speed of 200 rpm than at the higher speed of 300 rpm.

12. Having modified the gas nozzles and the liquid sampling system from the rotor , the mass transfer performance achieved by the rotor with the Declon HC20 packing was 2.3 - 3.4 transfer units for rotational speeds ranging from 200 - 400 rpm and equal gas to liquid flowrate ratios. This corresponds to the height of a transfer unit of between 8.2 - 5.6 cm.

13. The general mass transfer trends shown by the rotor are :
    (i) As the gas flow increases for a constant speed and liquid flow the mass transfer increases.
    (ii) As the liquid flow increases for a constant speed and gas flow the mass transfer falls.
    (iii) As the rotational speed is increased for a constant gas and liquid flow the mass transfer increases.
    (iv) The mass transfer achieved at half the radial packed length does not equal half the mass transfer achieved at the full radial length, and no obvious correlation linking the mass transfer to the radial length can be seen.
    (v) There is no significant improvement in the mass transfer performance of the rotor when using the finer Declon HC30 packing instead of the original Declon HC20 packing.

14. Some irregularities in the mass transfer performance can still be seen at the low liquid flowrate of 0.1 l/sec as the gas flow is increased, confirming that at the low liquid flow significant back mixing is still occurring in the rotor.

15. The inclusion of 48 radial vanes into the packing had a detrimental effect on the overall mass transfer performance of the rotor.

16. The preliminary mass transfer findings using salt water showed a factor of 1.5 - 3 improvement in the mass transfer achieved compared with that of ordinary water under identical operating conditions, although no fixed ratio between the performances could be seen. In fact, the performance ratio increased as the liquid flowrate increased.

CHAPTER 8 : RECOMMENDATIONS FOR FUTURE WORK

As with any research carried out in a limited time span, there are always further areas of investigation that may need to be covered. Before the implementation of such knowledge can be made into the oil industry, the following are some suggestions for further areas of research that would be useful to investigate :

1. The importance of an effective gas nozzle design has been shown during the course of this research and various nozzle designs should be tested in order to try and generate uniform small bubbles around the periphery of the rotor. One method of generating uniform small bubbles that is currently being investigated at Newcastle University is the use of slot nozzles typically less than 0.25 mm in width, for which initial work has shown prolific generation of small bubbles across the whole slot length at discrete intervals[60]. The application of the slot nozzle design to high gravitational environments may prove to be effective at producing small uniform bubbles around the periphery, and should therefore be tried on the rotor.

2. It would be useful to characterise the gas flow through the rotor and calculate the effectiveness of the packing in gas-liquid contacting for various nozzle designs.

3. Characterisation of the liquid flow through the rotor revealed significant improvements in the liquid flow and distribution as the liquid flow was increased from 0.1 - 0.5 l/sec. However the liquid flow through the machine is still small and limited at present by the hydraulic capacity of the pick-up tubes at the back of the rotor, which is dependant upon the rotational speed and frictional losses of the tubes. One suggestion for improving the liquid flow through the rotor would be to remove the pick-up tubes and let the back plate act as a weir, with a stationary liquid collection chamber situated adjacent to the plate to catch the water as it leaves. Experimental work by Lee[46] has shown the hydraulic capacity of the weir to be independent of the rotational speed and far superior to that of the pick-up tubes due to the larger area for flow.

4. Further work needs to be investigated to see how the mass transfer varies in the rotor along the radial depth. The research in this thesis has shown there to be little difference in the mass transfer achieved at the half radial length compared with that at the full radial length, and therefore some research should be carried out investigating the mass transfer profile of the liquid from the moment it enters the rotor packing until it passes by the gas injector nozzles.

5. Preliminary experimental work has been carried out in the rotor using salt water due to its corrosive nature when in contact with aluminium, but as sea water would be used in off-shore applications, further and more extensive research into the hydrodynamics and mass transfer of sea water, by using simulated salt water, in high gravitational fields needs to be carried out. This may include exploring the foaming characteristics and methods of suppressing this, tracer work in order to compare the flow patterns of salt water with ordinary water through a rotating packed bed, and further mass transfer studies to see if any correlation or link may be found between the performance of sea water and ordinary water. It would also be beneficial to investigate the effect of the surface tension of the liquid used in the rotor, and how this property effects the overall mass transfer performance.

6. Although much work has been done in producing a model that accurately describes the real phenomena that occur in the rotor, it has been shown that the model cannot accurately describe all the experimental observations, and possible ways of improving the accuracy and robustness of the model for all operating conditions should be investigated. These may include accounting for the liquid distribution through the packing as modelled by the multi-parameter model, and by also introducing a gas bubble size distribution rather than just a single size to account for bubble coalescence and splitting. Also at present the mass transfer is predicted using equation 2.5 for each segment and summed to give the overall mass transfer, but it may be more useful to predict the mass transfer to each bubble using equation 2.0, as a detailed understanding of where the mass transfer takes place within the rotor packing is not known.

Nomenclature

Symbol		Meaning	Units
English Alphabet			
A	-	cross sectional area of column	(m^2)
A_p	-	projected area	(m^2)
a	-	interfacial area	(m^2/m^3)
a_e	-	effective interfacial area	(m^2/m^3)
a_t	-	specific surface area of packing	(m^2/m^3)
a_w	-	wetted surface area of packing	(m^2/m^3)
C_d	-	drag coefficient	
C	-	concentration	($kmol/m^3$)
C_e	-	equilibrium concentration	($kmol/m^3$)
C_i	-	interfacial concentration	($kmol/m^3$)
C_T	-	overall concentration	($kmol/m^3$)
D	-	diffusivity	(m^2/sec)
D_{ax}	-	axial dispersion coefficient	(m^2/sec)
D_l	-	liquid diffusivity	(m^2/sec)
D_{or}	-	orifice diameter	(m)
d_b	-	diameter of bubble	(m)
d_c	-	critical bubble size	(m)
d_p	-	packing pore diameter	(m)
d_s	-	Sauter mean bubble diameter	(m)
E	-	residence time distribution	
f	-	fraction of fluid delayed	
f_1	-	fraction of fluid delayed once	
G	-	gas mass flux	(kg/m^2 sec)
G_m	-	molar gas flux (solute free basis)	($kmol/m^2$ s)
g	-	acceleration due to gravity	(m/sec^2)
g*	-	centrifugal acceleration	(m/sec^2)
H	-	Henry's Constant	(atm)
H_l	-	height of a transfer unit based on liquid phase	(m)
H_{TU}	-	height of a single transfer unit	(m)
h	-	liquid height in rotor	(m)
K_l	-	overall mass transfer coefficient based on liquid film	(m/sec)
k_g	-	gas film mass transfer coefficient	(m/sec)

Symbol		Meaning	Units
k_l	-	liquid film mass transfer coefficient	(m/sec)
L_m	-	molar liquid flux (solute free basis)	(kmol/m^2 s)
L	-	liquid mass flux	(kg/m^2 sec)
L	-	length or height	(m)
m	-	equilibrium constant	
m'	-	mass flux	(kg/m^2 sec)
N	-	number of tanks in series	
N_{TU}	-	number of mass transfer units	
P	-	Pressure	(N/m^2)
P_T	-	total gas pressure	(atm)
Q	-	gas volumteric flowrate	(m^3/sec)
R	-	universal gas constant	(J/mol-k)
r	-	radial depth	(m)
r_b	-	bubble radius	(cm)
T	-	temperature	(k)
t	-	time	(secs)
$\bar{t}$	-	mean residence time per tank	(secs)
t_f	-	packing filament thickness	(m)
u	-	average flow velocity	(m/sec)
u_g	-	gas superficial velocity	(m/sec)
u_I*	-	interfacial momentum transfer velocity	(m/sec)
u_{or}	-	gas velocity through nozzle orifice	(m/sec)
u_l	-	liquid superficial velocity	(m/sec)
u_r	-	relative velocity	(m/sec)
u_t	-	terminal velocity of a bubble	(m/sec)
V_b	-	volume of bubble	(m^3)
V_E	-	volume of bubble generated during expansion	(m^3)
V_g	-	gas volumetric flowrate	(m^3/sec)
V_l	-	liquid volumetric flowrate	(m^3/sec)
X	-	molar ratio in liquid phase	
x	-	mole fraction in liquid phase	
x	-	length along x axis	(m)
x_e	-	equilibrium mole fraction in liquid phase	
Y	-	molar ratio in gas phase	
y	-	mole fraction in gas phase	
z	-	height of column	(m)
z	-	dimensionless length	

Symbol		Meaning	Units
Dimensionless Quantities			
Fr	-	Froude Number	$(u/\sqrt{(gd)})$
Re	-	Reynolds Number	$(\rho ud/\mu)$
Sc	-	Schmidt Number	$(\mu/\rho D)$
Sh	-	Sherwood Number	$(k_l d/D)$
$\frac{R}{\rho u^2}$	-	Friction Factor	
Greek Alphabet			
δ	-	film thickness	(m)
ε	-	packing voidage	
ϕ_g	-	gas hold-up	
ρ_g	-	gas density	(kg/m^3)
ρ_l	-	liquid density	(kg/m^3)
$\Delta\rho$	-	density difference between phases	(kg/m^3)
σ	-	surface tension	(N/m)
μ_l	-	liquid viscosity	(kg/m sec)
μ_g	-	gas viscosity	(kg/m sec)
υ	-	kinematic liquid viscosity	(m^2/sec)
ν	-	specific volume	(m^3/kg)
θ	-	dimensionless time unit	
τ_f	-	bubble detachment time	(sec)
ζ	-	dimensionless parameter	
ω	-	angular velocity	(sec^{-1})
$\psi()$	-	unit step function	

BIBLIOGRAPHY

1. W.T.Cross, C.Ramshaw - *Chem. Eng. Res. Des.*, **64**, pp.293 - 301, (July 1986)
2. L.W.Lake - Enhanced Oil Recovery, Prentice Hall ©1989
3. Our Industry Petroleum - British Petroleum Company Ltd. ©1977
4. C.Ramshaw - *The Chemical Engineer*, pp.13-14, (Feb. 1983)
5. C.Ramshaw - *The Chemical Engineer*, pp.30-33, (July 1985)
6. C.Ramshaw - *Heat Recovery Systems & CHP*, **13**, pp.493-513, (1993)
7. K.Alshaban - Bubble Sizes in Centrifugal Fields, Ph.D.Thesis 1990, Dept.of Chemical Engineering, University of Newcastle-upon-Tyne
8. C.Ramshaw, J.Thornton - I.Chem.E. Symposium Series no.26, p.73, (1967)
9. T.K.Sherwood, R.L.Pigford - Absorption and Extraction, McGraw-Hill ©1952
10. J.Humphrey, A.Seibert, R.Koort - Separation Technologies Advances and Priorities, Final Report for U.S. Dept. of Energy (Feb.1991)
11. 'North Sea's First Big Flood Project Nears Peak Injection Rate' - *Oil & Gas J.*, **76**, pp.120-128, (1978)
12. A.Ostroff - Introduction to Oilfield Water Technology, Official NACE publication ©1979
13. C.Zheng - Beijing University of Chemical Technology, Dept. Chemical Engineering, Beijing. (Private Communication)
14. Orbisphere Laboratories - Technical Data, Orbisphere Labs., Staveley Hall, Chesterfield.
15. J.Coulson , J.Richardson - Chemical Engineering Volume 2, Pergamon Press
16. J.Backhurst, J.Harker -Process Plant Design, Heinemann Chemical Engineering Series © 1983
17. Perry R.H. - Perry's Chemical Engineers' Handbook (6th Edition), McGraw Hill
18. J.Coulson, J.Richardson - Chemical Engineering Volume 1 (3rd Edition), Pergamon Press © 1988
19. R.Higbie - *Trans.Am.Inst.Chem.Engrs.*, **31**, pp.365-388, (1935)
20. P.Danckwerts - Gas Liquid Reactions, pp.100-102, McGraw Hill ©1970
21. H.Toor, J.Marchello - *AIChemE.J.*, **4**, (1958)
22. K.Onda, E.Sado, Y.Murase, - *A.I.Chem.E.J.*, **5**, pp.235-239, (1959)
23. F.Valentin - Absorption in Gas Liquid Dispersions, E.&F.N. Spon Ltd ©1967
24. A.Cockx, M.Roustan, A.Line, G.Hebrard, - Modelling of Mass Transfer Coefficient in Bubble Columns. Dept.Genie des Procedes Industriels, EA833, INSA, 31077, Toulouse Cedex, France.
25. W.L.McCabe, J.Smith, P.Harriot - Unit Operations for Chemical Engineering (5th Edition), McGraw Hill ©1993
26. R.E.Treybal - Mass Transfer Operations (3rd Edition), McGraw Hill ©1980

27.K.Onda, H.Takeuchi, Y.Okumoto, - *J.Chem.Eng.Japan*, **1**, pp.56-16, (1968)

28.P.Calderbank, S.Jones, - *Trans.Inst.Chem.Eng.*, **39**, pp.363, (1961)

29.G.A.Hughmark, - *Ind.Eng.Chem.Process Des.Dev.*, **6**, pp.218-220, (1967)

30.H.Hikita, S.Asai, K.Tanigawa, K.Segawa, M.Kitao, - *Chem.Eng.J.*, **22**, pp.61-69, (1981)

31.F.Kastanek, J.Zahradnik, J.Kratochvil, J.Cermak - Chemical Reactors for Gas-Liquid Systems, Ellis Horwood (English Edition) ©1993, Chapter 3

32.O.Levenspiel - Chemical Reaction Engineering (2nd Edition), John Wiley & Sons Ltd © 1972

33.O.Levenspiel, W.Smith - *Chem.Eng.Sci.* **6**, pp.227-233 (1957)

34.R.Jackson - *The Chemical Engineer* pp.107-118 (May 1964)

35.J.Davidson, B.Schuler - *Trans.Inst.Chem.Eng.*, **38**, pp.335-341, (1960)

36.D.Azbel - Two Phase Flows in Chemical Engineering, Cambridge University Press ©1981

37.L.M. Milne-Thomson - Theoretical Hydrodynamics (5th Edition), Macmillan & Co. Ltd, © 1968 pp.244-247, 490-491

38.P.Calderbank, M.Moo-Young, R.Bibby - *Proc. Third European Symposium Chem. Reaction Eng.*, Amsterdam, (Sept.1964). Suppl. *Chem.Eng.Sci.*, **20**, (1965)

39.N.de Nevers, J-L.Wu - *A.I.Chem.E.J.* **17** pp.182-186 (January 1971)

40.O.Molerus - Principles of Flow in Disperse Systems, Chapman & Hall ©1993, Ch.4

41.M.Motarjemi, G.Jameson - *Chem.Eng.Sci,* **33**, pp.1418, (1978)

42.H.Allen - *Phil.Mag.*, **50**, pp.323-338, (1900)

43.W.D.Deckwer - Bubble Column Reactors, John Wiley & Sons Ltd ©1992

44.K.Schugerl, J.Lucke, U.Oels, - *Adv.Biochem.Eng.*, **7**, pp.21-33, (1977)

45.A.Bridge, L.Lapidus, J.Elgin, - *A.I.Chem.E.J.*, **10**, pp.819-826, (1964)

46.J.Lee - 'Liquid-Liquid Extraction in Centrifugal Fields' PhD Thesis (1993), Dept. Chemical Engineering, University of Newcastle-upon-Tyne

47.M.Keyvani, N.Gardner, - *Chem.Eng.Prog.*, pp.48-52, (Sept. 1989)

48.J.Vivian, P.Brian, V.Krukonis, - *A.I.Chem.E.J.*, **11**, pp.1088-1091, (1965)

49.R.Fowler - AP Technology, Amersham, UK 1992 (private communication)

50.K.Al-Shaban, V.Balasundaram, C.Howarth, C.Ramshaw, J.Peel - Proceedings of the International Conference on Energy Efficiency in Process Technology (Athens 1992), pp.475 - 484, Elsevier Science Publishers ©1993

51.V.Balasundaram, J.Porter, C.Ramshaw - 5th BOC Priestley Conference 1985 - *R.Soc.Chem.* 80 pp.306-329

52.'Hydrodynamic and Mass Transfer Characteristics of Two Phase Flow in Rotating Packings' (Final Report), SERC Grant no. GR/F 23897, (May 1992)

53.J.Peel - Research Project, Dept. Chemical Engineering, Newcastle University, 1992

54.H.Tung, R.Mah - *Chem.Eng.Commun.*, **39**, pp.147-153, (1985)

55.S.Keenan - Research Project, University of Newcastle-upon-Tyne (1990)

56.J.Bickerman - Surface Chemistry for Industrial Research, Academic Press, pp.68-95, © 1948

57.V.Stanek - Fixed Bed Operations, Ellis Horwood, ©1994

58.T.Baker, T.Chilton, H.Vernon - *Trans.A.I.Chem.E.*, **31**, pp.296-313, (1935)

59.D.Gunn - *Chem.Eng.Sci.*, **33**, pp.1211-1219, (1978)

60.R.Li, A.Wraith, R.Harris - *Chem.Eng.Sci.*, **49**, pp.531-540, (1994)

APPENDIX I

The following is a listing of the Fortran 77 code used in the modelling of the 1m diameter rotor as detailed in Chapter 4 of this thesis. (It should be noted that all the various liquid film correlations tried have been left in the program, and the program is currently set to use subroutine MTCOEFF1 which uses the Penetration Theory model to predict the liquid film side coefficient.)

```
      program model
c     The following program models the rotor de-aerator

      real L,G,INI,Ro,Ri,t,pore,rmms,rmml,rmmg,rhol,rhog(120),mul,Dl,Tl,
     +gamma,gr(120),db(120),vt(120),vgr(120),r(120),hold(120),tothold,Rn
     +ew,Reb(120),q,b,Kl(120),Ntu,Nto,xin,GP(120)
      integer LS,US,INC,i,j,speed

c     main program
c     The main program calls up all the subroutines

      call intro
      call specs(Ro,Ri,t,pore,rmms,rmml,rmmg,rhol,mul,Dl,Tl,gamma)
      call operate(L,G,INC,INI,US,LS)

c     set up of output file to xgraph
      open(10,FILE='rotor.dat')
      write(10,*)'TitleText: Rotor Mass Transfer Results'
      write(10,*)'BoundBox: 1'
      write(10,*)'YLowLimit: 0.0'
      write(10,*)'YHighLimit: 10.0'
      write(10,*)'XLowLimit: 200.0'
      write(10,*)'XHighLimit: 500.0'
      write(10,*)'XUnitText: Speed (rpm)'
      write(10,*)'YUnitText: N.T.U.'
      write(10,*)
      write(10,*)'"Output"'

      speed = LS
1     write(*,2) speed
2     format(1x,'RESULTS AT ',I4,' RPM')
      write(*,*)'======= == ==== ==='
c     Modelling of the Hydrodynamic characteristics of the rotor
      do 10 j =1,50
      call gravity(speed,Ri,Ro,gr,r,rmmg,rhol,Tl,rhog,GP)
      call bubble(gr,gamma,rhol,rhog,mul,db,vt,vgr,r,t,L,G,hold,Reb,pore
     +)
```

```
      call totholdup(r,hold,tothold)
      if (tothold.GT.26) then
            write(*,3) tothold
3           format(1x,'Hold-up = ',F5.2,' %  Rotor Flooding !!')
            write(*,*)'Terminating Calculations...'
            goto 1000
      else
      call interface(tothold,Ro,Rnew)
      if (abs(Ri-Rnew).LT.0.001) then
            q = 0
            b = 0
            do 5 i = 1,100
            q = q + vt(i)
            b = b + db(i)
5           continue
            q = q/100
            b = b*10
            write(*,11) tothold
            write(*,12) q
            write(*,13) b
            write(*,14) Rnew
11          format(1x,'Average Rotor Hold-up =',F5.2,' %')
12          format(1x,'Average Gas Velocity through Rotor = ',F5.3,' m/s')
13          format(1x,'Average Gas Bubble Diameter = ',F5.3,' mm')
14          format(1x,'Radial Position of Gas-Liquid Interface = ',F5.3,' m')
            goto 15
      else
            Ri = Rnew
      endif
      endif
10    continue

c     Modelling of the Mass Transfer taking place in the rotor

15    xin = INI
      Nto = 0
      do 20 i = 1,100
      call mtcoeff1(i,Reb,Dl,rhol,mul,vgr,Kl)
      call height(i,Kl,L,r,t,db,hold,rhol,rmml,Ntu,Nto)
      call outlet(i,L,G,r,rhol,rmml,rmmg,t,Ntu,xin,GP)
20    continue
      write(*,24) Nto
      write(10,*) speed,Nto
      write(*,25) xin
24    format(1x,'N.T.U. = ',F5.3)
25    format(1x,'Oxygen conc out = ',F5.3,//)

      speed = speed +INC
      if (speed.GT.US) then
```

```
                write(*,*)'Calculations for the rotor are complete!!'
                goto 1000
        else
                goto 1
        endif
1000    end


c       The introduction telling the user what the program models
        subroutine INTRO
        write(*,*) 'COMPUTER SIMULATION OF A HIGEE ROTARY DE-AERATOR'
        write(*,*) '======== ========== == = ===== ====== =========='
        write(*,100)
        write(*,110)
100     format(1x,'The following program is a computer simulation for a ro
       +tor that strips oxygen',3x,'from water using an inert gas typicall
       +y nitrogen.')
110     format(1x,'The following list details the dimensions, operating co
       +nditions for the machine and physical property data for the gas an
       +d liquid phases.')
        return
        end


c       The details of the rotor, gas and liquid physical property data
        subroutine SPECS(Ro,Ri,t,pore,rmms,rmml,rmmg,rhol,mul,Dl,Tl,gamma)
        real Ro,Ri,t,pore,rmms,rmml,rmmg,rhol,mul,Dl,Tl,gamma
        write(*,*)
        write(*,*) 'ROTOR DESIGN SPECIFICATIONS'
        write(*,*) '===== ====== ==============='
        write(*,120)
        write(*,121)
120     format(1x,'Outer Radius of rotor = 0.505m',7x,'Outer Radius of pac
       +king = 0.445m',/,1x,'Gas Nozzle Radius     = 0.400m',7x,'Liquid Pi
       +ck-up Radius   = 0.210m')
121     format(1x,'Axial Packing Depth   = 0.012m',7x,'Packing pore size =
       + 1.3 - 1.7mm')
        Ro = 0.4
        Ri = 0.21
        t = 0.012
        pore = 0.0013
        write(*,*)
        write(*,*) 'PHYSICAL PROPERTY DATA'
        write(*,*) '======== ======== ===='
        write(*,122)
        write(*,123)
        write(*,124)
122     format(1x,'Liquid Used = Water',18x,'Stripping Gas = Nitrogen',/,1
       +x,'Dissolve Solute = Oxygen',13x,'Solute RMM = 32')
123     format(1x,'Liquid Temperature = 10 C',12x,'Liquid Density = 998 kg
```

```
     +/m3',/,1x,'Liquid Viscosity = 1.2*10-3 Ns/m2',4x,'Liquid RMM = 18'
     +)
124   format(1x,'Gas Density at S.T.P.= 1.25 kg/m3',4x,'Gas RMM = 28',/,
     +1x,'Liquid Diffusivity = 2.5*10-9 m2/s',3x,'Liquid Surface Tension
     + = 0.0723 N/m')
      rmms = 32
      rmml = 18
      rmmg = 28
      rhol = 998
      mul = 1.2E-3
      Dl = 2.5E-9
      Tl = 283
      gamma = 0.0723
      write(*,*)
      write(*,*) 'Press [Enter] key to continue '
      read(*,*)
      return
      end

c     Subroutine allowing the user to input the operating conditions
      subroutine OPERATE (L,G,INC,INI,US,LS)
      real L,G,INI
      integer LS,US,INC
      write(*,*) 'USER SPECIFIED OPERATING CONDITIONS'
      write(*,*) '==== ========= ========= ==========='
      write(*,*)
      write(*,130)
      read(*,*) LS
      write(*,131)
      read(*,*) US
      write(*,132)
      read(*,*) INC
      write(*,133)
      read(*,*) L
      write(*,134)
      read(*,*) G
      write(*,135)
      read(*,*) INI
130   format(1x,'Please Input the following Operating Conditions: -',//,
     +24x,'Lower Rotor Speed [rpm] : ')
131   format(24x,'Upper Rotor Speed [rpm] : ')
132   format(25x,'Speed Incremental Step : ')
133   format(26x,'Liquid Flowrate [l/s] : ')
134   format(19x,'Gas Flowrate at S.T.P. [l/s] : ')
135   format(21x,'Initial Oxygen Conc. [ppm] : ')
      return
      end

c     The gravity subroutine calculates the gravitational acceleration
```

```
c       in the rotor and the gas density as a function of the radial
c       depth for a given speed and stores the values in an array
        subroutine GRAVITY(speed,Ri,Ro,gr,r,rmmg,rhol,Tl,rhog,GP)
        real w,r(120),Ri,Ro,gr(120),rhol,rmmg,GP(120),Tl,rhog(120)
        integer speed,i
        w = speed*(3.142/30)
        r(1) = Ro
        do 150 i = 2,101
        r(i) = r(i-1)-((Ro-Ri)/100)
150     continue
        do 151 i = 1,100
        gr(i) = w*w*r(i)
        GP(i) = ((rhol*(w**2)/2)*((r(i)**2)-(Ri**2)))+101325
        rhog(i) =(rmmg*GP(i))/(8314.4*Tl)
151     continue
        return
        end

c       Subroutine to calculate the size of the bubbles produced
        subroutine BUBBLE(gr,gamma,rhol,rhog,mul,db,vt,vgr,r,t,L,G,hold,Re
       +b,pore)
        real db(120),Dor,gamma,gr(120),rhol,rhog(120),vt(120),vgr(120),mul
       +,L,G,Gnoz,pore,a,b,c
        integer i
        Dor = 1E-4
        do 160 i = 1,100
        if (i.eq.1) then
                Gnoz = G*(1.206/(1000*240*rhog(i)))
                db(i) = (1.378*6*(Gnoz**1.2)/(3.142*(gr(i)**0.6)))**0.3333
                if (db(i).GT.pore) then
                        db(i) = pore
                endif
                call holdup(i,r,t,G,rhog,hold,gr,db)
                call velocity(i,db,r,gr,rhol,rhog,mul,hold,t,L,vt,vgr,Reb)
        else
                a = 1.8*(rhol-rhog(i))*gr(i)
                b = rhog(i)*(vt(i-1))**2
                c = -3.12*gamma
                db(i) = ((((b*b)-4*a*c)**0.5)-b)/(2*a)
                if (db(i).GT.pore) then
                        db(i) = pore
                endif
                call holdup(i,r,t,G,rhog,hold,gr,db)
                call velocity(i,db,r,gr,rhol,rhog,mul,hold,t,L,vt,vgr,Reb)
        endif
160     continue
        return
        end
```

```
c       Subroutine to find the holdup at each interval and sum them
        subroutine HOLDUP(i,r,t,G,rhog,hold,gr,db)
        real G,t,r(120),hold(120),rhog(120),vg,rhogstp,gr(120),db(120)
        integer i

        rhogstp = 1.206
        vg = G*(rhogstp/rhog(i))/(1000*2*3.142*t*r(i))
        hold(i) = 0.91*((vg/((gr(i)*db(i))**0.5))**1.19)
        if (hold(i).GE.1) then
                hold(i)=hold(i-1)
        endif
        return
        end

c       Subroutine to find the terminal velocity of the bubbles
        subroutine VELOCITY(i,db,r,gr,rhol,rhog,mul,hold,t,L,vt,vgr,Reb)
        real db(120),gr(120),r(120),rhol,rhog(120),vt(120),cd,t,L,mul,vl,v
       +gr(120),z,Reb(120),hold(120)
        integer i
        cd = 0.444
164     vt(i) = (((4*db(i)*gr(i)*(rhol-rhog(i)))/(3*cd*rhol))**0.5)
        vl = L/(1000*2*3.142*t*r(i)*(1-hold(i)))
        vgr(i) = vt(i) + vl
        Reb(i) = (rhol*db(i)*vgr(i))/mul
        if (Reb(i).LT.2) then
                cd = 24/Reb(i)
        elseif (Reb(i).LT.500) then
                cd = 18.5/(Reb(i))**0.6
        else
                cd = 0.444
        endif
        z = (((4*db(i)*gr(i)*(rhol-rhog(i)))/(3*cd*rhol))**0.5)
        if (abs(z-vt(i)).LT.0.0001) then
                vt(i) = z
                goto 165
        else
                goto 164
        endif
165     return
        end

c       Subroutine to calculate the average gas hold up in the rotor
        subroutine TOTHOLDUP (r,hold,tothold)
        real r(120),hold(120),rhold(120),tothold,x,y
        integer i

        x = 0
        y = 0
        do 170 i = 1,100
```

```
      rhold(i) = hold(i)*r(i)
      x = x + rhold(i)
      y = y + r(i)
170   continue
      tothold = (x/y)*100
      return
      end

c     Subroutine to correct the gas-liquid interface in the rotor to
c     account for the gas hold-up in the machine
      subroutine INTERFACE (tothold,Ro,Rnew)
      real tothold,Ro,Ridash,Rnew

c     Ridash is the radial position of the liquid pick-up tubes in rotor
      Ridash= 0.21
      Rnew = (((0.01*tothold*(Ro**2))-(Ridash**2))/((0.01*tothold)-1))**
     +0.5
      return
      end

c     Subroutine to calculate the Liquid Side Film Coefficient
c     (Ref : Penetration Theory)
      subroutine MTCOEFF1(i,Reb,Dl,rhol,mul,vgr,Kl)
      real Reb(120),Dl,rhol,mul,vgr(120),Kl(120),Sc
      integer i

      Sc = mul/(rhol*Dl)
      Kl(i) = vgr(i)*(1.13*(Reb(i)**(-0.5))*(Sc**(-0.5)))
      return
      end

c     Mass Transfer Coefficient (Ref: Frossling - Valentin P.49)
      subroutine MTCOEFF2(i,Reb,db,Dl,rhol,mul,Kl)
      real Reb(120),db(120),Dl,rhol,mul,Kl(120),Sc
      integer i

      Sc = mul/(rhol*Dl)
      Kl(i) = (Dl/db(i))*(2+(0.79*((Sc)**0.3333)*((Reb(i))**0.5)))
      return
      end


c     Mass Transfer Coefficient (Ref : Cockx,Roustan)
      subroutine MTCOEFF3(i,Dl,rhol,mul,vgr,Kl)
      real Dl,rhol,mul,vgr(120),Kl(120),Sc,cd,ui
      integer i

      Sc = mul/(rhol*Dl)
      cd = 0.16
```

```
      ui = ((cd/2)**0.5)*vgr(i)
      Kl(i) = 0.13*ui*(Sc**(-0.5))
      return
      end

c     Mass Transfer Coefficient (Ref: Perry 6th edition P18-69)
      subroutine MTCOEFF4(i,db,Dl,rhol,rhog,mul,gr,Kl)
      real db(120),Dl,rhol,rhog(120),gr(120),Kl(120),mul,a
      integer i

      a = ((db(i)**3)*gr(i)*(rhol-rhog(i)))/(Dl*mul)
      Kl(i) = (Dl/db(i))*(2+(0.31*(a**0.3333)))
      return
      end

c     Mass Transfer Coefficient (Ref : Hughmark)
      subroutine MTCOEFF5(i,Reb,db,Dl,rhol,mul,gr,Kl)
      real Reb(120),db(120),Dl,rhol,mul,gr(120),Kl(120),Sc,Grp
      integer i

      Sc = mul/(rhol*Dl)
      Grp = db(i)*(gr(i)**(0.3333))/(Dl**(0.6666))
      Kl(i) = (dl/db(i))*(2+(0.061*(Reb(i)**0.779)*(Sc**0.546)*(Grp**0.1
     +16)))
      return
      end

c     Volumetric (Kla) Mass Transfer Coefficient (Ref : Hikita)
      subroutine MTCOEFF6(i,G,Dl,rhol,rhog,mul,gamma,t,r,gr,Kl)
      real Dl,rhol,mul,mug,vg,gamma,a,b,Sc,r(120),t,gr(120),rhog(120),Kl
     +(120),rhogstp,G
      integer i

      rhogstp=1.206
      mug=1.8E-5
      vg=G*(rhogstp/rhog(i))/(1000*2*3.142*t*r(i))
      Sc = mul/(rhol*Dl)
      a=((vg*mul)/gamma)**1.76
      b=(((mul**4)*gr(i))/(rhol*(gamma**3)))**(-0.248)
      Kl(i)=(14.9/vg)*gr(i)*(a)*(b)*((mug/mul)**0.243)*(Sc**(-0.604))
      return
      end

c     Subroutine to calculate the height of a transfer unit
      subroutine HEIGHT(i,Kl,L,r,t,db,hold,rhol,rmml,Ntu,Nto)
      real Kl(120),L,Lm,r(120),t,db(120),hold(120),rhol,rmml,a,Ct,Ht,Ntu
     +,Nto
      integer i
```

```
      a = (6*hold(i))/db(i)
      Lm = (L*rhol)/(1000*rmml*2*3.142*t*r(i))
      Ct = rhol/rmml
      Ht = Lm/(Kl(i)*Ct*a)
      Ntu = (r(i)-r(i+1))/Ht
      Nto = Nto + Ntu
      return
      end

c     Subroutine to calculate the oxygen concentration in ppm
      subroutine OUTLET(i,L,G,r,rhol,rmml,rmmg,t,Ntu,xin,GP)
      real L,G,r(120),rhol,GP(120),rhogstp,rmml,rmmg,t,f,m,Lm,Gm,Ntu,xin
     +,xout
      integer i

      rhogstp = 1.206
      m = 32700*(101325/GP(i))
      Lm = (L*rhol)/(1000*rmml*2*3.142*t*r(i))
      Gm = (G*rhogstp)/(1000*rmmg*2*3.142*t*r(i))
      f = Lm/(m*Gm)
      xout=((1-f)*xin)/(EXP(Ntu*(1-f))-f)
      xin = xout
      return
      end
```

APPENDIX II

The following listing is for the MathCad program used in the modelling of the hydrodynamics of the liquid through the packing in the rotor. The actual model parameters produced are those for Fig. 5.9(i). The first graph shows the normalised distribution, the second shows the model fitted to the data points.

$xy := READPRN(f)$

$n := rows(xy)$

$n = 380$

$i := 0..n-1$

$c_i := xy_{(i,1)}$

$t_i := xy_{(i,0)}$

$f(x) := linterp(t, c, x)$

$$I := \int_{t_0}^{t_{n-1}} f(x)\,dx \qquad I = 0.092$$

$$c_i := \frac{c_i}{I}$$

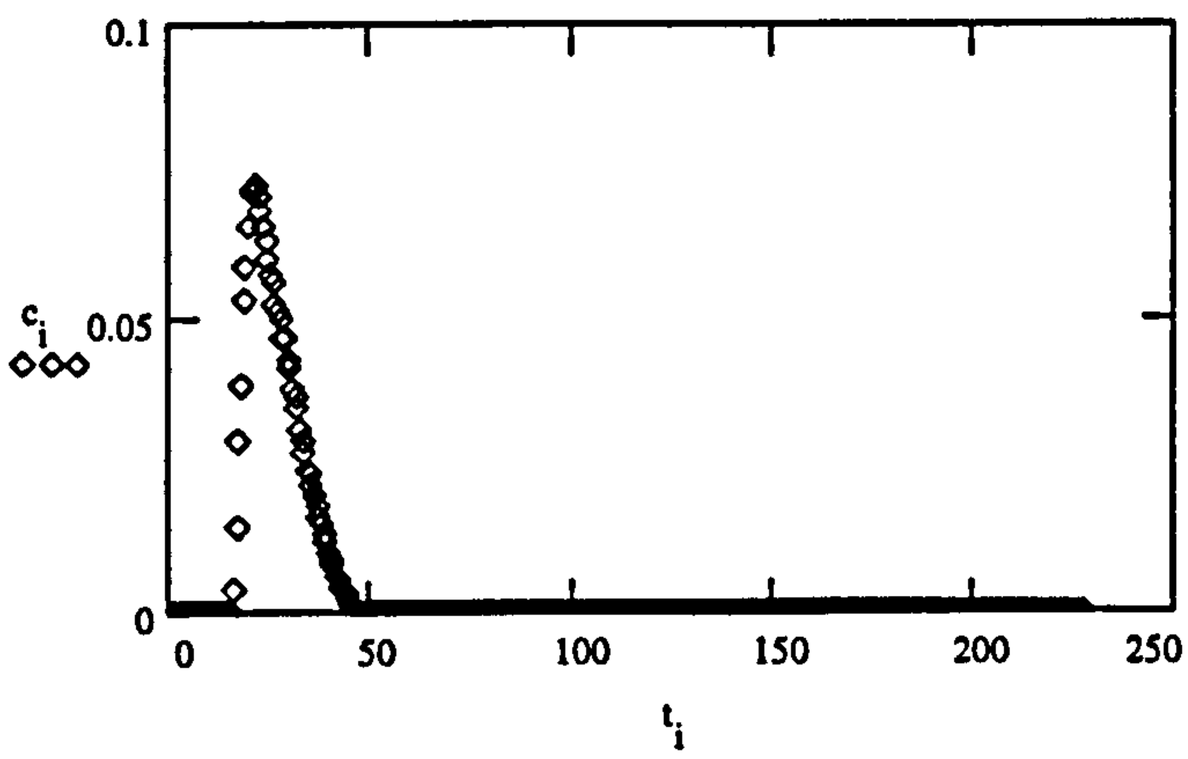

$$C(t,N,ta,td,f) := (1-f)\cdot\left[\frac{1}{ta}\cdot\left(\frac{t}{ta}\right)^{N-1}\cdot\frac{1}{\Gamma(N)}\cdot\exp\left(-\frac{t}{ta}\right)\right] + f\cdot\int_0^t \left[\frac{1}{ta}\cdot\left(\frac{\tau}{ta}\right)^{N-1}\cdot\frac{1}{\Gamma(N)}\cdot\exp\left(-\frac{\tau}{ta}\right)\right]\cdot\left(\frac{1}{td}\cdot\exp\left(-\frac{t-\tau}{td}\right)\right)d\tau$$

$$RMS(N,ta,td,f) := \sum_i \left(c_i - C\left(t_i,N,ta,td,f\right)\right)^2$$

$N := 49$

$ta := 0.43$

$td := 8$

$f := 0.81$

GIVEN

$RMS(N,ta,td,f) = 0$

$ta = ta$

$td = td$

$f > 0$

$$\begin{bmatrix} N \\ ta \\ td \\ f \end{bmatrix} := \text{MINERR}(N, ta, td, f)$$

$$\begin{bmatrix} N \\ ta \\ td \\ f \end{bmatrix} = \begin{bmatrix} 48.451 \\ 0.426 \\ 7.784 \\ 0.811 \end{bmatrix}$$

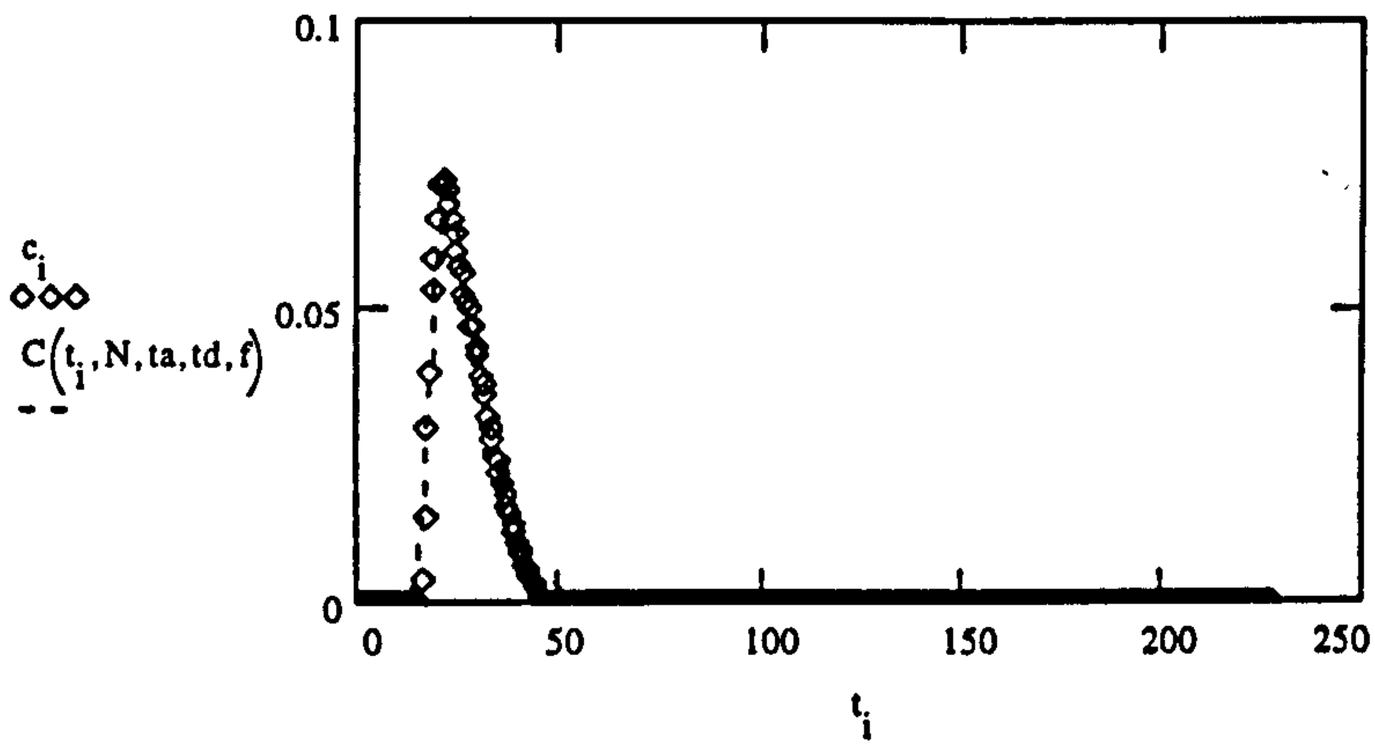

The dotted line in the above graph shows the model curve fit to the experimental data points.

APPENDIX III

The gas and liquid flowrates through the rotor were calculated as follows :

(a) Gas Flowrate

The nitrogen gas flow into the rotor was measured using two Nixon gas rotameters as specified in Table 3.2. However these two rotameters were calibrated using air at 293K and 1 Bar(a). Therefore in order to calculate the true flowrate of nitrogen gas entering the machine a scaling factor has to be used, to account for the variations in gas type, pressure and temperature where :

$$Factor = \sqrt{\frac{\rho_{air}(stp)}{\rho_{N_2}(stp)} \times \frac{P_{gas}}{P_{stp}} \times \frac{T_{stp}}{T_{gas}}}$$

ρ_{air}	Density of Air at STP	= 1.2929 kg/m^3
ρ_{N2}	Density of Nitrogen at STP	= 1.1647 kg/m^3
P_{stp}	Standard Pressure	= 1.0 Bar(a)
T_{stp}	Standard Temperature	= 293 K
P_{gas}	Pressure of the Nitrogen Gas into Rotor	= ?? Bar(a)
T_{gas}	Temperature of the Nitrogen Gas into Rotor	= 288 K

Substituting the abovevalues into the equation, the scaling factor becomes :

$$Factor = \sqrt{1.13 P_{gas}}$$

Therefore : *Gas Flow at STP = Nominal Gas Flow * Factor*

(b) Liquid Flowrate

The water flowrate into the rotor used a Fisher Type 35S flowmeter, the calibration curve for which is shown below.

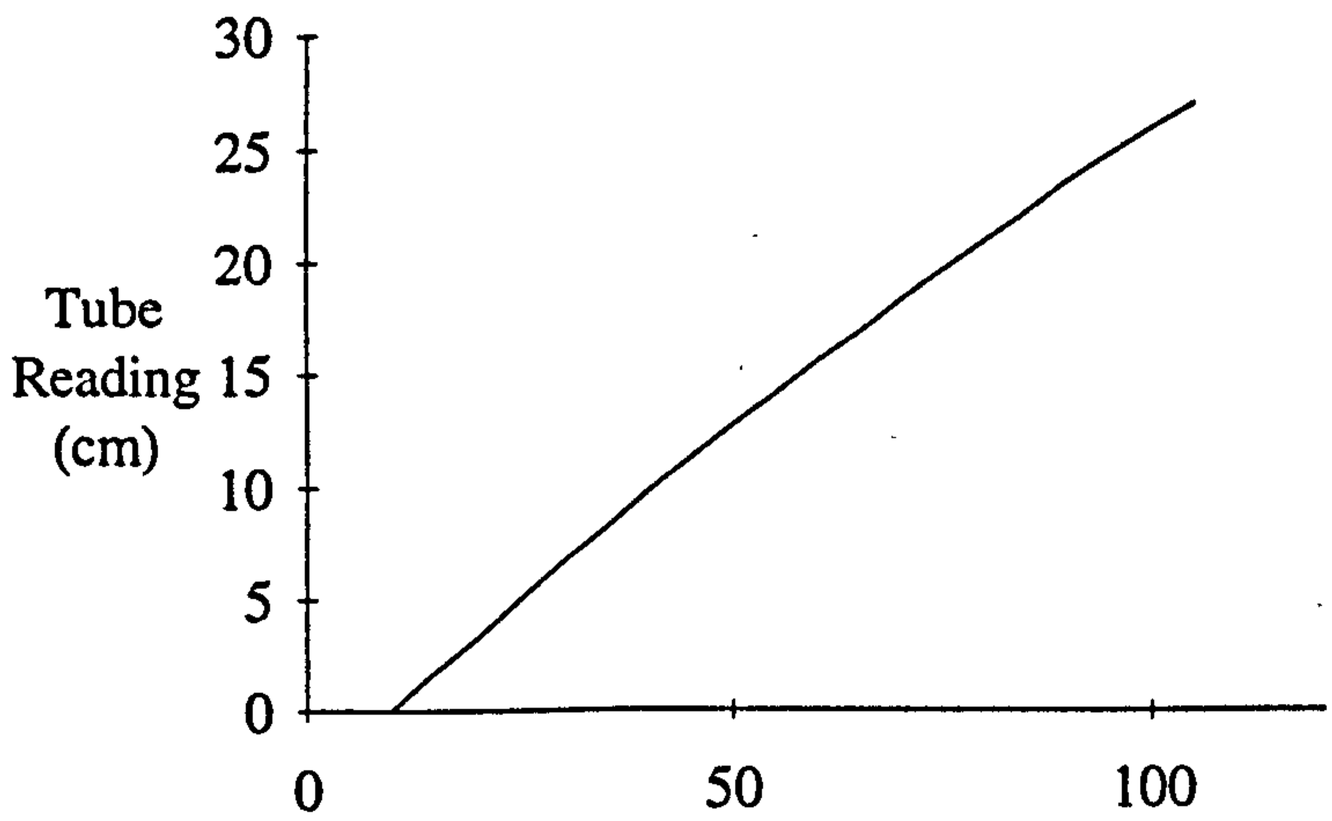

APPENDIX IV

The following outlines the initial procedure in which the mass transfer performance of the packed section of the rotor was calculated. As previously stated the role of the blanket was to prevent any recontamination of the water from the air. However as the sample is removed close to the liquid interface in the return chamber, the actual value of dissolved oxygen measured is unlikely to be an accurate representation of the level of dissolved oxygen in the water leaving the packed section of the rotor, due to further mass transfer taking place in the return chamber at the liquid surface through diffusion and turbulence caused by the pickup tubes. Figure(a) graphically illustrates this point.

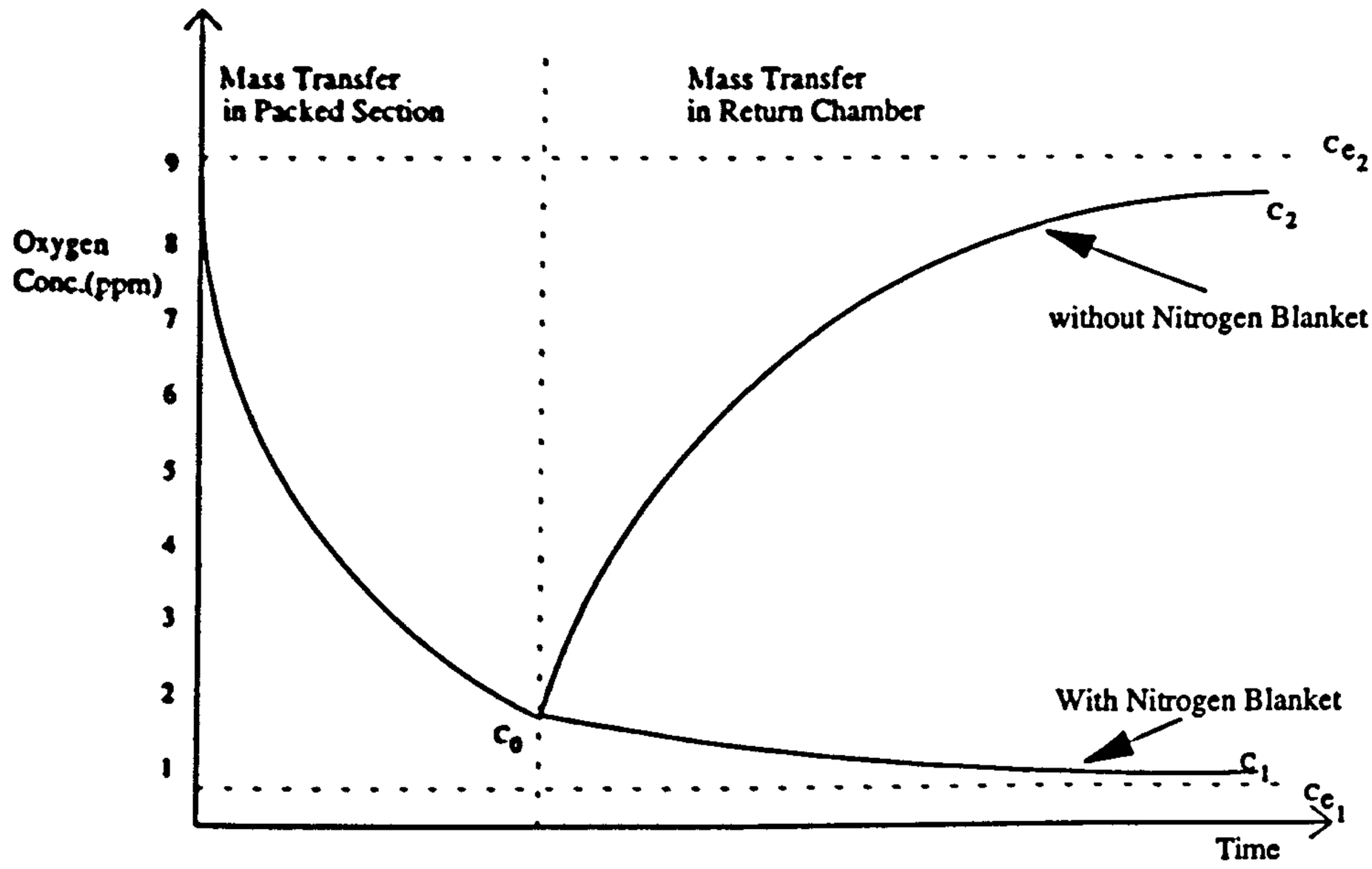

Figure (a) : Illustration of Mass Transfer Effect of Blanket in Rotor

where C_1 - Concentration of Oxygen in Water with Nitrogen Blanket
C_2 - Concentration of Oxygen in Water without Nitrogen Blanket
C_0 - Concentration of Oxygen in Water leaving Packed Section of Rotor
Ce_1 - Equilibrium Concentration of Oxygen in Water with Nitrogen Blanket
Ce_2 - Equilibrium Concentration of Oxygen in Water without Nitrogen Blanket

Assuming that the equilibrium concentrations (Ce_1, Ce_2) change only due to alterations in the oxygen concentration in the gas blanket, and that the pickup tubes and sample tube fluid dynamics are constant then :

$$\frac{C_0 - Ce_1}{C_1 - Ce_1} = \frac{Ce_2 - C_0}{Ce_2 - C_2}$$

and from this equation the oxygen concentration leaving the packed section of the rotor, C_0, may be found. Therefore for every operating condition of the rotor two readings would have to be taken, one without the blanket (C_2), and one with the blanket (C_1). The nitrogen blanket

was operated using OFN (oxygen free nitrogen) supplied by BOC Ltd., and a gas flowrate of 110 l/min was used. Gas samples taken from the blanket and analysed by a gas chromatograph showed the oxygen concentration in the blanket to be 1.04%. Therefore as the system obeys Henry's Law the equilibrium concentration of oxygen in the water (Ce_1) in contact with the blanket gas was found to be 0.446 ppm. The value for the equilibrium concentration of oxygen in the water without the blanket (Ce_2), i.e. air, was assumed to be equal to the initial inlet water concentration of the rotor. Tables (a) - (c) show the initial mass transfer results for the rotor.

Rotor Mass Transfer Results

Table (a) : Low Liquid Flowrate (0.1 l/sec)

Initial Oxygen Conc.(ppm) - 9.87									
Rotational Speed (rpm)	200			250			300		
Nominal Gas Flow(m3/hr)	Gas Flow at STP (l/sec)	C_0	Ntu	Gas Flow at STP (l/sec)	C_0	Ntu	Gas Flow at STP (l/sec)	C_0	Ntu
0.5	0.17	0.50	2.98	0.18	0.60	2.80	0.19	1.49	1.89
1.0	0.33	0.41	3.18	0.35	0.47	3.04	0.37	1.24	2.07
2.0	0.67	0.31	3.46	0.70	0.40	3.21	0.74	1.18	2.12
3.0	1.00	0.24	3.72	1.06	0.37	3.28	1.11	1.14	2.16
4.0	1.33	0.16	4.12	1.41	0.34	3.36	1.48	1.10	2.19

Table (b) : Average Liquid Flowrate (0.3 l/sec)

Initial Oxygen Conc.(ppm) - 10.15									
Rotational Speed (rpm)	200			250			300		
Nominal Gas Flow(m3/hr)	Gas Flow at STP (l/sec)	C_0	Ntu	Gas Flow at STP (l/sec)	C_0	Ntu	Gas Flow at STP (l/sec)	C_0	Ntu
0.5	0.17	1.41	1.97	0.18	1.70	1.79	0.19	3.01	1.22
1.0	0.33	0.81	2.53	0.35	1.08	2.24	0.37	2.63	1.35
2.0	0.67	0.46	3.09	0.70	0.55	2.92	0.74	2.11	1.57
3.0	1.00	0.32	3.46	1.06	0.47	3.07	1.11	1.92	1.67
4.0	1.33	0.19	3.74	1.41	0.38	3.29	1.48	1.78	1.74

Table (c) : High Liquid Flowrate (0.4 l/sec)

Initial Oxygen Conc.(ppm) - 10.72									
Rotational Speed (rpm)	200*			250			300		
Nominal Gas Flow(m3/hr)	Gas Flow at STP (l/sec)	C_0	Ntu	Gas Flow at STP (l/sec)	C_0	Ntu	Gas Flow at STP (l/sec)	C_0	Ntu
0.5				0.18	3.09	1.24	0.19	3.61	1.09
1.0				0.35	1.63	1.88	0.37	3.00	1.27
2.0				0.70	0.83	2.56	0.74	2.52	1.45
3.0				1.06	0.59	2.90	1.11	2.10	1.63
4.0				1.41	0.49	3.09	1.48	1.94	1.71

* No results at 200 rpm due to the high liquid throughput flooding the rotor and causing severe leakage of water from the machine.

In the above tables, the corrected gas flowrate under STP conditions was found as outlined in Appendix III. It was found that as the gas pressure drop across the nozzles was minimal, the gas pressure only varied with the rotational speed as shown in Table (d) below :

Table (d) : Variation of Gas Pressure into Rotor with Rotational Speed

Rotational Speed (rpm)	200	250	300
Gas Pressure (Bar g)	0.30	0.45	0.60

APPENDIX V

Table (a) shows the variation of the gas pressure entering the rotor using the new nozzle design, and the variation in the values of the gas pressure with gas flowrate at 200, 300, 400 rpm are displayed graphically.

Table (a)

	Pressure of Nitrogen Gas entering Rotor (Bar g)					
Speed (rpm) Nom. Gas Flow (m3/hr)	200	250	300	350	400	450
0.5	0.40	0.55	0.75	0.95	1.20	1.40
1.0	0.50	0.65	0.80	1.05	1.30	1.55
2.0	0.70	0.85	1.05	1.30	1.50	1.80
3.0	1.00	1.15	1.30	1.50	1.80	2.05
4.0	1.35	1.45	1.60	1.80	2.05	--*

* No result could be recorded as the hydrostatic pressure created in the rotor is greater than the exit pressure from the gas cylinder.

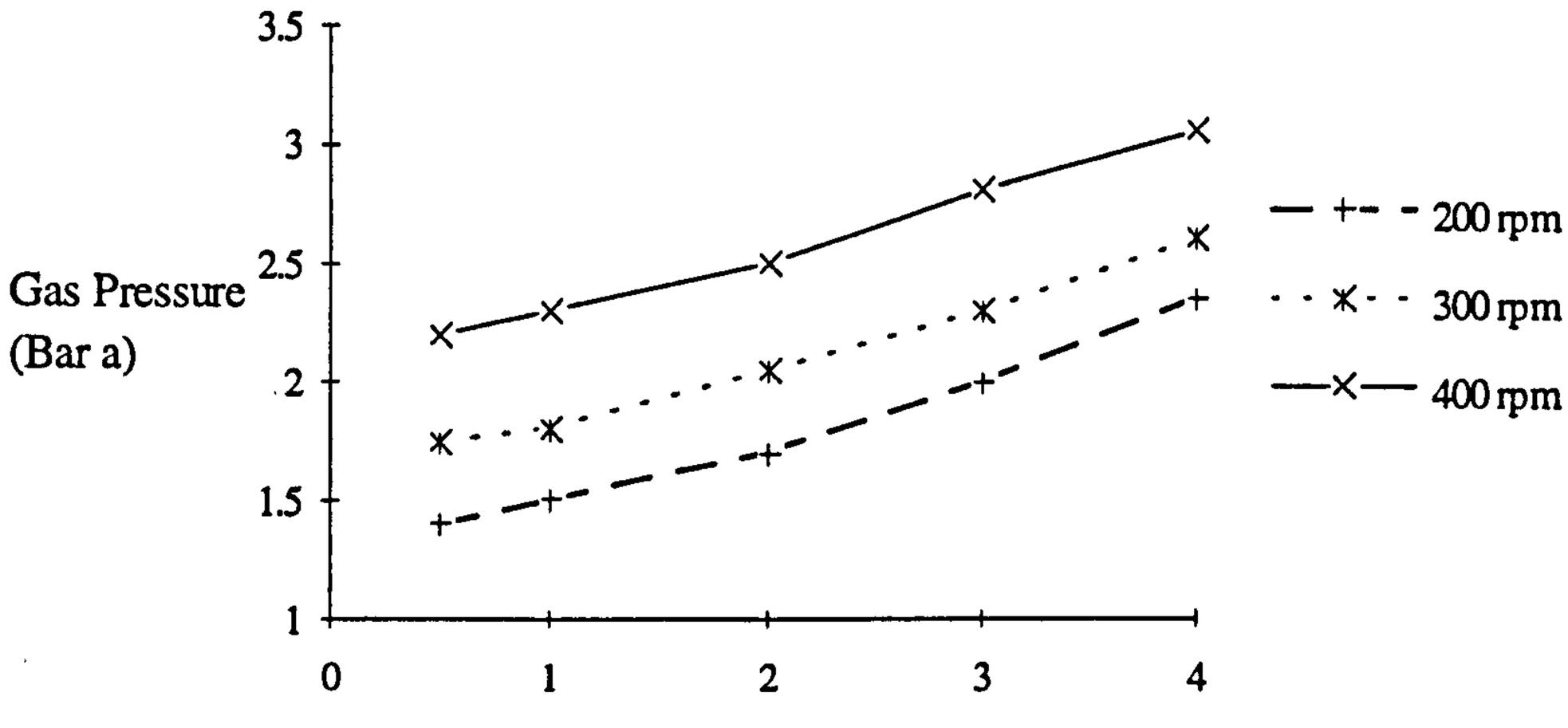

The following Tables (b) - (e) show the dissolved oxygen concentration at the various radial depths within the rotor. It should be noted that no mass transfer result was obtained at the high liquid flowrates for a rotational speed of 200 rpm as significant flooding of the rotor occured.

Table b(i) : Full Packed Length

Low Liquid Flow - 0.1 l/sec	Initial Oxygen Conc. - 10.50 ppm				
	Oxygen Concentration (ppm)				
Speed (rpm) / Nominal Gas Flow (m^3/hr)	200	250	300	350	400
0.5	1.10	0.70	0.64	0.43	0.27
1.0	0.71	0.43	0.36	0.25	0.14
2.0	0.47	0.30	0.20(5)	0.16	0.09
3.0	0.36	0.22	0.16	0.12	0.07(5)
4.0	0.28	0.18	0.15	0.09(5)	0.05(5)

Table b(ii)

Medium Liquid Flow - 0.3 l/sec	Initial Oxygen Conc. - 10.97 ppm				
	Oxygen Concentration (ppm)				
Speed (rpm) / Gas Flow (m^3/hr)	200	250	300	350	400
0.5	3.21	2.32	1.56	1.31	0.87
1.0	2.27	1.52	0.98	0.62	0.40
2.0	1.47	0.95	0.62	0.38	0.24
3.0	1.15	0.67	0.43	0.26	0.16
4.0	0.85	0.44	0.30	0.19	0.12

Table b(iii)

High Liquid Flow - 0.5 l/sec	Initial Oxygen Conc. - 11.18 ppm				
	Oxygen Concentration (ppm)				
Speed (rpm) / Gas Flow (m^3/hr)	200	250	300	350	400
0.5		3.45	2.80	1.87	1.34
1.0		2.33	1.62	1.04	0.63
2.0		1.28	0.83	0.59	0.39
3.0		0.89	0.57	0.34	0.28
4.0		0.58	0.36	0.22	0.19

Table c(i) : 3/4 Packed Length

Low Liquid Flow - 0.1 l/sec	Initial Oxygen Conc. - 11.24 ppm				
	Oxygen Concentration (ppm)				
Speed (rpm) / Gas Flow (m^3/hr)	200	250	300	350	400
0.5	0.39	0.33	0.18	0.14	0.09(5)
1.0	0.32	0.44	0.39	0.29	0.10(5)
2.0	0.25	0.29	0.19	0.20	0.22
3.0	0.20	0.12	0.14	0.13	0.12
4.0	0.17	0.09(5)	0.07	0.08	0.08

Table c(ii)

Medium Liquid Flow - 0.3 l/sec	Initial Oxygen Conc. - 10.90 ppm				
	Oxygen Concentration (ppm)				
Speed (rpm) / Gas Flow (m^3/hr)	200	250	300	350	400
0.5	1.24	0.98	0.64	0.54	0.37
1.0	0.59	0.38	0.31	0.23	0.17
2.0	0.29	0.20	0.18	0.17	0.14
3.0	0.19	0.17	0.15	0.15	0.13
4.0	0.15	0.14	0.15	0.10(5)	0.09

Table c(iii)

High Liquid Flow - 0.5 l/sec	Initial Oxygen Conc. - 11.36 ppm				
	Oxygen Concentration (ppm)				
Speed (rpm) / Gas Flow (m^3/hr)	200	250	300	350	400
0.5		2.24	1.78	1.48	1.06
1.0		1.04	0.84	0.54	0.40
2.0		0.36	0.42	0.25	0.19
3.0		0.20	0.28	0.17	0.12
4.0		0.16	0.23	0.14	0.09

Table d(i) : 1/2 Packed Length

Low Liquid Flow - 0.1 l/sec	Initial Oxygen Conc. - 11.20 ppm				
	Oxygen Concentration (ppm)				
Speed (rpm) / Gas Flow (m^3/hr)	200	250	300	350	400
0.5	1.00	0.91	0.78	0.57	0.48
1.0	0.64	0.61	0.59	0.41	0.35
2.0	0.32	0.28	0.33	0.14	0.15
3.0	0.20	0.15	0.20	0.08	0.08
4.0	0.15	0.12	0.17	0.06	0.06

Table d(ii)

Medium Liquid Flow - 0.3 l/sec	Initial Oxygen Conc. - 10.80 ppm				
	Oxygen Concentration (ppm)				
Speed (rpm) / Gas Flow (m^3/hr)	200	250	300	350	400
0.5	3.20	2.87	2.08	1.47	1.18
1.0	1.63	1.52	1.08	0.97	0.84
2.0	0.58	0.55	0.44	0.30	0.27
3.0	0.24	0.18	0.14	0.09(5)	0.11
4.0	0.14	0.10	0.08	0.06(5)	0.07

Table d(iii)

High Liquid Flow - 0.5 l/sec	Initial Oxygen Conc. - 11.22 ppm				
	Oxygen Concentration (ppm)				
Speed (rpm) / Gas Flow (m^3/hr)	200	250	300	350	400
0.5		3.96	3.95	3.02	2.48
1.0		2.49	1.99	1.64	1.25
2.0		0.83	0.65	0.50	0.38
3.0		0.33	0.26	0.21	0.16
4.0		0.20	0.16	0.20	0.11

Table e(i) : 1/4 Packed Length

Low Liquid Flow - 0.1 l/sec	Initial Oxygen Conc. - 11.30 ppm				
	Oxygen Concentration (ppm)				
Speed (rpm) / Gas Flow (m^3/hr)	200	250	300	350	400
0.5	1.09	1.35	0.79	0.58	0.43
1.0	0.70	0.81	0.48	0.41	0.29
2.0	0.37	0.41	0.26	0.21	0.16
3.0	0.17	0.16	0.10	0.09(5)	0.07(5)
4.0	0.08	0.07	0.05	0.06	0.04(5)

Table e(ii)

Medium Liquid Flow - 0.3 l/sec	Initial Oxygen Conc. - 11.30 ppm				
	Oxygen Concentration (ppm)				
Speed (rpm) / Gas Flow (m^3/hr)	200	250	300	350	400
0.5	3.91	3.31	2.18	1.96	1.45
1.0	2.53	1.60	1.27	1.14	1.04
2.0	1.06	0.69	0.50	0.52	0.52
3.0	0.60	0.32	0.19	0.21	0.20
4.0	0.32	0.18	0.09(5)	0.09	0.13

Table e(iii)

High Liquid Flow - 0.5 l/sec	Initial Oxygen Conc. - 10.93 ppm				
	Oxygen Concentration (ppm)				
Speed (rpm) / Gas Flow (m^3/hr)	200	250	300	350	400
0.5		4.32	3.87	2.94	2.00
1.0		2.27	1.90	1.60	1.24
2.0		0.77	0.62	0.50	0.48
3.0		0.31	0.27	0.21	0.25
4.0		0.20	0.19	0.16	0.16

The following table shows the preliminary mass transfer findings using salt water :

Table (f) : Preliminary Salt Water Concentration Results

Low Liquid Flowrate 0.1 l/sec		Initial Oxygen Conc. - 8.80 ppm		
Speed (rpm) Gas Flow (m^3/hr)	250	300	350	400
0.5	0.29	0.19	0.11	0.06
1.0	0.16	0.13	0.07	0.04
Medium Liquid Flowrate 0.3 l/sec		Initial Oxygen Conc. - 9.14 ppm		
Speed (rpm) Gas Flow (m^3/hr)	250	300	350	400
0.5	0.43	0.30	0.18	0.10
1.0	0.15	0.11	0.09	0.07
High Liquid Flowrate 0.5 l/sec		Initial Oxygen Conc. - 9.14 ppm		
Speed (rpm) Gas Flow (m^3/hr)	250	300	350	400
0.5	0.29	0.15	0.12	0.10
1.0	-	-	-	-

APPENDIX VI

The following results are the mass transfer data for the rotor using the 24, 48 radial vanes :

Table a(i) : 24 Radial Vanes

Full Packed Length		Initial Oxygen Conc.(ppm) - 10.45	
Rotational Speed (rpm)	Nom. Gas Flow (m^3/hr)	Liquid Flow (l/sec)	Oxygen Conc.(ppm)
200	1.0	0.1	1.60
300	1.0	0.1	0.80
300	2.0	0.1	0.45
300	4.0	0.1	0.24
300	1.0	0.3	2.40
300	1.0	0.5	2.93
400	1.0	0.1	0.34

Table a(ii)

3/4 Packed Length		Initial Oxygen Conc.(ppm) - 10.45	
Rotational Speed (rpm)	Nom. Gas Flow (m^3/hr)	Liquid Flow (l/sec)	Oxygen Conc.(ppm)
200	1.0	0.1	0.48
300	1.0	0.1	0.21
300	2.0	0.1	0.18
300	4.0	0.1	0.10
300	1.0	0.3	0.26
300	1.0	0.5	0.36
400	1.0	0.1	0.11

Table a(iii)

1/2 Packed Length		Initial Oxygen Conc.(ppm) - 10.45	
Rotational Speed (rpm)	Nom. Gas Flow (m^3/hr)	Liquid Flow (l/sec)	Oxygen Conc.(ppm)
200	1.0	0.1	1.02
300	1.0	0.1	0.32
300	2.0	0.1	0.16
300	4.0	0.1	0.10
300	1.0	0.3	1.81
300	1.0	0.5	2.36
400	1.0	0.1	0.25

Table a(iv)

1/4 Packed Length		Initial Oxygen Conc.(ppm) - 10.45	
Rotational Speed (rpm)	Nom. Gas Flow (m^3/hr)	Liquid Flow (l/sec)	Oxygen Conc.(ppm)
200	1.0	0.1	1.32
300	1.0	0.1	0.71
300	2.0	0.1	0.32
300	4.0	0.1	0.20
300	1.0	0.3	2.06
300	1.0	0.5	2.45
400	1.0	0.1	0.45

Table b(i) : 48 Radial Vanes

Full Packed Length		Initial Oxygen Conc.(ppm) - 8.60	
Rotational Speed (rpm)	Nom. Gas Flow (m^3/hr)	Liquid Flow (l/sec)	Oxygen Conc.(ppm)
200	1.0	0.1	1.36
300	1.0	0.1	0.62
300	2.0	0.1	0.41
300	4.0	0.1	0.27
300	1.0	0.3	2.33
300	1.0	0.5	2.74
400	1.0	0.1	0.45

Table b(ii)

3/4 Packed Length		Initial Oxygen Conc.(ppm) - 8.60	
Rotational Speed (rpm)	Nom. Gas Flow (m^3/hr)	Liquid Flow (l/sec)	Oxygen Conc.(ppm)
200	1.0	0.1	0.47
300	1.0	0.1	0.19
300	2.0	0.1	0.13
300	4.0	0.1	0.09
300	1.0	0.3	0.57
300	1.0	0.5	0.70
400	1.0	0.1	0.11

Table b(iii)

1/2 Packed Length		Initial Oxygen Conc.(ppm) - 8.90	
Rotational Speed (rpm)	Nom. Gas Flow (m^3/hr)	Liquid Flow (l/sec)	Oxygen Conc.(ppm)
200	1.0	0.1	1.18
300	1.0	0.1	0.65
300	2.0	0.1	0.40
300	4.0	0.1	0.19
300	1.0	0.3	2.45
300	1.0	0.5	2.93
400	1.0	0.1	0.47

Table b(iv)

1/4 Packed Length		Initial Oxygen Conc.(ppm) - 8.90	
Rotational Speed (rpm)	Nom. Gas Flow (m^3/hr)	Liquid Flow (l/sec)	Oxygen Conc.(ppm)
200	1.0	0.1	0.47
300	1.0	0.1	0.25
300	2.0	0.1	0.16
300	4.0	0.1	0.08
300	1.0	0.3	0.64
300	1.0	0.5	0.66
400	1.0	0.1	0.15

APPENDIX VII

Tables (a) - (d) show the mass transfer data attained for the rotor at the Full and 1/2 radial packed length positions, using Declon HC20, and Declon HC30 packing.

Table a(i) : Full Packed Length, Declon HC20 Packing

Liquid Flowrate (l/sec) - 0.1			Initial Oxygen Conc.(ppm) - 8.74			
Speed (rpm)	200		300		400	
Nom. Gas Flow (m^3/hr)	Oxygen Conc. (ppm)	N.T.U.	Oxygen Conc. (ppm)	N.T.U.	Oxygen Conc. (ppm)	N.T.U.
0.5	0.69	2.54	0.41	3.06	0.21	3.73
1.0	0.57	2.73	0.62	2.65	0.36	3.19
2.0	0.41	3.06	0.49	2.88	0.62	2.65
3.0	0.31	3.34	0.32	3.31	0.33	3.23
4.0	0.20	3.78	0.20	3.78	0.20	3.78

Table a(ii)

Liquid Flowrate (l/sec) - 0.3			Initial Oxygen Conc.(ppm) - 8.74			
Speed (rpm)	200		300		400	
Nom. Gas Flow (m^3/hr)	Oxygen Conc. (ppm)	N.T.U.	Oxygen Conc. (ppm)	N.T.U.	Oxygen Conc. (ppm)	N.T.U.
0.5	1.42	1.82	0.69	2.54	0.55	2.77
1.0	0.89	2.28	0.42	3.04	0.36	3.19
2.0	0.48	2.90	0.33	3.28	0.30	3.37
3.0	0.35	3.22	0.25	3.55	0.26	3.51
4.0	0.26	3.51	0.20	3.78	0.21	3.73

Table a(iii)

Liquid Flowrate (l/sec) - 0.5			Initial Oxygen Conc.(ppm) - 8.74			
Speed (rpm)	200		300		400	
Nom. Gas Flow (m^3/hr)	Oxygen Conc. (ppm)	N.T.U.	Oxygen Conc. (ppm)	N.T.U.	Oxygen Conc. (ppm)	N.T.U.
0.5	2.06	1.45	1.25	1.94	0.89	2.28
1.0	1.20	1.99	0.62	2.65	0.33	3.28
2.0	0.59	2.70	0.29	3.41	0.17	3.94
3.0	0.36	3.19	0.18	3.88	0.13	4.21
4.0	0.28	3.44	0.13	4.21	0.13	4.21

Appendices

Table b(i) : 1/2 Packed Length, Declon HC20 Packing

Liquid Flowrate (l/sec) - 0.1			Initial Oxygen Conc.(ppm) - 8.90			
Speed (rpm)	200		300		400	
Nom. Gas Flow (m^3/hr)	Oxygen Conc. (ppm)	N.T.U.	Oxygen Conc. (ppm)	N.T.U.	Oxygen Conc. (ppm)	N.T.U.
0.5	0.67	2.59	0.35	3.24	0.20	3.80
1.0	0.46	2.96	0.28	3.46	0.16	4.02
2.0	0.31	3.36	0.18	3.90	0.11	4.39
3.0	0.21	3.75	0.11	4.39	0.10	4.49
4.0	0.15	4.08	0.09	4.59	0.08	4.71

Table b(ii)

Liquid Flowrate (l/sec) - 0.3			Initial Oxygen Conc.(ppm) - 8.90			
Speed (rpm)	200		300		400	
Nom. Gas Flow (m^3/hr)	Oxygen Conc. (ppm)	N.T.U.	Oxygen Conc. (ppm)	N.T.U.	Oxygen Conc. (ppm)	N.T.U.
0.5	1.86	1.57	0.91	2.28	0.50	2.88
1.0	1.26	1.95	0.57	2.75	0.32	3.33
2.0	0.68	2.57	0.35	3.24	0.19	3.85
3.0	0.48	2.92	0.21	3.75	0.13	4.23
4.0	0.33	3.29	0.13	4.23	0.09	4.59

Table b(iii)

Liquid Flowrate (l/sec) - 0.5			Initial Oxygen Conc.(ppm) - 8.90			
Speed (rpm)	200		300		400	
Nom. Gas Flow (m^3/hr)	Oxygen Conc. (ppm)	N.T.U.	Oxygen Conc. (ppm)	N.T.U.	Oxygen Conc. (ppm)	N.T.U.
0.5	2.70	1.19	1.68	1.67	0.98	2.21
1.0	1.86	1.57	0.88	2.31	0.47	2.94
2.0	0.89	2.30	0.42	3.05	0.24	3.61
3.0	0.59	2.71	0.23	3.66	0.15	4.08
4.0	0.46	2.96	0.15	4.08	0.10	4.49

Table c(i) : Full Packed Length, Declon HC30 Packing

Liquid Flowrate (l/sec) - 0.1			Initial Oxygen Conc.(ppm) - 8.55			
Speed (rpm)	200		300		400	
Nom. Gas Flow (m^3/hr)	Oxygen Conc. (ppm)	N.T.U.	Oxygen Conc. (ppm)	N.T.U.	Oxygen Conc. (ppm)	N.T.U.
0.5	0.54	2.76	0.25	3.53	0.13	4.19
1.0	0.43	2.99	0.52	2.80	0.11	4.35
2.0	0.32	3.29	0.38	3.11	0.49	2.86
3.0	0.23	3.62	0.23	3.62	0.29	3.38
4.0	0.17	3.92	0.16	3.98	0.17	3.92

Table c(ii)

Liquid Flowrate (l/sec) - 0.3			Initial Oxygen Conc.(ppm) - 8.55			
Speed (rpm)	200		300		400	
Nom. Gas Flow (m^3/hr)	Oxygen Conc. (ppm)	N.T.U.	Oxygen Conc. (ppm)	N.T.U.	Oxygen Conc. (ppm)	N.T.U.
0.5	1.57	1.69	0.89	2.26	0.44	2.97
1.0	1.01	2.14	0.54	2.76	0.32	3.29
2.0	0.57	2.71	0.32	3.29	0.28	3.42
3.0	0.41	3.04	0.23	3.62	0.22	3.66
4.0	0.32	3.29	0.19	3.81	0.17	3.92

Table c(iii)

Liquid Flowrate (l/sec) - 0.5			Initial Oxygen Conc.(ppm) - 8.55			
Speed (rpm)	200		300		400	
Nom. Gas Flow (m^3/hr)	Oxygen Conc. (ppm)	N.T.U.	Oxygen Conc. (ppm)	N.T.U.	Oxygen Conc. (ppm)	N.T.U.
0.5	2.35	1.29	1.20	1.96	0.85	2.31
1.0	1.55	1.71	0.76	2.42	0.38	3.11
2.0	0.93	2.22	0.42	3.01	0.25	3.53
3.0	0.68	2.53	0.23	3.62	0.16	3.98
4.0	0.55	2.74	0.18	3.86	0.12(5)	4.23

Table d(i) : 1/2 Packed Length, Declon HC30 Packing

Liquid Flowrate (l/sec) - 0.1			Initial Oxygen Conc.(ppm) - 9.15			
Speed (rpm)	200		300		400	
Nom. Gas Flow (m^3/hr)	Oxygen Conc. (ppm)	N.T.U.	Oxygen Conc. (ppm)	N.T.U.	Oxygen Conc. (ppm)	N.T.U.
0.5	0.67	2.61	0.28	3.49	0.14	4.18
1.0	0.48	2.95	0.21	3.77	0.12	4.33
2.0	0.34	3.29	0.14(5)	4.14	0.08(5)	4.68
3.0	0.27	3.52	0.11	4.42	0.06	5.03
4.0	0.23	3.68	0.09	4.62	0.05(5)	5.11

Table d(ii)

Liquid Flowrate (l/sec) - 0.3			Initial Oxygen Conc.(ppm) - 9.15			
Speed (rpm)	200		300		400	
Nom. Gas Flow (m^3/hr)	Oxygen Conc. (ppm)	N.T.U.	Oxygen Conc. (ppm)	N.T.U.	Oxygen Conc. (ppm)	N.T.U.
0.5	1.83	1.61	0.86	2.36	0.47	2.97
1.0	1.43	1.86	0.58	2.76	0.34	3.29
2.0	0.93	2.29	0.43	3.06	0.23	3.68
3.0	0.75	2.50	0.31	3.38	0.16(5)	4.02
4.0	0.64	2.66	0.21	3.77	0.13	4.25

Table d(iii)

Liquid Flowrate (l/sec) - 0.5			Initial Oxygen Conc.(ppm) - 9.15			
Speed (rpm)	200		300		400	
Nom. Gas Flow (m^3/hr)	Oxygen Conc. (ppm)	N.T.U.	Oxygen Conc. (ppm)	N.T.U.	Oxygen Conc. (ppm)	N.T.U.
0.5	3.33	1.01	1.34	1.92	0.82	2.41
1.0	2.22	1.42	0.97	2.24	0.44	3.03
2.0	1.34	1.92	0.59	2.74	0.26	3.56
3.0	1.02	2.19	0.36	3.24	0.16	4.05
4.0	0.93	2.29	0.24	3.64	0.13	4.25

APPENDIX VIII

The following tables of results are repeated results taken at the full radial length in the rotor for the Declon HC30 packing.

Liquid Flowrate (l/sec) - 0.1			Initial Oxygen Conc.(ppm) - 8.50			
Speed (rpm)	200		300		400	
Nom. Gas Flow (m^3/hr)	Oxygen Conc. (ppm)	N.T.U.	Oxygen Conc. (ppm)	N.T.U.	Oxygen Conc. (ppm)	N.T.U.
0.5	0.53	2.77	0.29	3.38	0.16	3.97
1.0	0.43	2.98	0.22	3.65	0.11	4.35
2.0	0.36	3.16	0.46	2.92	0.63	2.60
3.0	0.25	3.53	0.27	3.45	0.32	3.28
4.0	0.18	3.85	0.18	3.85	0.19	3.80

Liquid Flowrate (l/sec) - 0.3			Initial Oxygen Conc.(ppm) - 8.50			
Speed (rpm)	200		300		400	
Nom. Gas Flow (m^3/hr)	Oxygen Conc. (ppm)	N.T.U.	Oxygen Conc. (ppm)	N.T.U.	Oxygen Conc. (ppm)	N.T.U.
0.5	1.55	1.70	0.87	2.28	0.47	2.90
1.0	1.05	2.09	0.52	2.79	0.35	3.19
2.0	0.62	2.62	0.37	3.13	0.28	3.41
3.0	0.46	2.92	0.30	3.34	0.23	3.61
4.0	0.35	3.19	0.22	3.65	0.16	3.97

Liquid Flowrate (l/sec) - 0.5			Initial Oxygen Conc.(ppm) - 8.50			
Speed (rpm)	200		300		400	
Nom. Gas Flow (m^3/hr)	Oxygen Conc. (ppm)	N.T.U.	Oxygen Conc. (ppm)	N.T.U.	Oxygen Conc. (ppm)	N.T.U.
0.5	2.30	1.31	1.14	2.01	0.88	2.27
1.0	1.55	1.70	0.74	2.44	0.42	3.01
2.0	0.94	2.20	0.46	2.92	0.26	3.49
3.0	0.68	2.52	0.25	3.53	0.18	3.85
4.0	0.55	2.74	0.19	3.80	0.13	4.18

APPENDIX IX

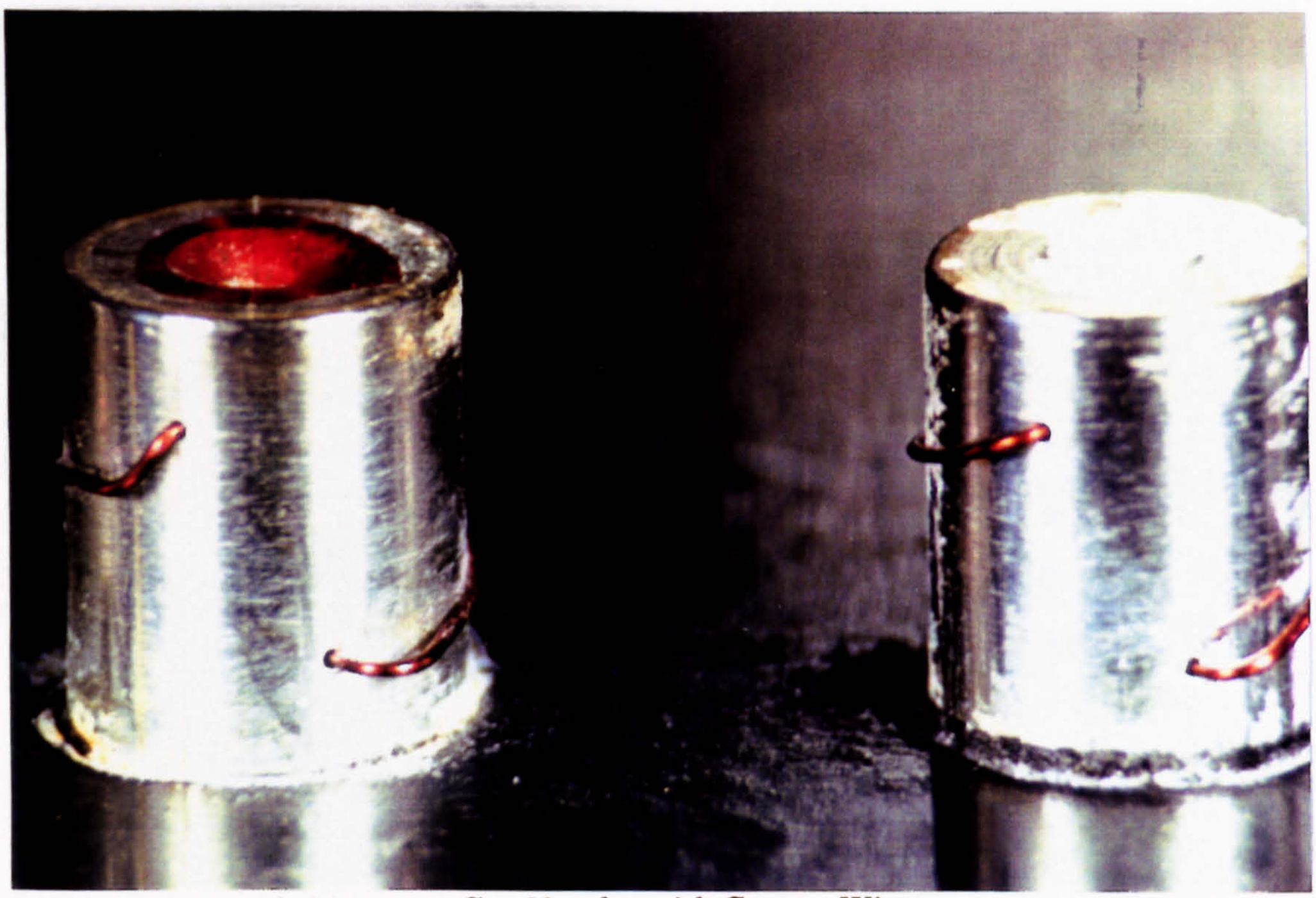

Photograph (a) : *Gas Nozzles with Copper Wire*

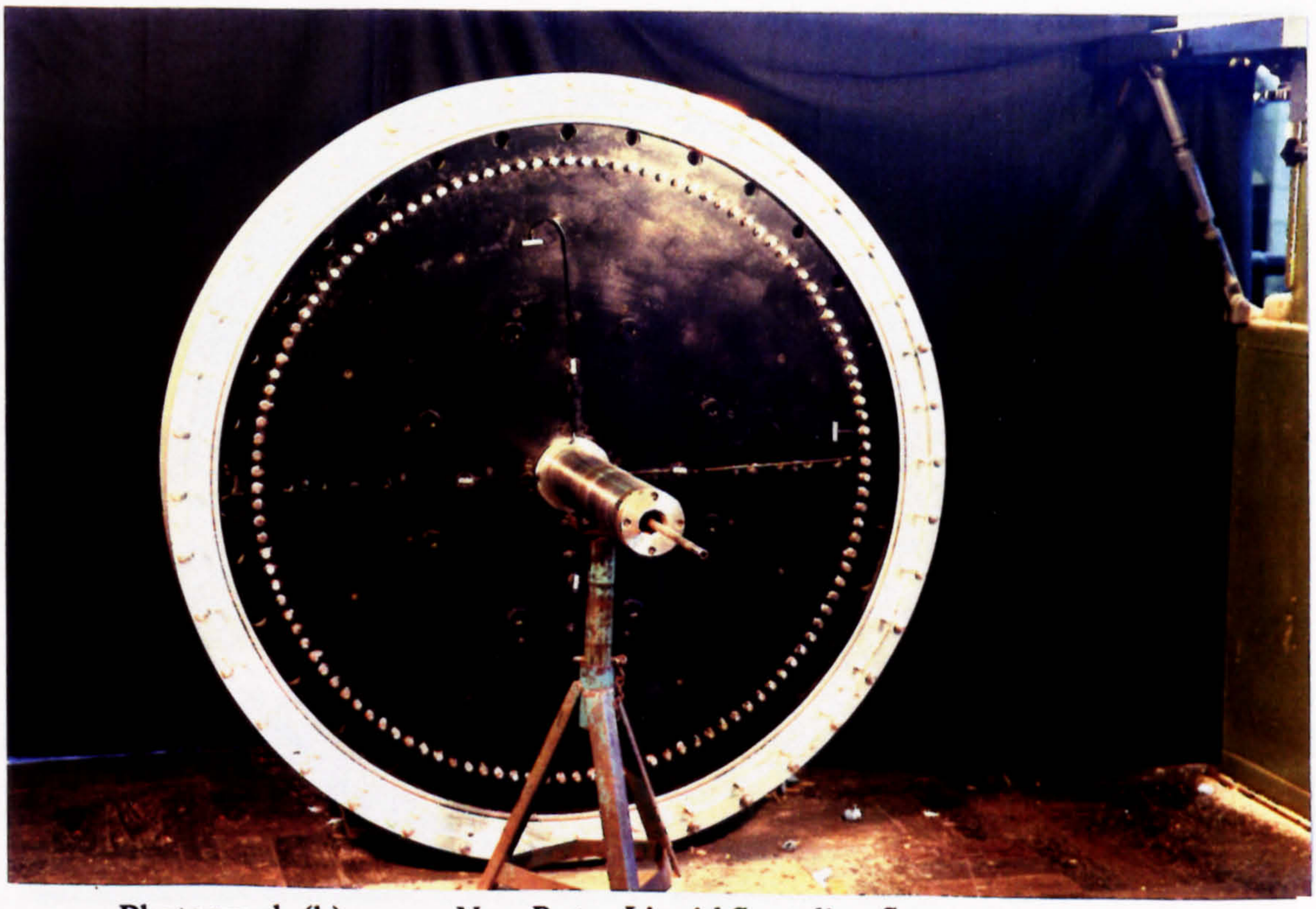

Photograph (b) : *New Rotor Liquid Sampling System*

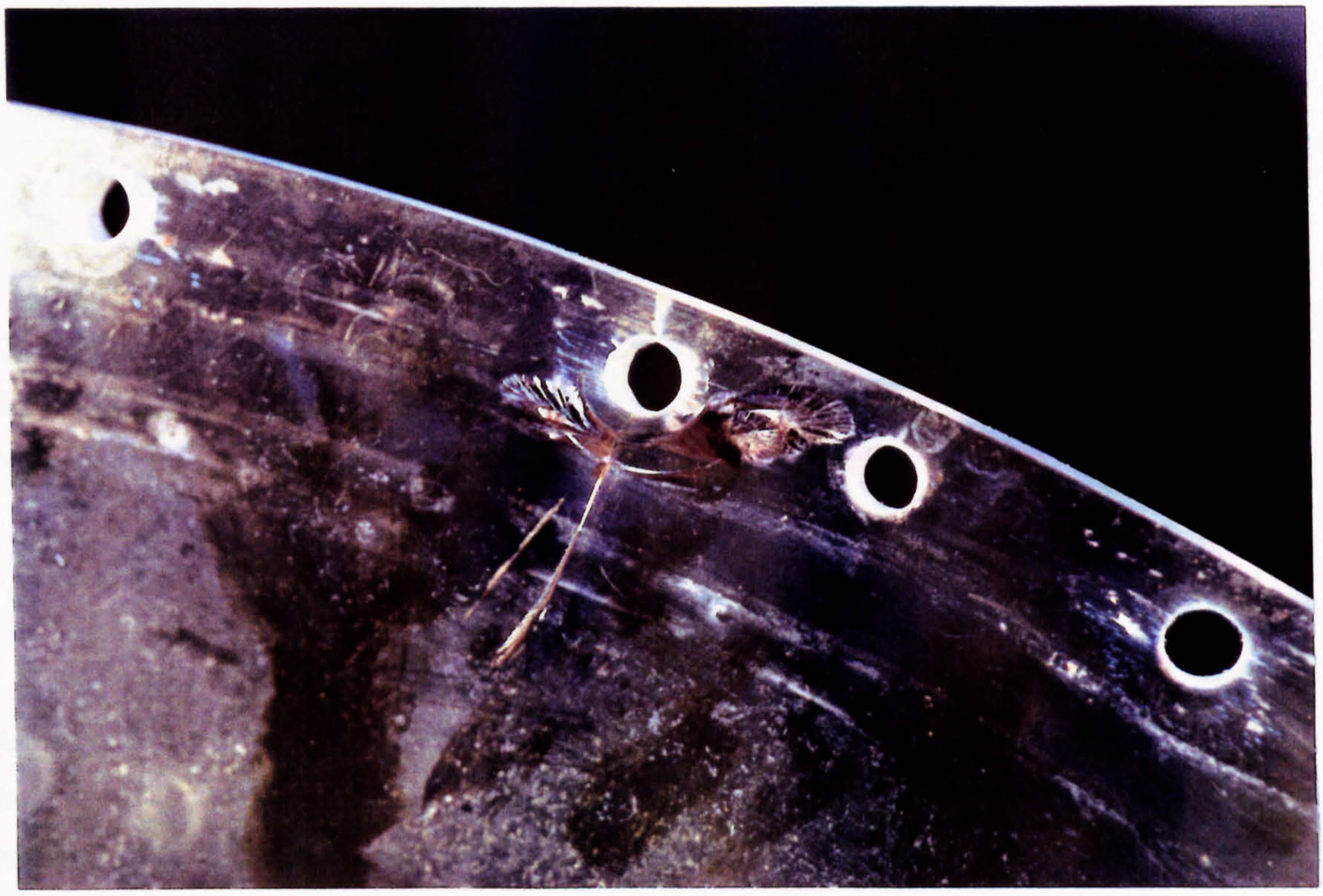

Photograph (c) : *Stress Fractures produced on the Polycarbonate Window*

Photograph (d) : *Salt Deposits found on Gas Injector Nozzles*

PUBLICATIONS

The following details publications resulting from this research :

The Hydrodynamic and Mass Transfer Characteristics of a Large Centrifugal Water De-oxygenator

Dr C R Howarth, Dr K Al-Shaban, Dr V Balasundaram, Professor C Ramshaw, Mr J R A Peel, Dept. of Chemical and Process Engineering, University of Newcastle-upon-Tyne, Newcastle-upon-Tyne, NE1 7RU. UK.

Abstract

A rotary stripper is being developed to de-oxygenate sea water to promote better oil recovery from marginal offshore oil fields. If the size of stripping equipment can be reduced and performance increased, there are benefits to be gained in terms of the reduced size and cost of the offshore platforms with consequential saving in energy. The characteristics of rotating contactors make them ideally suited for this type of duty therefore, in order to improve the design, small scale laboratory bubble impact studies together with mass transfer work on a 1m diameter de-oxygenator have been undertaken. 4.3 mass transfer units were obtained in this large unit, but it is clear that this can be improved if the maldistribution of the bubbles and the larger bubbles found in the peripheral zone of the packing can be eliminated.

(*Proceedings of the International Conference on Energy Efficiency in Process Technology, Athens 1992, pp.475 - 484, Elsevier Science Publishers © 1993*)